

ENGINEERING PHYSICAL STRUCTURE IN BIOMIMETIC
COLLAGEN SCAFFOLDS: STRATEGIES FOR
REGULATING CELL BEHAVIOR

By Ektoras Hadjipanayi, BA (Hons), MA, MB Bchir



University College London

Thesis submitted for the Degree of Doctor of Philosophy

July 2010

Institute of Orthopaedics and Musculoskeletal Science, University College London, Royal
National Orthopaedic Hospital, Brockley Hill, Stanmore, Middlesex, HA7 4LP

DECLARATION

I, Ektoras Hadjipanayi confirm that the work presented in this thesis is my own. Where information has been derived from other sources, i confirm that this has been indicated in the thesis.

ACKNOWLEDGEMENTS

Standing at the end of this road, I now look back and clearly see the importance of having the right people beside you, from the start. I express my most sincere gratitude to my primary supervisor, Robert Brown. Without his skillful guidance, emotional support and patience, I would certainly not have reached this far. He has been a true mentor to me, and for this I will always be grateful. I am also deeply thankful for all the help and invaluable advice i have received from my secondary supervisor, Vivek Mudera. His words will secretly accompany my every endeavour.

I would like to thank Umber Cheema for all her help, guidance and support over the last four years. It was a real privilege to work with such a charismatic researcher and I wish her all the best with her future career in science. Furthermore, I would like to thank especially some of my colleagues; Michael, Burcak, Laurent, Camilla, Ensanya, Rebecca, Sally, Dimitris, Michele, Fahad, Marcin, Ian and Neelam. I was truly blessed to have met them in my path and they have all, in different ways, shaped the way I now think of and approach research.

I would like to thank all the staff and students I have had the privilege of working with. I cannot name them all here, but their support has been invaluable, at a time when it was especially needed.

Last, but not least, I would like to thank my family. My two brothers, who have been there for me, throughout this challenging journey. My parents, who have put all their faith in me, and unconditionally supported my frustrations and aspirations at every level. I dedicate this thesis to them.

ABSTRACT

Tissue engineering has traditionally relied on the use of scaffolds as inert, durable materials for seeded cells to re-grow. However, a paradigm shift in the role of scaffolds has become necessary towards bio-functional ‘devices’ which directly mimic native tissue matrix. It is key to control extracellular matrix remodelling and tissue structure by building control cues into the initial cell support matrix. The aim of this study was to test the effect and predictability of physical cues, engineered into 3D native collagen scaffolds by a cell-independent fabrication method, Plastic Compression (PC).

Our findings indicated that fluid expulsion during collagen hydrogel compression produced anisotropic structuring and could be modelled as an ultrafiltration process. A groove/ridge topography engineered on collagen scaffolds through pattern-template-embossing influenced endothelial cell attachment/orientation and keratinocyte stratification in culture. Matrix collagen density and stiffness were directly related to its hydration level and could be controlled by limiting the extent of compression. Human-Dermal-Fibroblast (HDF) proliferation was proportional to matrix stiffness. In addition HDFs, seeded evenly within a PC collagen stiffness gradient, migrated and accumulated at the stiff end after 6 days. Bi-layer collagen matrices underwent cell-mediated integration, but despite higher cell migration across the interface in compliant than in stiff matrices at 24hrs, there was no significant difference in interface adhesive strength at 1 week. Core O₂ tension in 3D spiral constructs directly correlated with total cell number along the diffusion path, i.e. consumption path length. This model was used to engineer local cell-mediated hypoxia in 3D constructs to generate populations of hypoxia-induced-signalling cells

which produced angiogenic factor protein cascades. This in turn induced directed, functional micro-vascular ingrowth *in vitro* and *in vivo*.

These data indicate how directing physical cues can be built into the structure of biomimetic, tissue-like scaffolds. This helps to understand intricate cell-matrix behaviours without reliance on complex biological control mechanisms and points the way to using simple physical cues for tissue formation.

<u>CONTENTS</u>	<u>Page</u>
TITLE PAGE	1
DECLARATION	2
ACKNOWLEDGEMENTS	3
ABSTRACT	4
CONTENTS SECTION	6
LIST OF FIGURES	13
CHAPTER 1	18
INTRODUCTION	
1.1 BIOMIMETIC SCAFFOLDS FOR TISSUE ENGINEERING	18
1.1.1 Collagen-based scaffolds	24
1.2 ORGANISATIONAL LEVELS OF SCAFFOLD STRUCTURE	32
1.2.1 Biomimetic elements of nano-/micro-scale scaffold structure	34
1.2.2 Biomimetic elements of macro-scale scaffold structure	43
1.3 EFFECTS OF SCAFFOLD PHYSICAL STRUCTURE ON CELL BEHAVIOR	47
1.3.1 Effects of scaffold topography on cell function	47
<i>Topographic cell reaction on 2D substrates</i>	48
<i>Topographic cell reaction in 3D substrates</i>	52
<i>Specificity of cell reaction to patterned topography</i>	53
1.3.2 Effects of scaffold mechanics on cell function	54
<i>Cell proliferation</i>	54
	6

<i>Cell migration</i>	58
<i>Cell-mediated interface integration</i>	60
1.3.3 Effects of scaffold 3D spatial organisation on deep O ₂ cell perfusion	61
<i>Cell responses to changes in O₂ Microenvironment</i>	63
1.4 THESIS OVERVIEW	68
1.4.1 Hypothesis under test	69
1.4.2 Aims and Objectives	70
CHAPTER 2	72
MATERIALS & METHODS	
2.1 Cell culture	72
2.2 Formation of collagen gels	73
2.3 Plastic Compression of collagen gels	73
2.4 Scanning electron microscopy	74
2.5 Histology and immunohistochemical staining	75
2.6 Statistical analysis	76
CHAPTER 3	77
MECHANISMS OF STRUCTURE GENERATION DURING PLASTIC COMPRESSION OF NANOFIBRILLAR COLLAGEN SCAFFOLDS	
3.1 RESULTS	80
Testing of compression parameters	80
Structure-generating Mechanisms of Plastic Compression	83
Load-dependent vs. flow-dependent phase	88
Quantification of R _{FLS}	90
Correlation of R _{FLS} with C _{FLS}	92
Compression model development and validation	97
3.2 DISCUSSION	101
3.3 CONCLUSIONS	107

3.4 MATERIALS & METHODS	108
Collagen gel preparation and compression	108
Coomassie blue staining	109
SEM analysis of collagen gel structure along the compression axis	109
Collagen compaction assay	110
Measurement of FLS hydraulic resistance	110
Measurement of FLS collagen density	112
CHAPTER 4	115
ENGINEERING TOPOGRAPHY IN 3D COLLAGEN SCAFFOLDS: EXPANDING REGULATION OF EPITHELIAL CELL FUNCTION FROM SURFACES TO INTERFACES	
4.1 RESULTS	116
Topographic engineering by template embossing	116
2D culture model	119
3D culture model	124
4.2 DISCUSSION	129
4.3 CONCLUSIONS	137
4.4 MATERIALS & METHODS	138
Pattern template production	138
Microtextured topographic patterning of collagen constructs	140
SEM analysis of engineered topography	142
AFM analysis of engineered topography	142
Endothelial cell cultures	145
Development of skin equivalent	146
Histology and immunohistochemical staining	147
Polarized light microscopy	148

CHAPTER 5	149
CONTROLLING COLLAGEN MATRIX STIFFNESS: A TOOL FOR REGULATING CELL PROLIFERATION	
5.1 RESULTS	149
Fibroblast proliferation in free floating and attached matrices	149
Correlation of matrix collagen density with stiffness modulus	150
Effect of increasing matrix stiffness of fibroblast proliferation	151
Reversal of fibroblast quiescence	155
5.2 DISCUSSION	157
5.3 CONCLUSIONS	160
5.4 MATERIALS & METHODS	160
Collagen matrix models	160
Quantification of fibroblast proliferation	163
Measurement of collagen matrix Young's modulus	164
CHAPTER 6	165
A COLLAGEN MATRIX WITH GRADED DIRECTIONAL STIFFNESS: GUIDING CELL MIGRATION IN 3D	
6.1 RESULTS	165
Generation of stiffness gradient in 3D collagen matrices	165
Density gradient analysis	166
Fibroblast guidance by durotaxis in 3D collagen matrices	168
6.2 DISCUSSION	170
6.3 CONCLUSIONS	178
6.4 MATERIALS & METHODS	178
Fabrication of collagen constructs with graded stiffness	178
Measurement of collagen matrix Young's modulus	181
Quantification of density gradient	181
Cell-seeded constructs to test migration	182

Quantification of cell accumulation	182
-------------------------------------	-----

CHAPTER 7	184
------------------	------------

LAYERED COLLAGEN SCAFFOLDS WITH DEFINED MATRIX STIFFNESS: REGULATION OF CELL-MEDIATED INTERFACE INTEGRATION	
--	--

7.1 RESULTS	185
Finite Element Analysis of interface stresses	185
Interface integration of acellular vs cellular matrices	187
Effect of matrix stiffness on cell-mediated interface integration	189
Dependence of cell-mediated interface integration on cell migration	190
Interface structural analysis	192
7.2 DISCUSSION	193
7.3 CONCLUSIONS	199
7.4 MATERIALS & METHODS	199
Bilayer collagen scaffold development	199
Interface models	200
Finite Element Analysis	202
Assessment of mechanical integration of interfaces	203
Assessment of cell migration	204
SEM interface analysis	205

CHAPTER 8	206
------------------	------------

IDENTIFICATION OF KEY FACTORS IN DEEP CELL O₂ PERFUSION	
---	--

8.1 RESULTS	207
Correlation of core O ₂ tension with construct cell density	207
Correlation of core O ₂ tension with consumption path length	209

Comparison of PASMC vs HDF viability in static cultures	210
Effect of dynamic perfusion on PASMC viability	213
8.2 DISCUSSION	215
8.3 CONCLUSIONS	222
8.4 MATERIALS & METHODS	223
Preparation of 3D Plastic Compressed collagen gel constructs	223
Oxygen monitoring	224
Quantification of cell viability	227
Dynamic perfusion cell culture	227
CHAPTER 9	229
CONTROLLING PHYSIOLOGICAL ANGIOGENESIS BY HYPOXIA-INDUCED SIGNALLING	
9.1 RESULTS	230
<i>In vitro</i> induction of angiogenesis by hypoxia-induced signalling	230
Hypoxia-induced generation of angiogenic factors	237
Reversal of angiogenic response to hypoxia-induced signalling	240
Matrix remodelling during angiogenic induction	241
<i>In vivo</i> vascularization of constructs by hypoxia-induced signaling	244
9.2 DISCUSSION	251
9.3 CONCLUSIONS	258
9.4 MATERIALS & METHODS	259
Scaffold fabrication and culture	259
Quantification of IgG permeability through compressed collagen	263
ELISA	263
Implantation of collagen constructs	264
<i>In vivo</i> Oxygen monitoring	265
Tissue processing and immunohistochemical staining	266
Image analysis	266

CHAPTER 10	268
10.1 GENERAL DISCUSSION	268
10.2 CONCLUSIONS	286
10.3 SUMMARY	287
10.4 FUTURE WORK	288
REFERENCE LIST	291
APPENDIX	315
TABLE OF ABBREVIATIONS	315
LIST OF SYMBOLS	316
PUBLICATIONS	317

Figure 3.10 Correlation of FLS collagen density (C_{FLS}) with FLS hydraulic resistance (R_{FLS})	96
Figure 3.11 Compression model validation	99
Figure 3.12 Effect of changing pressure during compression on discharge rate	100
Figure 3.13 Schematic of experimental setup for stirred cell ultrafiltration unit	112

CHAPTER 4

Table 4.1 Dimensions of grooves embossed in collagen substrates patterned with two different phosphate-based glass fibre diameters	116
Figure 4.1 SEM and AFM analysis of patterned topography	117
Figure 4.2 Schematic showing how the expected groove depth can be calculated	119
Figure 4.3 Comparison of HUVEC adhesion for smooth (non-patterned) substrates and substrates patterned with a template of 36 μ m or 53 μ m diameter fibres	120
Figure 4.4 Endothelial cell viability/proliferation on smooth substrates and substrates patterned with a template of 36 μ m or 53 μ m diameter fibres	121
Figure 4.5 Endothelial cell alignment on collagen substrates with a patterned groove topography	122
Figure 4.6 Endothelial cell orientation on smooth and patterned substrates	123
Figure 4.7 Incorporation of microtopography at the dermo-epidermal (DE) interface influences keratinocyte stratification/differentiation	125
Figure 4.8 Effect of topography of the dermo-epidermal interface on epidermal thickness	126
Figure 4.9 Analysis of epidermal differentiation and keratin structure in constructs with smooth and patterned dermo-epidermal interfaces	128
Figure 4.10 Schematic showing oriented areas of keratin in human callus	136
Figure 4.11 Pattern template used for embossing	139
Figure 4.12 Schematic showing the two-step process used to create micro-topography on the surface of collagen scaffolds	141

CHAPTER 5

Figure 5.1. Proliferation of adult dermal fibroblasts cultured in attached and free floating (FF) collagen matrices	150
Figure 5.2 Correlation between matrix collagen density and stiffness modulus	151
Figure 5.3 Proliferation of adult dermal fibroblasts in PC collagen gels	152
Figure 5.4 Effect of increasing matrix stiffness on fibroblast proliferation	154
Figure 5.5 <i>In situ</i> plastic compression of free floating matrices reverses human dermal fibroblasts quiescence	156
Figure 5.6 Controlling fluid loss and matrix collagen density by plastic compression	162

CHAPTER 6

Figure 6.1 Engineered stiffness gradient analysis	166
Figure 6.2 Density gradient analysis	167
Figure 6.3 Fibroblasts seeded in collagen matrices with a built in stiffness gradient exhibit durotactic migration	169
Figure 6.4 Schematic showing three possible 3D spatial arrangements of rectangular collagen sheets containing a stiffness gradient	172
Figure 6.5 Theoretical, predicted plot of the dual antagonistic effects of increasing matrix density on overall average cell speed	176
Figure 6.6 Fabrication of collagen constructs with a gradient of biomaterial matrix stiffness	179
Figure 6.7 Schematic showing how the % fluid loss and % collagen density at the two ends and middle region of a construct can be calculated	180

CHAPTER 7

Figure 7.1 Analysis of interface stresses by Finite Element Analysis	186
Figure 7.2 Interface integration of acellular and cell-seeded bi-layer collagen constructs	188
Figure 7.3 Comparison of cell-mediated interface integration of stiff vs. compliant bi-layer matrices	190
Figure 7.4 Comparison of cell migration across the interface in compliant	

	and stiff collagen matrices	191
Figure 7.5	Interface structural analysis for acellular, stiff and compliant cell-seeded bi-layer constructs	193
Figure 7.6	Experimental setup for measuring interface integration in bi-layer collagen constructs	201
Figure 7.7	Assessment of cell migration out of cell-seeded collagen matrices using the 'nested collagen matrix' model	205
CHAPTER 8		
Figure 8.1	Correlation O ₂ tension in the core of 3D collagen constructs with cell density and cell type	208
Figure 8.2	Effect of increasing consumption path length on core O ₂ tension	210
Figure 8.3	Comparison of PASMCM core and surface viability over a 6 day culture period	211
Figure 8.4	Dynamic perfusion increases PASMCM viability	214
Figure 8.5	Schematic showing how O ₂ tension could be 'tuned' within a 3D layer/sheet-based scaffold	218
Figure 8.6	Comparison of core and surface cell viability for 3D collagen constructs seeded with HDFs or PASMCMs at high density over 6 days static culture	220
Figure 8.7	Experimental setup used for monitoring O ₂ tension in the core of 3D collagen constructs	226
Figure 8.8	Schematic showing setup used for dynamic perfusion culture of constructs	228
CHAPTER 9		
Figure 9.1	Induction of <i>in vitro</i> angiogenesis by hypoxia-induced signalling (HIS)	232
Figure 9.2	Localised exposure of HDFs to physiological hypoxia resulted in up-regulation of angiogenic factor protein expression <i>in vitro</i>	239
Figure 9.3	Blocking the function of VEGF only partially abolished the angiogenic response to hypoxia-induced signalling	241

Figure 9.4	Localised exposure of HDFs to physiological hypoxia results in up-regulation of angiogenic factor-regulated MMPs <i>in vitro</i>	243
Figure 9.5	Hypoxia-induced signalling <i>in vivo</i> promoted rapid vascularization of cellular constructs	245
Figure 9.6	Assessment of the functionality of invading host blood vessels into implanted constructs by real-time monitoring of O ₂ levels <i>in vivo</i>	249
Figure 9.7	Schematic showing the proposed 3D spatial organisation of angiogenic factor gradients in the <i>in vitro</i> model used to investigate the induction of angiogenesis by hypoxia-induced signalling	254
Figure 9.8	Experimental design for development of constructs used for <i>in vitro</i> and <i>in vivo</i> testing	261

CHAPTER 10

Figure 10.1	Anisotropic material properties form the link between mechanical, chemical and topographic cell control processes	271
Figure 10.2	Schematic illustration of how a tissue-like multidimensional map could be ‘encoded’ into the structure of a 3D biomimetic scaffold for driving/regulating cell function	281
Figure 10.3	Schematic showing the proposed model of dynamic interplay of scaffold structural elements for regulation of cell function	284

CHAPTER 1

INTRODUCTION

1.1 BIOMIMETIC SCAFFOLDS FOR TISSUE ENGINEERING

Tissue engineering is a multi-disciplinary field where biology, material science, modelling and engineering combine towards the development of biological substitutes that restore, maintain, or improve tissue function [1]. Tissue engineering has traditionally relied on the use of scaffolds as temporary surrogates for the native extracellular matrix (ECM) to host cells harvested from natural tissue. In that respect, the role of scaffolds was limited to that of ‘cell-friendly’ vehicles that could support cell viability/growth and efficiently deliver the cells to a target site (e.g. wound bed, bone repair site etc.). However, the field is currently experiencing a steady progression away from this minimalist concept of cell scaffolds as largely inert (i.e. inoffensive or bio-invisible) and long-lived as possible. The concept of biomimetic scaffold fabrication has instead evolved around the principle that scaffolds should confer bio-functionality, along with biodegradability. This need is indeed reflected in a recent definition of tissue engineering by Williams as “*the creation of new tissue for the therapeutic reconstruction of the human body, by the deliberate and controlled stimulation of selected target cells, through a systematic combination of molecular and mechanical signals*” [2].

The underlying big question then shifts from how functionally durable and stable can we make scaffolds to how much dynamic cell-control information can we get into their temporary structure. In other words, we are now facing a *cellular control* question. It is important, however, to understand that at present incorporation of ever

more biological function into scaffolds will come at the price of having to surrender some of the excellent properties (e.g. physical function, durability) of conventional prosthetic implants (e.g. metals, polymers, ceramics). Furthermore, there is a wide consensus that these new forms of clinical implants will only live up to their promise if they are cell-seeded. Indeed this is the basis for rapid expansion of interest in technologies for cell acquisition (autologous, allogeneic, even xenogeneic), as adult and embryonic stem/progenitor cells. However, it is also increasingly clear that production of the cells alone is only part of the answer. Tissue architecture is the key to native function in solid 3D implants[3]. This is particularly true in mammalian connective tissues, which almost always undergo repair with scarring, rather than functional regeneration [4]. Inevitably, then, advanced, biomimetic 3D scaffolds will be required to provide the range of controls for cell functions that critically determine tissue organization e.g. differentiation, migration, and extracellular matrix production [3].

Accumulating evidence now suggests that these key cues most often need to be *built into* the structure of the scaffold extracellular matrix, as they are in nature[3,5]. In other words, these are best considered as biomimetic cues, rather than supra-physiological doses of single cytokines, growth factors, or pharmacological agents. The exact nature of such cues will depend on the type of tissue we want to repair/replace. For highly cellular tissues (e.g., secretory, metabolic, and barrier), cellular control will be dominated by cell–cell controls such as cell signalling (e.g. growth factor levels), cell perfusion and nutrient (e.g. O₂, glucose) consumption and cell adhesion. For connective and contractile tissues, the emphasis is on mechanical

and substrate properties, 3D topographical and directional cues, including external mechanical-loading, and neuro-vascular innervation.

The spatial dimensions of a scaffold form one of the fundamental criteria as to what constitutes biomimesis. It is self-evident that use of a scaffold, as opposed to a flat culture surface, is the essence of growth in three dimensions. From the cell viewpoint, the pivotal feature for cells in a scaffold is not that they are able to grow in a vertical plane (gravity itself has minimal direct controlling effect on cells as they have such small mass). Rather, substrate attachment cues can and do act through all three axes of the cell, generating completely new directional information, comparable to that in tissues. These can be homogeneous or polarized, in contrast to two-dimensional monolayer cultures that always provide polarized directional cues, with a 'dorsal' fluid-covered surface and a 'ventral' plastic-attached surface. Clearly, this is not a native system for non-epithelial cells such as fibroblasts or other stromal cells.

Early examples of 3D scaffolds concentrated on basic properties of pore size (to allow cell 3D penetration and perfusion) and stability (rates of disappearance from beneath the cells they support). The bulk fabric of such scaffolds can be divided into either:

(1) Synthetic polymer base, especially polylactide/glycolic acids [1,6]

or

(2) Bioartificial natural polymers such as collagen/ collagen-GAG (e.g. Integra) sponges [7], collagen gels[8], and fibrin[9].

This has proved to be a key division, seen most clearly in the respective approaches to the question of scaffold degradation. It is inescapable that for any form of 3D engineered tissue, the initial scaffold must disappear. Importantly, disappearance needs to relate to the production of new, replacement tissue from the resident cells. Given the diversity of physicochemical conditions at any given implant/pathological/injury site, this level of control is almost inconceivable for conventional biodegradable polymers. This is because they hydrolyze/dissolve in a manner *independent* of cell activity. On the other hand, scaffolds constructed from native protein aggregates commonly are susceptible to metabolism by the normal array of extracellular matrix proteases. In other words, biomimetic (native protein-based) scaffolds represent a natural part of the cell-matrix economy (participating in biological turnover and remodeling). They will tend to be removed by cell action as new matrix is produced. This is not possible for conventional polymers, which either disappear too rapidly, providing poor support, or more commonly disappear too slowly, inhibiting or counteracting cell-based renewal[3]. The scaffold removal-replacement cycle is known to be central to tissue formation both during growth and natural repair[10-12]. In connective tissues, it is a coordinated, cell-dependent process in which a series of scaffold proteins are sequentially deposited and then replaced by more permanent substrates. Although it is neither feasible nor desirable to try to mimic the entire sequence, cells clearly will not be able to fabricate native structures if they are actively blocked from completing the sequence. Such blocking is likely where the mechanical support/attachment cues of a synthetic polymer fail to disappear and so dominate the cell mechanical environment [3].

A fundamental question to scaffold design is how much or how little similarity with the target tissue is needed for it to qualify as biomimetic. In other words, does the exquisite design of the target native tissue need to be faithfully reproduced in order to achieve adequate function? If true, the objective is equivalent to engineering native tissue, which clearly is not realistic at present. The success of tissue engineering therefore rests on the assumption that adequate function can be achieved via compositions and structures that are much simpler than the native tissues, and which are realizable via manipulation of cells and biomaterials *in vitro* [13]. An example of this is bioprosthetic heart valves comprising bovine pericardium that yield adequate function despite lacking the trilayered structure of native leaflets [13]. Evidently, the development and analysis of tissue models to identify solutions consistent with adequate function would aid in identification of realizable objectives for achieving similarly successful outcomes. In view of the huge diversity of tissues it is possible to mimic, this can be simplified by considering two extreme types of construct design: *cell-rich* and *matrix-rich*. Naturally, there are many intermediate types, and frequently the aim is to develop one format into the other over a time period. However, it is clear that many systems at least start as either cell-rich or matrix-rich constructs. The aim with a cell-rich construct (an extreme example would be engineered cell sheets [14,15]) is to produce 3D structured adherent cell masses. Such constructs most closely resemble embryonic tissue templates (prior to full stromal differentiation and matrix accumulation, e.g. limb buds) or soft tissue glands and organs (e.g. pancreas and kidney) with limited connective tissue content. Matrix-rich constructs, on the other hand, are commonly designed to develop significant mechanical function, including support and/or contraction. Examples include tube structures such as blood vessels, urothelial replacements, and nerve

guides. For many, if not most current applications (particularly for clinical implants), mechanical function is paramount, and production of a strong extracellular matrix to replace the initial scaffold is essential. Clearly cell layers/sheets alone have limited mechanical strength. As a result, 3D cell-rich constructs are important for biomimesis of certain tissues and developmental stages, but the overwhelming majority must either be designed as, or become matrix-rich constructs.

Lessons learned from years of grafting experience emphasise the necessity of an instantaneous restoration of certain functions (e.g., covering a skin wound or repairing a ruptured tendon) without waiting for *de novo* tissue formation, while at the same time creating an environment in which better function is eventually restored through regenerative processes (e.g., integration of a bone graft or restoration of nerve function). The initial design requirement of an implantable device then seems to be that it must mimic the structure and function of the tissue involved sufficiently well to form an initial repair template, while providing an environment for final structure and function to be reconstituted *in situ*.

The discussion thus far highlights certain basic elements that a biomimetic scaffold must possess; it should be three-dimensional, rich in matrix that is able to undergo cellular remodelling, and have built in physicochemical cues for directing cell behaviour. Central to this design lays the ability of cells to function as ‘*structure regulators*’ that, given the appropriate environment, can synthesize, dismantle, and modify the extracellular matrix. In theory, then, if the right cells are given the right environment, a perfect tissue can be grown and maintained using the innate processes that have evolved so successfully. Therefore, the complex nature of tissue

structure and the ability of cells to create and maintain it dictates that the scaffold logically needs to be sufficiently robust to support strictly local cell/tissue function (immediate repair) without taking on *prosthetic* functions which frequently impair local cell-based regeneration. Critically, as discussed above, such scaffolds need to be susceptible to cell-mediated remodeling (after implantation). Because following cellular remodelling the *actual* extracellular matrix environment rapidly becomes protein-based (either as molecular attachment elements or bulk ECM material), principally collagen, this work has focused on how cell controlling cues can be adapted and incorporated into the physical structure of 3D biomimetic collagen scaffolds. The following section provides a brief introduction into the area of collagen-based scaffold fabrication and how this relates to our approach.

1.1.1 Collagen-based scaffolds

The collagens are a large complex family of molecules that interact with each other and the other ECM molecules to provide a huge range of structures and functions throughout the tissues of the body. For most soft and hard connective tissues (bone, cartilage, tendon, cornea, blood vessels, and skin) collagen fibrils and their networks play a dominant role in maintaining the biologic and structural integrity of ECM, while being highly dynamic, undergoing constant remodeling[16]. In addition to their key functional role as biomechanical structures, the collagens interact directly with cells to influence adhesion, growth, differentiation, and many other cellular activities in addition to interacting with growth factors and cytokines during tissue development and repair.

Collagens are a family of proteins (28 molecular species having been identified to date[16]) that share a triple helical structure formed from three α -chains. This structure is dependent upon each α -chain containing an amino acid sequence with a repeating (Gly-X-Y) tripeptide, where X and Y are frequently proline and hydroxyproline. The triple helices may be homotrimers or heterotrimers with various α -chain combinations. The various types of collagen exhibit differences in structure, splice variants, the presence of additional non-helical domains, the extent of glycosylation and hydroxylation, and their assembly and function [17]. The most abundant group within the collagen family are the fibril-forming collagens (types I, II, III, V, and XI) which assemble into highly organized supramolecular fibrils. The process of collagen self-assembly is only partially understood and is thought to involve no fewer than nine separate steps (Fig.1). The complex structure of fibrillar type I collagen presents different morphologies in different tissues performing different functions. When associated with HA crystals in bone, it provides rigid and shock-resistant tissues with high Young modulus, while it behaves like an elastomer with low rigidity and high deformation to rupture in tendon and shows optical properties such as transparency in cornea[16]. Other than the fibril-forming collagens, there are non-fibrillar collagens, the most important of which is type IV, the principal component of basement membranes, where it integrates other ECM molecules (e.g. laminin) into sheet aggregates. In addition, there are also the fibril-associated collagens with interrupted triple helices (types IX, XII, XIV, XVI, XIX, and XX) which tend to be located on the surface of collagen fibrils in a tissue-specific manner. Type VI is a microfibrillar collagen that forms a distinct network of fine filaments throughout most connective tissues, while the short chain collagens (types X and VIII) form hexagonal networks.

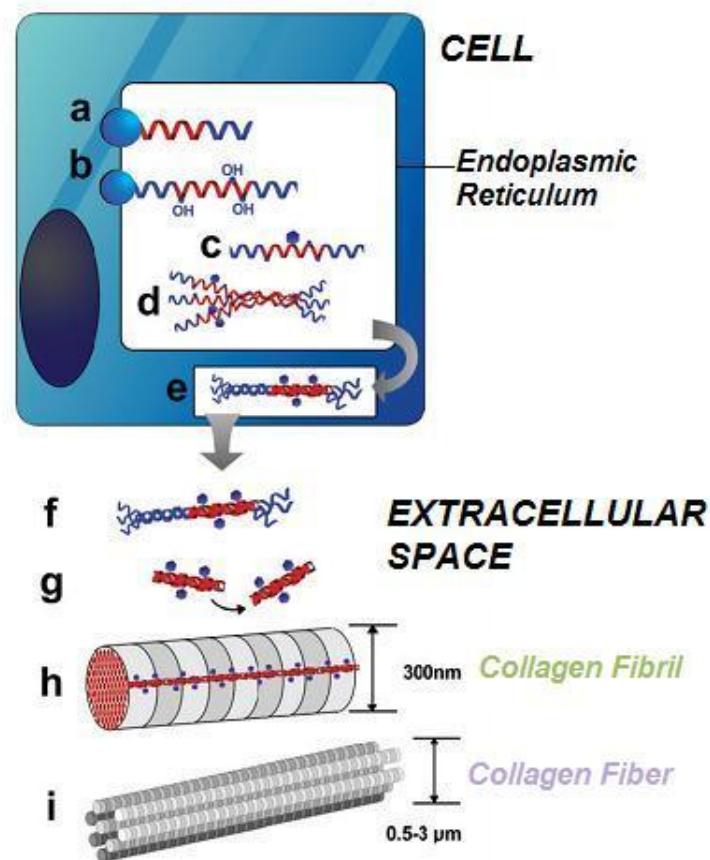


Fig.1 Schematic showing the natural assembly of collagen fibers. (a) Pro- α chains are synthesized in the lumen of the endoplasmic reticulum, where (b) hydroxylation of selected prolines and lysines occurs. (c) This is followed by glycosylation of selected hydroxylysines. (d) Three pro- α chains self-assemble and (e) form a procollagen triple helix. (f) These are secreted into the extracellular space, and (g) the protective propeptides are cleaved. (h) Finally, the procollagen self-assembles into fibrils, and (i) these aggregate into collagen fibers. Modified from Stevens and George, 2005 [5].

Collagen as a basic biomaterial has been used for a considerable period in various forms such as injectable fillers for cosmetic surgery (e.g., Zyplast, Zyderm, Contigen)[18], meniscal implants (CMI), and tubes for blood vessel, nerve and skin repair (e.g. Integra, Apligraf)[19]. These kinds of applications exploit the low antigenicity of collagen (collagen varies little between species) and the lack of

harmful breakdown products (because it is an endogenous ECM protein), and have established the general clinical acceptability of using collagen from bovine and porcine sources. Some studies use atelocollagen in which the proteolytic removal of the non-helical, telopeptide extensions to the collagen molecule could further reduce the immunogenicity of implanted collagen [20]. This history of collagen usage (in terms of safety and biocompatibility) adds to the suitability of using collagen as the basis for more advanced tissue engineering applications.

We can distinguish between two general strategies that have been employed for utilisation of collagen as a biomimetic protein for scaffold fabrication. The first, *top-down* approach, takes a complex collagen-rich matrix (whole connective tissue, sometimes, the actual tissues from cadavers or animals) that resembles the required architecture and removes all cell components. The second, *bottom-up* approach, starts with the molecular building blocks and aims to assemble them into a scaffold. Therefore, while the *top-down* approach tends to break down or reduce the complexity of native tissues, the *bottom-up* approach works to assemble or engineer increasing complexity using simple, isolated collagen-based building blocks. Examples of each approach with some of their applications are summarised in Table 1.

<i>TOP-DOWN APPROACH</i> <i>Decreasing Complexity</i>		<i>BOTTOM-UP APPROACH</i> <i>Increasing Complexity</i>	
EXAMPLE	APPLICATION	EXAMPLE	APPLICATION
Small Intestinal Submucosa (SIS) (from bovine jejunum) [21]	Ureter/Urethra repair Bladder augmentation Dural/Skin Substitute Vascular Grafts Rotator cuff repair	Collagen Hydrogels -Cell-mediated contraction [8] -Fibrillar alignment (e.g. by magnetic fields,tethering, uniaxial-tensile loading) [22-24] -Plastic Compression[25-27]	Skin-substitutes(e.g. Apligraf) Nerve repair Skin,muscle,blood vessel,bladder,bone, corneal constructs
Urinary-Bladder Submucosa [21]	Orthopaedic-soft tissue repair	Porous Scaffolds -Sponges (freeze-dried dispersions of collagen fibers +/- cross-linking)[28-31] -Foams [32]	Absorbable-wound dressings Absorbable-haemostatic sponges Dermal Substitutes (e.g. Integra, Neuragen, OrCell) Growth factor (e.g. BMP) /drug release depots Bone tissue engineering
Acellular Dermis [21,33]	Skin Substitutes	Fibrous Scaffolds Molecular self-assembly of collagen into fibrils / fibers and bundles [34]	Nerve repair
Amniotic Membrane [35,36]	Corneal repair	Electrospun Collagen Nanofibers (combined with other materials e.g. elastin,gelatin,glyco-saminoglycans, silk,fibrinogen, chitosan,synthetic polymers)[34,37-40]	Bioresorbable-vascular grafts

Table 1. Comparison of the two general strategies employed for utilisation of collagen as a biomimetic protein for scaffold fabrication, i.e. by progressive reduction in complexity of native, living tissues (left hand columns) vs. by assembly (engineering) to increase the complexity of isolated elements (right hand columns). The table summarises examples of each strategy with their relevant applications. This study is focused on the use of Plastic Compression fabrication for engineering structure in collagen hydrogel scaffolds (highlighted).

The advantages of using native ECM grafts are that (1) although they are predominantly collagen, they also contain the other ECM proteins in their final relative proportions [21], (2) some of their 3D structure is maintained [21,41] and (3) a dense, native collagen matrix is provided immediately [21]. However, use of ‘ready-made’ ECM has several limitations: (1) newly added cells have to repopulate a very dense, relatively impervious material, which can be slow, uncontrolled, and associated with major remodelling, (2) it is critical that all debris of the previous cell population is removed to avoid the problems of human and non-human grafts/transplants (residual antigens in animal tissues or cryptic infectious materials represent a major immunity/infection hazard), (3) removal of such cellular and macromolecular elements through the dense 3D structure, without disrupting it, is clearly problematic and (4) use of human (cadaveric) materials tends to have the same supply-limit problems of many other transplant organs. Therefore, when regeneration is considered to be the ultimate aim, it is unlikely that this approach alone will be sufficient to recapitulate the cellular responses observed during *de novo* tissue development. Because the cellular component is so intimately related to the matrix component in all tissues, as previously discussed, integrated cellular/ECM scaffolds which are simpler in terms of their composition and architecture represent the most promising emerging technologies for regenerative repair [3]. This approach

enables cells and matrix to develop *in parallel* to recapitulate the developmental pattern of tissue generation and furthermore allows the rational incorporation of factors such as alignment, architecture, growth factors, differentiation, and so forth, based on increased understanding of regenerative processes.

Extensive work has previously been carried out on porous collagen scaffolds, in particular collagen sponges, as these provide a useful substrate for the bulk delivery of cells[42,43]. However, due to their large pore size, their 3D architecture which the cell perceives is *pseudo-3D* (see next section), and is therefore unlikely to provide the kinds of topographic/mechanical cues conducive to the alignment required in many tissues. Indeed, their primary usefulness has been in tissues in which initial fiber alignment is not necessarily critical for function (e.g. skin replacement). In contrast to collagen sponges, collagen hydrogels comprise nanoscale fibers and therefore represent true 3D substrates. They have a long track record as potential scaffolds for tissue modeling and repair/regeneration applications [8,9,44]. Although they have been developed for a variety of therapeutic uses, including the sustained delivery of soluble factors, their major application is as substrates for the growth and delivery of cells [45], which can be easily seeded interstitially within the fibril network. This is because collagen hydrogels provide the necessary engineering properties desired in a non-immunogenic ECM-like scaffold, including water retention capacity, tenacity for holding cells in stretched position, nano/microporosity to allow cells to grow and arrange in 3D (after seeding), biodegradability to create space for nascent cells and pore inter-connectivity to allow free flow of oxygen and nutrients in and around the growing cell mass[46].

The general principal underlying collagen hydrogels is that purified fibrillar collagen (typically type I but occasionally other types or blends) in acidic solution can be adjusted to physiological (neutral) pH and temperature to form a stable gel [47]. Solubilised collagen monomers are known to spontaneously self-assemble into native type fibrils under physiological conditions [48]. This process is essentially pre-programmed into the protein primary and helical structure and is driven by electrostatic, hydrophobic and covalent interactions between monomers [49]. Gels take between 5 and 30 minutes to set at physiological pH and room temperature, allowing them to be molded into shape and/or seeded with cells. Fibrillar collagen gels therefore comprise a network of intertwined collagen fibrils of indeterminate lengths, various thicknesses, and no inherent orientation. Importantly they have a large excess of fluid (>99.5%) to collagen protein (0.1 and 0.5%) [50], which is typically two orders of magnitude lower collagen density than native connective tissues. This results in poor mechanical properties which, together with the lack of orientated architecture, forms a principal limitation in the use of collagen hydrogels as scaffolds for tissue engineering applications [9,13,33,50]. It is well known that cells seeded within a collagen hydrogel can expel some of this excess interstitial fluid from the gel [8] and increase the collagen density by around one order of magnitude by exerting traction forces on their surrounding fibres [51]. This process, however, can take several days and gives only a modest increase in mechanical strength with limited precision and control.

Brown et al. previously reported that a compressive load can be applied on hyperhydrated collagen hydrogels to rapidly expel a large proportion of the fluid content through the basal surface of the gel. This takes a small fraction of the time

required for cell-driven compaction and takes the process to much higher collagen densities (>20% wet weight) without cell damage [25]. The development of the Plastic Compression (PC) fabrication process (see Chapters 2 for full description of method) was critically influenced by the realization that the excess fluid present in untreated collagen gels is a result of the casting rather than any inherent swelling property of the polymer i.e. this fluid is not bound and does not form any part of the native collagen structure. In fact, this is a major cause for the poor mechanical properties of pre-compressed gels [52]. PC of collagen hydrogels rapidly produces dense fibrillar collagen sheets (100-200µm thick) with a tissue-like architecture, strong mechanical properties (approaching those of native tissue collagen) and biomimetic function (e.g. supporting high cell viability) [25]. This process is versatile in terms of the volumes, densities, and shapes that can be produced (e.g. sheets can be layered or rolled up), thus creating the possibility to fabricate a wide range of final scaffold structures. Indeed, several studies have demonstrated the suitability of PC collagen scaffolds in engineering biomimetic tissue constructs e.g. skin [53], bladder [27], muscle [54], blood vessel [55], bone [26] and cornea [56].

1.2 ORGANISATIONAL LEVELS OF SCAFFOLD STRUCTURE

Regeneration and production of functional tissue is the ultimate goal in Tissue Engineering. The human body comprises about 100 trillion cells, with about 260 different phenotypes, that divide, differentiate and self-assemble over time and space into an integrated system of tissues and organs[46]. Evidently, biomimetic tissue engineering is no mean task. Artificial biomaterial scaffolds designed to support cell and tissue growth have traditionally aimed on a macroscopic level to match the gross architecture and mechanical properties of the organs they are to replace (e.g. hard

scaffolds for bone and elastic for bladder, veins, and arteries), without recreating the complexity and, nano-, micro- and meso-scale detail observed in real organs, at the level of the cell-matrix interaction[5]. However, this organisational complexity is not only intrinsic to the native structure of organs, but also vital for their specific functionality (Fig. 2). It is self-evident, therefore, that the structure of a biomimetic cell scaffold should incorporate the length-scale hierarchical organisation of the target tissue, and not merely provide a morphologically ‘correct’ cell carrying template.

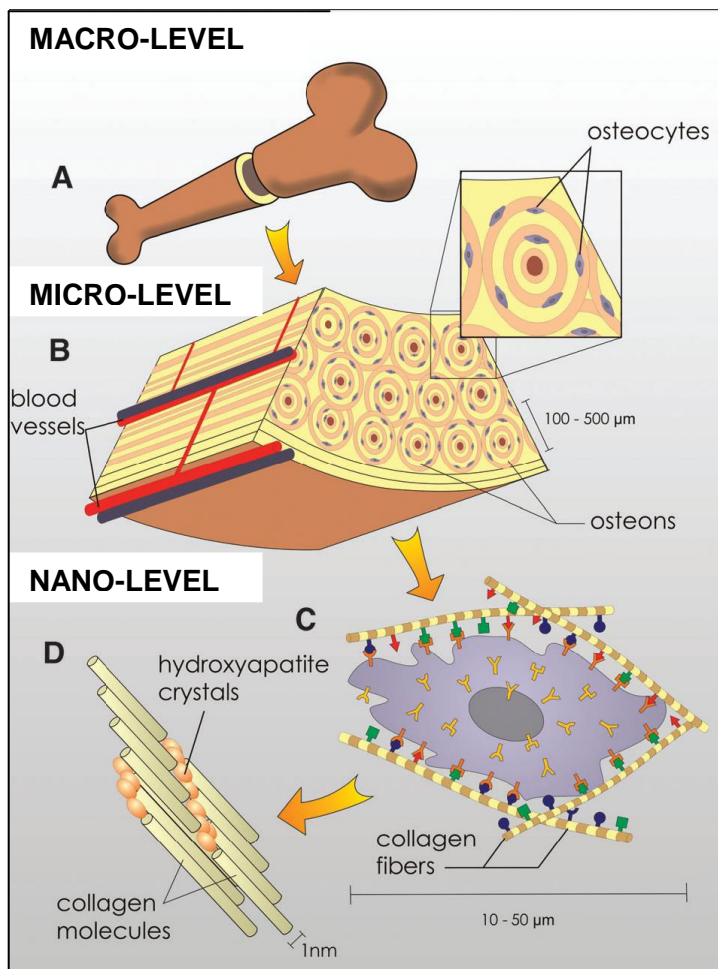


Fig.2 Hierarchical organization of bone over different length scales. Bone has a strong calcified outer compact layer (A), which comprises many cylindrical Haversian systems, or osteons (B). The resident cells are coated by multiple cell membrane receptors that respond to specific binding sites (C) and the well-defined nano-

architecture of the surrounding extracellular matrix (D). Modified from Stevens and George, 2005 [5].

While real tissue structure is remarkably characterised by continuous variation across the whole length-scale spectrum (i.e. from subcellular to cellular and organ level), our ability to reproduce this into the structure of scaffolds is currently far below optimal[5]. It is possible, however, to make a defined distinction between nano-/micro-scale and macro-scale structural elements that can be engineered into the structure of scaffolds to improve their cell-regulating capacity and ultimately their bio-functionality. Such properties affect not only cell survival, signalling, growth and reorganization, but also play major roles in influencing cell shape and gene expressions that relate to cell growth and the preservation of native differentiated phenotypes[57]. In this section we discuss important aspects of hierarchical native tissue organisation and present recent advances in attempts to incorporate such elements into the structure of biomimetic scaffolds. In the context of this work particular emphasis is placed on physical structure (as opposed to chemical structure) fabrication.

1.2.1 Biomimetic elements of nano-/micro-scale scaffold structure

In the body the nanoscale structure of the ECM provides a natural web of intricate nanofibers to support cells and present an instructive background to guide their behavior [58,59]. Unwinding the fibers of the ECM reveals a level of detail unmatched outside the biological world. Each fiber hides clues that pave the way for cells to form tissues as complex as liver, heart, kidney and bone. Cells are highly sensitive to their surroundings. Typically between 10 and 50 μm in diameter, cells

respond to environmental features at all length scales from the macro down to the molecular. The outer membrane of a typical cell is covered by at least six different receptor systems that can be activated by interactions with adjacent cells, ligands in the surrounding ECM, and secreted signaling molecules [5,60]. Hundreds of different proteins play a role in the composite stimulation of cell receptors, which in turn determine a plethora of responses, including cell migration in the early embryo, coordinated organogenesis, and wound repair throughout adult life [58,59]. Collectively, these extrinsic factors make up a highly defined and specialized cell microenvironment, which is essential for correct tissue development and continued function.

The ECM takes a variety of forms in different tissues and at different stages of development in the same tissue [60,61]. Diversity arises through combinations of specific molecular interactions between numerous isoforms, ratios, and geometrical arrangements of collagens, elastins, proteoglycans, and adhesion proteins such as fibronectins and laminins. This creates an environment that is replete with informational cues. In addition to this, a wealth of molecular mechanisms modulates the dissemination of this information. For example, the ECM plays a major role in regulating growth factor signaling, acting as a local reservoir for latent forms, and rapidly releasing and activating them on demand [62].

Each ECM protein carries multiple motifs that target/bind specific cell surface receptors. The transmembrane integrin receptors, with more than 20 members identified, are the most extensively characterized, and they recognize motifs such as Arg-Gly-Asp (RGD) within proteins of the ECM such as fibronectin and vitronectin

[63]. These receptors tether the cell cytoskeleton to the fibers of the ECM, forming local focal adhesions. When bound, integrins activate a cascade of intracellular signaling pathways, leading to changes in gene expression and affecting most aspects of cell behavior. They modify differentiation, proliferation, expression of ECM proteins, activation of growth factors, and the maintenance of survival signals to prevent apoptosis [64-66]. For example, the 3D ECM environment *in vivo* strongly influences changes in cell shape that affect the differentiation process [61]. Importantly, the binding of integrins and the formation of focal adhesions, their structure, localization, and function in 3D tissues is substantially different from their binding and formation in 2D culture [67]. This is a key concept that highlights the role of a 3D nanofibrous matrix for maintaining cell phenotypic shape and establishing natural behaviour patterns, and should be carefully considered when engineering biomimetic scaffold structure at the nano-/micro-scale (see below).

While it is accepted that matrix surface chemistry tends to exert stronger influences on biological responses and rates, such as cell differentiation and division, ECM physical cues (e.g. topographic features, mechanical properties, 3D spatial organization etc.) have been shown to have a far greater influence on cell orientation, locomotion and direction of the cell-extracellular matrix[3]. The role of the ECM physical microenvironment appears, however, not to be limited to these functions, as suggested by recent findings that endorse its direct influence on cell lineage specification. For example, cell phenotype has been shown to be extremely sensitive to tissue level elasticity and compliant matrices that mimic brain tissue are found to be neurogenic, whereas stiffer matrices that mimic muscle are myogenic and comparatively rigid matrices that mimic bone prove to be osteogenic [46]. Indeed, in

many aspects of tissue engineering it is now becoming clear that physical cues are at least as important as chemical ones, and frequently more critical to regulate [3,4,68,69]. Unfortunately, our knowledge of the role and operation of material-based cues remains far less clear.

In considering the role of cell-ECM architectural organisation in scaffold design, it is first essential to determine the meaning and ambiguities behind the concepts of 2D and 3D cell culture. It is clearly evident that many cells respond differently when cultured in 3D compared to traditional 2D cultures, and often adopt more *in vivo* like morphologies[39]. Culturing cells in 3D radically alters the mechanical signals from those provided in 2D, thus affecting cell-receptor ligation, intercellular signaling and critical cell behaviours such as cellular migration[39]. A 3D environment also influences the diffusion and adhesion of proteins, growth factors and enzymes, which ensures cell viability and optimal function[46]. Furthermore, it is well established that scaffold architecture affects cell attachment and spreading. Cells binding to fiber-based scaffolds with micro-scale architectures flatten and spread as if cultured on flat surfaces, which is almost universally regarded as 2D culture (Fig.3). Incorporation of pores/grooves/channels of cellular dimensions into that substrate may be taken to represent a form of *pseudo*-third dimension in the system (Fig.3). This is a consequence of the large pore size, which presents to seeded cells as a series of effectively flat surfaces, but in all three planes. In other words, where spacing of scaffold support elements is far larger than cell dimensions, most cells can only attach to one surface at a time, effectively 2D monolayer conditions. Biomimetic, i.e. true 3D culture can only be assumed where cells are able to attach to the substrate through most of their membrane surface. For example scaffolds with

nano-scale architectures have larger internal surface area to volume ratios to adsorb proteins, presenting many more binding sites to cell membrane receptors[5,34,40]. It is thus not surprising that several cell types, including osteoblasts, fibroblasts, smooth muscle cells, neural and embryonic stem cells show increased attachment and proliferation on various nano-fibers compared to non-fiber based materials [34]. It is important to clarify, however, that 3D cell attachment is not such a simple concept as it appears, because the possibility for attachment is almost never the same on all sides of the cell in 3D scaffolds. Even where 360-degree attachment is possible, cell behaviours such as locomotion, neighboring cells, and structural asymmetries in the scaffold will tend to lead to local differences in attachment.

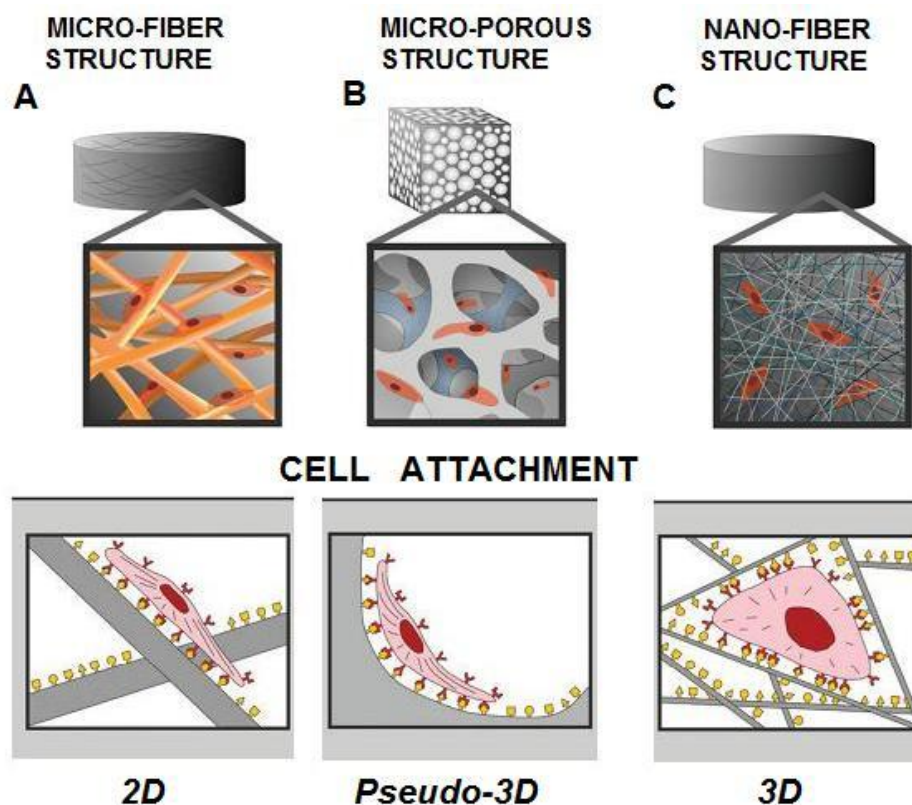


Fig. 3 Schematic showing how scaffold architecture affects cell binding and spreading. Cells binding to scaffolds with fiber-based microscale architectures flatten and spread as if cultured on flat 2D surfaces (A). Scaffolds containing pores/grooves/channels of cellular dimensions provide a *pseudo*-third dimension in the system as cells are

presented with a series of effectively flat surfaces, but in all three planes (B). Scaffolds with nanoscale architectures can support true 3D culture as they have larger surface areas to adsorb proteins, presenting many more binding sites to cell membrane receptors, allowing cell attachment to the substrate through most of their membrane surface (C). Modified from Stevens and George, 2005 [5].

The diverse nature of tissue architectures requires that different microenvironments are provided for their repair/regeneration. This principle can be demonstrated in the employment of scaffolds with tissue-specific pore sizes. For example, in regenerating bone tissues *in vitro*, some researchers have indicated the need for pore sizes ranging from 200 to 400 μm , while scaffolds with pore sizes between 20 and 125 μm have been used for regenerating adult mammalian skin and 45–150 μm for regenerating liver tissues[57]. Early work on synthetic polymer and native protein 3D scaffolds (polylactic-glycolic acids and collagen-GAG sponges [1,6,7]) concentrated on identifying ideal ranges of pore size, frequently in *random, non-directional* materials[70,71]. These were developed to facilitate adequate nutrient exchange and space for cell in-growth, population expansion or matrix production. Furthermore, a high porosity and pore interconnectivity have been conventionally perceived as critical properties in ensuring spatially uniform cell distribution, cell survival, proliferation and migration[57]. However, such criteria can only operate successfully at early culture stages. By definition, effective and dynamic cell growth, and matrix accumulation, must inevitably lead to infill (i.e., loss) of the initial pore structure. In addition to limiting cell perfusion, this effect will therefore generate randomly distributed pockets of cells and extracellular matrix, which mirror the random or homogeneous spatial distribution of the original pores. This is generally not a good biomimetic template for spatial organization in tissues, but rather resembles the disorganized structure of scar tissue formation throughout the body

[3,4]. Present understanding suggests, then, that scaffold structures designed on the pores-for-perfusion strategy will generate poor templates for biomimetic structures. Rather, it is critical that cell guidance cues (e.g. topography) are *built into* the initial scaffold structure [3,72]. Importantly, introduction of such *anisotropic* (i.e. directional) cues (channels, fibers, planes) into 3D scaffolds inevitably and automatically generates structures which facilitate nutrient perfusion[3,50].

Micrometer-range topographic features such as grooves/ridges, pits and channels are key ECM architectural cues whose role in directing cell behaviour has been well established for decades [72-75]. Studies are currently exploring how substrate topography, if engineered with similar nano-scale structural features, can be used to control cell function. Micro-/nano-scale alterations in topography elicit diverse cell behavior, ranging from changes in cell adhesion, cell orientation, cell motility, surface antigen display, cytoskeletal condensation, activation of focal adhesion kinases (FAKs), and modulation of intracellular signaling pathways that regulate transcriptional activity and gene expression [72,73,76,77]. It is not only the scale of topography (nm vs. μm scale) that modulates cell behavior but also its pattern (e.g. ridges/grooves, steps, pillars, and pits) and symmetry (e.g. orthogonal or hexagonal packing of nanopits) [73]. Furthermore, several studies have established that similar scale topographic features may elicit similar biological effects *independent* of the underlying material chemistry. For example, there is close agreement between smooth muscle cell behaviour on both nano-patterned poly(methyl methacrylate) and poly(dimethylsiloxane) substrates, whereas the differing surface chemistry of the two polymers is unlikely to result in the same adsorption of proteins [78]. This

emphasises once again the important (even dominating) role that ECM physical cues play in regulating cell functions in native tissue.

Fiber orientation is an intrinsic, critical element of matrix 3D micro-architecture that not only directly determines its mechanical properties [79], but also provides a dynamic (i.e. adaptable by matrix remodelling) topographic cue to resident cells[37,39]. Indeed, there is a remarkable diversity in terms of tissue-specific orientation of fibrils e.g. parallel and aligned in tendon, concentric weaves in bone, orthogonal lattices in cornea, and meshlike in skin. Many cell types are known to orient and often move rapidly along fibres of a fairly narrow range of diameters (5–50 μm). For example, cell alignment and migration have previously been demonstrated on fibrous shear-aggregated fibronectin substrates for Schwann cells, neurites, macrophages, and fibroblasts [80,81]. Importantly, cell alignment also leads to parallel alignment of newly deposited collagen fibrils as the ECM is remodelled/replaced, thus providing a tool for feedback regulation in this structure-function cycle.

Because of the dimensions of cells and cell processes, 3D guidance by patterns of channels, galleries and gaps are most likely to range from ~ 1 to 50 μm . This contrasts with the scale of surface features capable of orientating cell membrane receptors in 2D monolayer, which reach down to <20 nm [72,82]. This difference is key because it is clear that there is a close inverse relationship in 3D materials between the presence of scaffold material (a fiber or ridge) and its absence (as pores, cavities, or channels). For example, in a 3D bundle of parallel aligned fibers, resident cells either migrate along adjacent fibers or through the channels formed by the

spaces between fibers. The factor of *space to move* helps us to understand why cells can be aligned by nanopatterns in 2D monolayer (with a free dorsal surface) but would not easily migrate on these where the 3D gaps or channels are substantially less than the nuclear diameter. This is perhaps clearly illustrated through the contrasting requirements in neural regeneration where glial cell migration is obstructed by channels smaller than the nucleus, whereas axon migration, not involving nuclear translocation, is unaffected [3]. Scaffold channelling (and its dimensions), then, is a key element distinguishing topographical control of cells in 2D and 3D.

The material properties of the ECM constitute the third element in what could form a triad of factors that underpin nano-/micro-scale scaffold structure (the other two being ECM chemistry and architecture, as discussed above). Material properties of the ECM include ECM density, mechanical properties (e.g. stiffness/compliance, elasticity/viscosity etc.) and importantly anisotropy, i.e. the *direction* of material properties. In contrast to many current assumptions, cells *in vivo* almost never lie within mechanically homogeneous substrates[3,83,84]. In 3D natural systems cell attachment to the ECM is essentially an interaction with a pleomorphic landscape, in the form of integrin attachment through fibronectin, vitronectin, or minor, pericellular collagen-types, including basement membrane type IV collagen. Less obvious is the influence of cell-substrate ligand density. For example, stiffness of the cell-ECM ligand interface will be proportional to the *number* of integrin-ECM interactions/ μm^2 , as well as ligand elasticity[3]. Importantly, continued remodeling of more complex 3D matrix structure is the accumulated *consequence* of cell motility and traction which is itself *directed by* the mechanical properties of that substrate, as

seen in the phenomena of durotaxis and haptotaxis (where cell migration occurs along a rigidity or ligand density gradient, respectively). This suggests that in 3D systems, resident cells presented with random or mechanically homogeneous scaffolds will tend to deposit random or homogeneous ECM structure, reminiscent of scar tissue [4]. Biomimetic 3D structure is only likely, then, where cell-scale, biomimetic mechanical features (together with structural guidance cues e.g. topography) are available in the initial scaffold, in the form of tissue-like inhomogeneity and anisotropy [3]. This in turn argues that cell scaffolds need to have meso-scale structure from the start; in other words, they need to be biomimetic tissue templates rather than random porous sponges or meshes.

1.2.2 Biomimetic elements of macro-scale scaffold structure

Many tissue engineering approaches must supply a scaffold that immediately mimics the functional architecture of the damaged tissue. A good example would be replacement of heart valves which need to be functional from the outset, as opposed to a bone repair site which could be supported and immobilized until functionally mature. Such functionally active biomimetic implants therefore are effectively mimicking traditional grafts by assuming certain key properties of the undamaged tissue. Previous work has indeed primarily focused on engineering homogeneous tissues that can mimic the gross architecture of an organ. To this end, construct fabrication has made use of native (e.g. collagen, fibrin, fibronectin) or synthetic (e.g. polylactic acid, glycolic acid, capriolactone) biomaterial scaffolds that function as integral units that provide three dimensional support to cultured cells [85]. An alternative approach, recently reported, is that of sheet-based engineering, i.e. layer-by-layer tissue reconstruction using either cell sheets [86] or biomaterial sheets [25].

This carries the potential for engineering composite tissue structures with macro/micro-scale heterogeneity e.g. osteo-chondral, nerve-fascia and vascular wall structures.

Cell-sheet engineering involves the use of temperature-responsive polymer culture surfaces that facilitate the non-destructive (protease free) harvest of cultured cells as intact sheets. Cell sheets have been applied directly to a range of regenerative therapies such as oesophageal and tracheal replacement, skin and corneal reconstruction and cardiac tissue repair, without the use of traditional scaffold-based methods [86-88]. However, unlike the scaffold-based approach, engineered tissues created using cell sheets contain relatively little ECM and therefore are not suitable for the generation of matrix-rich, cell-sparse tissues, such as skin, tendon, bone or cartilage [86]. Another limitation of the cell-sheet approach is the difficulty in production of organ-like structures that possess a 3D organizational architecture such as that encountered in cardiac tissue and liver. These difficulties could be overcome by layering individual cell-sheets to produce millimeter thick tissues and by integrating multilayer cell sheets with other biomaterial sheet scaffolds that could provide structural support to the construct.

An important example of biomaterial sheet scaffolds is that of Plastic Compressed collagen sheets [25]. As described above, Plastic Compression (PC) involves the irreversible, cell-independent removal of fluid from collagen hydrogels to rapidly produce dense, mechanically strong collagen sheet scaffolds (~100/200 μm thick) that can support a high cell viability [25]. The ability to integrate cell sheets with biomaterial sheet scaffolds could provide new opportunities to apply sheet-based

engineering to complex tissue reconstruction [86]. Indeed, the concept of layered fabrication, whereby 3D objects are engineered with layer-by-layer building via the processing of solid sheets, is currently being explored in Solid Freeform Fabrication (SSF) techniques which use computerized fabrication to rapidly produce highly complex 3D physical objects using data generated by computer-aided design (CAD) [57]. However, successful utilisation of this approach will critically depend on optimal and functional integration of the construct's individual components (i.e. layers) [89-93]. Integration of engineered interfaces is therefore a key component of scaffold macro-scale architecture, and effectively not different from host-implant integration, which is in many ways the same process as that seen during natural tissue repair.

In addition to its homo-/heterogeneity, the dimensions (i.e size, thickness) of a scaffold are a key element of its macro-level structure. This is because cell perfusion becomes an acute problem for engineered large/thick constructs ($>3\text{mm}^3$) due to limitations in passive diffusion of nutrients (e.g. glucose, oxygen) to the construct core, both *in vivo* and *in vitro* [94]. It has been proposed that layer-by-layer assembly of (sheet-based) constructs could be used to circumvent this problem by carrying out layer integration at multiple steps, prior or during implantation [95], or by multi-step transplantation *in vivo* [96], effectively reducing the minimum passive diffusion distance to a single cell or matrix sheet layer. As discussed above, this approach requires effective integration of construct layers and zones, in order to give functional, integral tissue. Undoubtedly, however, the optimum approach for successful large construct fabrication must rely on engineering angiogenesis, i.e. inducing the formation of a functional microvascular network that is integrated with the other

scaffold components and can support their viability. Evidently, scaffold structure should be engineered around this necessity, by being accommodative or, ideally, facilitative to angiogenic induction.

In the previous section we discussed the importance of nano-/micro-topography as a cell guidance cue. The 3D spatial organisation of sheet-based scaffolds could provide an additional form of cell guidance, termed interface guidance. Though less rigid than fiber-based guidance, this could mimic at least as many natural, tissue guidance systems. Guidance by micrometer diameter fibrils in general works by constraining cell motility/migration to only one plane at a time. That is, if cells can only migrate up/down a fiber, e.g. in the y plane, its movement in the x and z planes (i.e., off the fiber) is constrained. In such systems, changes in guidance direction will be limited by the constancy and range of orientation of the scaffold fibers, as well as by the efficiency of cell guidance (i.e., the percentage of cells or time cells are guided by the topography). In contrast, interface guidance is an example of single plane constraint. In this case, restriction of motion is in only one plane, with movement permissible in both the other two planes, that is, between adjacent sheets (i.e. within the interface) This can be demonstrated between compacted sheets of plastic compressed collagen, formed into many thin layers (e.g. as a spiral 3D construct). In effect, the collagen sheets form dense and relatively (i.e., slowly) impervious barriers producing relative containment between the planes, that is, in the z plane only. However, free cell motion between the layers or interfaces, and along the length of the construct is possible, such that cells follow the interface [54]. It is important to note that while constraint here is achieved entirely by the density of the substrate (in this case collagen), this is gradually degraded by migrant cells. This emphasizes the

importance of *temporary, early cues* to guidance. Despite the temporary nature of such interfaces *in vivo*, the initial guidance they provide over the first 1–3 weeks is retained even after ingrowing tissues have broken down and delaminated many of the sheets by 5 weeks post-implantation [54]. In culture, resident cells grown in such spiral constructs tend to take on a flat discoid morphology, appearing to be long and thin when sectioned in both transverse and longitudinal planes [54]. This form of guidance is clearly similar to that seen in growth, repair, and maintenance of tissue gliding function, particularly in dynamic connective tissues, notably in fascia, gliding surfaces between organs and conduit structures such as nerves and blood vessels [97-99]. Cell guidance through engineered interfaces represents a relatively simple, but so far underexploited, biomimetic approach to the control of tissue structure. Its potential role for improving scaffold bio-functionality is further evident in the clear correlation between sheet/layer 3D spatial organisation and perfusion of resident cells within the participating layers[100].

1.3 EFFECTS OF SCAFFOLD PHYSICAL STRUCTURE ON CELL BEHAVIOR

1.3.1 Effects of scaffold topography on cell function

Engineering scaffold topography is a non-invasive and non-biological method of regulating cell function, because textured substrates serve simply as an extracellular physical milieu without involving biomolecules (chemical patterning). Topography could, however, provide a biomimetic cell-stimulating cue, because cells *in vivo* contact mesoscale structured, not smooth, interfaces. Topography can be classified with regards to its scale and pattern. Because basement membranes of various tissues

are composed of complex mixtures of nanoscale (5–200 nm) pits, pores, protrusions, striations, particulates, and fibers, nano-topography may be more biomimetic in affecting cell behavior than micro-topography[101]. With regards to pattern, studies have examined whether cells align along anisotropic topographies such as ridges and grooves, while for isotropic topographies, such as evenly or randomly distributed pits or protrusions, studies have mainly focused on how these affect collective cell functions, such as differentiation and proliferation[73]. In addition to scale and pattern, a fundamental distinction can be made on the basis of whether the patterned substrate is two- or three-dimensional (i.e. if it allows interstitial, as well as superficial cell seeding), as cell reaction to surface topography cannot be safely extrapolated to non-epithelial (e.g. stromal) cell types such as fibroblasts. Despite this limitation, the majority of studies investigating the role of topography in cell function regulation have been carried out on 2D substrates[73].

Topographic cell reaction on 2D substrates

Cell orientation and migration along the anisotropic direction of ridges and grooves produced using lithographic techniques or micromachining has long been observed on 2D substrates (i.e. monolayer culture) [73,102,103]. Along with elongated cell shape, the cell cytoskeleton also displays directional organization. Orientation of actin filaments or microtubules was identified as the primary event in contact-guided cell alignment[102,103]. Interestingly, however, even when microfilaments or microtubules were destroyed with pharmaceutical disruptors, cells still displayed contact guidance[104]. Additionally, localization of focal adhesion proteins (e.g. vinculin) has been positively correlated with cell alignment[105].

Most of the early studies of substrate topography used several millimetre sized ridges and grooves. However, it is now clear that the scale of anisotropic topography plays an important role in deciding cell alignment. Cell orientation generally increases with increasing groove depth but decreases with increasing groove width or pitch [73]. At the microscale, with increasing groove depth and decreasing groove width, cells tend to bridge the ridges without descending into the grooves, while vinculin formation has been found to display ridge-width-dependent anisotropic orientation. With the development of lithographic techniques, recent studies have focused on whether cells align on nanoscale ridges and grooves and, if so, how small the topographic size can become while still inducing contact guidance. Teixeira et al. observed that human corneal epithelial cells aligned on ridges, produced by e-beam lithography, as small as 70 nm wide [106]. Aligned axonal outgrowth was also observed on 100- to 400-nm-wide nano-imprinted grooves [107]. The minimum effective dimension of grooved features has now fallen to as low as 11 nm [72]. Importantly, a study using polystyrene nanogrooves (~70-nm depth) has shown that stem cell-derived osteoblasts displayed anisotropic orientation not only in cell/actin but also in mineralized matrix, suggesting that topography could also direct cellular synthetic activity [108]. Topographic scale also affects whether cells bridge between ridges or conform to grooves through selective focal adhesion formation on ridge tops or down to groove floors [109]. While cells tend to bridge the ridges without descending into narrow/deep micro-grooves, at the nanoscale, epithelial cells on 150-nm-deep grooves descended into 2.1- μ m-wide grooves but formed bridges over 950- to 330-nm-wide grooves [106]. These findings demonstrate that cells can sense micro- and submicroscale topography and react to it by bridging or conforming in a selective manner.

Relative to obvious changes in cell shape on grooved substrates, gene expression and differentiation of aligned cells is currently being investigated. Fibroblasts cultured on V-shaped 3- μm deep micromachined grooves displayed greater FN mRNA and protein levels than planar controls, while osteoblastic cells cultured on multigrooves displayed higher osteopontin and osteocalcin mRNA than cells on flat surfaces[110]. Importantly, it has been shown that in fibroblast cultures on lithographic microgrooves early upregulation of several genes involved in cell signaling (e.g. Developmentally regulated GTP-binding protein DRG, Protein kinase C substrate, Basic fibroblast growth factor receptor 1 precursor), cytoskeletal organisation (e.g. Tubulin beta-3 Chain), transcription (e.g. Transcription initiation factor IIE, Chromodomain-helicase-DNA-binding protein 1 (CHD-1)) and translation (e.g. 40s ribosomal protein S6, Eukaryotic translation initiation factor 3 beta subunit) was followed by down-regulation on day 5[111]. It has been suggested that topography-induced changes in morphology may have mechanotransductive effects, accounting for some of the gene regulation changes observed. Dalby et al. have proposed that distortion of the cell nucleus (e.g. during cell alignment) will alter the relative positions of chromosomes and their accessibility for transcription, thus changing gene expression. As the cells align, and thus take on far less random morphologies than those produced on flat surfaces (where the cells may spread in all directions), nuclear shape (and chromosomal arrangement) is being restricted throughout the new tissue being formed, which may result in gene down-regulation. This suggests that mechanical forces effect both morphological and biochemical cellular behaviour.

When surfaces are uniformly or randomly textured with topographic features (nodes, pits, protrusions, pillars, channels, etc.) with no directional order (i.e. isotropic), cells

do not generally display anisotropic alignment. Instead, such cues operate by controlling more collective cell functions (e.g. division, differentiation etc.) [73]. As with anisotropic topographies, scale is a key determinant of whether cells exhibit specific behaviours on isotropically patterned substrates. The ability to precisely control topographic feature scale is therefore a prerequisite to their use as cell directing cues. Lithographic techniques provide well-defined topographies in the range of mm to 250 nm (photolithography) or down to 10 to 20 nm (e-beam lithography)[101]. Photoresist thickness or reactive ion etching provide further control over feature height or depth. However, cell response to isotropic topographies produced using lithographic methods is often inconsistent. For example, fibroblasts have been shown to display greater proliferation on 2- and 5- μm -diameter nodes (0.5 μm high) than on 2- and 5- μm -diameter wells (0.5 μm deep), whereas cells on 10- μm nodes and wells did not differ from planar controls[112]. Furthermore, while progenitor cells displayed greater proliferation on 5- to 40- μm -diameter posts than did on planar controls, macrophage spreading was much less on 5- μm -diameter features than on smooth surfaces[73]. Recently, the ability to assess cell reaction to nano-topography has been developed using polymer demixing and colloidal lithography, because they can produce large areas of nanotextured surfaces economically and at reasonable uniformity. Using polymer demixing, Dalby et al. demonstrated that fibroblast focal adhesion formation and spreading are greater on 13-nm-high islands but lower on 95- nm-high islands, than on planar controls[113]. In contrast, endothelial cells on colloidal lithographic pillars (100 nm high, 168 nm diameter) displayed lower spreading and decreased cytokine production than cells on planar surfaces[114]. These findings suggest not only that cell response is specific to the dimensions of topography, but also that there

is substantial variation in topographic cell reaction between different cell types. Although comparison of the effects of isotropic topographies may currently be difficult, because of diversity in topographic size, shape, uniformity, and even chemistry[115], a tentative trend can be drawn for a limited range of nano-topographic scale such that collective cell functions are positively stimulated at smaller nano-topographic scale (~10 nm in height or depth), but this reduces with increasing feature size up to approximately 100 nm[73].

Topographic cell reaction in 3D substrates

Fibrous and porous 3D substrates present cells with a complete spectrum of surface/interface attachment site densities. Indeed, the density of binding sites adjacent to some parts of the cell surface can approach zero, such as within parallel fiber bundles, pore/channel openings, between scaffold layers and at cleavage planes. Clearly, local absence of scaffold material adjacent to motile cells can come to define the front and rear of motion. In this case, no material equates to no contact and so represents the direction of least resistance, thus providing a guidance cue. Such guidance is most easily seen in scaffold channeling. The concept of topography-regulated cell migration is dominated by the statistical availability of sufficient scaffold binding sites for the cell to apply traction force, and adjacent gaps in the scaffold into which the cell can actually move (i.e. *space to move*). Indeed, a similar principle has also been described for the influence of cell-substrate adhesion site density on cell migration speed [116].

Recent studies have demonstrated the feasibility of using the alignment reaction of cells to fibre-based topographies to guide cells through/along channels within 3D

scaffolds. For example, fibroblasts seeded within dense collagen scaffolds, incorporating aligned soluble phosphate-based glass fibers (PGFs), showed alignment along these fibers[117], suggesting that cells will be guided by the microchannels (30-40 μ m diameter) left after the PGF has dissolved.

Specificity of cell reaction to patterned topography

As discussed above, certain cell phenotypes show greater sensitivity to particular nanoscale features than others. For example, osteoblasts have been found to adhere preferentially to carbon nanofibers in competition with chondrocytes, fibroblasts, and smooth muscle cells [118]. These cell type-specific effects/behaviors serve to highlight one of the main (yet unsurprising) challenges faced in understanding cell-material interactions: cell behaviours differ. In other words, conclusions drawn from one cell type cannot be readily applied to another. While this might appear as a practical limitation at first glance, it also provides an incentive for understanding potential opportunities presented by this behavioural specificity. For example, studies have shown that topography alone can be used to elicit different responses from the same cell phenotype (e.g. uroepithelial cells seeded on titanium surfaces engineered with well-defined nanometer topographies displayed modified cell morphologies and cytokine production to cells cultured on flat titanium controls [114]). This has important implications for utilisation of a scaffold's physical structure as a self-sufficient controller of cell function.

1.3.2 Effects of scaffold mechanics on cell function

Cell proliferation

The role of substrate mechanics in directing cell behaviour has long been investigated and is now well established [44,119-122]. It is becoming increasingly evident that cell interaction with the extracellular matrix (ECM) produces two different but concurrent signalling mechanisms. (1) Ligation-induced signalling, i.e. ECM ligand-receptor mediated signalling (e.g. RGD-Integrin binding), which depends on ECM surface chemistry, and (2) traction-induced signalling, which depends on mechanical stimuli transmitted through the ECM. Discher et al have discussed how substrate mechanics modulate cell phenotype and proliferation in a manner similar to biochemical signals[123]. These studies have been performed on a variety of substrates, more commonly on the collagen-coated silicone or polyacrylamide gels[124]. A study using a more biomimetic ECM composed of hyaluronan and fibronectin, found that adult human dermal fibroblasts cultured on stiffer substrates had a higher cytoskeletal modulus and an increasingly stretched and organized actin cytoskeleton, exerted greater traction on the substrate and proliferated normally only on the stiffest hydrogels[125]. In this study, however, cells were seeded on the surface and not within the substrate. In order to fully understand cell proliferation in the context of specific tissues, it is important to create a three-dimensional environment that mimics as closely as possible the cell-matrix interaction *in vivo*. This has necessitated the development of physiologically relevant, tissue-engineered constructs that resemble native tissue and whose mechanical properties can be controlled to allow detailed correlation with cell responses [13,122].

Collagen is the most abundant protein of the extracellular matrix and thus collagen-based substrates provide perhaps the most physiological and mammalian biomimetic environment in which cellular function can be studied. Many studies have replicated the findings of Bell et al. who demonstrated that fibroblasts cultured within (hyper-hydrated) low density collagen hydrogels contract the matrix into a denser, 'tissue-like' structure [126] (Fig.4). However, starting collagen density in this model is 0.2 to 0.5% (1-2 orders of magnitude lower than tissues) and does not reach more than 1-2% after cellular contraction. When such collagen gels are mechanically restrained to a stiff backing material (container) as 'attached' matrices, the contraction forces of resident cells generate an isometric tension (no gel contraction). As the stiffness of the collagen matrix increases, cells eventually proliferate. However there is little or no proliferation in the same gel when it is unattached and free floating, i.e. unable to develop isometric tension, with a significant proportion of cells undergoing apoptosis [127,128]. In addition to differences in their growth response, fibroblasts undergo significant morphological changes during mechanical unloading of collagen matrices. Fibroblasts in attached matrices have polarized cell morphology and form prominent actin stress fibers, resembling proliferating cells of granulation tissue, but these cells undergo loss of stress fiber organization when gel attachment (and thus stress) is released [129].

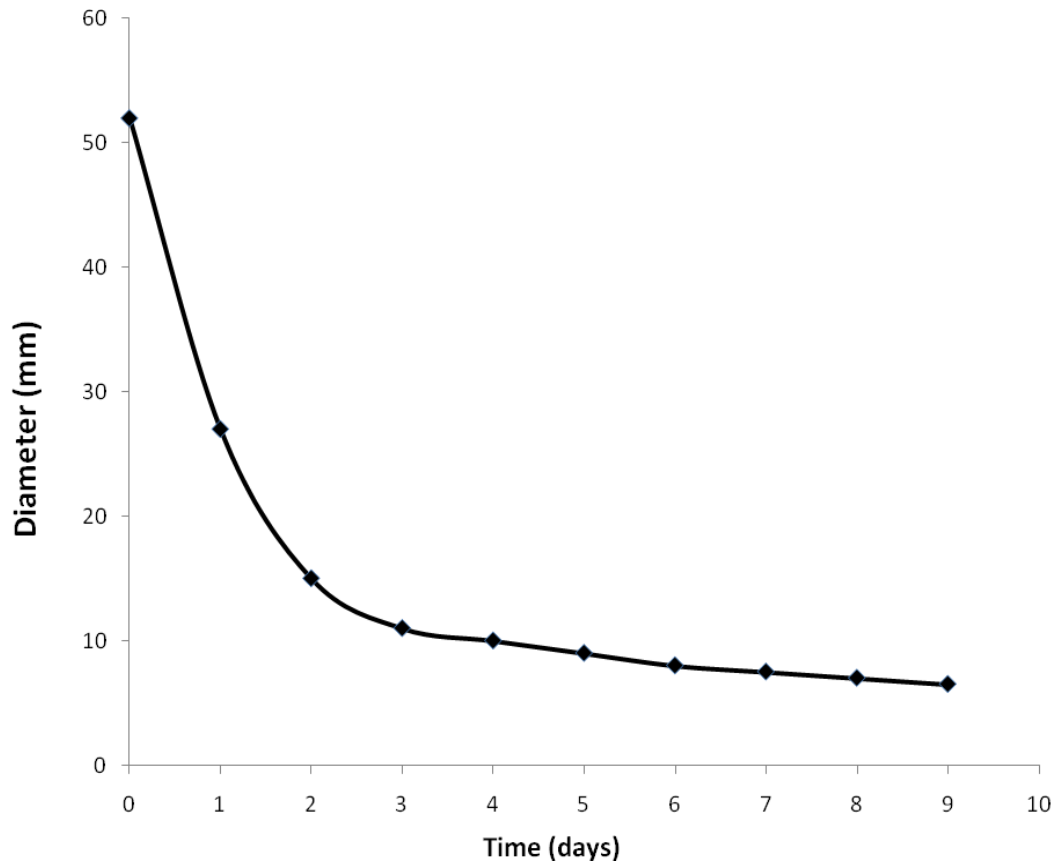


Fig.4 Plot showing cell-mediated contraction of a hydrated collagen lattice (gel) by 7.5×10^6 fibroblasts, expressed as reduction in gel diameter. Adapted from Bell et al, 1979[8].

The isometric tension that develops in attached collagen matrices is said to be equivalent to that found in skin wounds[130,131], though this has been questioned[3]. Wound healing is an example of a physiological response that critically depends on an orchestrated sequence of events, involving cellular adhesion, infiltration and proliferation along with appropriate migration and differentiation [130]. Unlike fibroblasts of mature dermis that are quiescent and stationary, fibroblasts of granulation tissue are proliferative and motile[132]. The stress-relaxation model has been used to study fibroblast activation and quiescence during wound repair. Based on this, the assumed mechanically-linked switch from

proliferation to quiescence/apoptosis has been interpreted as a feature of fibroblasts at the end of cutaneous repair, at which stage granulation tissue regresses [133-138]. Extrapolation of this model to physiological repair is, however, difficult as it does not take into account the extremely low stiffness of the collagen gel-cell substrate used.

Cell-mediated collagen matrix contraction results not only in changes in fibroblast tensional homeostasis[139] but inevitably in changes in collagen matrix stiffness[122]. Whereas the effect on fibroblast proliferation of endogenously generated tension[128,131] or exogenously applied cyclic strains [140] have been extensively studied in the collagen gel model, the influence of matrix stiffness is not well understood. This is part due to technical difficulty of precisely controlling the density, and so modulus of collagen hydrogels, in the same way that has been possible for polyacrilamide-based substrates. However, removal of interstitial fluid from collagen hydrogels through a cell-independent process, such as plastic compression (PC) fabrication [25], would allow sufficiently precise control of the matrix hydration level (water content and so collagen density) to control stiffness modulus over a range. This creates the possibility to directly test the effect of 3D matrix stiffness on cell proliferation within a mechanically controllable, but biomimetic environment, with important implications for understanding repair and regeneration.

Cell migration

Understanding the mechanisms of cell guidance would provide an invaluable tool for understanding cell-matrix physiology, designing biomimetic scaffolds and ultimately engineering functional tissues. It is already well established that directional movement of cells is an important component of developmental patterning, wound healing and tumor metastasis [141,142]. While cells migrate in response to cues such as gradients of soluble chemoattractants [143,144], they also appear to receive additional signals from the insoluble ECM. Changes in bound adhesive ligands, topographic features, and stiffness across a substrate are all thought to guide the migration of cells [122,145-148].

The use of patterned adhesivity and topography to organize cells is now a widely used strategy in tissue engineering. When substrates are patterned with ECM coated regions and nonadhesive regions, cells only attach to the ECM-coated regions [149], while cells exposed to a gradient of immobilized ECM proteins migrate up the gradient (haptotaxis) [150]. Cells also organize and align in response to topographic cues, including surface grooves and ridges (substrate guidance) [151], as discussed above. However, in contrast to the maturity of engineering surface adhesivity and topography, cell guidance systems based on controlled substrate mechanics (e.g.stiffness) are only now being developed [68,125,152-154].

A recent study based on an ECM composed of hyaluronan and fibronectin, found that adult human dermal fibroblasts migrate faster on softer substrates and demonstrate more dynamic lamellipodia activity [125]. Perhaps more significantly, in addition to having an effect on the speed of migration, substrate stiffness has also been implicated in controlling the direction of cell movement. A previous report

suggested that cells migrate preferentially towards stiffer surfaces, a phenomenon termed durotaxis [119] In this study, the durotactic response was observed in isolated cells, as cells were seeded at low density to reduce interfering by cell-cell contacts. Another study of mechanotaxis, using polymer cell culture surfaces containing micrometer-scale regions of variable stiffness, showed that over several days fibroblasts and endothelial cells accumulated preferentially on the stiffer regions, even in the presence of cell-cell contacts [68]. These studies used polyacrylamide/PDMS surfaces of varying stiffness [68,155,156] which introduced two major limitations in terms of experimental design. Firstly, cells must be seeded on top of the polymer surface and not within a physiological three dimensional environment. Any observations of cellular response, then, must be extrapolated to engineering of three dimensional structures. Secondly, most of these patterned surfaces presented the cells with sharp boundaries between soft and stiff regions (step gradients) instead of smooth gradients as is the case with chemotactic signaling. The ability to engineer continuous stiffness gradients within biomimetic 3D matrices would enable investigation of the phenomenon of durotaxis within a native micro-environment. Furthermore, incorporation of such drivers of physiological cell movement into a scaffold's structure would provide an invaluable tool for controlling locomotion-dependent cell processes, such as ECM remodeling, that ultimately influence its architectural organization and mechanical properties.

Cell-mediated interface integration

Previous studies on interface integration have primarily focused on fibro-cartilage engineering and repair [157] or fibroblast-mediated integration relevant to skin or tendon [158]. Adhesion strength has been found to correlate with collagen deposition [90,159,160] and length of culture period [158,161,162]. Cell migration has also been suggested as one of the mechanisms mediating integration of closely apposed structures [158,160]. However, most studies of cartilage-cartilage or osteo-chondral integration have been based on explant cultures [91,92,161,163,164]. The resulting lack of tight control over individual parameters such as the architectural organization of the interface, cell density and substrate stiffness has hindered full understanding of the type of connections and the cellular mechanisms by which mechanical linkages are generated across the interface.

Tissue engineering provides the necessary flexibility to tailor the mechanical and degradation properties of a material, and in particular to incorporate gradients of material properties, which is of paramount importance in reconstruction of tissue interfaces. For example, to mimic the anterior cruciate ligament (ACL)-bone interface, a triphasic scaffold has been developed that consists of a soft-tissue phase formed from a highly degradable poly(D-L-lactide-co-glycolide) (PLGA) mesh fused to a fibrocartilage phase of more-slowly-degrading PLGA, which itself was fused to a stiffer bone phase made of aPLGA and bioactive glass composite[33]. The soft-tissue and bone phases were seeded with fibroblasts and osteoblasts, respectively, and over several days the scaffold supported cell growth while maintaining phase-specific matrix deposition[33].

As discussed above, an important regulator of the processes that facilitate cell-mediated interface integration, namely cell migration, proliferation and collagen deposition is matrix stiffness [68,122,123,125,165-167]. Indeed, it has been suggested that identification of variations in matrix stiffness could provide a useful method for assessing interface integrity at step-off edges during cartilage repair[168]. As resident cells lay down extracellular matrix (mainly collagen) at the interface between layers of sheet-based scaffolds, during *in vitro* culture [25] or *in vivo*, post implantation [54,169], matrix density and stiffness increase. Increasing matrix stiffness would, in turn, be expected to affect the integration process by feedback regulation of critical cell functions[122]. The ability to predictably control matrix stiffness at an interface, and therefore downstream cell responses, could thus provide an important tool for modelling and regulating multi-layer integration within sheet-based scaffolds (and other types of heterogeneous, multi-component scaffolds), as well as host-implant integration.

1.3.3 Effects of scaffold 3D spatial organisation on deep O₂ cell perfusion

As we have already discussed, the native 3D structure of most tissues is characterized by specific and essential 3D cell-matrix architecture at the nano- and micro-scale [170,171]. By culturing cells in appropriate spatial locations and by engineering the density and fibrillar architecture of their supporting ECM this 3D tissue geometry could be mimicked [25,172-175]. Attempts to build such spatially biomimetic systems have been developed around 3D collagen scaffolds [176] in which the rapid fabrication process of plastic compression (PC) is used to produce controlled collagen densities to levels comparable with native tissue [25]. However,

in the process of solving many of the basic questions of directly engineering simple, living collagenous tissues with biomimetic structure, it is now important to tackle the perceived, but poorly understood question of deep O₂ cell perfusion which is key to cell survival in engineered constructs.

Given the obvious limitations of mass transport (without microvascular perfusion) in 3D culture a clear evidence-based understanding of the formation and effects of prevailing O₂ tension gradients on deep cell behaviour is essential [177-181]. Previous work has examined the formation of such diffusional oxygen gradients in statically cultured cardiac constructs and their effects on spatial cell distribution and cell viability[178]. Indeed, cardiovascular engineering is a particularly stark example of potential 3D construct/*in vivo* mismatch. In this, as in other types of static culture, O₂ / nutrient gradients form from the surface to the core of the 3D construct. In contrast, even the earliest naturally perfused vessel will have a reverse radial gradient from the core to the outer layer[182].

This mismatch in O₂/ nutrient gradient direction is a direct consequence of a scaffold's 3D spatial organisation, which inevitably determines cell spatial positioning and distribution. In particular, recent studies have shown that layering cells specifically compromises deep O₂ cell perfusion[173]. Importantly, there is substantial evidence that in matrix-rich ECM systems diffusion distance and matrix density contribute, but do not dominate gradient formation [94,173]. In contrast, the role of cell O₂ consumption in determining the local O₂ microenvironment is evident in the remarkable variation of O₂ tension prevailing in different tissues. For example, while respiratory epithelium and outer skin layers are exposed to atmospheric levels of O₂ (21%; 160mmHg), physiological hypoxia (1 -10% O₂; 7.6-76mmHg) is by far the most common natural environment for most mammalian tissues[183].

Furthermore, a substantial body of literature already suggests that different cell types are exposed to different ranges of O₂ tensions, governed by their own metabolic activity (i.e. O₂ requirement) and spatial positioning, and respond differently to varying O₂ tension. It is well known, for example, that the wall of pulmonary blood vessels is home to a number of distinct cell phenotypes, including inner and outer layer pulmonary arterial smooth muscle cell (PASMC) types [184-186] which, by their nature, generate steep O₂ gradients both across (radial gradients) and along (longitudinal gradients) the vessel axis[182]. Outer PASMCs (i.e. furthest from the lumen) are not only more contractile, but respond to chronic hypoxia by reducing contractility. In contrast, inner PASMCs (adjacent to the vessel lumen) show no change in their contraction profile [184]. It is possible, therefore, that cells in specific spatial locations within tissues develop and adapt to utilise defined ranges of O₂ tension. Unintended or uncontrolled tendencies for O₂ gradients to produce locally inappropriate cell phenotypes or behaviours would then be a serious problem, even detrimental to scaffold biofunctionality. Consequently, controlling cell spatial positioning/distribution, in addition to cell density, is an important element of scaffold 3D spatial organisation as it provides a key directing cue for regulating deep O₂ cell perfusion and generating spatially biomimetic O₂ gradients in artificial 3D tissues where they are functionally important. 3D engineered tissue models provide an ideal route to study this question.

Cell responses to changes in O₂ Microenvironment

It is becoming clear that changing local O₂ tension can affect multiple aspects of cell phenotype and behavior, including proliferation and differentiation [187-189]. Furthermore, cells appear to respond to changes in their O₂ microenvironment in a tissue specific manner. For example, while in most well-oxygenated tissues, hypoxia

regulates angiogenesis through growth of new capillaries, in cartilage, which is avascular, sustained hypoxia upregulates the synthesis of major matrix components, such as proteoglycan and collagen type II[190].

Mammalian tissues operate in oxygen tensions ranging from 1-10% O₂ (pO₂ between of 7.6-76 mmHg) [191], termed physiological hypoxia. This range is distinct from ‘pathological’ hypoxia (<1% O₂ or <7.6 mmHg), where O₂ tension is low enough to compromise cell metabolism and damage/kill cells. Culturing cells under physiological hypoxia is currently employed as a strategy to control cell behavior *in vitro*, in particular, up-regulating the production of angiogenic signaling molecules[173,192].

As O₂ tension drops in a tissue, cells primarily respond by up-regulating Hypoxia Inducible Factor I alpha (HIF-1 α), which is a transcriptional activator [193,194]. HIF-1 α is considered to act as a regulator of O₂ by controlling cell production of potent angiogenic proteins, for example vascular endothelial growth factor (VEGF) [194] (Fig.5). Angiogenesis *in vivo* relies on gradients of angiogenic factors guiding endothelial cells, and ultimately vessels, to tissue areas where O₂ and nutrients are required [195-197]. In particular, gradients of VEGFA₁₆₅, basic fibroblast growth factor (bFGF) and platelet derived growth factor (PDGF) have been shown to direct endothelial cell (EC) migration and differentiation[195,196].

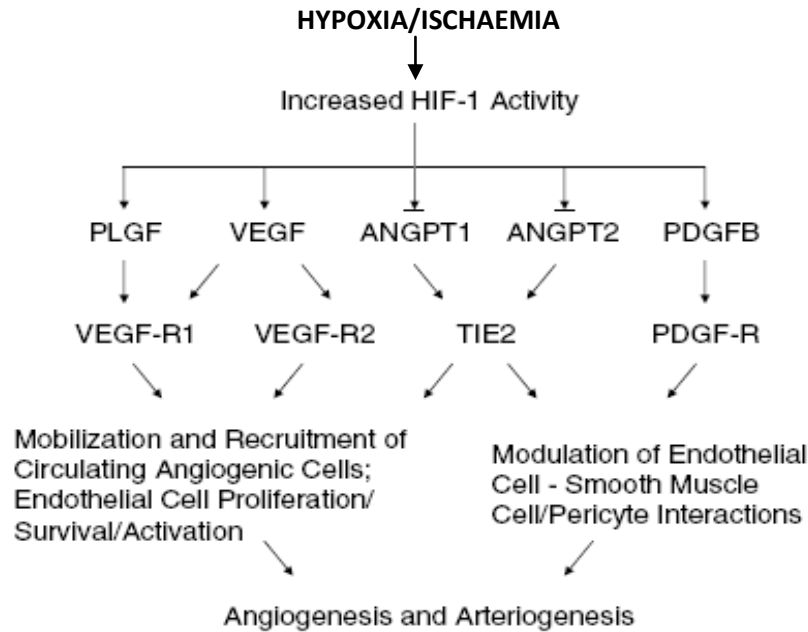


Fig.5 Diagram showing how angiogenesis and arteriogenesis are regulated by HIF-1. In ischaemic tissue, reduced O₂ availability induces the expression of the HIF-1 α subunit and HIF-1 transcriptional activity, leading to increased expression of genes encoding placental growth factor (PLGF), vascular endothelial growth factor (VEGF), angiopoietins 1 and2 (ANGPT1, ANGPT2) and platelet-derived growth factor B (PDGFB), which bind to cognate receptors (VEGF-R1, VEGF-R2, TIE2 and PDGF-R). This promotes the mobilization and recruitment to ischaemic tissue of circulating angiogenic cells, the activation, proliferation and survival of endothelial cells, and the interaction of endothelial cells with pericytes and vascular smooth muscle cells. This response mediates the budding of new blood capillary branches (angiogenesis) and the remodelling of existing blood vessels to accept increased blood flow (arteriogenesis). Modified from Semenza, 2007 [198].

The ability to induce a controlled angiogenic response within an engineered 3D construct would clearly be the most biomimetic, and therefore ideal, solution to the problem of poor deep O₂ cell perfusion (current alternatives include culturing constructs in perfusion bioreactors [199]). It is self-evident, then, that reproducing these complex angiogenic factor gradients within a tissue construct would have huge therapeutic and experimental value. As we discussed above, scaffold 3D spatial

organisation (which directly controls cell density and position) could provide a tool for generating functionally useful cell O₂ consumption gradients, in other words, engineering local cell-mediated physiological hypoxia. The idea would be to induce cells to act as factories producing a complete, potentially functional cascade of angiogenic proteins that can generate a physiological angiogenic response on demand. Additionally, the ability to induce controllable cell-mediated, and therefore physiologically regulated hypoxia[200], at predictable spatial locations in tissues would make it possible to direct the angiogenic response to any chosen point in 3D.

It is well documented that cell-generated angiogenic cascades (following prolonged exposure to reduced O₂) result in a more functional vasculature. This is almost certainly because the component proteins work best in concert to orchestrate vessel formation [201,202]. Simple addition of unbalanced levels of single factors such as VEGF has been shown to result in the formation of non-functional, 'leaky' vessels [201]. Consequently, it is proposed here that well-orchestrated biomimetic production of angiogenic factors with feedback regulation (angiogenic engineering) is only likely to be a practical proposition using whole cell systems. By these means the need to reproduce a complex sequence of angiogenic proteins is conveniently avoided by harnessing the innate biological programming. This can be achieved by engineering controlled cell hypoxia, i.e. mimicking physiological tissue hypoxia, which automatically elicits physiological angiogenesis in the body [197,203].

A major advantage in the use of scaffolds for tissue fabrication is the potential to control cellular micro-environments by customizing parameters such as diffusive properties, cell densities and 3D spatial positioning [55,173]. Previous work by this

group has shown that high density seeding of 3D collagen constructs with human dermal fibroblasts (HDFs) produced rapid reductions of core O₂ tension (~25mmHg / 3.2%), i.e. at the low end of physiological hypoxia [173]. Importantly, this elicited a multifold up-regulation of VEGF gene expression up to 8 days, in a spatially predictable manner, with highest expression in the core vs. mid and surface layers [173]. This contrasts with other studies where cells have been incubated (e.g. by gas chamber culture) in a low O₂ atmosphere, i.e. exposed to locally-uncontrolled, global hypoxia [204-208]. Cell hypoxia in the present model is created by local cell O₂ consumption and measured directly in specific construct locations (core and surface).

By controlling the seeding cell type, density and position, therefore the total cell-depot O₂ consumption, it is possible to define accurately where and when the hypoxia will develop within the 3D construct (i.e. core O₂ < surface O₂) [173]. This makes it possible to engineer distinct populations of Hypoxia-Induced Signaling (*HIS*) cells that function independently of other cell populations, such as responding endothelial cells (ECs). Importantly, since hypoxia in this model is cell-generated, it is also physiologically regulated, as it has been shown that cells respond and adapt to tissue hypoxia in a time and O₂ concentration-dependent manner[200]. Hence, a by-product of this model is a surprisingly potent source of basic knowledge on how cells regulate their angiogenic signalling in time, space and O₂ tension. Indeed, exposing HDFs to physiological hypoxia in this model produced only modest reductions in cell viability, at the construct core, after 5 days static culture [173]. Furthermore, the possibility to precisely engineer the other key controllers, i.e. diffusion path length, matrix density/diffusion coefficient, matrix anisotropy (by using plastic compression fabrication), makes this system predictable and

mechanistic. This presents the potential to model the behavior of *HIS* cell populations and to apply these predictions (e.g. rate of response, hypoxia trigger level etc.) to optimize engineered angiogenesis, and ultimately the ability of scaffolds to support deep O₂ and nutrient cell perfusion.

1.4 THESIS OVERVIEW

The purpose of this work was to understand how physical cues can be adapted and incorporated into the structure of 3D biomimetic scaffolds for controlling/regulating cell behaviour. Plastic Compression (PC) was employed as a *cell-independent* fabrication method to engineer structure in collagen hydrogel scaffolds, thus removing the need to rely on cellular activity from the initial scaffold fabrication stage. Since these are native collagen materials, scaffold structure not only directs, but is itself also directed by dynamic cell functions (e.g cell locomotion), through ECM synthesis and remodelling. PC fabrication has enabled the deliberate introduction of desired cues into the *initial* scaffold structure to test their individual effect on cell function at the beginning of a physiological feedback cycle. Native collagen Type I was used as scaffold material, as collagen is the most abundant mammalian connective tissue protein, therefore providing a biomimetic microenvironment. The central question addressed by this study was to what extent is cell behavior regulated by physical cues and how these can be built into the initial scaffold structure, as cell controlling/regulating tools.

1.4.1 Hypotheses under test:

1. Fluid loss from collagen hydrogels undergoing Plastic Compression will result in accumulation of retained collagen fibrils at the fluid leaving surface (i.e produce a collagen density gradient along the compression axis) which will limit the discharge rate over time. Gel compression can thus be modelled as an ultrafiltration process with cake layer formation.
2. Embossing a customised pattern template on the surface of 3D collagen hydrogel scaffolds will generate a permanent topography of controlled dimensions (width, depth, pitch). Surface topography will influence the attachment, morphology and orientation of endothelial cells cultured on acellular scaffolds (2D culture), while interface topography will influence the stratification of keratinocytes seeded on fibroblast-seeded scaffolds (3D culture).
3. The stiffness of collagen hydrogels will be directly related to their collagen density and therefore to their hydration level. The proliferation rate of human dermal fibroblasts (HDFs) will be closely related to collagen matrix stiffness such that stiffer matrices will support higher proliferation rates.
4. HDFs seeded within a 3D collagen matrix containing a stiffness gradient will preferentially migrate towards the stiff end of this gradient.
5. Layered collagen matrices can undergo cell-mediated integration, while interface adhesive strength will depend on matrix stiffness at the interface.
6. O₂ consumption by resident cells (pulmonary artery smooth muscle cells), rather than matrix density/diffusion coefficient or diffusion path length, is the predominant factor controlling O₂ tension in the core of 3D nano-fibrillar collagen scaffolds.

7. Spatially controlled hypoxia-induced angiogenic factor signalling by fibroblast populations, exposed to local cell-mediated hypoxia in 3D collagen matrices, will promote directed endothelial cell migration and tubule formation *in vitro* and *in vivo*.

1.4.2 Objectives:

Establish basic operating conditions for engineering physical structure in 3D collagen hydrogel scaffolds, using Plastic Compression (i.e. cell-independent) fabrication, and use the embedded resident cells as the sensing system (cyto-sensors) in order to quantify the effect of scaffold built-in cues on cellular responses.

Aims of study:

1. Develop a functional model of the Plastic Compression process that correlates fluid discharge rate to applied compressive load/pressure, duration of compression, gel initial volume and fluid leaving surface area.
2. Quantify the dimensions (width and depth) of topographic features (grooves) embossed on collagen hydrogel scaffolds and test the effect of surface and interface topography on epithelial cell responses in 2D and 3D culture, respectively.
3. Test the ability to increase collagen hydrogel matrix stiffness by removing interstitial fluid and increasing collagen density.
4. Test the effect of increasing collagen matrix stiffness on fibroblast proliferation over a 7 day culture period.
5. Test the ability to engineer a continuous stiffness gradient within a 3D collagen matrix and test its effect on the direction of fibroblast migration over a 6 day culture period.

6. Test the effect of matrix stiffness on cell-mediated interface integration of bi-layer collagen hydrogel scaffolds by quantification of interface adhesive strength and cell migration across the interface over a 7 day culture period.
7. Measure O₂ tension in the core of 3D collagen constructs to identify the relative contribution of key factors such as matrix density/diffusion coefficient, diffusion path length, cell density and consumption path length on deep O₂ cell perfusion.
8. Test the ability of HDF populations, exposed to local cell-mediated hypoxia, to upregulate production of angiogenic factor protein cascades in 3D collagen constructs. Test the ability of spatially controlled hypoxia-induced signalling to induce a directed angiogenic response by quantifying endothelial cell migration and tubule formation in 3D *in vitro* culture and in *in vivo* implanted constructs over 2 weeks. Assess the functionality of infiltrating host blood vessels by extended real-time monitoring of O₂ tension in the core of implanted constructs.

CHAPTER 2

MATERIALS & METHODS

2.1 Cell culture

Adult human dermal fibroblasts (HDFs) and male New Zealand white rabbit dermal fibroblasts (RDFs) (<10 passages) were cultivated in complete culture media composed of Dulbecco's modified Eagle's medium (DMEM) supplemented with 10% (v/v) fetal calf serum (FCS, First Link,UK), 2 mmol/l glutamine (Gibco Life Technologies, UK), 1,000 U/ml penicillin and 100 mg/ml streptomycin (both from Gibco Life Technologies, UK).

Human primary keratinocytes were cultivated in KER- medium (80% DMEM, 20% HAM's F12, 2% glutamine, 10% FCS, 0.2% hydrocortisone, 0.1% insulin, 0.1% T3/T, 0.1% cholera toxin, 2.5% adenine).

Human umbilical vein endothelial cells (HUVECs) were cultured in endothelial cell growth medium (Promo Cell, Germany) supplemented with ECGS/H (0.4%), fetal calf serum (2%), epidermal growth factor (0.1ng/ml), hydrocortison (1 µg/ml) and basic Fibroblast Factor (1 ng/ml).

Pulmonary arterial smooth muscle cells (PASMC's) were isolated from elastic intrapulmonary arteries from five normal 14 day-old Large White piglets. All piglets were kept in accordance with the NIH (USA) *Guide to the Care and Use of Laboratory Animals* (1996) and Home Office (UK) regulations. Immediately after death, the lungs were removed and 1 cm lengths of the main intrapulmonary artery dissected from both lower lobes. PASMCs were isolated by dissection and enzyme dissociation from the outer (50%) medial layers, as described previously[209]. The

cells were grown in F12-Hams medium supplemented with 20% fetal calf serum (First Link, West Midlands, UK), 2 mM glutamine and penicillin/streptomycin (1000 U/ml; 100 mg/ml, Gibco Chemicals) and used between passages 3 and 8. For removal of cells from monolayer culture, flasks containing cells were washed with PBS, and incubated with trypsin (0.5% in 5 mM EDTA, Invitrogen,UK) for 5 min at 37⁰C.

2.2 Formation of collagen gels

Collagen gels were prepared as described by Eastwood et al. [210]. Briefly, for forming 5ml gels a collagen gel mixture composed of 4 ml acid soluble collagen type I (2.20 mg/ml; First Link, UK) and 0.5ml 10× DMEM (Gibco Life Technologies, UK) was neutralized by 235.5 µl of 5M NaOH, using the indicator colour change from yellow to cirrus pink. While still in liquid form, 4.5 ml collagen solution was mixed with 0.5-ml cell suspension at the desired cell density. For acellular gels, 0.5ml of medium containing no cells was mixed with the collagen solution. The neutralized collagen suspension was poured into round/rectangular wells (depending on application, see separate chapters) and incubated at 37⁰C in a 5% CO₂ humidified incubator for 30 min.

2.3 Plastic Compression of collagen gels

Following setting and incubation, gels were compacted by a combination of compression and blotting, as described by Brown et al. [25]. Briefly, a 165µm thick stainless-steel mesh (mesh size 300µm) and a layer of nylon mesh (50 µm mesh size) were placed on double layer absorbent whatman paper (grade 1: 11µm, 185mm diameter). The collagen matrix was placed on the nylon mesh, covered with a second nylon mesh and loaded with a 120 g metal block for 5min at room temperature leading to formation of a flat collagen sheet (50-100 µm thick) protected between

two nylon meshes (Fig.1). Compressed collagen matrices were peeled off the nylon meshes and placed in culture wells containing 5 ml complete culture medium. Plastic Compression did not significantly reduce cell viability[25].

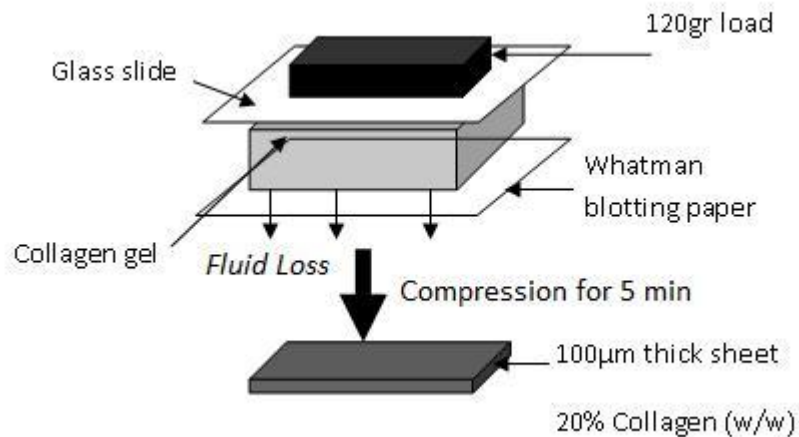


Fig.1 Schematic showing the plastic compression fabrication process. Collagen gels are compressed under fixed mechanical loading over a porous support substrate (blotting paper) so that rapid fluid removal (~99% fluid loss within 5 min) is achieved by a combination of compression and blotting. Compression for typically 5min produces collagen sheets of ~100- 200µm thickness (depending on initial gel volume/thickness).

2.4 Scanning electron microscopy

Compressed gels were washed in 0.1M phosphate-buffered saline (PBS) and fixed in 2.5% gluteraldehyde in 0.1M PBS for 1 hr at 5 °C. Gels were then washed twice with 0.1M PBS, fixed with 0.1% osmium tetroxide in 0.1M Na cacodylate buffer for 1 h at room temperature and dehydrated through an alcohol series with air-drying. Dry specimens were mounted onto stubs, gold-palladium sputter-coated, and viewed in a JEOL 5500LV SEM.

2.5 Histology and immunohistochemical staining

After culture collagen constructs were fixed in 4% neutral buffered formaldehyde. Sections of approximately 5 mm in thickness were made by cutting samples in a plane perpendicular to the construct's surface. The constructs were dehydrated through a xylene-ethanol series and embedded in paraffin for routine histology. Cross sections, 7 µm thick, of the paraffin embedded collagen constructs were stained using the hematoxylin-eosin technique and observed with an Olympus BX41 microscope, while images were captured with an Olympus DP70 CCD camera.

For immunofluorescent staining cultured constructs were washed in 5ml PBS, fixed in 100% ice-cold methanol for 1h and incubated for 30 min with primary and then secondary antibody (see separate chapters for specific antibodies used). After washing with PBS, bound antibody was localised using a fluorescence Olympus BX41 microscope at approximate absorption 495 nm, and fluorescence emission 519 nm, and captured using a Olympus DP70 CCD camera.

Immunohistochemical staining was carried out using Vectastain ABC-HRP kit (Vector Laboratories, USA) according to the manufacturer's instructions. After dewaxing and serum blocking (0.25% Triton-X in PBS for 15 min, followed by 30 min incubation with 10% goat serum), the sections were incubated with primary antibody for 30 minutes at room temperature, rinsed in PBS, and incubated with biotinylated secondary antibody for 30 minutes (see separate chapters for primary antibody used). Sections were then incubated with Vectastain ABC Reagent, followed by peroxidase substrate solution until desired stain intensity developed. Peroxidase substrate used was DAB (brown) (Vector Laboratories, USA), with haematoxylin counterstaining.

2.6 Statistical analysis

For each experimental condition a sample size of $n=3$ or more was used, as noted. Data is expressed as mean \pm standard deviation, unless mean \pm standard error is noted. Statistical analysis was carried out using T-test where a maximum of 2 groups was used per analysis or oneway ANOVA (or Kruskal-Wallis test for non-parametric distribution) accompanied with multiple comparison tests for analysis of 2 or more groups, using SPSS 14 software. Differences were considered significant when $p<0.05$, unless otherwise noted.

CHAPTER 3

MECHANISMS OF STRUCTURE GENERATION DURING PLASTIC COMPRESSION OF NANO-FIBRILLAR COLLAGEN HYDROGEL SCAFFOLDS

Operator control of cell/matrix density of plastically compressed collagen hydrogel scaffolds critically depends on reproducibly limiting the extent of scaffold compaction, as fluid expulsion. During compression the main (basal) fluid leaving surface (FLS) acts as a filter, allowing out fluid and solutes but retaining collagen fibrils, cells and some macromolecules [25]. This fluid-filtration ('caking') effect results in the formation of multiple layers of compacted lamellae (1 to 5 μm thick) of collagen fibrils running parallel to the FLS, throughout the body of the gel, with the densest layer forming at the FLS. The presence of lamellae has previously been identified both by birefringence and transmission electron microscopy and was measurable as an increase in mean collagen fibril density in compressed vs. non-compressed gels [25]. The formation of this dense lamellar layer might explain why over time, for sufficiently high pressures, the flux ceases to become pressure-dependent and becomes time-dependent [53], a problem commonly encountered with ultrafiltration of macromolecules (gel layer formation or fouling) [211,212]. In this study we used ultrafiltration theory to develop a functional model of the compression process. We hypothesised that the FLS of a collagen hydrogel undergoing compression behaves as an ultrafiltration membrane. Increasing accumulation of collagen material at the FLS during compression (equivalent to concentration polarisation) produces anisotropic structuring, but also increases the FLS hydraulic resistance (R_{FLS} ; m^{-1}), which in turn reduces the volumetric discharge rate (Q ; m^3/s)

through the FLS, cross-sectional area (A ; m^2), as predicted from Darcy's law for a pressure-driven membrane operation (Fig. 1) [213]:

$$Q = \frac{A \cdot \Delta P}{\mu \cdot R_{FLS}}$$

where ΔP is the hydraulic pressure difference across the FLS (Pa) and μ is the dynamic viscosity of water (Pa.s). Darcy's law is valid for incompressible, homogeneous Newtonian fluids moving slowly through a rigid porous medium with uniform porosity under isothermal and steady state conditions, assumptions that generally hold true in our model (i.e. water flowing slowly through a homogeneous, isotropic collagen matrix). Importantly, the above equation, neglects the inhomogeneity in the thickness (or mass) of the collagen lamellar layer arising from time-dependent accumulation of collagen fibrils at the FLS [213]. However, Ho and Zydney have shown that in membrane fouling during protein microfiltration this spatial variation (if it occurs in our model) has relatively little effect on the flux decline due to the self-leveling nature of the cake growth process[214].

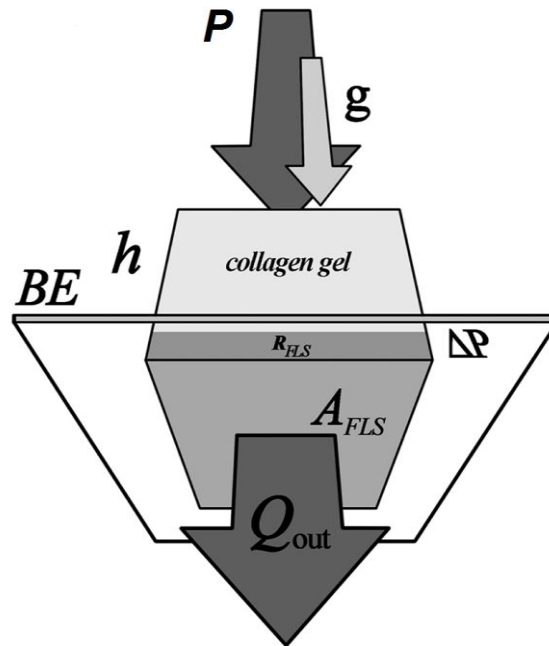


Fig. 1 3D Schematic showing the plastic compression process and how Darcy’s law can be applied to calculate the discharge rate (Q_{out}). Pressure (P) is applied on a collagen hydrogel, placed on blotting elements (BE), by applying a compressive load. This adds to the hydrostatic pressure (ρgh) of the gel’s fluid (gel height h , water density ρ) to create a hydraulic pressure difference (ΔP) across the fluid leaving surface (FLS) which forces fluid out of the main FLS area (A_{FLS}). The pressure and the hydraulic resistance of the FLS (R_{FLS}) are the key factors determining the discharge rate.

We tested the hypothesis that while compressive load, i.e. applied pressure, is the primary determinant of flux at the beginning of compression (load-dependent phase), increasing FLS collagen density (C_{FLS}) (measured by X-ray attenuation) and therefore increasing R_{FLS} become the key factors governing flux as the process proceeds (flow-dependent phase). Experimental data were used to derive empirical equations describing these two consecutive, but distinct, phases of the compression. We developed a model integrating these two phases and used this to predict changes in fluid loss over time for a range of applied pressures. The model predictions were then compared to experimental data. This allowed us to test the hypothesis that

changing pressure over time, to match changes in R_{FLS} , could maintain a steady flux during plastic compression of collagen hydrogels.

3.1 RESULTS

Testing of compression parameters

The effect of varying the FLS cross-sectional surface area (A) on discharge rate was tested first. As expected from Darcy's law for a pressure-driven membrane operation (see Chapter 3 introduction), the initial (0-1 min) rate of fluid loss was linearly correlated to A ($3.6 < 9 < 19.6 \text{ cm}^2$) (Fig.2).

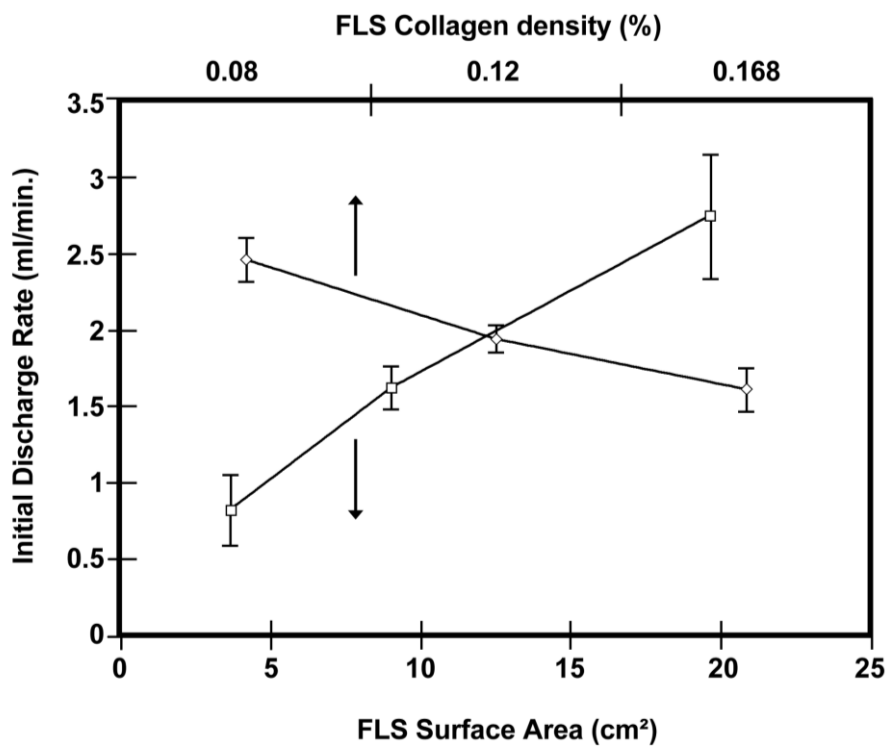


Fig. 2 Correlation of discharge rate with FLS surface area and FLS collagen density. Plot of initial (0-1 min) discharge rate for 5ml cylindrical collagen gels (initial collagen density 0.168%) of varying FLS area (3.6, 9, 19.6 cm²) and for 5ml cylindrical collagen gels (FLS area 9cm²) of varying initial collagen density (0.168, 0.12, 0.08 %). All gels were allowed to compress under their own weight (n=5 for each point).

In contrast, increasing the initial FLS hydraulic resistance (R_{FLS}) by increasing the initial collagen density (C_{FLS}) from 0.08 to 0.12 and 0.168% indicated that a near inverse-linear relation exists between the initial (0-1 min) rate of fluid loss and C_{FLS} ($0.168 < 0.12 < 0.08\%$), confirming that C_{FLS} and R_{FLS} are directly correlated (Fig. 2).

To test the effect of varying the hydraulic pressure difference across the FLS (ΔP) on discharge rate we applied a range of compressive loads/pressures (0, 10g/ $P=109$ Pa, 90g/ $P=980$ Pa and 120g/ $P=1306$ Pa) on 5ml collagen gels ($A=9\text{cm}^2$) and measured fluid loss over 12 min. As expected, increasing the compressive load resulted in a higher initial discharge rate and a greater cumulative volume of fluid being expelled from the gel (Fig. 3A, B). Figure 3B shows that the discharge rate decreased exponentially with time for all compressive loads tested. The maximal initial (0-1 min) rate of fluid loss was achieved with application of a 90g load ($P=980$ Pa) (Fig. 3B). Application of a 120g load ($P=1306$ Pa) did not significantly increase the rate of fluid loss (Fig.3A), but instead induced deformation along the x-y plane of the gel (indicating fluid loss along this plane), such that after 5 min of compression, gel diameter had increased from 34.16 ± 0.95 mm to 37.8 ± 1.43 mm. This increase was statistically significant ($p<0.05$, $n=4$), demonstrating that during unconfined compression a threshold was crossed between pressures of 980 Pa and 1306 Pa where the nature of the process changed substantially, in effect fluid flow and deformation becoming multi-axial (Note; up to this point compression on blotting elements ensured that flow occurred overwhelmingly uni-directionally, along the vertical axis of the gel). Importantly, a 15ml gel compressing under its own weight had the same initial discharge rate as a 5ml gel compressed with a 10g load (Fig. 3B), implying that gel weight acts additively to external load. The increase in initial

(0-1 min) discharge rate observed with increasing compressive load was not linearly correlated with the increase in applied load. Instead, a 3 and 19 fold increase in load (from 5 to 15 and 95g, respectively) resulted in approximately 1.4 and 2 fold increase in discharge rate, respectively, consistent with the idea that increasing R_{FLS} gradually limited the effect of compressive load on discharge rate during compression.

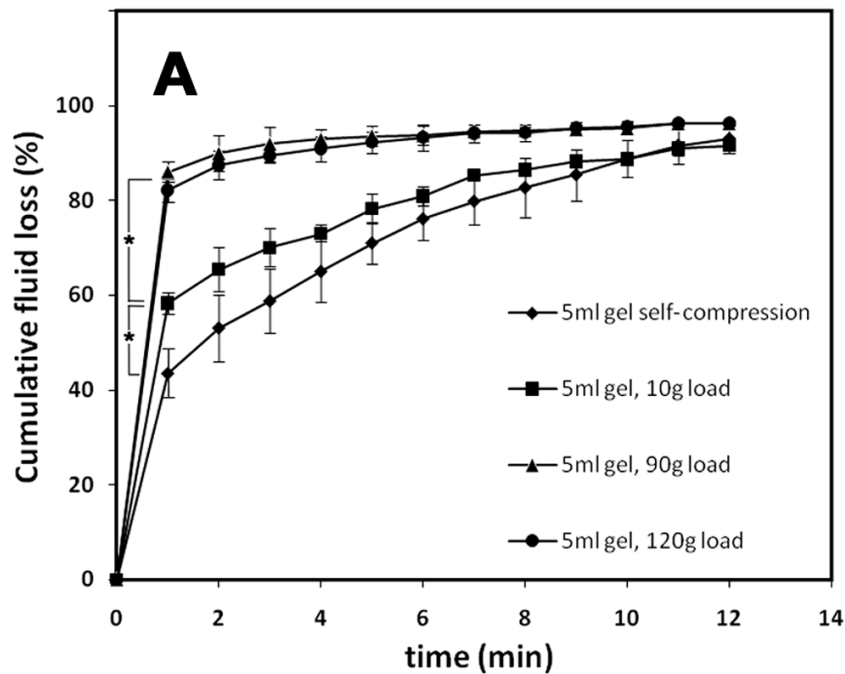
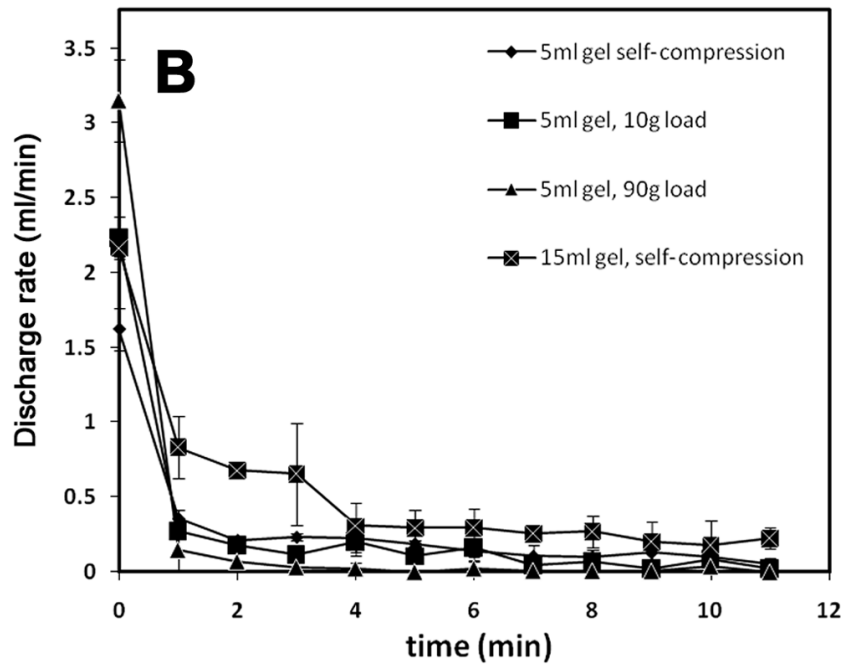


Fig.3 Change in rate of fluid loss during plastic compression. (A) Plot of cumulative fluid loss (%) vs. time for 5ml cylindrical collagen gels (initial collagen density 0.168%, FLS area 9 cm²) compressed under their own weight (self-compression) or by application of a 10, 90 or 120 g load, * p<0.05.



(B) Plot of discharge rate vs. time for 5 ml cylindrical collagen gels undergoing self-compression or compression with a 10 or 90g load. The discharge rate of a 15 ml collagen gel undergoing self-compression is shown for comparison with a 5 ml gel compressed with a 10g load (n=5 for each loading condition).

Structure-generating mechanisms of Plastic Compression

Based on previous work on Plastic Compression by this group showing that the uni-directional outflow of fluid from a single surface results in retention of collagen at the leaving surface [25], comparable to particle accumulation (caking) at a filtration surface (Fig. 4A), the formation of this layer was examined further. Preferential fluid loss and increased collagen density at the FLS could be seen macroscopically (based on the lighter area of the FLS, Fig.4B) and by coomassie-blue staining (in which dye staining of a denser protein (collagen) line was evident at the FLS, Fig.4C). SEM analysis of the same FLS structure (Fig.4D) showed multiple layers of compacted lamellae (1 to 5 μm thick) made up of collagen fibrils running parallel to the FLS. These ran parallel to the FLS, throughout the body of the gel, with the densest layers

forming at the FLS (Fig.4D). We hypothesised that these anisotropic, biomimetic structures [25] were generated by the directionability of fluid flow and so fibril accumulation which would translate into a collagen density gradient along the compression axis of the gel. This prediction suggests that the highest collagen density would be at the FLS, as shown in Fig. 4A.

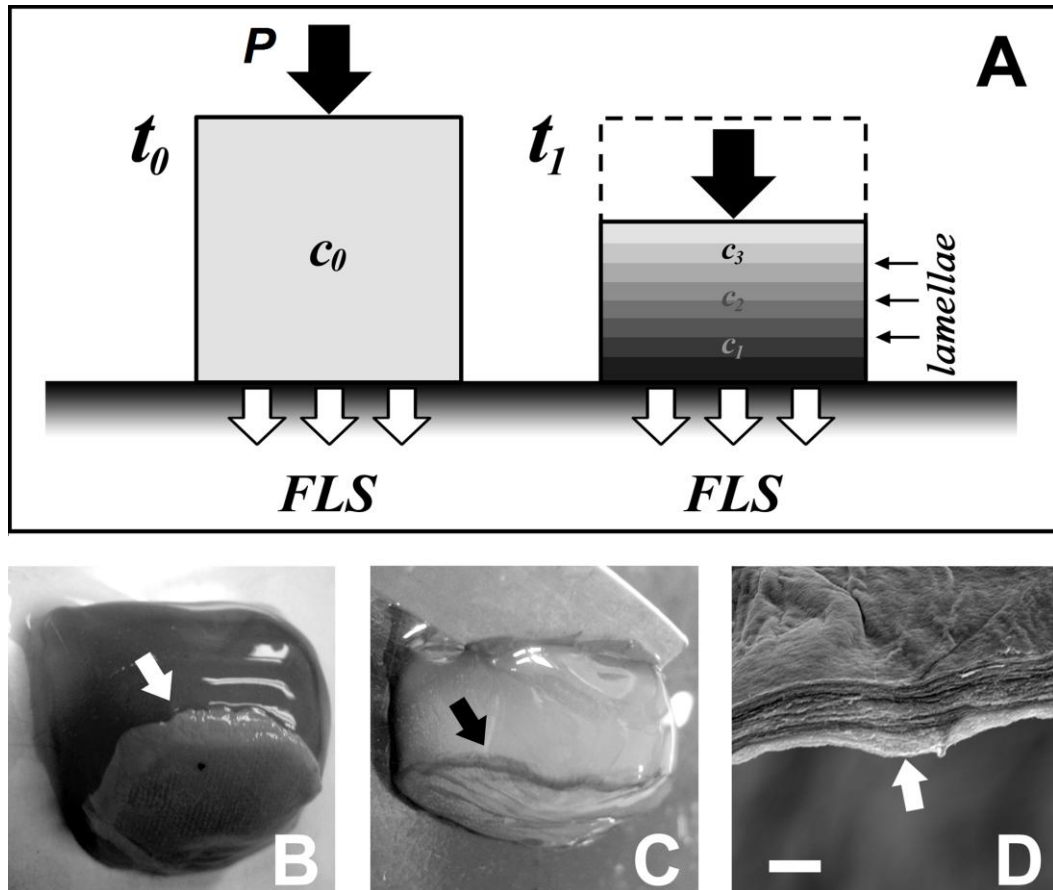


Fig. 4 Meso-scale structure generation during plastic compression of collagen hydrogels. (A) Schematic showing the structure-generating effect of fluid loss for a collagen gel undergoing plastic compression. At the beginning of compression ($t=t_0$), the gel is homogeneous throughout its body, having a uniform collagen density (C_0). Over time ($t=t_1$) the directional egress of fluid from the FLS results in compaction of fine lamellae (1 to 5 μ m thick) of collagen fibrils, parallel to the FLS with the densest layer forming at the FLS. This results in a collagen density gradient along the compression axis of the gel, such that $C_1 > C_2 > C_3$. (B) Macroscopic view of a 5 ml collagen gel after 5 min compression. The lighter area (arrowed) seen at the FLS formed due to greater loss of indicator-containing fluid at the FLS, compared to the gel's body. (C) Image

showing a coomassie blue-stained collagen gel after 5 min of compression. The darker area (arrowed) seen at the FLS shows the increased density of collagen at the FLS compared to the gel body. (D) SEM image of the cross-section of a 5 ml collagen gel (FLS area 9 cm²) after 5 min compression with a 90g load. Multiple layers of packed fine collagen fibril networks (lamellae), typically 1-5µm thick, can be seen throughout the body of the gel but by far the densest layer is seen at the FLS (arrowed) (bar=20µm).

As a measure of collagen fibril compaction, the relative positions of marker carbon particles, trapped between collagen fibrils, were measured during compression (Fig. 5A). For this analysis 8 prominent carbon aggregates were identified within a carbon-loaded gel (after setting) and their positions relative to the FLS were measured over time (15 min) in 45-60s intervals. While all particles showed a gradual reduction in their relative position over time, this occurred faster for particles closer to the FLS, indicating that collagen compaction occurred preferentially in the lower collagen gel layers than at the top and middle sections during compression (Fig. 5B). This differential would tend to generate delamination (i.e. lamella formation) as seen in Fig. 4D.

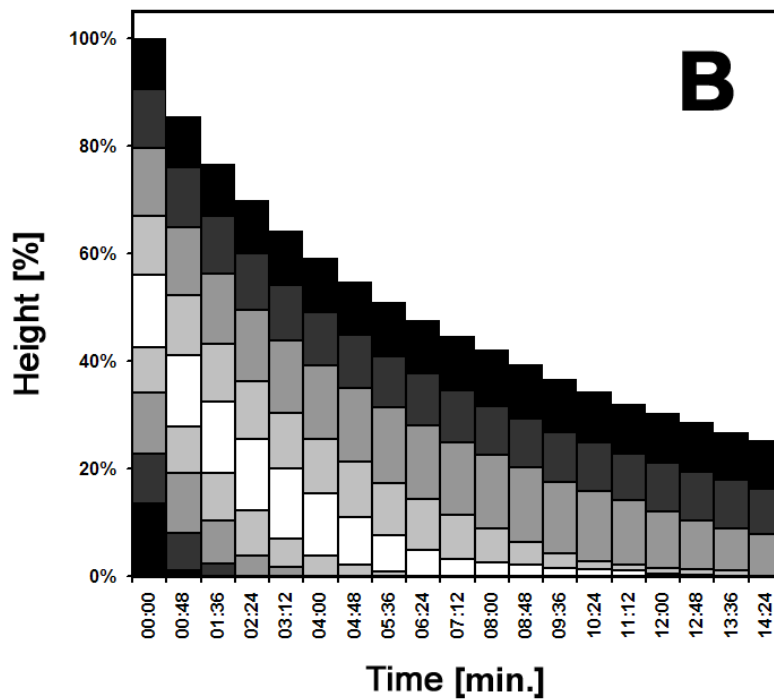
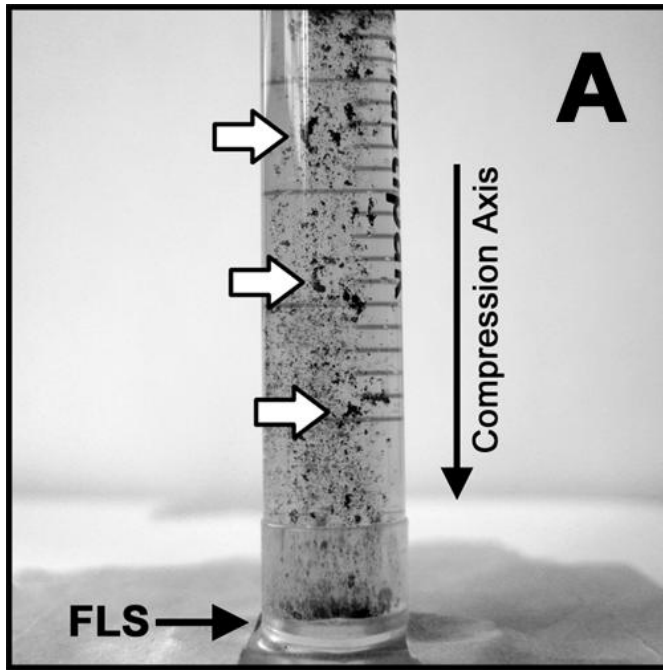


Fig. 5 Analysis of the spatial distribution of collagen compaction along the compression axis (A) Setup used in the collagen compaction assay. The collagen gel was allowed to compress under its own weight, within the syringe, for 15 min. Clearly visible carbon particles (white arrows) can be seen trapped within the polymerized collagen hydrogel (image taken at start of compression). (B) Analysis of the compaction of material in each layer of the gel, as indicated by the loss of relative heights of 8 carbon particle aggregates over time (shown by the horizontal lines within the bars). Note that while

those that start at the top of the gel just drop down with little change in height (minimum compaction and loss of fluid), those starting in the gel middle or lower either compact dramatically by the end of PC or are unmeasurable before the end of the PC process.

Preferential fluid loss at the main (bottom) fluid-leaving surface would imply that FLS collagen density (which determines the FLS hydraulic resistance) and not *average* gel collagen density is the key determinant of discharge rate. We found that a self-compressing 5ml gel of 0.2% initial collagen density had a significantly higher ($p < 0.05$) initial (0-1 min) discharge rate compared to a self-compressing 10 ml gel of 0.1% initial collagen density that was pre-compressed to remove 50% of its fluid, to produce a 5ml gel with 0.2% average collagen density (Fig. 6A). It is assumed that pre-compression of the 10ml gel resulted in an anisotropic distribution of collagen density along the compression axis with the highest density occurring at the FLS (as in all other PC tests). This pre-compression in turn increased the FLS hydraulic resistance which limited the subsequent discharge rate. We thus tested whether inverting the gel between the initial and final compression stages would abolish the rate-limiting effect of increasing collagen density at the FLS (typical where there was no inversion). This 180° inversion of gel position, so fluid flow direction, would effectively place the gel upper surface at the bottom, making it the new FLS. Fig. 6B shows that there was no significant difference in % fluid loss over 2 time windows (0-1min and 1-2 min) of compression when this top-bottom gel inversion was performed. This test confirms the fluid flow rate-limiting nature of the FLS and suggests that reversal of fluid flow direction, during PC processing, could be a powerful tool in controlling both average flow rates and the resultant collagen micro-structure (Fig. 4D).

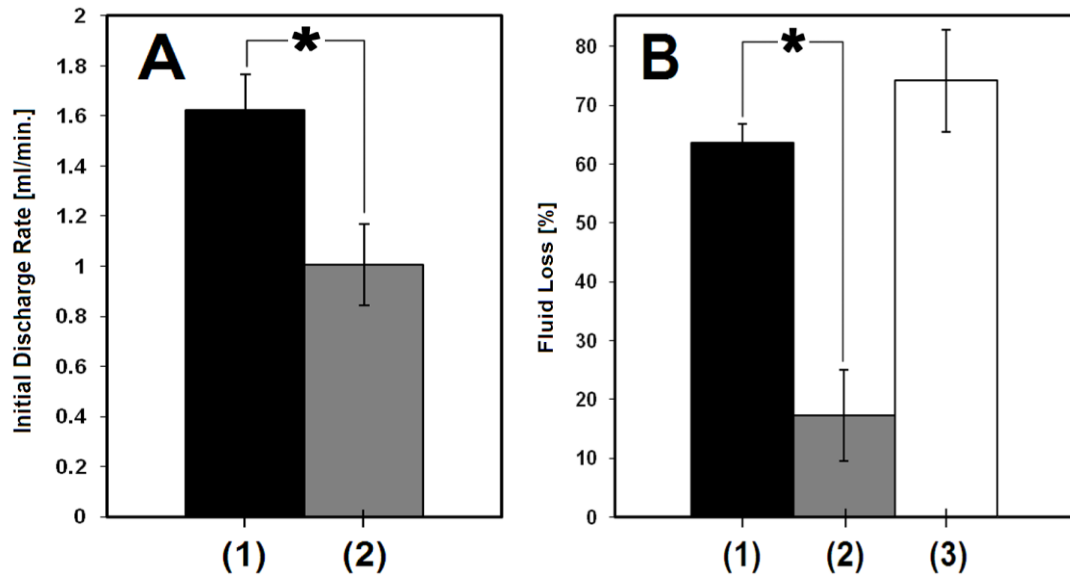


Fig. 6 Close dependence of discharge rate on FLS collagen density. (A) Comparison of the initial (0-1 min) discharge rate of a self-compressing 5ml gel (0.2% initial collagen density) (1) to that of a self-compressing 10 ml gel (0.1% initial collagen density) which was pre-compressed to remove 50% of its fluid (2) (this produced a 5ml gel with 0.2% average collagen density), * $p < 0.05$ ($n=4$ for each condition). (B) Comparison of the % fluid loss within 0-1min (1) and 1-2 min (2) and (3) of compression when 5ml gels were compressed with a 10g load. Gels were either left in their initial position (1) and (2) or inverted after 1 min of compression to place the FLS at the top (3), * $p < 0.05$ ($n=4$ for each condition).

Load-dependent vs. flow-dependent phase

The above findings led to the hypothesis that while the initial flux depends on compressive load (load-dependent phase), later stage flux becomes flow dependent. This will occur as the R_{FLS} becomes limiting (generating a flow-dependent phase), i.e. the FLS behaves like a typical ultrafiltration membrane with a built-up cake [211]. With further build up of collagen fibrils and increasing cake density, the R_{FLS}

would subsequently become the key factor governing the flux during the flow-dependent phase (and ultimately the practical end-point of compression).

Figure 7 shows a plot of initial (0-1 min) flux (J_0) vs. pressure (P) for 5ml gels (FLS area=9cm², initial collagen density=0.168%) compressed with a range of compressive loads.

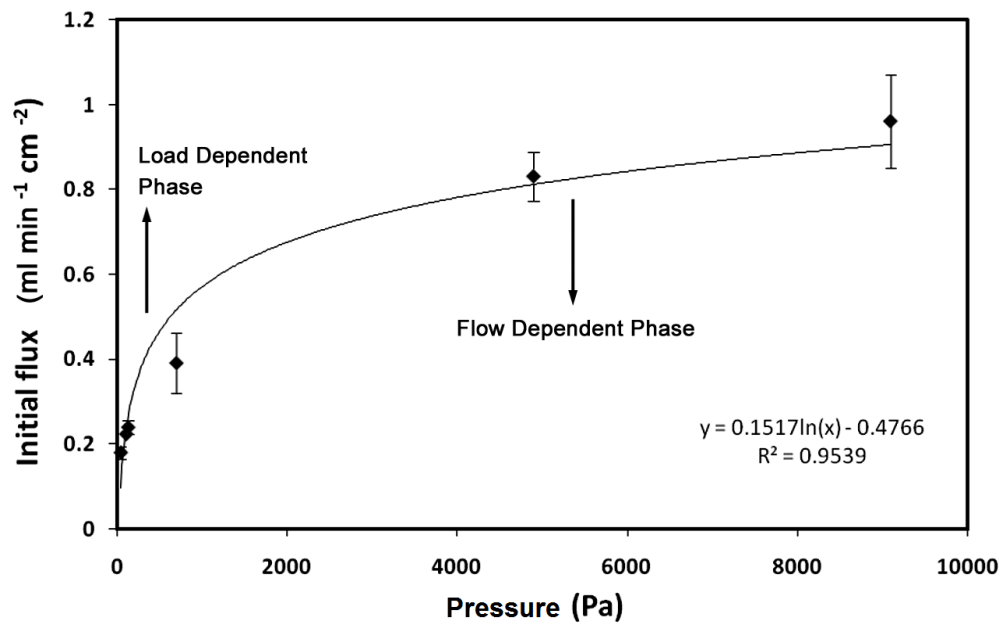


Fig.7 Analysis of the two consecutive flux phases during the plastic compression process. Plot of initial (0-1 min) flux (J_0) out of collagen hydrogels vs. Pressure (P), during compression with a range of compressive loads. The linear part of the curve represents the ‘load-dependent’ phase of the compression (flux depends on pressure) while the plateau region represents the ‘flow-dependent’ phase of the compression (flux is almost independent of pressure). The best-fit line is given by $J_0 = 0.1517\ln P - 0.4766$, $R^2 = 0.9539$.

While for small applied pressures (40-130 Pa) J_0 was proportional to P (load-dependent phase), the flux-pressure relation became non-linear as P increased above 700Pa, i.e. the flux gradually became less dependent on compressive load as a flow-

dependent phase was established. These experimental data could be fitted with empirical equation (1):

$$J_o = 0.1517 \ln P - 0.4766 \quad R^2 = 0.9539 \quad (1)$$

Quantification of R_{FLS}

By applying Darcy's law it was possible to quantify the R_{FLS} for collagen gels (5ml, 0.168 % initial collagen density) compressed with a 10g load (see Chapter 3 Methods section). The R_{FLS} was found to increase exponentially with time during compression (Fig. 8A). Correlation of R_{FLS} with gel cumulative fluid loss showed a rapid increase in R_{FLS} when >60% of the gel's fluid content was expelled (Fig. 8A). This correlated closely with the decrease in discharge rate previously identified at this point (Fig. 3A, B). Since discharge rate in the final stages of compression was too low for reliable measurement, R_{FLS} for highly compressed gels (>93% total fluid loss) was directly measured by permeability test. In the test the resulting collagen membranes, obtained from compression of collagen gels (5ml) with a pressure of 1306Pa for 5min (~96% fluid loss), were subjected to a constant flux filtration test with a set flow rate (1 or 9 ml/min) while the pressure required to deliver such a flow rate was measured (see Chapter 3 Methods section). The value of hydraulic resistance obtained was $R_{FLS} = 1047 \pm 343 \text{ nm}^{-1}$. This value was used to predict the discharge rate out of 5ml collagen gels compressing for 5min with a pressure of 1306Pa. Figure 8B shows that there was no significant difference between predicted and experimental values of discharge rate, indicating a good estimation of R_{FLS} . This

was also supportive of the hypothesis that fluid loss during compression could be reliably modeled as an ultrafiltration process.

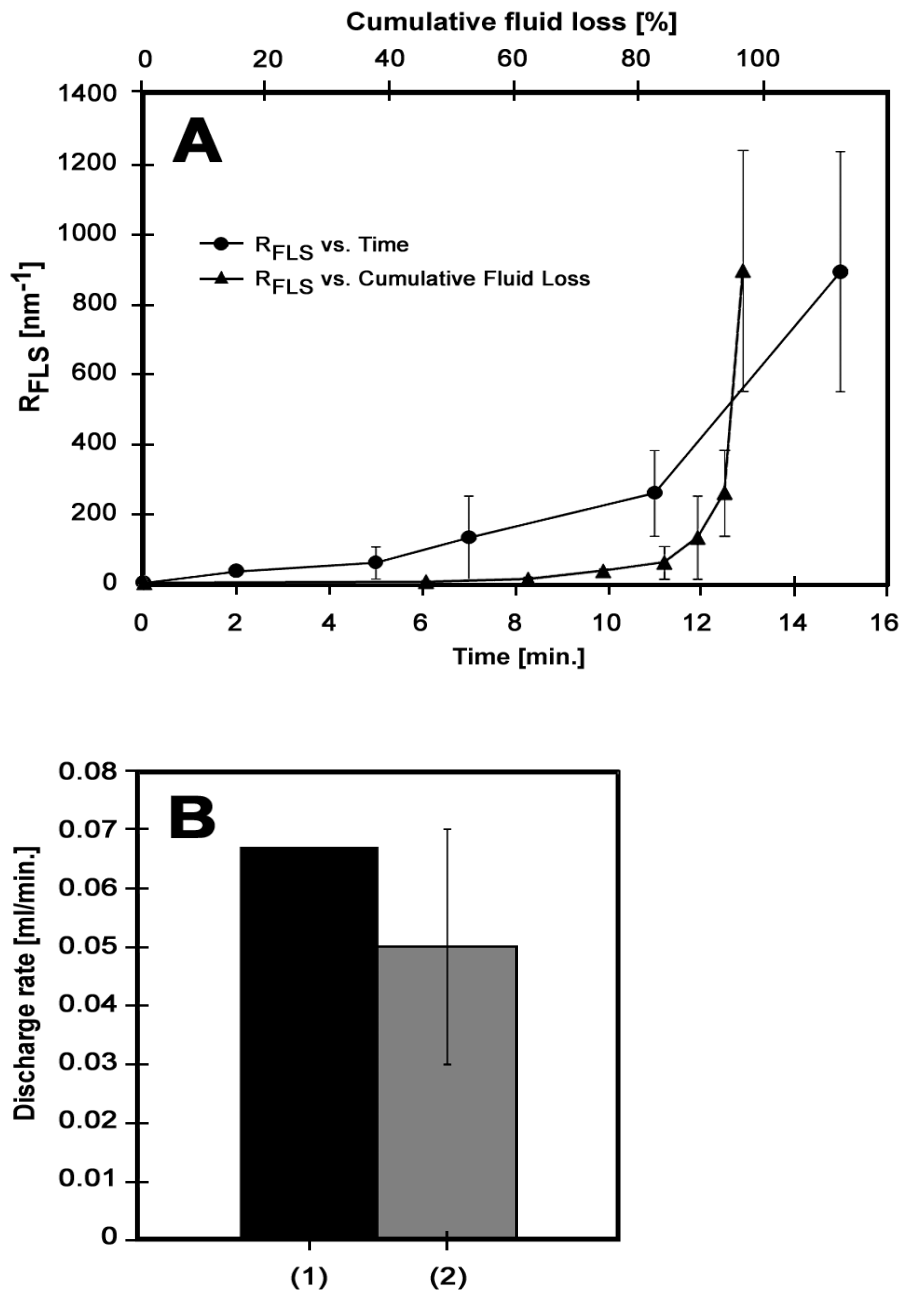


Fig. 8 (A) Change in FLS hydraulic resistance (R_{FLS}) during plastic compression. Plot of FLS hydraulic resistance (R_{FLS}) vs. time and cumulative fluid loss (%) for a 5 ml cylindrical collagen gel undergoing compression with a 10g load. **(B)** Comparison of predicted (1) and experimental (2) values of discharge rate for cylindrical collagen gels

(5ml) compressed with a pressure of 1306Pa for 5min (96% fluid loss). A value of $R_{FLS} = 1047 \text{ nm}^{-1}$ was used to calculate the predicted discharge rate (by application of Darcy's law).

Correlation of R_{FLS} with C_{FLS}

In order to quantify C_{FLS} , we first quantified the collagen density gradient formed along the compression axis of the gel at various stages of compression, by measuring the attenuation of X-rays transmitted through the gel. This provided direct information on water distribution, and thus of collagen density along the compression axis (Fig. 9A, B). The variation in % collagen density along the compression axis at four stages of compression (0, 60, 80 and 98% fluid loss) is shown in figure 9C, D (note: the 1.4 to 2 fold collagen density gradient observed was in the range reported by a previous study where collagen density along the compression axis was quantified by measurement of fluorescence intensity of fluorescein-labeled collagen monomers incorporated in the collagen gel [215]).

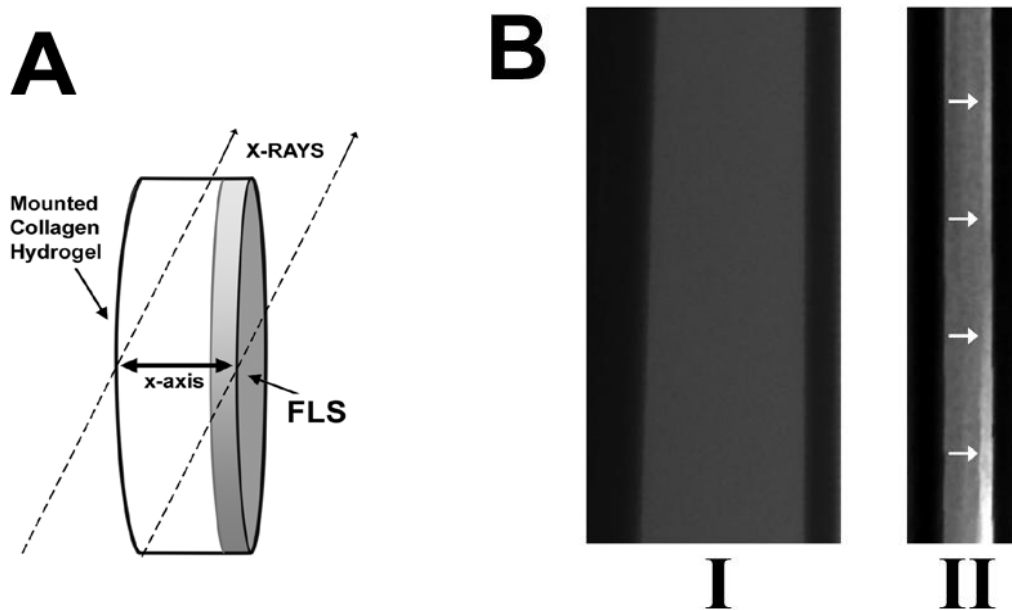
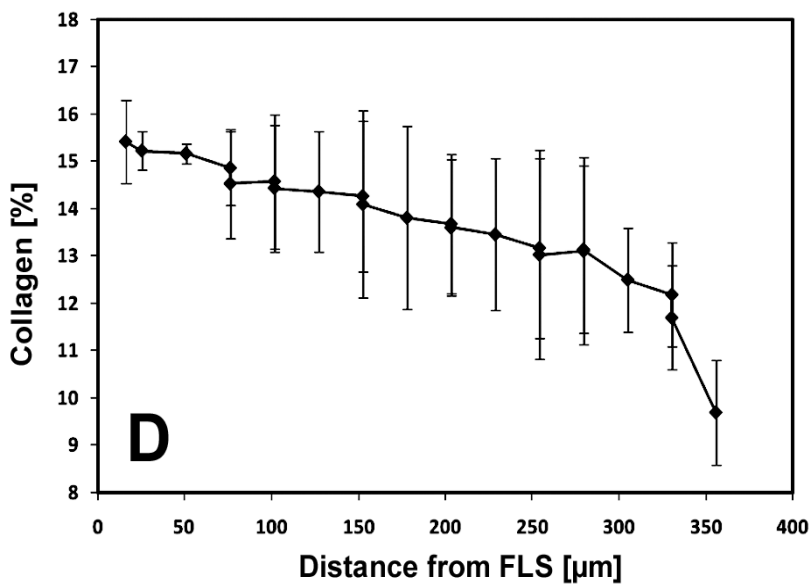
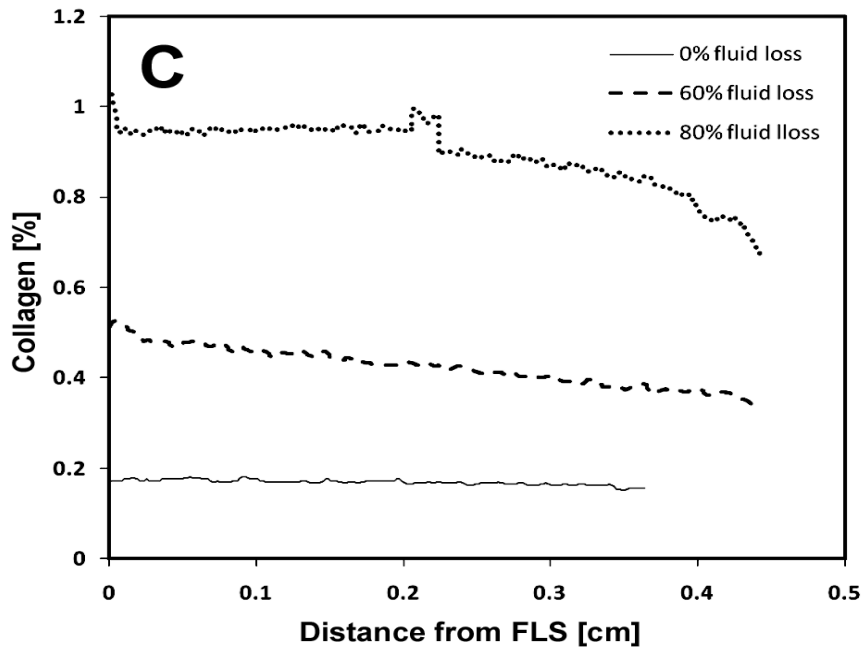


Fig. 9 Quantification of collagen density along the compression axis at various stages of compression. (A) Schematic showing the setup used to measure the attenuation of X-rays, transmitted through a collagen gel. Gels were placed between 2 glass slides and mounted vertically, in the scanner chamber. X-axis denotes the compression axis of the gel. (B) X-ray radiograms of collagen gels prior to compression (I) and after compression (98% fluid loss) (II). White areas in compressed collagen gels (arrowed) show areas of lower water content (higher x-ray intensity), at the FLS.



(C) Representative traces of % collagen density vs. distance from the FLS along the x-axis of the gel for three levels of compression (0, 60 and 80%). (D) Detailed plot of collagen density (%) vs. distance from the FLS along x-axis of gels compressed to 98% fluid loss (n=4).

Figure 10A shows a plot of $1/C_{FLS}$ (%) vs. % cumulative fluid loss (FL_{cum}).

Experimental data could be fitted with empirical equation (2a):

$$\frac{1}{cfls} = 5.7144 - 0.0587FLcum \quad R^2 = 0.9946 \quad (2a)$$

Eq. 2a could be rearranged to Eq. 2b:

$$Cfls = \frac{0.97C_0}{(0.97 - 0.01FLcum)} \quad (2b)$$

where $Cfls$, C_0 (the gel initial collagen density) and $FLcum$ are expressed as a percentage.

R_{FLS} was linearly correlated to C_{FLS} (Fig. 10B). Experimental data could be fitted with empirical equation (3):

$$Rfls = 70.093Cfls \quad R^2 = 0.9972 \quad (3)$$

where $Rfls$ is in nm^{-1} and $Cfls$ is expressed as a percentage.

Eq. 2b was combined with Eq. 3 to obtain Eq. 4:

$$Rfls = \frac{68 C_0}{(0.97 - 0.01FLcum)} \quad (4)$$

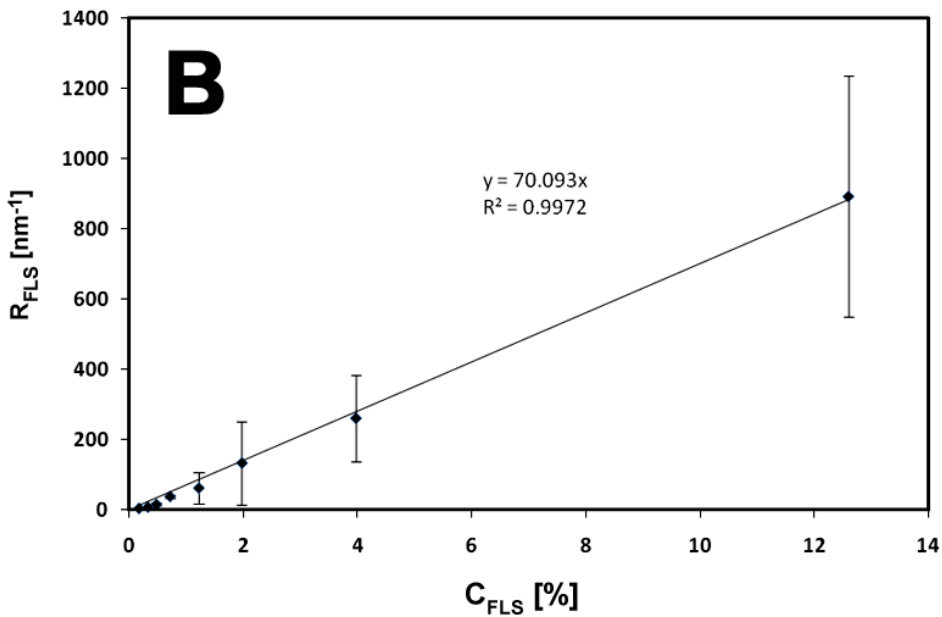
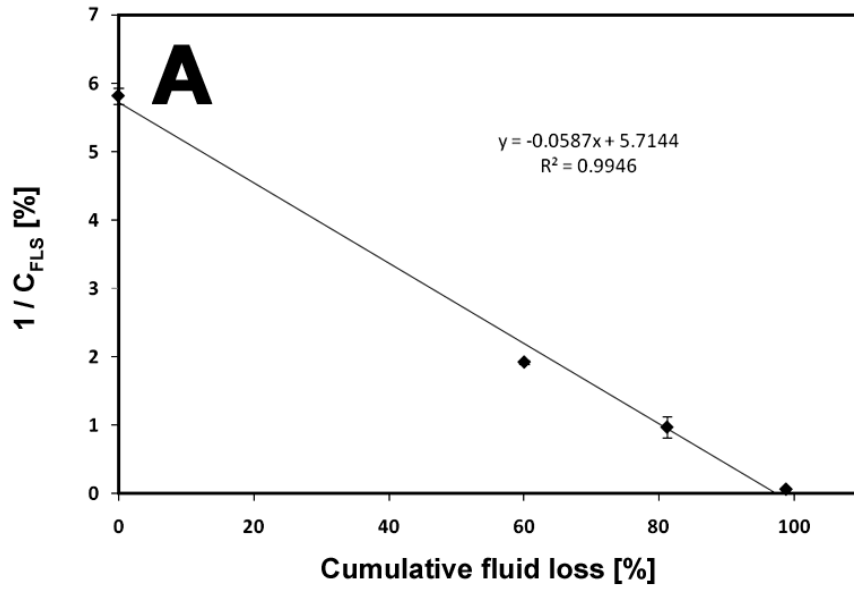


Fig. 10 Correlation of FLS collagen density (C_{FLS}) with FLS hydraulic resistance (R_{FLS}). (A) Plot of $1/C_{FLS}$ (%) vs. FL_{cum} (%). The best-fit line is given by $\frac{1}{C_{fls}} = 5.7144 - 0.0587FL_{cum}$, $R^2 = 0.9946$. (B) Plot of R_{FLS} vs. C_{FLS} (%). The best-fit line is given by $R_{fls} = 70.093C_{fls}$, $R^2 = 0.9972$.

Compression model development and validation

For gels undergoing compression with a constant compressive load, the instantaneous flux (J) during compression could be obtained by dividing the initial flux (J_0) by the fold increase in R_{FLS} as shown in Eq. 5a:

$$J = J_0 \frac{R_0}{R_{fls}} \quad (5a)$$

where R_0 is the initial FLS hydraulic resistance expressed in nm^{-1} .

Combining Eq.4 with Eq.5a and substituting for $R_0 = 68C_0/0.97$ we obtain Eq.5b:

$$J = J_0 (1 - 0.01FLcum) \quad (5b)$$

From Eq.5b, and integrating flux with respect to time (t), we obtain Eq. 6a:

$$FLcum = 100 \left(1 - e^{-\frac{AJ_0}{V_0} t} \right) \quad (6a)$$

where A is the FLS area (in cm^2), V_0 is the initial gel volume (in ml), J_0 is the initial flux (in $\text{ml min}^{-1} \text{cm}^{-2}$), t is time (in min) and $FLcum$ is expressed as a percentage (note J_0 is a function of applied pressure can be calculated using Eq.1).

Combining Eq.5b with Eq.6a, we obtain Eq.6b that relates J with t :

$$J = J_0 e^{-\frac{AJ_0}{V_0} t} \quad (6b)$$

Combining Eq.5a with Eq.6b, we obtain Eq.6c that relates R_{FLS} with t :

$$R_{fls} = R_0 e^{\frac{A J_0}{V_0} t} \quad (6c)$$

Eq.6a was used to model FL_{cum} over time for collagen gels compressed with a range of pressures (130, 707, 4900 and 9100 Pa). Model data were compared with experimental data, showing a close correlation (Fig. 11). The greatest difference between experimental data and model predictions was seen at low pressures (130 and 707 Pa), especially towards the end of the compression period (4-5 min) where experimental values were substantially below those expected. This effect progressively disappeared with higher pressures (4900 and 9100 Pa), suggesting that the model could be a better fit for higher pressures.

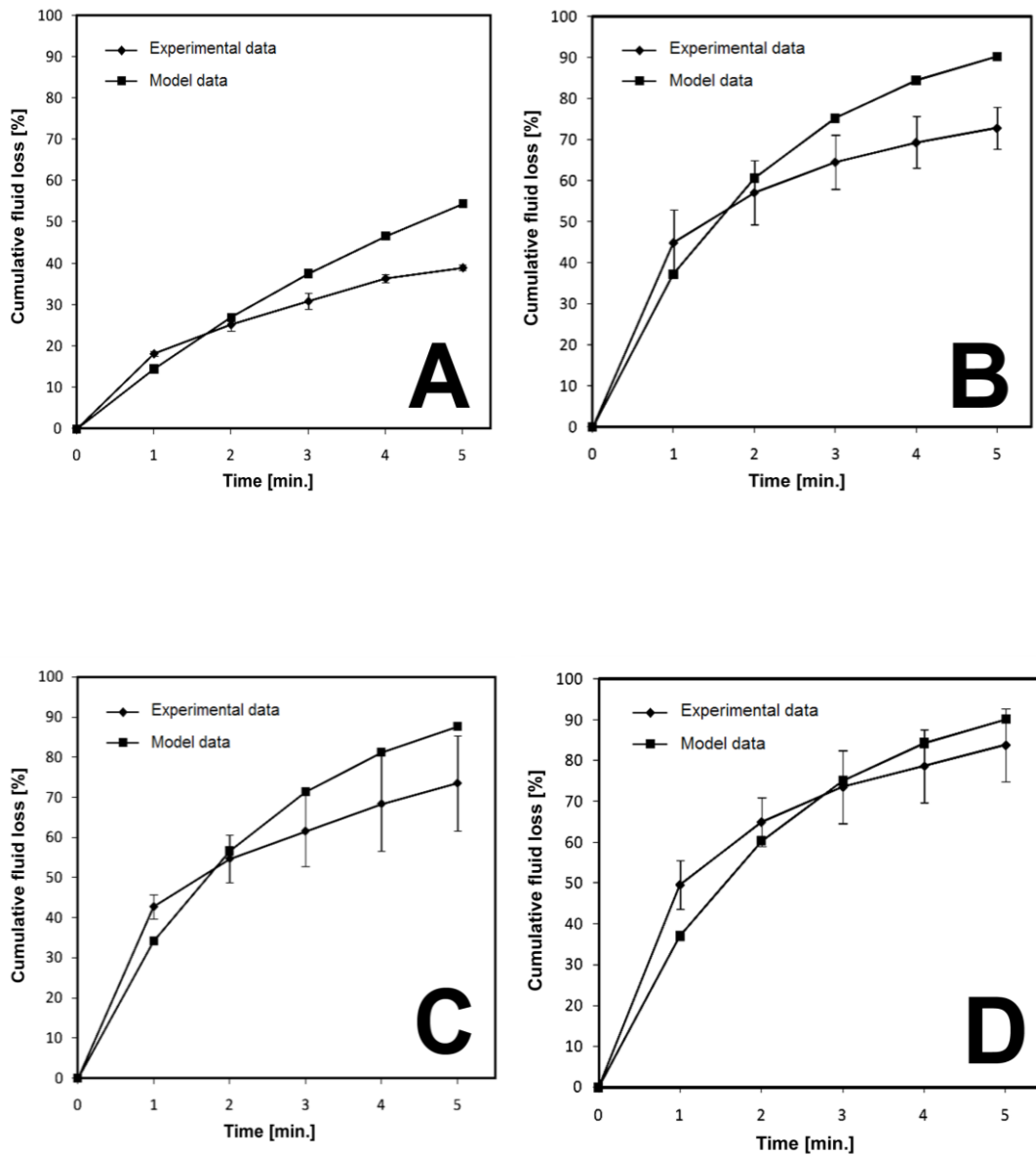


Fig. 11 Compression model validation. Comparison of experimental and model values of cumulative fluid loss (%) over time for cylindrical (A, B) and cuboidal (C, D) collagen gels compressed with a range of pressures (A: 130 Pa, B: 707 Pa, C: 4900 Pa, D: 9100 Pa).

We finally tested the effect of varying the pressure over time, in proportion to the increase in R_{FLS} , on discharge rate. Figure 12 shows the profile of discharge rate vs. time when a constant pressure of 707 Pa was applied on a 10 ml gel ($C_0=0.168\%$) for the full 5 min compression period. Use of Eq.6c to calculate the R_{FLS} at 1 min

predicted a 2 fold increase in R_{FLS} between 0 and 1 min (reflected by a ~50% decrease in discharge rate over the period) (Fig. 12). To match this increase in R_{FLS} the pressure was increased to 1414 Pa at 1 min. This resulted in a significant ($p<0.05$) increase in discharge rate relative to the base rate at 1 min. However, this effect was only transient as discharge rate fell back to the base rate by 2 min. There was a gradual dissipation in the effect of increasing pressure with time, such that a 4 fold increase in pressure to 2828 Pa at 2 min, matching a 4 fold increase in R_{FLS} from 0 to 2 min, resulted in a less pronounced, but still significant ($p<0.05$), increase in discharge rate (Fig. 12). These effects were in agreement with the model prediction of a rapid (exponential) increase in R_{FLS} with time. Therefore, based on the correlation developed to predict the R_{FLS} increase with time (Eq.6c), it is possible to apply a gradual increase of pressure (or load) to compensate for the increase in R_{FLS} , to achieve a near-linear discharge rate.

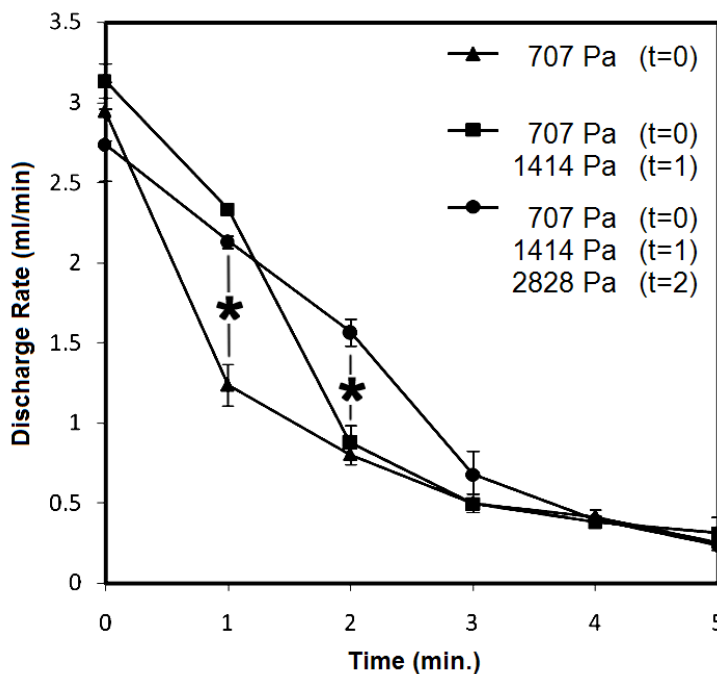


Fig. 12 Effect of changing pressure during compression on discharge rate. Plot of discharge rate vs. time for 10 ml collagen gels (initial collagen density 0.168%) initially

compressed with a pressure of 707 Pa. The pressure was either left unchanged (707 Pa) during compression (1-5 min), doubled to 1414 Pa at 1 to 5 min to match a 2 fold increase in R_{FLS} at 1 min or increased to 1414 Pa between 1 and 2 min, then further increased to 2828 Pa between 2 and 5 min to match the 2 and 4 fold increases in R_{FLS} at 1 and 2 min of compression, respectively. Enhanced flow rates at 1 and 2 min due to this progressive increase in pressure were significant (* $p < 0.05$) (n=4 for each loading regime).

3.2 DISCUSSION

Original Hypothesis: Fluid loss from collagen hydrogels undergoing Plastic Compression will result in accumulation of retained collagen fibrils at the fluid leaving surface (i.e produce a collagen density gradient along the compression axis) which will limit the discharge rate over time. Gel compression can thus be modelled as an ultrafiltration process with cake layer formation.

The primary objective of this study was to develop a functional model of the plastic compression process, to reproducibly and accurately predict the effects of interstitial fluid removal from collagen hydrogels. The dependence of a hydrogel scaffold's spatial dimensions on its fluid content makes this a key determinant of the density of any element retained within the scaffold during the compression e.g. collagen fibrils and cells [50]. Collagen fibrillar density directly determines matrix mechanical properties in a number of ways. It is clear from this and other studies for example that compression of collagen hydrogels changes their behaviour generally from poroelastic to viscoelastic [52]. This will therefore also change cell behaviour [44,123,166]. However, this study has shown how much asymmetric meso-scaled anisotropy (layering) the PC process introduces to an initially isotropic structure. This is key to the importance of PC as a mechanism for generating tissue-like or

biomimetic properties. Such anisotropic structures regulate critical biological control processes such as mass transport and nutrient perfusion to deeper cells [216]. These parameters are subsequently regulated by cellular synthetic and metabolic activity, both of which are direct functions of cell density. Successful and optimal use of the plastic compression fabrication process within tissue engineering, then, critically depends on our understanding and precise control of how fluid is expelled from the collagen nano-fibre network. Importantly, this also provides clues as to how cell-generated tissue structures are built up naturally.

The transient mechanical behavior of a collagen hydrogel is related to its interstitial fluid flow, which is governed by the hydraulic permeability (k). Previous studies have already established that the hydraulic permeability of hydrogels (e.g. agarose gels [217], matrigel [218,219]) and indeed tissues (e.g. cartilage [220], dermis [221], arterial intima [222] and basement membrane [223,224]) is deformation-dependent. However, quantification of the hydraulic permeability of hydrogels (by applying a pressure gradient and measuring the flow rate) is difficult because of flow-induced matrix compaction, which can deform the matrix (i.e. change of the flow-path length) and thereby alter the parameter being measured. Furthermore, measurement of the simple *average* hydraulic permeability (k_{avg}) of collagen hydrogels undergoing plastic compression would be a seriously limiting, even flawed understanding as the real (and key biomimetic) properties are dominated at the cell-molecular levels by structural asymmetry and anisotropies . Such complex structures are generated by the PC process in this system, as demonstrated in terms of collagen density and hydraulic permeability in this study. The fact that they can be controlled and tuned to materials for tissue engineering needs represents a major processing opportunity. The model presented here is based on the hypothesis that loss of fluid

from a collagen hydrogel, during compression, can be modeled as an ultrafiltration process with a compressible cake formation. Filtration theory has previously been used to predict the hydraulic resistance of the arterial intima under compression [222], while importantly collagen has been shown to significantly contribute to the hydraulic resistance of the aortic wall [225] and synovium [226]. Indeed, interstitial conductivity correlates negatively with collagen concentration [227]. In our model, fluid-filtration through the FLS results in increasing accumulation of retained collagen material at the FLS which correlates with increasing FLS hydraulic resistance. This has a limiting effect on flux over time, as indicated by the non-linear pressure-flux relation. Interestingly, non-linear pressure-flux relations have previously been reported for arterial wall and cartilage [227]. The finding that increasing pressure over time only resulted in a transient increase in flux further supports the hypothesis that the FLS behaves like an ultrafiltration membrane with cake or gel layer formation [211]. Empirical quantification of R_{FLS} , which is a compound measure of FLS hydraulic permeability (k_{FLS}) and FLS collagen lamellar (cake) layer thickness (δ_{FLS}), i.e. $R_{FLS} = \delta_{FLS}/k_{FLS}$, did not require differential estimation of either of these parameters, both of which change with time, thus circumventing this problem. The experimental setup shown in figure 13 (Methods section) could be used to estimate k_{avg} for highly compressed gels, assuming that the high stiffness modulus ($\sim 2\text{MPa}$ [166]) prevented significant pressure-induced compaction of the gel during testing. For gels compressed to remove 96% of their fluid (gel thickness $\approx 250\mu\text{m}$) a value of $k_{avg} = 2.82 \pm 1.64 \times 10^{-16} \text{ m}^2$ could be obtained (using Darcy's law), which was in the range of hydraulic permeability previously reported for 5% agarose gels [217]. However, this value represents the gel's *average* hydraulic permeability and is only an approximation of k_{FLS} .

In our model FLS hydraulic resistance (and permeability) were assumed to directly correlate with FLS collagen density (i.e. porosity). While this was a reasonable assumption (as shown by the linear correlation of experimental values, Fig.10B), it might be an oversimplification, since the permeability of a fibrous structure has been shown to also depend on additional factors such as fibre orientation[228]. Indeed, most of the permeability models established for fibrous materials are only suitable for specific ranges of porosity (e.g. drag-force theory is more applicable to highly porous materials). Similarly, our model might be more applicable for a certain range of porosities, which might be reached more quickly with higher pressures. This could explain the model's better fit for higher pressures. It is important to note that while the actual fouling mechanism(s) (e.g. pore blocking, cake filtration etc. [229]) mediating an increase in R_{FLS} during compression remain to be examined, this is unlikely to be caused by concentration polarization (i.e. increase in local osmotic pressure resulting in lower effective driving pressure, as seen in reverse osmosis), as collagen fibrils have only weak inherent swelling potential (i.e. osmotic activity) at neutral pH [52]. Furthermore, while beyond the scope of this study, investigation of the effects of cell-seeding (and cell type) on R_{FLS} (e.g. magnitude, rate of change) is an essential requirement for wide-range application of the PC process within tissue engineering and will be the focus of future work (as outlined in the Future Work section).

This study indicates that control of fluid loss from a collagen hydrogel scaffold could be achieved by alteration of one or more parameters; compressive load, duration of compression, gel initial volume, and FLS area. Importantly, while the model (flow-dependent phase) was constructed based on data obtained from testing cylindrical gels, its predictive ability was also satisfactory with cuboidal gels (Fig.11 C, D),

suggesting that it could be applied to multiple gel geometries. Modifications of the plastic compression technique could further facilitate the fabrication of desirable scalar or directional structural features within scaffolds. For example, the axial direction of compression (short vs. long axis of the construct) could determine the final construct dimensions and (average) collagen density reached, while the introduction of a second (or more) FLS(s) during compression could provide control over the spatial configuration of collagen density anisotropy within the scaffold (e.g. symmetric vs. asymmetric structural anisotropy). Moreover, it has been shown that a further increase in collagen density (from 12.6 to 23.1%) and mechanical properties could be produced by subjecting the material to a secondary compression process (double compression) [52,230]. The ability to control the flux, as well as the cumulative fluid loss, during compression of cell-seeded scaffolds is equally important as it has been shown that the severity of cellular damage depends on both the magnitude and the duration of fluid shear stress [231]. Indeed, cell injury in articular cartilage under load depends both on compressive stress and strain rate [232]. Importantly, collagen fiber architecture determines the level of shear stress experienced by cells within 3D matrices [233]. Specifically, fibers oriented along the flow direction shield cells more effectively from shear stress, which might explain why plastic compression results in only a small (~10%) reduction in cell viability (fibril orientation in lamellae is in the Z (vertical) plane) [25].

We showed that directional fluid outflow through the FLS causes differential gel compaction (bottom greatest, top least (Fig.5B)) which must generate lamination forces in the gel, parallel to the FLS. This would indeed explain the formation of separate 1-5 μ m lamellae in the gel body. Importantly, while collagen density was anisotropically distributed along the compression axis, collagen density lateral to the

central compression axis was relatively uniform (data not shown), which was in agreement with the findings of a previous study [215]. The development of such uniaxial anisotropic structuring could provide a useful tool for engineering on demand spatially distinct gradients within the scaffold (e.g. stiffness, haptotactic or chemotactic gradients) and thus a means of regulating cell behaviour (e.g. cell migration, proliferation and differentiation). For example, durotactic gradients could be used to guide cells (e.g. fibroblasts) within a 3D collagen matrix [167] (see Chapter 6). The ability to generate localised 3D structures and zones at a meso-scale could also have important implications for tailoring the structure of the collagen fibril network (e.g. fibril diameter, alignment and porosity) to match the native architecture of specific tissues [50]. Indeed, confined compression of collagen gels has also been shown to induce collagen fibril and cell alignment through a contact guidance response [215]. Furthermore, 3D structural features could be superimposed with nano- or micro-scale topographic patterns (e.g. by template embossing [25]), thus providing an additional tool for regulating epithelial cell function (e.g. alignment, attachment, contact guidance) [73] (see Chapter 4). Importantly, control of local matrix density could allow the density and distribution of a resident cell population to be precisely engineered to native tissue levels [50].

We have shown that the collagen density of these nano-fibrous scaffold materials (and by extrapolation porosity [234]) is critically related to fluid outflow. PC fabrication could therefore be used to precisely control collagen density and scaffold hydro-permeability, in a predictable manner [235]. Since compressed collagen matrices comprise nano-fibrillar meshes with corresponding nano-porosity, they have predictable properties in terms of small and macro-molecule transport to and from resident cells. Notably nutrients such as oxygen and glucose have rapid access

to deeper cells (being much smaller than the matrix nanopores) [173,236] whilst macromolecules such as proteins (e.g. cell products, growth factors etc.) will have much longer transit times [237]. Indeed, we have shown that IgG antibodies and cell-secreted Matrix Metalloproteinases (MMPs) and vascular endothelial growth factor (VEGF) are partially retained within compressed collagen scaffolds (see Chapter 9). This diffusional asymmetry could be further enhanced, or used to mimic actual tissue function (e.g. the anisotropic hydro-permeability in compressed articular cartilage [220]), by the incorporation of predictable nano-micro scale structural asymmetry.

3.3 CONCLUSIONS

The advent of the plastic compression fabrication process has made it entirely feasible to construct collagen-based, biomimetic tissues (including a resident cell population) without the need for metabolic/synthetic input from cells [25]. This is a key stage in understanding how to engineer collagen nano-fibrous materials with the control and precision that we currently engineer other forms of polymer materials. In other words, it is now possible to progressively shift from cell cultivation to the engineering of new tissues [50]. However, such *bulk matrix production* will critically depend on successful process scale-up. The current model defines parameters (compressive load, time, gel volume and FLS area) that enable precise and predictable control of the process and of the 3D tissue-like structures produced. It is an important tool, therefore, for engineering scaffold properties such as cell/matrix density, mechanical properties and complex (e.g. anisotropic) mesoscale structure in

a highly controlled manner. Furthermore, this work paves the way for process automation and up-scaling.

3.4 MATERIALS & METHODS

Collagen gel preparation and compression

Collagen gels were prepared as previously described [210]. Briefly, a 5 ml collagen gel mixture composed of 4 ml acid soluble collagen type I (First Link, UK) of varying collagen concentration (2.1, 1.5 or 1 mg/ml) and 1 ml 10×DMEM (Gibco Life Technologies, UK) was neutralized drop-wise by 5M NaOH. For preparation of 10 and 15 ml gels, 8 and 12 ml acid soluble collagen type I (2.1 mg/ml) was mixed with 2 and 3 ml 10×DMEM, respectively, and neutralized with NaOH. Neutralised collagen solution was poured into either round wells of varying surface area (3.6, 9, 19.6 cm²) or into rectangular moulds (size: 2.2 (length) x 0.7 (width) x 6 (height) cm, FLS= 1.54 cm²) made from Derlin polymer blocks (Intertech, UK) and incubated at 37°C in a 5% CO₂ humidified incubator for 60 min.

Following setting and incubation, gels were compacted by a combination of compression and blotting [25], as shown in figure 1 (see Chapter 2). Briefly, a 165µm thick stainless-steel mesh (mesh size 300µm) was placed on water-soaked double layer absorbent Whatman paper (grade 1: 11µm, 185mm diameter). The collagen gel was placed on the mesh and was either left to compress under its own weight (self-compression) or covered with a glass slide and loaded with a metal block (10, 90 or 120g) for 12 min at room temperature, in a dry chamber. Use of absorbent Whatman paper during unconfined compression ensured that fluid loss

occured overwhelmingly uni-directionally along the vertical axis of the gel. Fluid loss during compression was quantified indirectly by measuring gel wet weight every minute (gel removed from blotting elements, placed on digital weighing device and returned to compression station; timer stopped during weight measurements). Collagen gels (5ml) cast in custom-made rectangular moulds were compressed while within the mould with a metal plunger (70 or 140 g). The use of partially confined compression, in this case, allowed application of high pressures (4900 and 9100 Pa, i.e. higher than the burst pressure for unconfined compression, ~1300 Pa, where fluid loss and gel deformation occured along both the x and z planes). Fluid loss was measured every minute, indirectly, by measuring the movement of the plunger-gel interface, as it descended. For all loading regimes, 5 separate gel samples were tested (n=5).

Coomassie blue staining

Coomassie blue (a protein-staining dye) staining was used to visualize differences in collagen density between the FLS and the body of the gel after compression. Collagen gels (5ml) were cast in 3.6cm² wells. After setting and incubation, gels were soaked in Coomassie blue R-250 (0.025% in deionized water) (BDH, laboratory supplies, UK) for 1hr and excess stain was removed with 3 washes (15 min) in deionized water. Gels were self-compressed on double layer whatman paper, for 5 min, mounted vertically to expose the FLS, and photographed with a digital camera (CANON IXUS 960 IS, Canon inc., Tokyo, Japan).

SEM analysis of collagen gel structure along the compression axis

Collagen gels (5ml, FLS area=9 cm²) underwent plastic compression with a 90g load for 5 min. Dry specimens were fractured transversely (perpendicular to the FLS

plane) to expose the internal structure along one edge. They were mounted vertically onto stubs, gold-palladium sputter-coated, and viewed in a JEOL 5500LV SEM.

Collagen Compaction Assay

Activated carbon particles were used to examine the compaction of collagen during the compression process. Directly after neutralization, 10 mg of activated carbon (Aldrich, UK) was added to 3.5 ml of collagen. The solution was briefly agitated to achieve an even distribution and poured into the barrel of a 2 ml syringe (2-mL Luer BD syringe, ref 300185, Becton Dickinson, S. Agustin del Guadalix, Madrid, Spain) with its tip removed. After 30 minutes the syringe with the polymerized collagen gel was transferred onto double layer absorbent whatman paper. The gel was detached from the wall of the syringe with a spatula and allowed to self-compress (under its own weight). The compression process was filmed in real time with a digital photo camera (CANON IXUS 960 IS, Canon inc., Tokyo, Japan) and the images were analyzed with ImageJ (v.1.41, NIH, Bethesda, Maryland, US) by measuring the changing positions of 8 large carbon particles within the hydrogel, relative to the FLS, over time (15 min). The viscoelastic behavior of collagen gel in confined compression [215] resulted in minimal gravitational force transfer on carbon particles, preventing any significant carbon particle accumulation towards the bottom of the gel during compression [44]. This ensured that carbon particle position was a reliable marker of local collagen gel compaction around each particle.

Measurement of FLS hydraulic resistance

Collagen gels (volume = 5ml) were cast in round wells of 9cm² surface area. Following setting and incubation, gels were compressed with a 10g load on a porous substrate, in this case water-soaked double layer Whatman paper, for 15 min. The

discharge (Q) through an area (A) of a compressing gel was calculated every minute, indirectly, by measuring the change of gel wet weight. The FLS hydraulic resistance (R_{FLS}) was calculated by adapting Darcy's law (Fig. 1A):

$$R_{FLS} = \frac{(m_L + m_G) \cdot g}{\mu \cdot Q}$$

where m_L (in Kg) is the mass of the external load and m_G (in Kg) is the gel mass, g is acceleration due to gravity (ms^{-2}) and μ is the dynamic viscosity of water (1×10^{-3} Pa's at 20°C).

The discharge rate at the final stages of compression was extremely low and varied significantly between samples. To measure R_{FLS} directly, a constant flux stirred cell ultrafiltration unit was used (Fig. 13) to deliver a set flow rate through collagen membranes (240 ± 55 μm thick, calculated from histological specimens in cross-section). For this a pressure of 1306 Pa was applied on collagen gels (5ml) for 5 min (giving ~96% fluid loss). The collagen membrane to be tested was assembled in a 16.9 ml stirred cell, with a membrane area (A) of 5cm^2 . An integral HPLC pump capable of delivering flow rates in the range of 0.1-20ml/min was used to pump deionized water through the collagen membrane (Fig. 13). The flow rate (Q) was set at either 1 or 9 ml/min and the transmembrane pressure (pressure difference across the collagen membrane, TMP) was measured by an on-line pressure sensor integrated with the HPLC. For flow rates of 1 and 9 ml/min TMP was measured to be 0.04 and 0.13 MPa, respectively, corresponding to a pressure gradient of 166 and 540 MPa/m through the collagen membrane, respectively. No TMP fluctuations or declines were recorded, indicating that collagen membrane permeability remained

constant during testing. At least 5 samples were tested. R_{FLS} was calculated using Darcy's law equation:

$$R_{FLS} = \frac{A.TMP}{\mu.Q}$$

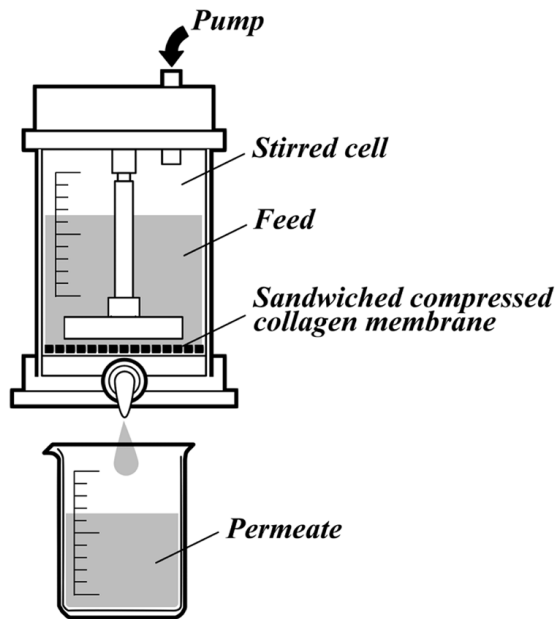


Fig. 13 Schematic of experimental setup for stirred cell ultrafiltration unit, used to measure the hydraulic resistance of compressed (96% fluid loss) collagen gels (membranes).

Measurement of FLS collagen density

The attenuation of X rays, transmitted through a collagen gel, was used to provide information on water and therefore collagen distribution along the compression axis of the gel, for various levels of compression [238]. All specimens were tested by a laboratory microtomography system (Skyscan 1172), which was used to provide two dimensional X-ray digital radiograms. The scanner was equipped with a Hamamatsu

1.3Mp X-ray camera, which has a camera pixel size equal to 22.82 μm . The X-ray beam was produced using a source voltage equal to 70 keV, a source current equal to 141 μA , and an aluminium filter 0.5 mm thick. The manufacturer software was used to control the scanning process and acquisition of the X-ray projections. The images were stored on the computer hard drive in 16-bits tiff files, which were converted to 8-bits bmp files, which enabled quantitative analysis of the 256 grey values (0-black, 256-white). Image analysis was carried out using Image J software (NIH). Collagen gels (10 ml) were cast in 9 or 3.66 cm^2 round wells (gel diameter 3.45 or 2.2 cm respectively) and were then either left uncompressed (no fluid loss) or allowed to compress under their own weight to remove 60, 80 and 98 % of their fluid. Four samples (of each gel diameter) were tested for each level of compression. Specimens were placed between 2 glass slides and mounted vertically, in the scanner chamber (Fig. 9A). This enabled better visualization of the FLS. We did not follow full microtomography protocol, as measurement of required parameters was done successfully based on only single projections for each sample. The ratio of X-ray intensity relative to the densest area of the gel was calculated along the compression axis (relative X-ray intensity, I_r). For each sample, I_r along the compression axis (x-axis) was the average of three measurements of I_r at 3 positions (top, middle and bottom) along the gel's vertical axis (Fig. 9A). Importantly, the path length of material through which the radiation beam passed was the same for all points along the compression axis, irrespective of level of compression. X-ray intensity was inversely proportional to fluid (water) content along the compression axis of the gel. The gel was divided into 25 μm thick layers (along the compression axis) and the volume of water per layer was calculated from the distribution of total water volume (measured as gel wet weight) along the compression axis. The collagen density in each layer

was then calculated as a % of the layer's water content. FLS collagen density was taken as the average collagen density in the bottom 5 layers of the gel (i.e. the average of the 5 highest collagen density values).

CHAPTER 4

ENGINEERING TOPOGRAPHY IN 3D COLLAGEN SCAFFOLDS: EXPANDING REGULATION OF EPITHELIAL CELL FUNCTION FROM SURFACES TO INTERFACES

Topographic patterning provides a useful tool for regulating cell function, such as adhesion, proliferation, differentiation and contact-guidance. While current (e.g. lithographic) techniques allow precise control of topographic pattern (anisotropic vs isotropic) and scale (nano- vs micro-topography) , they are only applicable to 2D surface patterning, which compromises their relevance to 3D tissue engineering. In this study we developed a novel method for rapid fabrication of micro-textured 3D collagen scaffolds. We employed a two-step process to firstly increase matrix stiffness, by removing interstitial fluid from collagen hydrogels using Plastic Compression, followed by embossing a customized pattern template of parallel-aligned phosphate-based glass-fibers on the scaffold's surface. We hypothesised that varying the width and depth of the engineered grooves/ridges would directly influence epithelial (endothelial) cell responses (adhesion, orientation, elongation) in 2D culture. Furthermore, we developed an *in vitro* model of the dermo-epidermal junction as an exemplar of engineered topography at an interface, to test its effect on epithelial (keratinocyte) cell responses (stratification, differentiation) in 3D culture.

4.1 RESULTS

Topographic engineering by pattern template embossing

We were able to produce pattern templates composed of two different phosphate-based glass fibre (PBG) diameters by changing the pulling speed from 100 to 300 RPM. There was a decrease in fibre diameter with increasing RPM speed, as expected. The 100 RPM fibres averaged out at approximately 53 μ m and the 300 RPM fibres at approximately 36 μ m (table 1).

RPM	FIBRE Diameter (μ m) \pm SD (MICROSCOPY)	GROOVE Width (μ m) \pm SD (SEM)	GROOVE Depth (μ m) \pm SD (AFM)
300	36\pm3	30.5 \pm 3.3	0.95\pm0.49μm
100	53\pm6	49.5 \pm 11.6	1.55\pm0.31μm

Table 1. Dimensions of grooves embossed in collagen substrates patterned with two different phosphate-based glass fibre diameters. Values of phosphate-based glass fibre diameter for the two pulling speeds tested (100 and 300 RPMs), as measured by light microscopy, and corresponding values of embossed groove width, as measured by SEM, and depth, as measured by AFM. Values represent the mean \pm standard deviation (SD). For each RPM 30 fibres were tested, while for SEM and AFM measurements, five fields were analysed per construct (4-5 grooves/field), with 4 constructs per condition.

Embossing the pattern template of parallel aligned PBGs onto the upper (i.e. non FLS) surface of compressed collagen sheets resulted in a regular pattern of grooves and ridges, as shown by SEM (Fig.1). Average groove width, as quantified by SEM, was 30.5 ± 3.3 and $49.5\pm 11.6\mu\text{m}$ for $36\mu\text{m}$ and $53\mu\text{m}$ diameter fibres, respectively (table 1). Average groove separation distance was 50-100 μm , corresponding to the spacing of PBGs on the pattern template. Therefore, the pattern template was faithfully embossed onto the surface of collagen substrates.

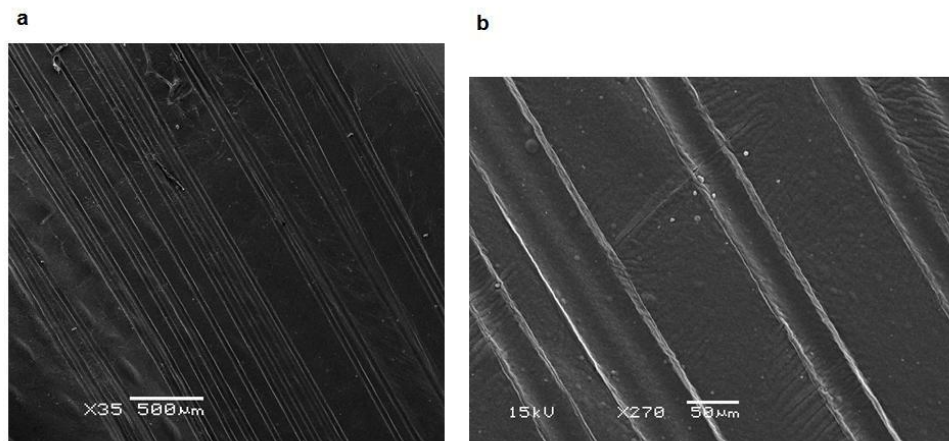
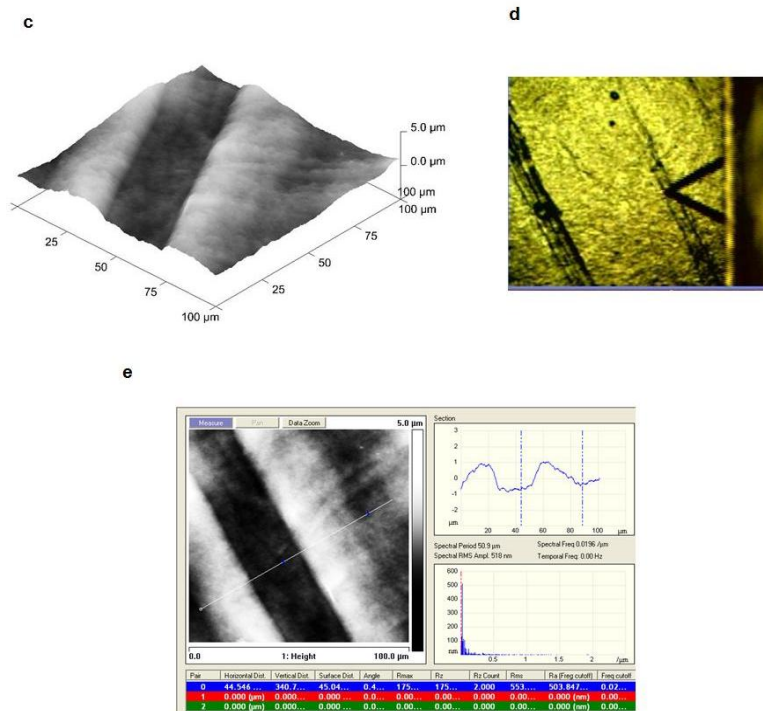


Fig.1 SEM and AFM analysis of patterned topography. Low (a) and high (b) magnification SEM images of patterned collagen substrates embossed with a pattern template comprising $36\mu\text{m}$ diameter fibres, showing a regular pattern of grooves and ridges.



(c) The 3D profile of patterned substrates was characterised by AFM. Panel (d) shows the tip of the AFM probe at a groove on the substrate surface. Panel (e) shows a digital snapshot of the imaging software used to analyse groove depth.

AFM was used to characterize the profiles of embossed topographic features and to quantify groove depth. This analysis confirmed successful embossing of a regular pattern of grooves and ridges on the surface of collagen substrates (Fig.1). Average groove depth was 0.95 ± 0.49 and $1.55 \pm 0.31 \mu\text{m}$ for $36 \mu\text{m}$ and $53 \mu\text{m}$ diameter fibres, respectively (table 1). There was a significant discrepancy between the values of groove depth measured by AFM and the expected values, calculated based on the values of groove width measured by SEM, as shown in Fig. 2. For $36 \mu\text{m}$ diameter fibres expected groove depth was $8 \mu\text{m}$, while for $53 \mu\text{m}$ fibres it was $17.7 \mu\text{m}$, i.e. 8 and 11 fold difference, respectively. Therefore, while groove width could be precisely controlled by varying the fibre diameter, this method only allowed limited control over control of groove depth.

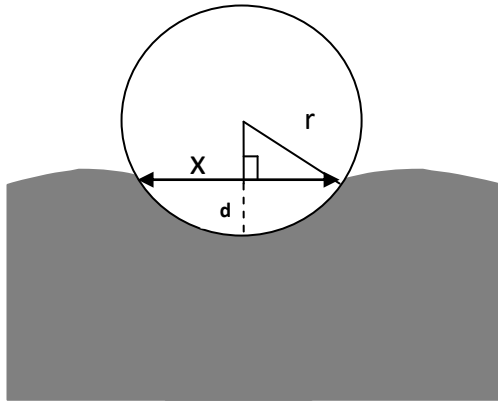


Fig.2 Schematic showing how the expected groove depth (d) can be calculated based on the groove width (x), measured by SEM and the radius (r) of the glass fibre embossed on the substrate surface, using the equation $d=r-\sqrt{[r^2-(x/2)^2]}$.

2D culture model

Human umbilical vein endothelial cells (HUVECs) were cultured on the surface of smooth (non-patterned) and patterned collagen substrates to test the effect of micro-topography on endothelial cell adhesion, morphology and orientation. For quantification of cell adhesion HUVECs were seeded on smooth or patterned substrates at a density of 2×10^4 cells/cm² and were allowed to attach for 4hrs before substrates were washed to remove non-adherent cells. Collagen substrates patterned with 36µm diameter fibres supported the maximum number of adherent cells, which was significantly higher than the number of cells adhering on smooth substrates and substrates patterned with 53µm diameter fibres ($p < 0.05$) (Fig.3). There was no significant difference in cell adherence between smooth substrates and substrates patterned with 53µm diameter fibres.

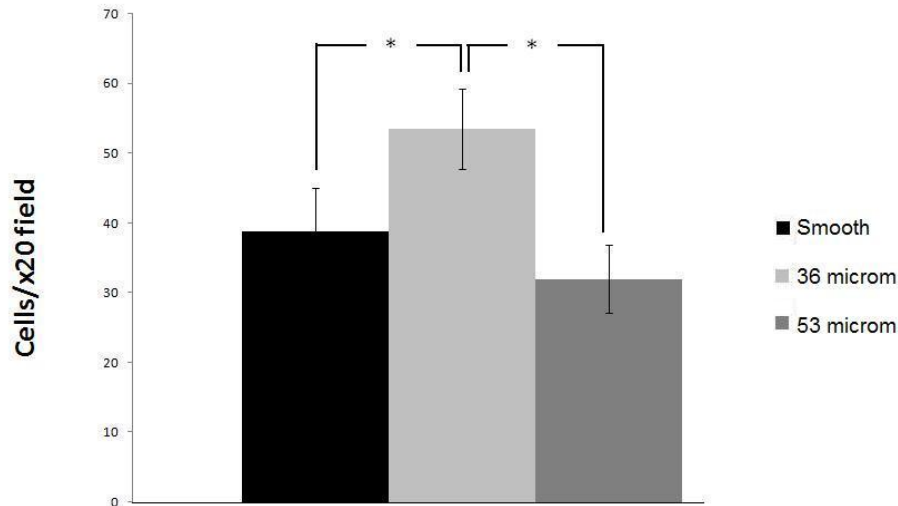


Fig.3 Comparison of HUVEC adhesion for smooth (non-patterned) substrates and substrates patterned with a template of 36µm or 53µm diameter fibres. Cells were seeded on substrates at a density of 2×10^4 cells/cm² and allowed to attach for 4hrs before washing substrates with PBS to remove non-adherent cells. Substrates were visualised using a light microscope. The number of cells per x20 microscopic field was counted manually. Five fields were analysed per substrate with 4 substrates tested per condition. Bars represent standard deviation of the mean,* p<0.05.

Analysis of endothelial cell viability/proliferation, by Alamar blue assay, showed that endothelial cells did not proliferate on smooth or grooved collagen substrates over 48hrs of culture. Differences in cell number between smooth and grooved substrates at 24 and 48hrs were not significant ($p > 0.05$) (Fig.4). These results indicated that while the presence of micro-patterns or their dimensions appeared to have no effect on cell proliferation, topographic patterning was not disruptive to endothelial cell viability.

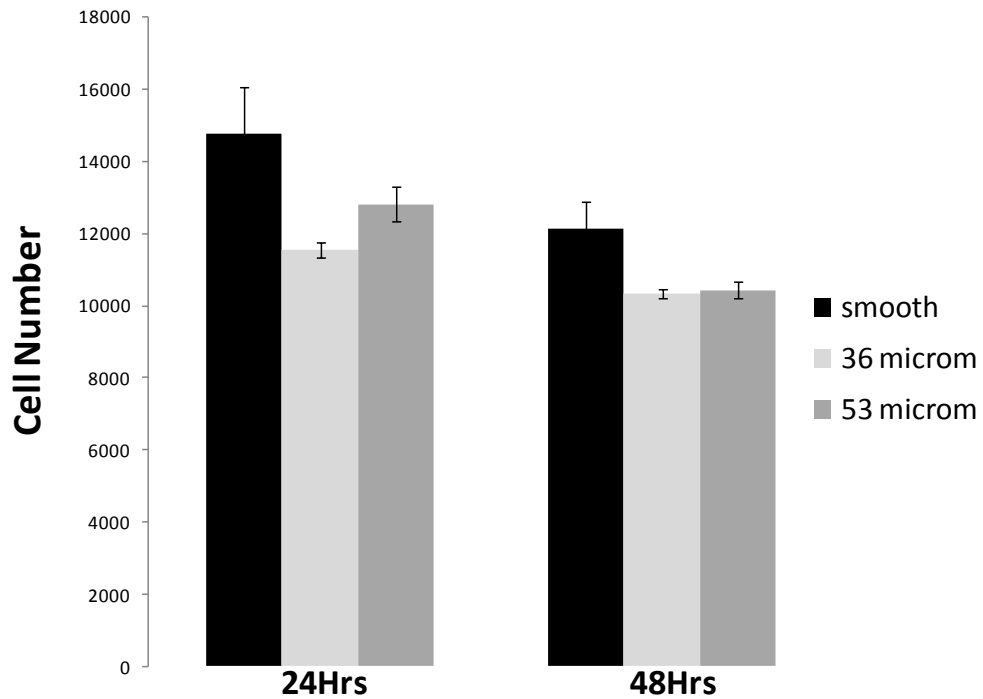


Fig.4 Endothelial cell viability/proliferation on smooth substrates and substrates patterned with a template of 36 μ m or 53 μ m diameter fibres. Endothelial cells were seeded on each construct at a seeding density of 5×10^3 cells/cm² and cultured for 24 or 48hrs. Cell number was quantified by Alamar blue assay. Four constructs were tested for each condition. Bars represent standard deviation of the mean.

SEM was used to analyse the morphology and orientation of endothelial cells cultured on collagen substrates for 48hrs. While cells cultured on smooth substrates and substrates patterned with 53 μ m diameter fibres maintained a round morphology, the majority of cells cultured on substrates patterned with 36 μ m diameter fibres were more elongated and appeared to align with the direction of the grooves (Fig.5).

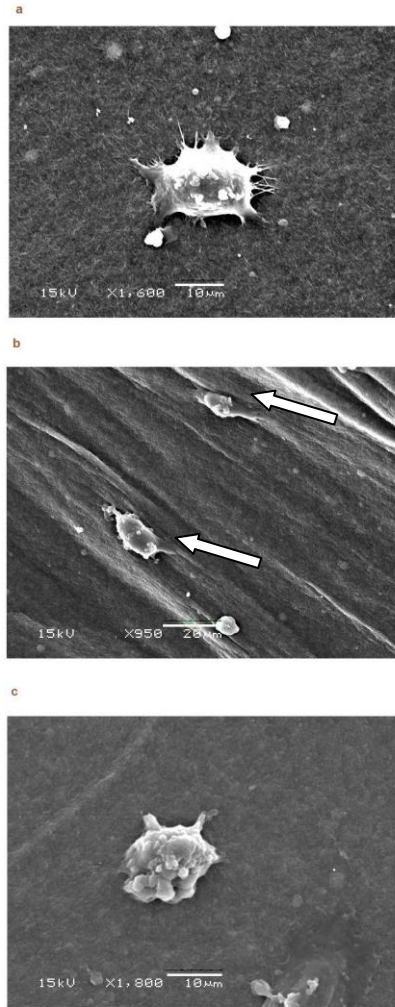
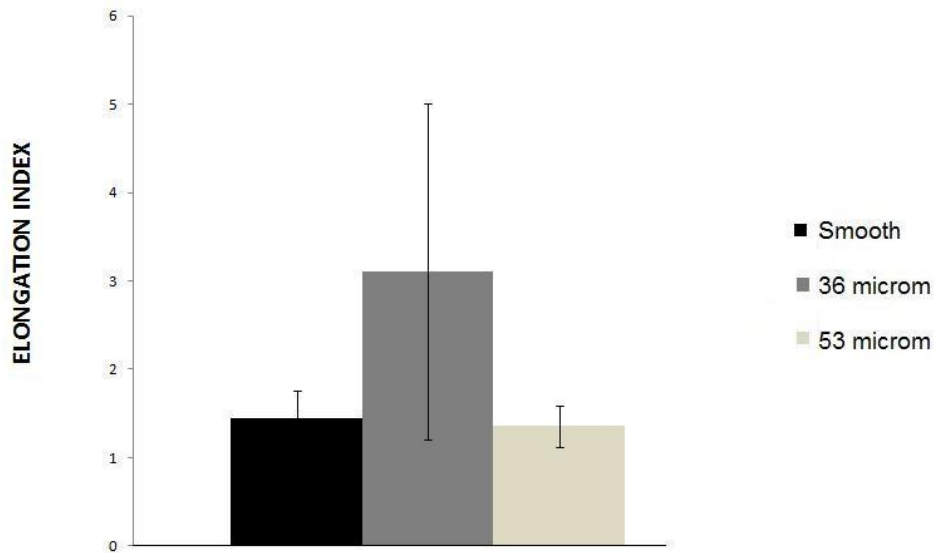


Fig.5 Endothelial cell alignment on collagen substrates with a patterned groove topography. SEM images showing single endothelial cells on the surface of smooth (non-patterned) substrates (a) and substrates patterned with a template of 36µm (b) or 53µm (c) diameter fibres, 48hrs post seeding. While endothelial cells in images (a) and (c) have a round morphology, cells in image (b) appear elongated, aligning in the direction of the engineered grooves (arrows).

Cell elongation index (ratio of cell major axis to cell minor axis) was almost 3 fold higher on substrates patterned with 36µm diameter fibres than on smooth substrates and substrates patterned with 53µm diameter fibres (Fig.6a). Furthermore, while 65% of cells aligned with the groove direction on substrates patterned with 36µm

diameter fibres, only 10% of cells were aligned on substrates patterned with 53 μ m diameter fibres. This difference was statistically significant (Fig.6b).

a)



b)

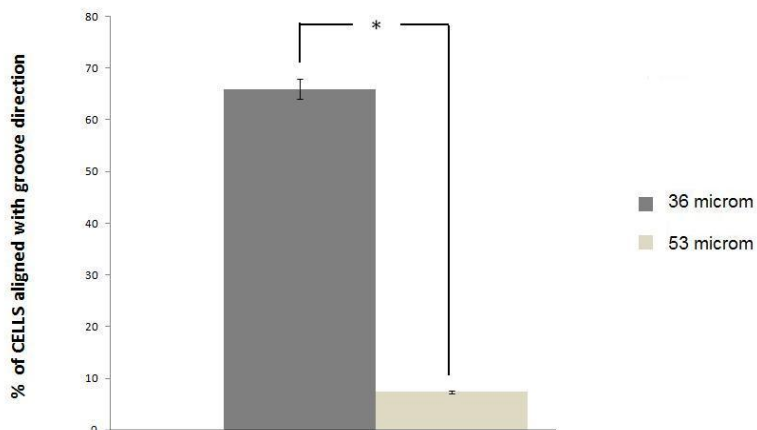


Fig.6 Endothelial cell orientation on smooth and patterned substrates. (a) Comparison of the cell elongation index (ratio of cell major axis to cell minor axis) for endothelial cells cultured on smooth (non-patterned) substrates and substrates patterned with a template of 36 μ m or 53 μ m diameter fibres for 48hrs. (b) Comparison of the percentage of cells aligned with the direction of engineered grooves for substrates patterned with a

template of 36µm or 53µm diameter fibres. At least 10 random fields were analysed per sample, with 4 constructs tested per condition. Bars represent standard deviation of the mean,* p<0.05.

3D culture model

An *in vitro* 3D model of the dermo-epidermal (DE) junction was developed to test the effect of topography on epithelial cell responses at an interface. Collagen constructs were prepared as two layer mimics of native skin. A dense ‘dermal’ layer was developed by plastic compression of collagen gels seeded with human dermal fibroblasts (HDFs). Human keratinocytes were seeded onto the surface and constructs were submerged in media for 2 days before being raised to the air-liquid interface and cultured for an additional 12 days. One set of constructs was embossed with a regular pattern of grooves and ridges at the DE interface during the PC process, by embossing the putative interface of the HDF-seeded collagen gel with a pattern template of 36 or 53µm diameter glass fibres (aligned parallel and 50-100µm apart) before keratinocyte seeding. The skin-like ECM construct formed rapidly, taking a maximum of 1 hour to fabricate and up to 14 days to culture keratinocytes to a multilayer. Histological analysis and immunofluorescence staining (anti-cytokeratin AE1/AE3) indicated that in constructs with a smooth (non-patterned) DE interface a uniform, stratified and differentiated epidermis was formed by 2 weeks culture (Fig.7A, 9A). However, incorporating a micro-topography of grooves/ridges at the DE interface appeared to influence epidermal morphogenesis such that epidermal thickness increased at the grooves, while a thinner epidermis formed in the ridge/inter-groove regions. This pattern was consistent for both glass fibre diameters tested (36 or 53µm) and for two sets of constructs, cultured over 2 and 3 weeks (Fig. 7 C-F).

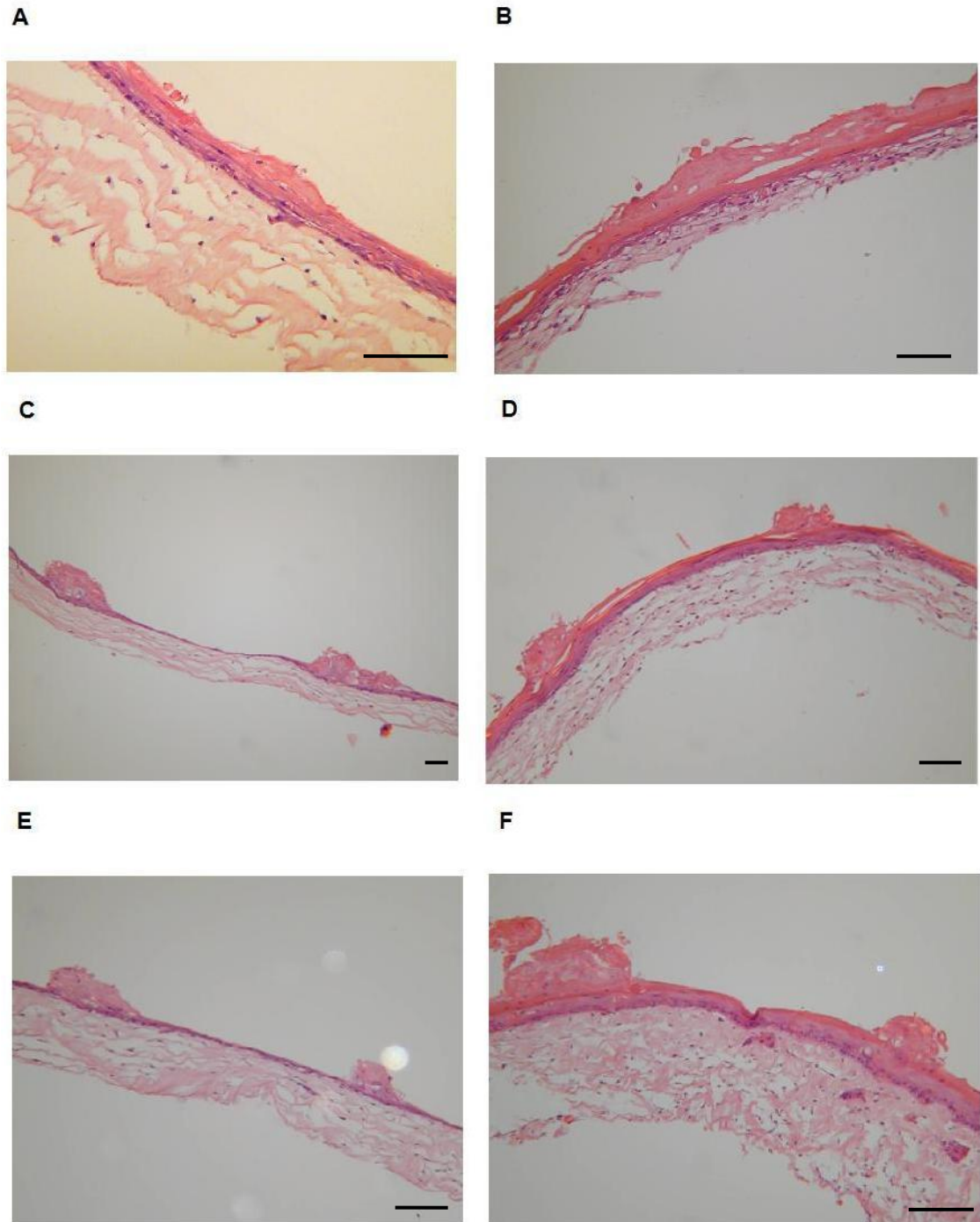


Fig.7 Incorporation of micro-topography at the dermo-epidermal (DE) interface influences keratinocyte stratification/differentiation. H&E-stained cross-sections of ‘skin-like’ collagen constructs seeded with HDFs and human keratinocytes and cultured for 2 (A, C, E) or 3 weeks (B, D, F). Constructs had either a smooth (non-patterned) DE interface (A,B) or were embossed with a regular pattern of grooves and ridges at the DE interface, by embossing the HDF-seeded ‘dermal’ layer with a template pattern

of 36 μm (C,D) or 53 μm (E,F) diameter glass fibres (50-100 μm apart) before keratinocyte seeding. Bars=100 μm .

In constructs with a smooth (non-patterned) DE interface, epidermal thickness was $60\pm 20\mu\text{m}$ after 2 weeks of culture (Fig.8). Constructs with a patterned DE interface showed a ~ 1.5 fold increase in epidermal thickness at the grooves ($p>0.05$) and a ~ 3 fold reduction in thickness at the inter-groove regions ($p<0.05$) (Fig.8). For both fibre diameters tested epidermal thickness was significantly greater at the grooves than at the inter-groove regions at 2 weeks ($p<0.05$). Constructs cultured for 3 weeks showed an overall increase in epidermal thickness, regardless of the presence or absence of micro-topography at the DE interface. However, for patterned substrates the difference between epidermal thickness at the grooves and inter-groove regions continued to remain significant after 3 weeks of culture ($p<0.05$) (Fig.8).

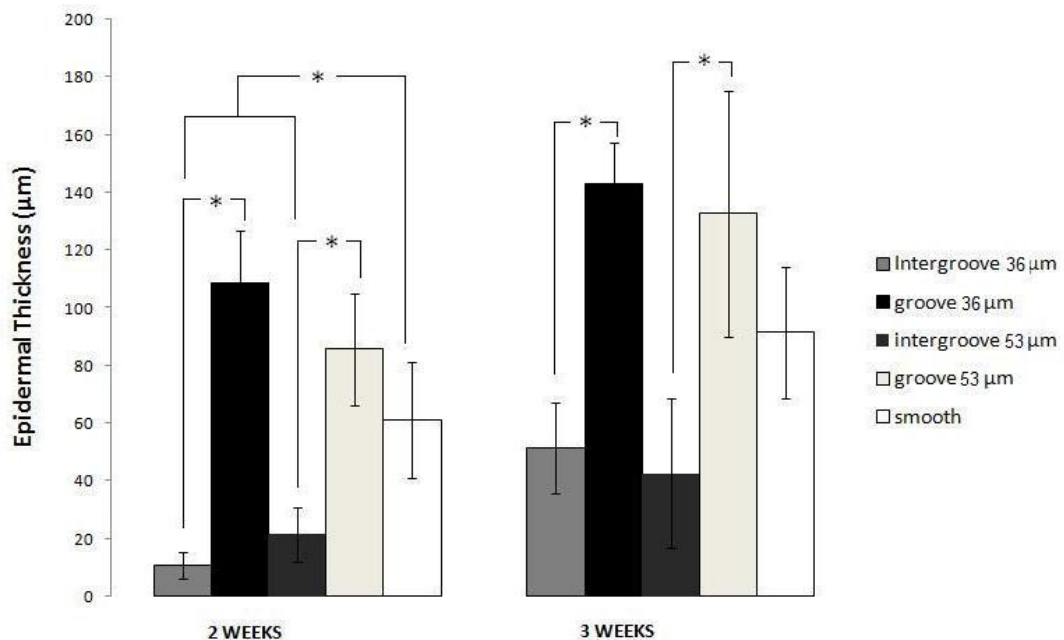


Fig.8 Effect of topography of the dermo-epidermal interface on epidermal thickness. Comparison of epidermal layer thickness in constructs with a smooth (non-patterned) DE interface or with a patterned DE interface, embossed with a template pattern of

36um or 53um diameter glass fibres, over 2 and 3 weeks of culture. Epidermal layer thickness at the groove and intergroove regions of constructs with a patterned DE interface was analysed separately. Three fields were analysed per H&E-stained cross-section, with three sections per sample and three samples for each condition tested. Bars represent standard deviation of the mean, *p<0.05.

Examination of cross-sections with a polarizing microscope showed that keratin was positively birefringent in all constructs tested, confirming formation of a cornified epidermis (Fig.9D-F). The optic axis of groove regions was parallel to the construct longitudinal axis, considered to be running perpendicular to the plane of construct cross-sections in the direction of the grooves, indicating that in groove areas keratin was oriented parallel to groove direction (Fig.9E, F). In contrast, keratin in smooth constructs and in ridge (inter-groove) regions appeared linearly oriented in the plane of construct cross-sections (Fig.9D, E), in the latter running perpendicular to groove direction, forming 'cross-bands' that connected adjacent grooves.

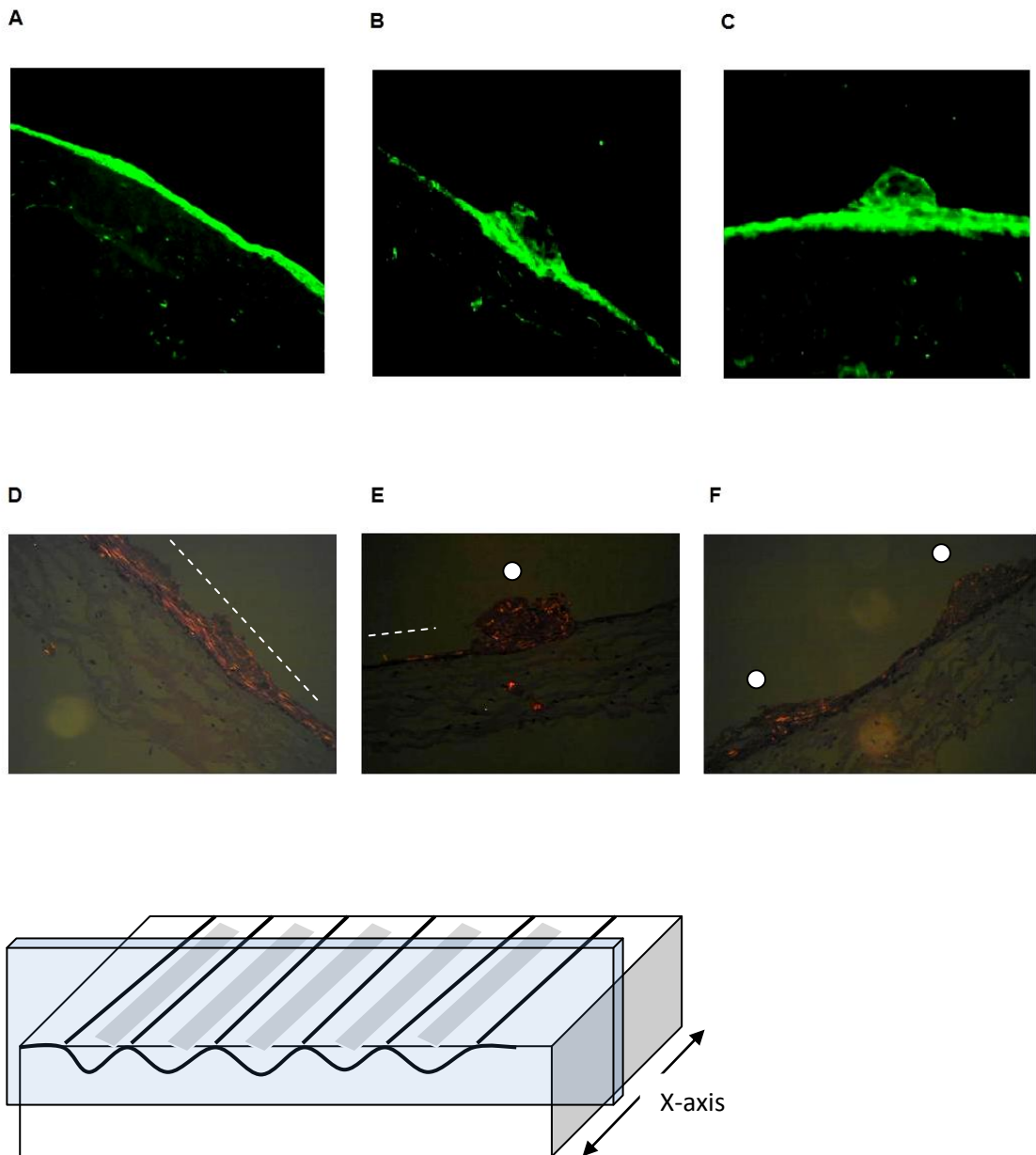


Fig.9 Analysis of epidermal differentiation and keratin structure in constructs with smooth and patterned dermo-epidermal interfaces. Immunofluorescence staining with anti-cytokeratin AE1/AE3 indicated that a stratified and differentiated epidermis was formed after 2 weeks culture for all conditions tested, i.e. constructs with a smooth (non-patterned) DE interface (A) or with a patterned DE interface, embossed with a template pattern of 36µm (B) or 53µm (C) diameter glass fibres (upper panel). Lower panel shows the positive birefringence of keratin in constructs with a smooth (non-patterned) DE interface (D) or with a patterned DE interface, embossed with a template pattern of 36µm (E) or 53µm (F) diameter glass fibres. Dashed white lines in images D and E indicate the linear orientation of keratin in smooth and ridge (inter-

groove) regions, respectively, while white circles in images E and F indicate the parallel orientation of keratin to the direction of the grooves, i.e. perpendicular to the plane of the image. 3D schematic shows the plane of cross-sections in grooved constructs, perpendicular to the direction of the grooves (X-axis denotes the longitudinal axis of the construct).

4.2 DISCUSSION

Original Hypothesis: Embossing a customised pattern template on the surface of 3D collagen hydrogel scaffolds will generate a permanent topography of controlled dimensions (width, depth, pitch). Surface topography will influence the attachment, morphology and orientation of endothelial cells cultured on acellular scaffolds (2D culture), while interface topography will influence the stratification of keratinocytes seeded on fibroblast-seeded scaffolds (3D culture).

The purpose of this study was to develop a method for engineering topography in 3D collagen hydrogel scaffolds and to test its effect on epithelial cell function. Substrate topographic patterning is recognized as a powerful tool for regulating important cell functions such as cell alignment, proliferation and differentiation[73]. Topography could provide a biomimetic cell-stimulating cue because *in vivo* cells contact textured, not smooth interfaces[239]. Indeed, basement membranes of various tissues are composed of complex mixtures of nano-scale pits, pores, protrusions, striations, particulates, and fibers [101,239]. While current patterning techniques (e.g. lithography, micromachining) allow precise control of topographic pattern (anisotropic vs. isotropic) and scale (nano- vs. micro-topography), they are only applicable to 2D surface patterning, which inherently compromises their utility in 3D tissue engineering. Shifting the focus from flat surface (i.e. 2D) to interface (i.e. 3D) topographic patterning requires the ability to engineer the desired topography in 3D

scaffolds, which can be interstitially, as well as superficially, seeded with cells. The findings of this study indicate that it is possible to engineer topography in 3D plastically compressed collagen hydrogel scaffolds by incorporating an embossing stage during the compression process. While in this study we only engineered an anisotropic topographic pattern of grooves/ridges it would be possible, by pattern template customization, to produce any desired (e.g isotropic) topography. For example, a previous study by this group showed that it is possible to emboss an isotropic pattern of microgrooves on a collagen hydrogel's surface by compressing it on a nylon mesh support with a fibrous structure ranging from <1 to $>100\mu\text{m}$ [25]. Furthermore, application of uniaxial strain of 25% realigned this embossed topography into an anisotropic pattern of grooves parallel to the aligned strain [25]. Since the process is a plastic deformation, this restructuring of the surface was also plastic i.e. stable, suggesting that embossing and tension pre-alignment could be used in combination for converting initially isotropic into anisotropic topographies.

The embossing method described here was successful in creating a regular pattern of grooves and ridges on the surface of collagen substrates, as shown by SEM and AFM. While it was possible to control groove width and periodicity with relative precision by controlling PBG fibre diameter and spacing, respectively, this was not the case for groove depth, where significant discrepancy was observed between expected and obtained values. The two proposed explanations for this effect are: **1)** Pulling off the pattern template from the substrate surface following embossing could have resulted in some level of collagen recovery (elastic recoil), leading to the formation of shallower grooves. This is a likely possibility given the viscoelastic nature of collagen [44,215]. Indeed, we found that fixing the collagen substrate (in

glutaraldehyde solution for 1hr) prior to pattern template removal resulted in visually better retention of the embossed topography, as assessed by SEM (data not shown). This method, however, would compromise the ability to interstitially seed scaffolds with cells. 2) The AFM method used to quantify groove depth required that the material was dehydrated prior testing, which must have affected the parameter being measured. It is therefore likely that both factors have contributed to some extent in this discrepancy. Future work should thus focus on developing fabrication, as well as quantification methods, for improving the precision of topographic depth control. For example, ongoing work by this group is investigating the effect of fluid flow direction during compression/embossing (i.e. embossing in the direction / against the direction of fluid outflow) on the stability of topographic features, while employing histological analysis for determination of feature depth.

It is important to note that in the method described here the pattern template was compressed (for 2.5min) on a pre-compressed collagen gel i.e. a double compression process was employed (see Methods section). Fluid removal during the first compression stage (2.5min) resulted in an increase in average matrix stiffness modulus from 42.2kPa \pm 22 to 2240 kPa \pm 846, as quantified previously using dynamic mechanical analysis [166] (note: the anisotropy of collagen density along the compression axis (Chapter 3) must have produced a higher stiffness at the FLS than the average matrix stiffness recorded by mechanical analysis). Therefore, embossing the pattern template on a stiff substrate resulted in faithful imprinting of the desired topography on the hydrogel's surface. However, compressing the pattern template directly (for 5 min) onto uncompressed, compliant hydrogels only resulted in partial embossing of the intended pattern onto the surface (as assessed by SEM,

data not shown), suggesting that matrix stiffness modulus must exceed a given threshold for adequate retention of the embossed topography.

The functionality of the engineered topography was first investigated using a 2D *in vitro* model, where endothelial cells were seeded on the surface of patterned or smooth collagen substrates. We found that endothelial cells did not proliferate on either smooth or grooved collagen substrates, indicating that topography might not directly affect endothelial cell proliferation, as suggested by previous studies [240,241]. Endothelial cell adhesion was greater on substrates patterned with 36 μ m diameter fibres than on smooth substrates or substrates patterned with 53 μ m diameter fibres, suggesting that the dimensions of the engineered topography are also important. The increase in cell adhesion observed here when micro-groove dimensions (groove width) matched cell size, i.e. on substrates patterned with 36 μ m diameter fibres, was likely due to an increase in the level or strength of individual cell attachment zones[73]. Certainly, the micro-patterned surfaces present a greater surface area for cells to interact with or attach to the substrate, resulting in higher molecular interaction between the cells and the surface. Indeed, a previous study has shown that the dimensions of grooves/channels influence endothelial cell adhesion on nano-patterned surfaces under shear stress [241]. Endothelial cells cultured on substrates patterned with 36 μ m diameter fibres were also more elongated and showed greater alignment with groove direction than cells cultured on substrates patterned with 53 μ m diameter fibres. Since groove depth was not significantly different for the two fibre diameters tested (table 1), the observed difference in cell adhesion, morphology and orientation must have largely been mediated through the difference in groove width, which was significant (table 1). Indeed, it is well known that the scale of anisotropic topography plays an important role in deciding cell

behavior. Cell orientation generally increases with increasing groove depth [73,240], but decreases with increasing groove width or pitch. If pitch is large relative to cells (as was the case with substrates patterned with 53 μ m diameter fibres), cells may sense each ridge as an individual topographic feature to traverse [73]. Importantly, a previous study reported that maximum alignment of bovine aortic endothelial cells was observed for 1 μ m deep channels [240], i.e. in the range tested in our study, suggesting that groove depth here was not a limiting factor for the observed cell behavior. Topographic scale has also been shown to affect whether cells bridge between ridges or conform to the grooves, through selective focal adhesion formation on ridge tops or down to groove floors [73,109]. At the microscale, with decreasing groove width and increasing groove depth, cells tend to bridge the ridges without descending into the grooves [73,109]. Investigation of such effects using the current method would require more precise control of the depth of topographic features.

After establishing the functionality of the engineered topography in directing epithelial cell function on 2D surfaces, we further explored its potential in regulating cell behaviour in 3D interfaces, by reconstructing an *in vitro* model of the dermo-epidermal (DE) junction. The ability to seed cells both interstitially and on the surface of micro-patterned collagen substrates, allowed formation of a biomimetic interface, similar to the basal lamina found in native skin [239]. As with most tissues, the basal lamina in the skin is not a simple flat plane of connective tissue, rather it conforms to a series of ridges and invaginations known as rete ridges and papillary projections. In native skin, cellular microenvironments produced by the topographic features at the DE junction appear to regulate the spatial organization

and function of keratinocytes[242]. In skin with thin epidermis, such as foreskin, breast skin, and scalp, clusters of keratinocyte stem cells are found at the peaks of dermal papillae. Each stem cell divides to give rise to another stem cell and a transient amplifying cell that laterally migrates down into the rete ridges and undergoes 3–4 divisions producing postmitotic cells that migrate up from the basal layer to form differentiated features of the tissue. In contrast, skin with thicker epidermis, such as palmar epidermis, has longer dermal papillae and rete ridges which have clusters of epidermal stem cells at their bottom. Transient amplifying cells migrate up the basal layer as they produce postmitotic cells that, in turn, migrate to the surface of skin over a period of weeks, where they are eventually sloughed off. Although these cellular events are well characterized in native tissue, the underlying physiological or topographical mechanisms that mediate them remain unclear. In our study, immunohistological analyses showed that the epidermal layer in grooved substrates was composed of differentiated and stratified keratinocytes that conformed to the surface of the dermal layer, forming rete ridge-like structures comparable in dimensions to those observed in native skin. Moreover, stratification was enhanced in the groove regions, suggesting that epidermal organisation is critically influenced by the topography of the basal lamina. The topographical micro-environment might influence keratinocyte differentiation/proliferation by affecting the spatial arrangement of cell–matrix contacts and/or cell-cell contacts [69], e.g. keratinocyte migration could be enhanced when cells have a non-attached dorsal surface. Indeed, it has previously been shown that expression of $\alpha 2\beta 1$ integrin, a marker of epidermal stem cells, varies with topography such that high expression is found in patches of basal cells located on the tips of the dermal papillae (foreskin, scalp) or at the bottom of the deep rete ridges (palm) [243].

Previous studies have reported that keratinocyte stratification and differentiation increases as channel depth increases and channel width decreases[69,239]. However, in these studies photolithography and replica molding techniques were used to incorporate microtextured features into collagen membranes, preventing seeding of the membranes with fibroblasts. In our study, fibroblast-seeded collagen substrates were patterned using embossing micro-fabrication, which is a gentler method (plastic compression did not significantly reduce fibroblast viability[25]), enabling co-culture of fibroblasts with keratinocytes. This is a key improvement from previous techniques, since it permits investigation of the effects of topography at a 3D cellular interface. Importantly, we found that culturing keratinocytes onto acellular (i.e. fibroblast-free) collagen substrates resulted in poor epidermal differentiation (data not shown), indicating that the presence of a fibroblast-seeded dermal layer is vital for normal epidermal morphogenesis. It has indeed been shown that activation of keratinocytes seeded on collagen matrices may depend, in part, on paracrine signaling from dermal fibroblasts[244]. In the presence of fibroblasts, keratinocyte proliferation is stimulated and epidermal morphology is improved. These interactions may be mediated through cytokines such as keratinocyte growth factor (KGF), a fibroblast-secreted growth factor that regulates epithelial cell growth. Ponec and colleagues found that in keratinocyte cultures on scaffolds, without fibroblasts, no proliferative cells were detectable in the epidermis after 2 weeks at the air/ liquid interface. Such epidermis consisted of only three or four viable cell layers[244]. These findings emphasise the principle that engineering truly biomimetic constructs will require development of micro-textured 3D scaffolds that

can be interstitially, as well as superficially, seeded with cells (i.e. on either side of the patterned topography).

The 3D model of the DE junction presented here may also be useful for investigating the critical topographical features of skin that contribute to its mechanical stability. In areas of the skin exposed to high friction/loading (i.e. shear at the plantar and palmar surfaces), the dermal papillae and epidermal ridges are longer and more numerous, suggesting that the enhancement of the interface between the epidermis and dermis provides additional mechanical stability[245]. For example, it has been shown that thickened cornified epithelium such as the human callus contains surface ridges and grooves, and that the cross-bands between ridge and groove areas form a fairly regular lattice-like pattern [245]. This lattice-like pattern comprises an additional structural modification of the keratin in the submicroscopic dimension, as keratin is oriented in the direction of the grooves and ridges (Fig.10) [245]. This was indeed in agreement with the findings of our study (Fig.9E).

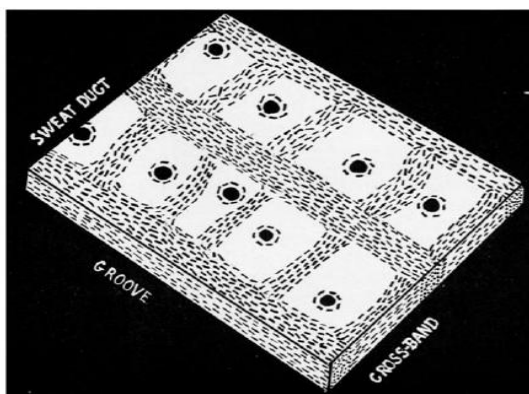


Fig.10 Schematic showing oriented areas of keratin in human callus. Broken lines indicate the direction of orientation of keratin fibres in groove and inter-groove regions of the callus (Reproduced from Matoltsy et. al., 1955 [245]).

It is proposed that this lattice structure functionally increases the mechanical strength of the stratified squamous epithelium, as well as assuring iso-dimensional mechanical and physical responses to mechanical stress. A microfabricated basal lamina that creates a complex interdigitating interface between the epidermal and dermal layers might therefore be expected to improve the resistance of engineered skin substitutes to failure under shear forces. By testing the properties of skin equivalents incorporating rete ridges and dermal papillae of various geometries, it should be possible to establish a direct and quantitative correlation between topography and mechanical properties. Moreover, these studies can be extended to the molecular level by examining the distribution/numbers of known adhesive proteins such as integrins and hemidesmosomes.

Engineering such complex interfaces might also facilitate improved mass transport of nutrients and growth factors to the epidermis (e.g. by providing a greater surface area for transport/ diffusion) [69], potentially aiding the surgical take of tissue engineered skin substitutes (i.e. integration to host tissue margins). Furthermore, since the embossing microfabrication technique presented here can be used to create more complex patterns, it should be possible to mimic the fine lines and pore structures of native skin (e.g. hair follicles, glands etc.), thus creating more ‘natural’ and perhaps cosmetically acceptable skin constructs.

4.3 CONCLUSIONS

This study presents a novel method for engineering topography on 3D collagen scaffolds. Pattern template embossing ensures rapid, faithful fabrication of a desired topography, while importantly maintaining the viability of cells seeded within the

collagen matrix. This effectively enables interstitial, as well as superficial cell seeding of patterned scaffolds, therefore fulfilling the pre-requisite for expanding topographic control of epithelial cell functions from 2D surfaces to 3D interfaces. This represents a new strategy for engineering *in vitro* 3D models of biomimetic tissue interfaces (e.g. basement membranes), to investigate the effects of topography on epithelial cell behaviour, with important implications for regulating cell function in engineered 3D tissue constructs.

4.4 MATERIALS & METHODS

Pattern template production

Glass fibre production

Glass for PBG preparation was obtained by using NaH_2PO_4 , CaCO_3 , P_2O_5 and Fe_2O_3 (BDH, UK) as starting materials. The precursors were weighed out and then placed into a 200 ml volume Pt/10% Rh crucible type 71040 (Johnson Matthey, Royston, UK). The crucible was then placed into a Carbolite furnace at between 950 °C and 1050 °C for 1hr. The glass was poured into a graphite mould, which had been preheated to 350 °C. The mould was placed back into the furnace and left to slowly cool to room temperature, to remove any residual stress. The glass rods obtained from the mould, of final composition $\text{P}_{50}\text{C}_{30}\text{N}_{15}\text{Fe}_5$, were cut into disks of 15mm diameter, and 2mm thickness, using a Testbourne diamond saw. Glass fibres were obtained using a fibre drawing method, from a newly acquired Fibre-rig (Biomaterials Department, UCL). The fibre-rig consists of a top loading furnace (Lenton Furnaces) with a Pt/10% Rh crucible (Johnson Matthey, UK) consisting of a bushing with an approximate 1mm hole, and a tip approximately 15mm long. Glass

was placed into the crucible and left for an hour to melt and to homogenise. The temperature of the furnace was then dropped to achieve a viscosity suitable for fibrillation of the glass. Different fibre diameters were obtained by pulling the glass at different RPMs. To obtain fibres of $\sim 35 \mu\text{m}$ diameter 300 RPMs were used, while for fibres of $\sim 55 \mu\text{m}$ diameter 100 RPMs were used.

Determination of glass fiber diameter

To measure fiber diameter, a small bundle of parallel aligned fibres from each RPM were placed into a PTFE mould and covered with resin (Struers, UK). The resin was then polished and examined under a light microscope, which was attached to a CoolSnap Digital Image Analysis system (ISS Group Ltd, Manchester). Image Pro Plus software was used to measure the diameter of the fibres in microns. The mean values presented and the errors were calculated from measurements on 30 fibres.

Pattern template preparation

Unidirectional parallel aligned fibres (35 or 55 μm diameter) were arranged in bundles (~ 200 fibers) with a constant spacing of 50-100 μm (Fig.11a,b). Bundles were held in place by fixing each edge of the bundle using cyanoacrylate glue.

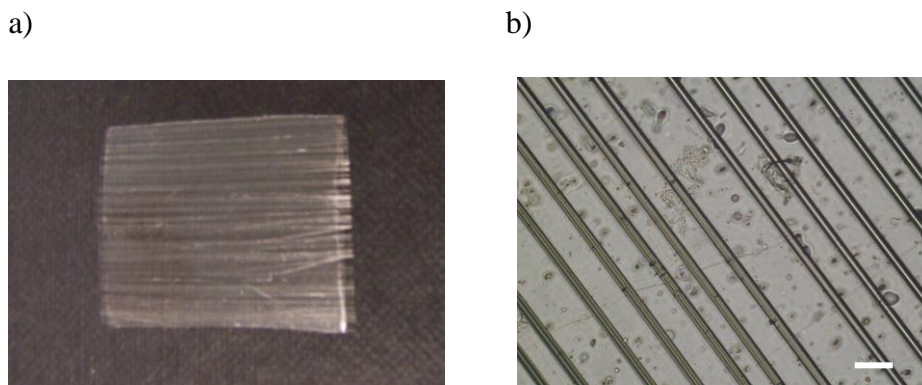


Fig.11 Pattern template used for embossing. (a) Macroscopic view of a phosphate-based glass (PBG) fibre pattern template, comprising of parallel aligned fibres. (b)

Light microscope image of the same pattern template showing parallel aligned fibres (35µm diameter) with a constant spacing of 50-100 µm (bar=100µm).

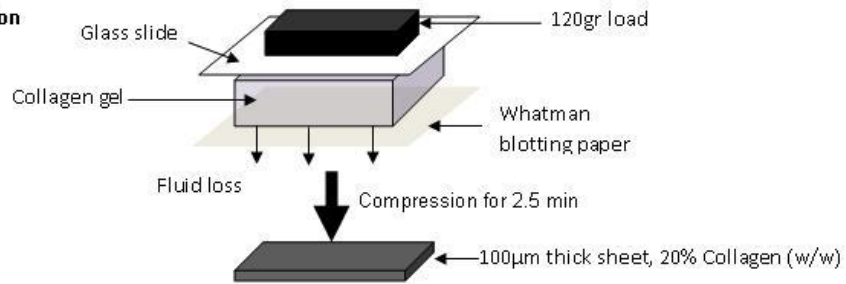
Microtextured topographic patterning of collagen constructs

Pattern template embossing

Collagen gels were prepared as previously described [210] (see Chapter 2). Following setting and incubation, gels were compacted for 2.5 min by a combination of compression and blotting, as shown in figure 12a. This led to formation of a flat collagen sheet (~100 µm thick) protected between two nylon meshes. (Note: for control smooth/non-patterned constructs the duration of this first stage of compression was 5 min, as they did not undergo a second stage of embossing compression - see below). Following plastic compression of collagen hydrogels (2.5min), the resulting dense collagen sheets underwent a second stage of compression, during which a pattern template of parallel aligned phosphate-based glass fibres (PBGs) was embossed onto their surface. After the first compression, the top nylon mesh was removed and constructs were turned over and placed onto the PBG pattern template, which was in turn placed on double layer absorbent Whatman paper. Note that in this arrangement the non-FLS was in contact with the pattern template. Constructs were compressed for 2.5 min using a 120g load (Fig. 12b). The pattern template was then removed and the constructs were fixed in 2.5% gluteraldehyde for 1 hr.

1st Step

Plastic Compression



2nd Step

Embossing

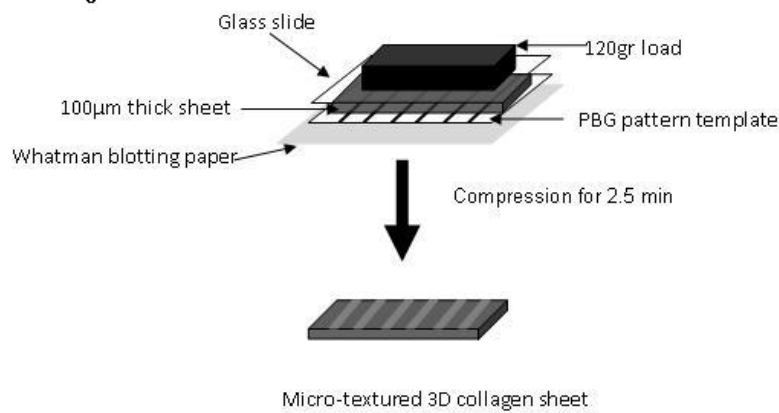


Fig.12 Schematic showing the two-step process used to create micro-topography on the surface of collagen scaffolds. During the first step of the process collagen hydrogels underwent compression under fixed mechanical loading over a porous (blotting paper) support to remove the majority (~98%) of their interstitial fluid, resulting in formation of ~100 µm thick collagen sheets. In the second step of the process, dense (~20% collagen w/w) collagen sheets underwent a second stage of compression, during which a pattern template of parallel aligned phosphate-based glass fibres was embossed onto their surface, resulting in the formation of a topographic pattern of parallel grooves/ridges.

SEM analysis of engineered topography

Conventional SEM (Philips CM12 electron microscope; Agar Scientific, UK) was used to study the micro-groove topographic pattern embossed on the surface of collagen constructs. After embossing constructs with a 35 or 55 μm diameter fiber pattern template, constructs were prepared for scanning electron microscopy as previously described (see Chapter 2). Five fields were randomly selected per construct, with 4 constructs used for each condition. SEM images were analysed for quantification of the width of patterned grooves, using an imaging software (Image J, NIH, USA).

AFM analysis of engineered topography

Atomic Force Microscopy (AFM) was used in this study to quantify the depth of grooves once the PBG pattern template was embossed on the collagen scaffold surface.

Basic principles

Atomic force microscopy, or scanning force microscopy, is a relatively new technique that was initially proposed in 1986 by Binnig et al [246]. Only in the 1990s did it become widely used. AFM, unlike usual microscopy, creates an image by 'feeling' the surface of material and not by seeing it directly as in optical microscopy. Pictures are obtained by measuring small vertical displacements of the probe scanning along the surface. These deflections are caused by number of forces (chemical, capillary, Van der Waals, etc.) and can be measured using Hooke's law. Several approaches were suggested of how to detect the tip displacement (e.g. capacitive sensing, optical interferometry) but typically the laser spot displacement is

used. The laser beam is focused on the tip and reflected onto the quartered photodiode detector. When the tip is displaced it results in a change in the laser spot position on the quartered surface of the sensitive photodiode, that makes possible to measure either normal and lateral motions of the tip. This complex signal goes through a differential amplifier into a feedback loop which maintains a pre-programmed parameter (deflection or amplitude) as a constant by manipulating with a piezo scanner (usually tubular type is used) (note: this is not the only possible design of the instrument but all of them consist of the same tip scanning deflection mechanism).

AFM modes

AFM can be used in several modes and conditions (liquid, air or vacuum), but in terms of this study tapping or contact AFM in air was used. Contact (in air) mode of AFM is performed by probe scanning along the surface in constant contact with it. Deflection of probe in each point, caused by surface features, is measured and maintained as a constant by feedback loop mechanism and after computer processing recorded as an image. Spring constant of probes used is in the range 0.01 - 1.0 N/m and typical interaction forces are of the order of 1nN. In contrast with contact, in tapping (air) mode stiffer probes are used within the range of 30 - 60 N/m and interaction forces of about 0.1 nN are applied. Here the tip is oscillated with a frequency close to the natural resonance and the amplitude is reduced as the tip approaches the surface. The reduced amplitude is measured and maintained at a constant level by feedback loop.

AFM limitations

As well as many other techniques AFM has its limitations. There are some common problems of all modern electronic methods: thermal drift, stability of amplifiers, bandwidth etc. Due to high sensitivity of ultra small displacement measurements, it is very sensitive to background vibration, which should be eliminated. But there are some problems specific to AFM, which should be taken into account, such as tip effects. There are several tip effects that can be outlined: tip broadening (arising when the radius of probe curvature is comparable with the radius of the feature being measured), compression (some soft biological materials show dependence of width upon the pressure applied), tip convolution effects (which can be seen with a collagen sample, where the fibre appears as a hilly structure on the surface and not as a cylindrical object), multiple tip effects (the features observed on the image are multiplied). Importantly, in terms of this study, samples had to be dehydrated prior testing, which expectedly must have affected the parameter being measured (i.e. groove depth). This effect was likely a major contributing factor for obtaining a lower value for groove depth than expected from groove diameter measured by SEM (see results).

AFM image analysis

Five fields were randomly selected per construct, with 4 constructs used for each condition. Images were analysed for quantification of the depth of patterned grooves by measuring the distance from the bottom of each groove to the tip of the lowest of the two ridges, using an imaging software (WSxM 2.2., Nanotec Electronica S.L., Spain).

Endothelial cell cultures

For cell attachment and orientation studies HUVECs were seeded on non-patterned or patterned collagen substrates (surface area=3.66cm²) at a seeding density of 2x10⁴ cells/cm². This seeding density ensured that there was no direct cell-cell contact. For quantification of cell attachment cells were allowed to attach for 4hrs before substrates were washed twice with PBS (5ml) to remove non-adherent cells. For quantification of cell orientation and elongation cells were cultured on substrates for 48hrs before being washed with PBS and fixed in 100% ice-cold methanol and processed for SEM. For analyses of cell proliferation HUVECs were seeded on non-patterned or patterned collagen substrates (surface area=3.66cm²) at a seeding density of 5x10³ cells/cm² and cultured for 24 or 48hrs. Medium was removed from all culture wells every 24hrs and 5ml alamar blue (Serotec, UK) solution (diluted 1 in 10 with phenol-red free culture medium) was added. The collagen matrices were incubated in alamar blue solution at 37°C for 4 hrs. Alamar blue solution was then removed and 100 µl was sampled from each well. Samples were transferred into a 96 multiwell plate and absorbance readings were taken at 510 and 590 nm using a microplate spectrophotometer (MR 700 microplate reader, Dynatech Laboratories). Readings were converted to cell number using a standard curve. The collagen matrices were washed in PBS (for 5 min, twice) before fresh medium (5ml) was replaced, allowing monitoring to continue. Four constructs were tested per condition.

Quantitative morphometric analyses

For quantification of HUVEC attachment, substrates were visualised using an Olympus BX41 light microscope and images were captured with an Olympus DP70 CCD camera. The number of cells per x20 microscopic field was counted manually.

Five fields were randomly selected per substrate, with 4 constructs tested per condition. For quantification of HUVEC orientation SEM images were analysed using an imaging software (Image J, HIH, USA) to calculate the cell orientation angle. This was defined as the angle between the direction of the major axis in the cell and the direction of the groove and ranged between 0 and 90 degrees. Cells were considered to be aligned parallel to the ridges/grooves when cell orientation angles were less than 20° and non-aligned if angle was 20-90°. HUVEC elongation was quantified by calculating the ratio between the major and minor axes of each cell. The major and minor axes were defined by the long direction of the cell body and the direction perpendicular to the major axis, respectively. The ratio of cell major axis to cell minor axis was used to define an elongation index. At least 10 random fields were analysed per sample, with 4 constructs tested per condition.

Development of skin equivalent

Dermal layer

The dermal layer of the skin equivalents was developed by Plastic Compression (PC) of collagen hydrogels seeded with 2×10^5 human dermal fibroblasts (HDFs) (<10 passages). Compressed HDF-seeded collagen matrices were peeled off the nylon meshes and placed in cell culture inserts (BD Falcon, Stockholm, Sweden). A topographic pattern of parallel 3D micro-ridges was embossed into the putative dermal-epidermal (DE) interface, by embossing the dermal layer with a pattern template of phosphate-based glass fibres (PBGs), as described above. For control constructs with a smooth DE interface, 5 min of conventional plastic compression was used.

Epidermal layer

Human primary keratinocytes were seeded onto the surface of compressed collagen gels at seeding density 150 000 cells/cm² and constructs were submerged in 5 ml KER- medium (80% DMEM, 20% HAM's F12, 2% glutamine, 10% FCS, 0.2% hydrocortisone, 0.1% insulin, 0.1% T3/T, 0.1% cholera toxin, 2.5% adenine) for 2 days before being raised to the air-liquid interface and cultured for an additional 12 days (2 weeks culture) or 19 days (3 weeks culture) in KER+ (EGF 10 µg/ml added to the KER- medium).

Histology and immunohistochemical staining

Histological and quantitative morphometric analyses

After 12 or 19 days of culture, the collagen constructs were fixed and processed for routine histology (see Chapter 2). Cross sections were H&E stained and epithelialisation was determined with an Olympus BX41 microscope. Three fields were measured per section, three sections per sample and three samples for each condition were tested. The thickness of the stratified epidermal layer in each channel and between channels was measured vertically from the lower surface of the stratum basale to the outer edge of the stratum corneum, using an imaging software (Image J, NIH, USA).

Immunostaining for PAN-cytokeratin

To verify differentiation of the epidermis in the skin equivalent, immunohistochemistry targeting human epidermal cytokeratin was performed. After

dewaxing and serum blocking, the sections were incubated with primary antibody (Mouse anti-cytokeratin AE1/AE3, Chemicon International, UK) for 30 minutes at room temperature, rinsed in PBS, and incubated with secondary antibody (Alexa Fluor 488, Molecular probes, Inc. OR, USA) for 30minutes (see Chapter 2). AE1 reacts with the acidic keratins, while AE3 reacts with the basic keratins. After washing, bound antibody was localised using a fluorescence Olympus BX41 microscope at approximate absorption 495 nm, and fluorescence emission 519 nm, and captured using a Olympus DP70 CCD camera. For each condition, at least three samples of collagen constructs were examined.

Polarized light microscopy

For the polarization optical studies an Olympus BX41 polarizing microscope was used. The sign of birefringence was determined by means of a first order red retardation plate. Birefringence was referred to the optic axis of a component structure, or to a characteristic structural feature, in the epidermal layer of H&E-stained construct cross sections. Sections were cut perpendicular to the construct surface and to the direction grooves (in embossed constructs).

CHAPTER 5

CONTROLLING COLLAGEN MATRIX STIFFNESS: A TOOL FOR REGULATING CELL PROLIFERATION

Human dermal fibroblasts (HDFs) in free floating collagen matrices show minimal proliferation, though this may increase when the matrix is ‘under tension’. We have investigated the detailed mechanics underlying one of the possible controls of this important cell behavior, in particular the idea that this is a response to substrate stiffness. Hyper-hydrated collagen gels were plastically compressed to give a pre-determined collagen density and stiffness, resulting in a series with increasing stiffness modulus. Using these physiologically relevant, biomimetic 3D ECMs we tested the hypothesis that matrix stiffness directly regulates the proliferation rate of resident adult HDFs. Mechanical properties were tested using a Dynamic mechanical analyser; and cell number by Alamar Blue assay (see Methods section).

5.1 RESULTS

Fibroblast proliferation in free floating and attached matrices

Consistent with the previous literature [127,247] we found that fibroblasts cultured in free floating collagen matrices at an initial cell density of 4×10^4 cells/ml showed no proliferation after 8 days of culture (Fig. 1). In contrast, fibroblasts cultured at the same initial cell density and in the same matrices, but attached (i.e. matrices were allowed to develop isometric tension), showed some proliferation (doubling time of 6 days) after an initial lag period of 4 days (Fig 1).

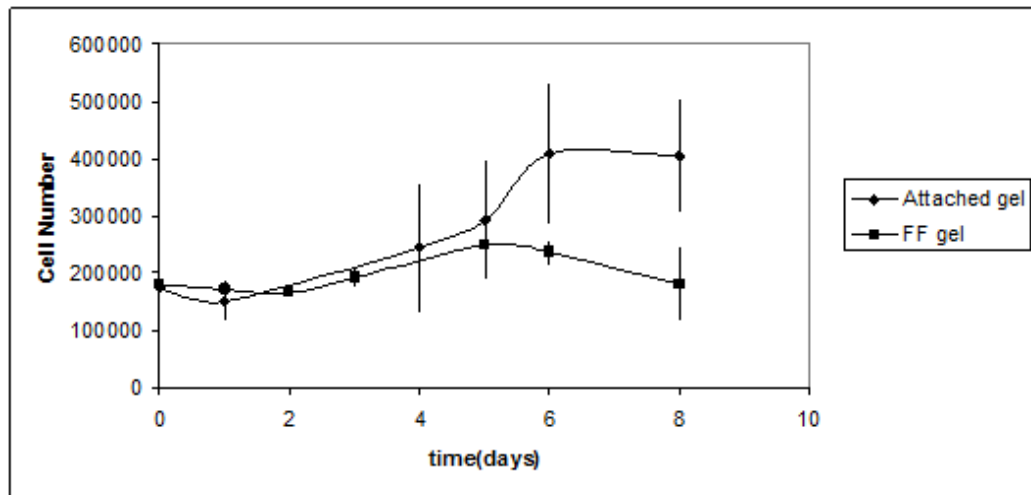


Fig. 1. Proliferation of adult human dermal fibroblasts cultured in attached and free floating (FF) collagen matrices. Fibroblasts were cultured for eight days. Proliferation was assessed using the alamar blue assay. Initial cell density was 4×10^4 cells/ml for both conditions.

Similar patterns of growth were also seen at a higher initial seeding density (1×10^5 cells/ml: data not shown). This agrees with previous findings and indicates that the alamar blue technique is an effective method for quantification of cell growth in collagen gels.

Correlation of matrix collagen density with stiffness modulus

Since the objective here was to test the effect of matrix stiffness on cell proliferation, we measured the change in Young's modulus for collagen gels compressed to three different levels of fluid loss (50, 75 or 99% fluid removal). This process produced collagen matrices with 0.4, 0.7 and 20% (w/w) collagen density, respectively (see methods). Dynamic mechanical analysis established that increasing the collagen matrix density resulted in proportionately higher matrix stiffness (Young's modulus) (Fig.2). There was a more than fifty fold increase in the modulus between the 20%

collagen gels (2240 ± 846 kPa) compared to 0.4% gels (42.2 ± 22 kPa) ($P < 0.05$), which interestingly corresponded with an almost identical (50 fold) increase in collagen density.

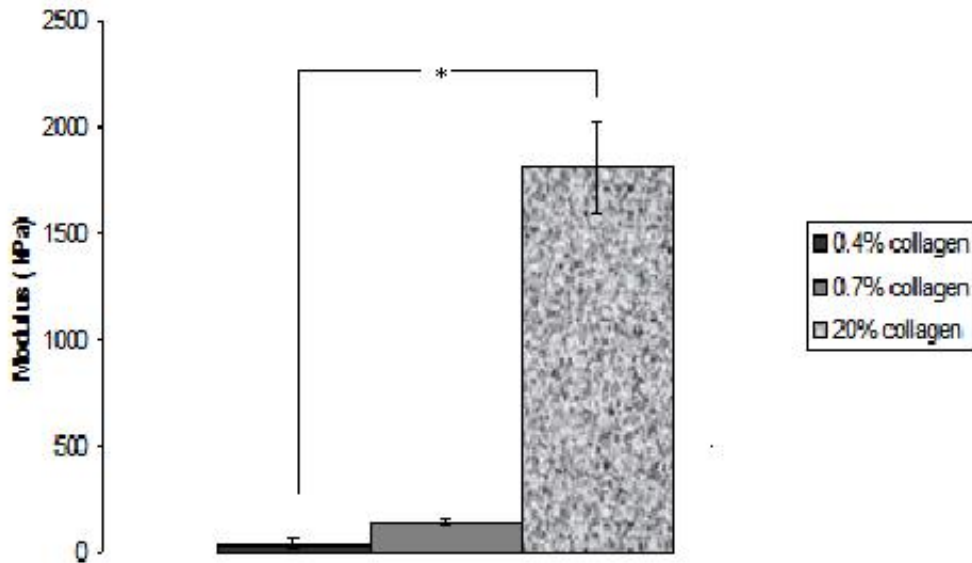


Fig. 2. Correlation between matrix collagen density and stiffness modulus. Mean Young's moduli as measured by dynamic mechanical analysis (DMA) for collagen matrices compressed to 50, 75 and 99% fluid removal, corresponding to 0.4, 0.7 and 20% (w/w) collagen density. Three collagen constructs were tested for each level of compression (n=3), *p<0.05.

Effect of increasing matrix stiffness of fibroblast proliferation

Fibroblasts cultured in compressed matrices with a collagen density of 20% w/w (modulus of 2240 ± 846 kPa), at an initial seeding density of 1×10^6 cells/ml, showed rapid proliferation without any lag period. Doubling time was 48hrs ($p < 0.05$) (Fig 3a). Proliferation rate was seeding-density dependent (though never showed a lag

phase) with a doubling time of 96 hrs at an initial seeding density of 4×10^6 cells/ml (Fig 3b) and zero net growth in matrices seeded with 20×10^6 cells/ml, indicating that this was the cell density at which cell-cell contact inhibition occurred in this 3D system (Fig 3c). Indeed, at this high seeding cell density, cell number showed a cyclical pattern over the first 6 days, indicating that growth is initiated once cell density (i.e. cell-cell contact inhibition) is reduced. However, a negative trend in cell number seemed to be established, such that by 8 days cell number was 50% lower than at the beginning of culture ($p < 0.05$). Cell death, in this case, could be the result of apoptosis or necrosis.

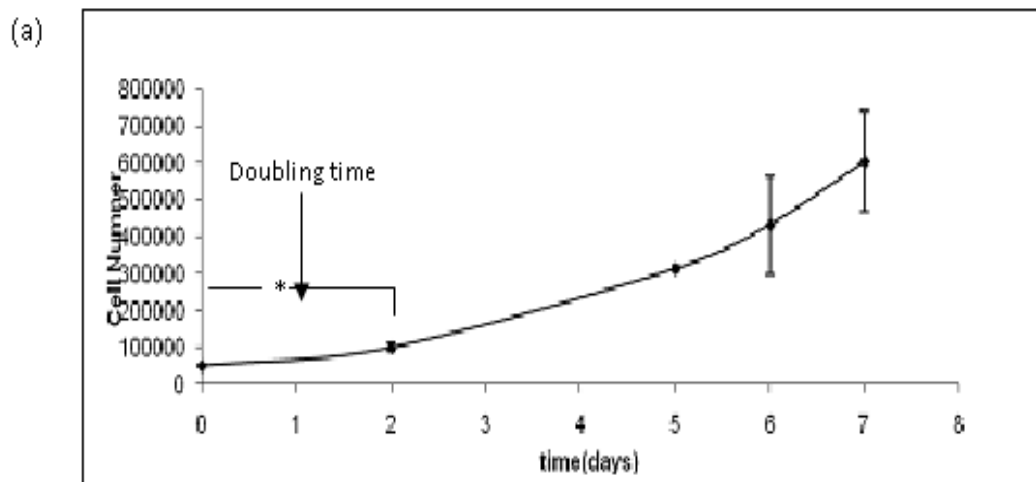
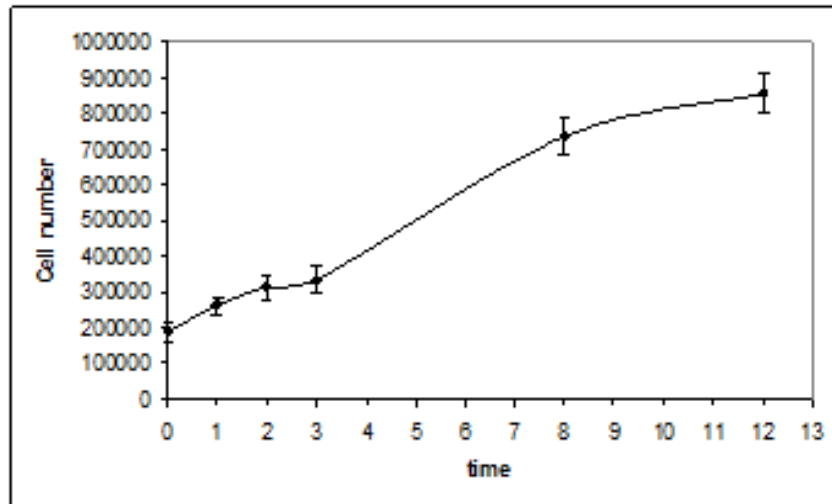
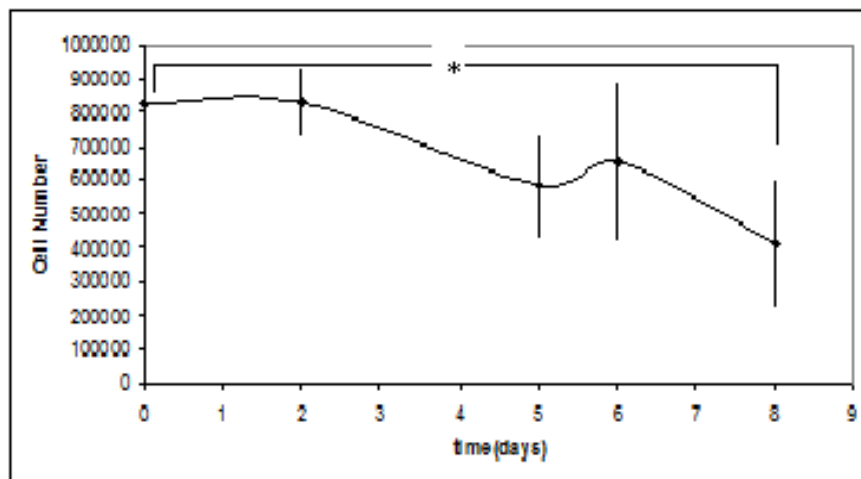


Fig. 3. Proliferation of adult human dermal fibroblasts in PC collagen gels. 5ml collagen gels were plastically compressed with a 120g load for 5min resulting in >99% fluid removal and 20% (w/w) collagen density. Initial cell densities immediately after compression were (a) 1×10^6 cells/ml, (b) 4×10^6 cells/ml and (c) 20×10^6 cells/ml. Asterisk indicates significant increase in cell number from day 0 to day 2 (a) and significant decrease from day 0 to day 8 (c) ($*p < 0.05$).

(b)



(c)



Having established that collagen matrix stiffness correlates directly with fibroblast proliferation in three-dimensional culture, we tested the hypothesis that there was a continuous, graded relation between proliferative response and stiffness rather than the effect of a threshold stiffness, above which fibroblast division is initiated. Fibroblasts were cultured in collagen matrices of 0.2, 0.4 or 0.7 % collagen density at the same initial cell density of 4×10^4 cells/ml. Figure 4a shows that greater

proliferation (87% increase in cell number) was observed in matrices of 0.7% collagen compared to matrices of 0.4 % collagen (25% increase in cell number), after 2 days of culture. As expected, no proliferation was observed in matrices of 0.2 % collagen (uncompressed free floating). A similar pattern of growth was observed after 6 days of culture (Fig 4b). These results indicate not only that cell proliferation responds in a graded manner to matrix stiffness but that it is also highly sensitive to relatively small absolute changes in matrix stiffness (note: collagen densities of 0.4% and 0.7% resulting in matrix stiffness of 42 kPa and 143 kPa, respectively, are within the physiological range[248]).

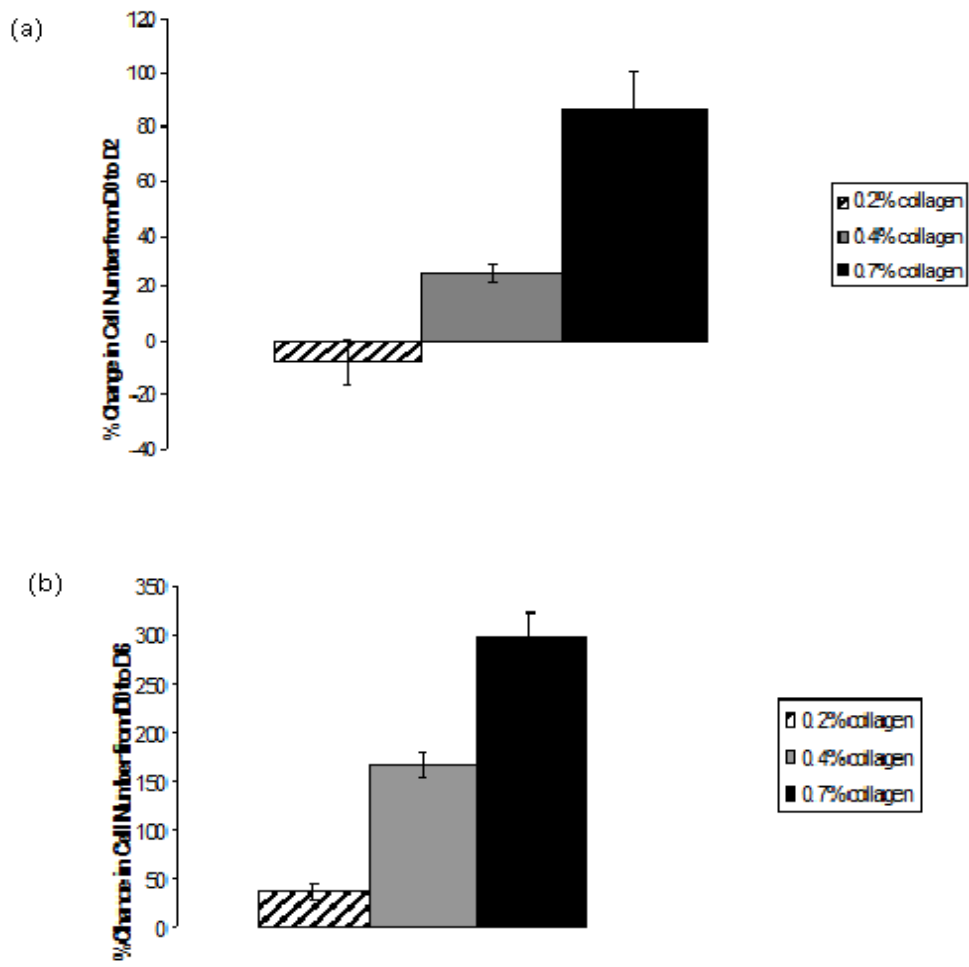


Fig. 4. Effect of increasing matrix stiffness on fibroblast proliferation. Proliferation of adult human dermal fibroblasts in collagen matrices of 0.2, 0.4 and 0.7% collagen

density (w/w). Initial cell densities immediately after compression were 4×10^4 cells/ml for all three conditions. Mean percentage increase in cell number over (a) a two day (day 0 to day 2) or (b) a 6 day (day 0 to day 6) culture period.

Reversal of fibroblast quiescence

These results provide evidence that fibroblast proliferation is directly regulated by the stiffness of the matrix in which the cells reside. However, in the previous experiments, fibroblasts were seeded within matrices that were compressed at day 0 of culture, and thus any signaling relating to extracellular matrix stiffness was present at the initial stage of the growth response. Previous studies indicated that quiescent fibroblasts in free floating gels are in a distinct state (they become arrested in the Go phase of the growth cycle) and that their lack of growth is not due to cell-cell contact inhibition or deficiency of growth factors [249]. To examine whether this represents a permanent change in cell behaviour or an example of dynamic (i.e. reversible) cell regulation, we examined the proliferation of fibroblasts where matrix stiffness was increased *in situ* at specific time points in the culture period. Fibroblasts were seeded at 4×10^4 cells/ml and cultured in free floating matrices. As expected, no proliferation was observed after 24 hours (Fig 5). The first set of matrices was then compressed *in situ* (after 24 hours) to give a collagen density of 20% (w/w) and returned to culture (we have previously shown that the Plastic Compression process does not cause any cell death [25]). Within the next 24hrs (day 2 of culture), fibroblast proliferation was significantly increased (by 62%, $p < 0.05$) in *in situ* compressed but not in uncompressed matrices. Similarly, *in situ* compression of free floating matrices on day 5 initiated proliferation within 24hrs. It is important

to note that while matrix compression itself inevitably increases cell density, this did not block proliferation, as might have been expected if cell-cell contact inhibition was a limiting factor. This indicates that fibroblast quiescence in free floating matrices cannot be a consequence of the increased cell density due to cell-mediated matrix contraction, as sometimes suggested.

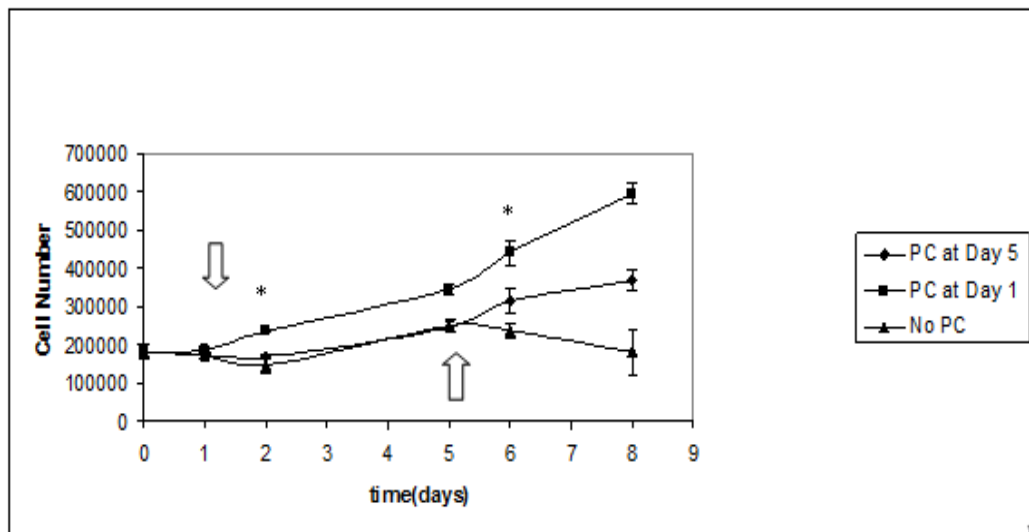


Fig. 5. *In situ* plastic compression of free floating matrices reverses human dermal fibroblast quiescence. Fibroblasts were seeded in free floating matrices at an initial cell density of 4×10^4 cells/ml. Collagen matrices were taken out of culture and compressed on day 1 or day 5 (arrow) before being returned to culture. A set of gels was left in culture for 8 days, without compression at any point (for each condition three gels were tested). Asterisk indicates significant difference in cell number between compressed and uncompressed matrices (* $p < 0.05$) at day 1 and day 5.

5.2 DISCUSSION

Original Hypothesis: The stiffness of collagen hydrogels will be directly related to their collagen density and therefore to their hydration level. The proliferation rate of human dermal fibroblasts (HDFs) will be closely related to collagen matrix stiffness such that stiffer matrices will support higher proliferation rates.

The purpose of this study was to investigate whether cell proliferation is directly regulated by matrix stiffness. It has already been established that fibroblasts cultured in free floating matrices divide very little and undergo apoptosis[128]. In contrast, cells cultured in attached matrices begin to divide after a lag period of approximately four days. While this observation indicates that mechanical loading stimulates cell division, and inversely that loss of mechanical tension inhibits proliferation and induces apoptosis, the effects of matrix stiffness on cell proliferation have yet to be isolated. Using plastic compression to rapidly remove fluid out of collagen hydrogels, we have been able to precisely control matrix stiffness. Fibroblasts seeded within matrices of high stiffness began to divide rapidly with a doubling time of two days. Expansion was seeding density-dependent with inhibition of cell proliferation been observed at 1×10^6 cells/ml. At such high seeding density, cell-cell contact inhibition likely becomes significant. HDF proliferation was related to matrix stiffness such that increasing matrix stiffness lead to increasing proliferation rates from 5 to 3 days doubling time, and this in turn related to increasing matrix stiffness modulus. Since there was a 50 fold difference between the stiffness of the most compliant and stiffest substrates, this indicates that cells respond to a wide range of stiffness levels, as it has previously been suggested[125].

Previous studies employing two dimensional substrates have indeed implicated matrix stiffness as a significant factor influencing cell proliferation [125,250]. Direct regulation of cell proliferation by matrix stiffness within a biomimetic, three-dimensional environment has not previously been tested. It is important to note that compression of collagen matrices, as a means of controlling stiffness, does not alter the tension within the matrix, thus enabling the isolation of any effects of stiffness on cell behaviour. It has been proposed that the magnitude of tractional forces fibroblasts exert on their substrate may influence cell proliferation, and that fibroblast quiescence in compliant hydrogels is related to their failure to exert strong tractional forces[125]. It has also been previously shown that fibroblasts which have lost contact with their surrounding extracellular matrix, undergo reversible growth arrest [251]. On the other hand, Niland et al have demonstrated that fibroblasts display a marked reduction of apoptosis in mechanically relaxed (i.e. contractile) collagen matrices in the presence of adhesion-blocking antibodies against $\alpha 1\beta 1$ or $\alpha 2\beta 1$ integrins, while cells lacking alpha2 integrin displayed no apoptosis [252], suggesting that cell-matrix interactions are important for cell survival/growth in natural ECMs. In our system, increasing stiffness by increasing matrix collagen density, inevitably resulted in alterations in the number of binding sites and thus in cell-matrix interactions. This would ultimately lead to changes in the expression of genes related to cell division [253].

Previous studies indicated that quiescent fibroblasts in free floating gels are in a distinct state, as they become arrested in the Go phase of the growth cycle[254] and that their lack of growth is not due to cell-cell contact inhibition or deficiency of growth factors [249]. In addition, PDGF receptor desensitization and disruption of the ERK signalling pathway have been observed in quiescent fibroblasts in free

floating matrices[137,138,255-257]. Here we show that increasing matrix stiffness at specific points during the culture period initiates cell proliferation. This finding indicates that fibroblast quiescence in free floating matrices, and presumably the mechanism(s) that facilitates this, represents an example of dynamic (i.e. reversible) feedback regulation. Since matrix compression itself inevitably increases cell density, but does not block growth, this also provides supportive evidence against the idea that fibroblast quiescence in free floating matrices is a consequence of the increased cell density due to cell-mediated matrix contraction[249].

Regulation of cell proliferation by matrix stiffness could have important implications in our understanding of the mechanisms mediating wound healing. Unlike fibroblasts of dermis that are quiescent and stationary, fibroblasts of granulation tissue are proliferative and motile[258]. During repair, tensile forces develop within the matrix of the wound bed. Fibroblasts in a mechanically loaded (attached) matrix resemble proliferating cells of granulation tissue, and the isometric tension that develops is equivalent to that found in skin wounds. In this study, we have shown that matrix stiffness, rather than tension, can itself directly regulate cell division, thus potentially providing an additional mechanism for controlling cell proliferation within the wound bed. As normal repair progresses, tensional force is normally relieved through a combination of biosynthetic activity and wound contraction and the cells of granulation tissue disappear over a period of weeks. This removal of cells happens at least in part via apoptosis[133,134]. In skin tissues, the development of hypertrophic scars after burns or other skin trauma is characterized by a non-disappearance of myofibroblasts [259] and an overproduction of extracellular matrix[260]. A lack of apoptotic induction is thus thought to be a prominent factor in this phenomenon [261]. Our findings indicate that increasing matrix stiffness during

hypertrophic scarring could also induce excessive cell proliferation and, together with the lack of apoptosis could contribute to the excessive cellularity and contraction associated with hypertrophic scars. This hypothesis is consistent with the finding that fibroblast proliferation *in vivo* is increased in keloid scars which are characterized by excessive collagen synthesis within the wound, and thus higher matrix stiffness [262,263].

5.3 CONCLUSIONS

The ability to control the hydration level of a collagen hydrogel scaffold provides a means for controlling its collagen density which is directly related to matrix stiffness modulus. In this study we have shown that adult HDFs cultured within 3D collagen matrices proliferate preferentially within stiffer matrices, while the quiescence of HDFs observed in compliant matrices is reversible by increasing matrix stiffness. These findings represent an important advance in our ability to test regulated cell proliferation with important implications for improving our understanding of the mechanisms governing wound healing and designing engineered connective tissues based on collagen and other hydrogel-based scaffolds.

5.4 MATERIALS & METHODS

Collagen matrix models

HDF-seeded collagen gels (5ml) were prepared as previously described [210] (see Chapter 2). The collagen-cell suspension was poured into a rectangular mould (size: 4×3x1 cm) made from Derlin blocks (Intertech, UK) and incubated at 37°C in a 5%

CO₂ humidified incubator for 20 min. Finally, the set gel was covered with 5ml complete culture medium and 50 mg/ml ascorbic acid.

Attached matrices

After setting, collagen matrices were left attached to their culture wells. Within 24hrs, the matrices underwent isometric compaction. The matrices were cultured at 37°C for the times indicated in the experiments.

Free Floating matrices

Attached matrices were gently released from the underlying culture well with a spatula to initiate mechanical unloading. Within 24hrs, the matrices underwent cell-mediated isotonic contraction. The matrices were incubated at 37°C for the times indicated in the experiments.

Plastic compressed matrices

Following setting and incubation, gels were compacted by a combination of compression and blotting [25], as shown in Fig 6(a) (also see Chapter 2). Compressed collagen matrices were peeled off the nylon meshes and placed in culture wells containing 5 ml complete culture medium. In order to produce collagen matrices of a desired level of hydration, and thus (average) collagen density, collagen gels were allowed to compress under their own weight (no application of load) on blotting paper for a given period of time, determined by the fluid loss vs. time standard curve (Fig 6b). This was obtained by measuring gel weight at one minute intervals during compression and indirectly calculating the %fluid loss from the gel. For a given level of fluid loss, it was possible to calculate the resulting matrix % collagen density (wet/weight, w/w), as shown in Fig 6c.

(a)

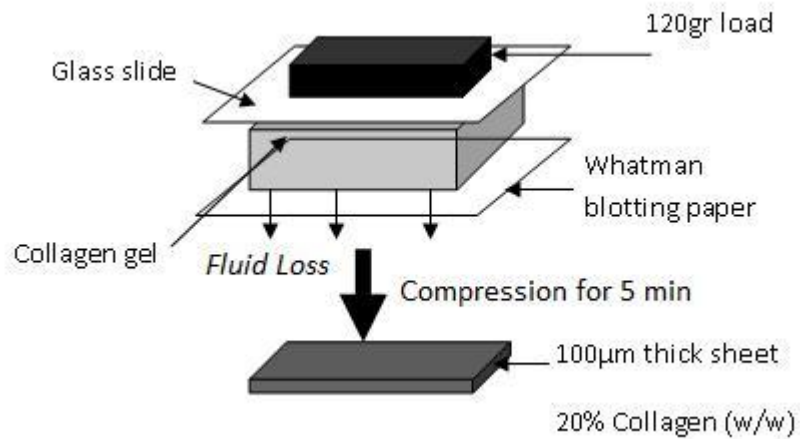
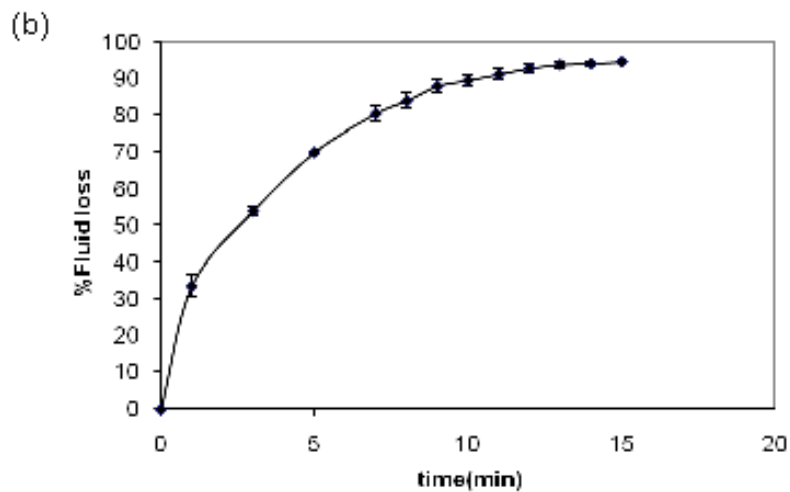
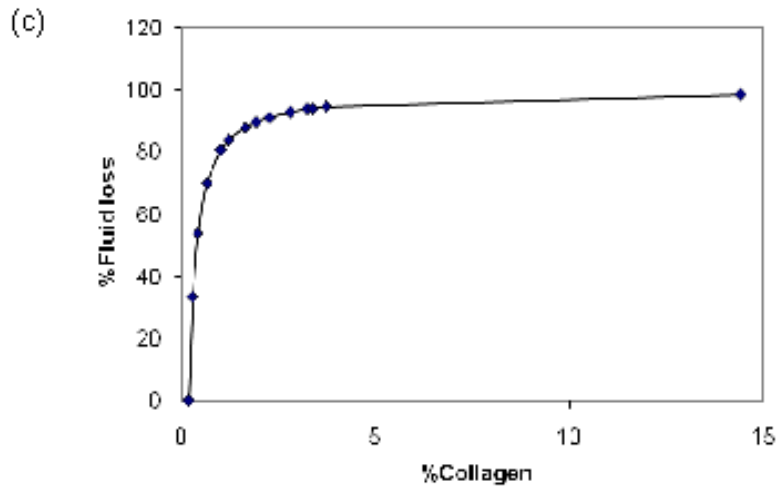


Fig. 6. Controlling fluid loss and matrix collagen density by plastic compression. (a) Schematic showing the plastic compression fabrication process. Collagen gels are compressed with an applied mechanical load and rapid fluid removal (99% fluid loss within 5 min) is achieved by a combination of compression and blotting.



(b) Relation between %fluid loss vs. time during compression of collagen matrices (5ml) under their own weight.



(c) **Relation between %fluid loss vs. matrix %collagen density for the same compression. This is a mathematical calculation assuming a pre-compression collagen density of 0.2% (w/w). By varying the duration of compression it was possible to control fluid loss and matrix collagen density to produce a collagen density/stiffness series.**

Quantification of fibroblast proliferation

Alamar blue is a redox indicator that both fluoresces and changes colour in response to the chemical reduction of culture medium which results from cell proliferation and division[264]. Alamar blue (10x concentrate, Serotec) was diluted 1 in 10 with phenol-red free culture medium. Medium was removed from all culture wells every 24hrs and alamar blue solution (5ml) was added. The collagen matrices were incubated in alamar blue solution at 37°C for 4 hrs. Alamar blue solution was then removed and 100 µl was sampled from each well. Samples were transferred into a 96 multiwell plate and absorbance readings were taken at 510 and 590 nm using a microplate spectrophotometer (MR 700 microplate reader, Dynatech Laboratories). Readings were converted to cell number using a standard curve. The collagen

matrices were washed in PBS (for 5 min, twice) before fresh medium (5ml) was replaced, allowing monitoring to continue.

Measurement of collagen matrix Young's modulus

Mechanical properties of plastic compressed collagen matrices were measured using a dynamic mechanical analyser (Perkin Elmer, UK)[25]. Collagen sheets (1 mm wide, 1 cm long) of three different levels of compression (50, 75, 99% fluid loss) were uniaxially deformed along their longest axis with the amount of tension required to produce a 5–30% strain. Samples were perfused with PBS between measurements. The stress–strain relationships were linear for the tested samples. Young's modulus was calculated using the formula: $E = (F/A) \times (L/\Delta L)$, where F=force applied on the sample, A=unstressed cross sectional area through which the force is applied, L= unstressed length, and ΔL =change in length. The values reported are the averages of at least three samples for each compression level.

CHAPTER 6

A COLLAGEN MATRIX WITH GRADED DIRECTIONAL STIFFNESS: GUIDING CELL MIGRATION IN 3D

Matrix stiffness has been implicated in the mechano-biological control of a range of cell behaviours such as cell adhesion, proliferation (Chapter 5) and migration. In particular, cells have been shown to preferentially migrate towards areas of greater stiffness, a phenomenon termed durotaxis. However, most studies of mechano-taxis have focused on the effects of substrate stiffness in 2D. This part of the work describes a novel model of a continuous stiffness gradient engineered within 3D collagen scaffolds and tests the hypothesis that cell migration will be guided by such a gradient. Wedge-shaped collagen scaffolds were compressed to produce sheets of a desired (0.1mm) uniform thickness, but with increasing collagen density along the length of the sheet, while the number of growth-arrested HDFs in compliant, middle and stiff areas was quantified as a measure of cell migration.

6.1 RESULTS

Generation of stiffness gradient in 3D collagen matrices

We hypothesised that vertical compression of collagen gels with a wedge-shaped cross section, by a horizontal/level plate (zero tilt), must leave more collagen material at one end (thick end of the wedge) than the other and so produce an increasing density along the length of the construct. Production of a gel with a flat wedge surface will produce a linear gradient (rate of change proportional to the angle of that surface). However, non linear (e.g. exponential) density gradients could be formed by casting the gel surface in a curved profile.

In order to quantify this stiffness gradient we measured the elastic modulus at the two extreme ends and in the middle of the compressed sheet. This was measured by loading 1 mm wide strips of these 3 construct regions, perpendicular to the axis of the density gradient, using Dynamic Mechanical Analysis (DMA) (see Methods section). The Young's modulus increased from 1057±487 KPa at the soft end to 2305±693KPa at the stiff end ($p<0.05$) and was 1835±31 KPa in the middle. This represented a near linear increase in modulus along the construct (Fig 1).

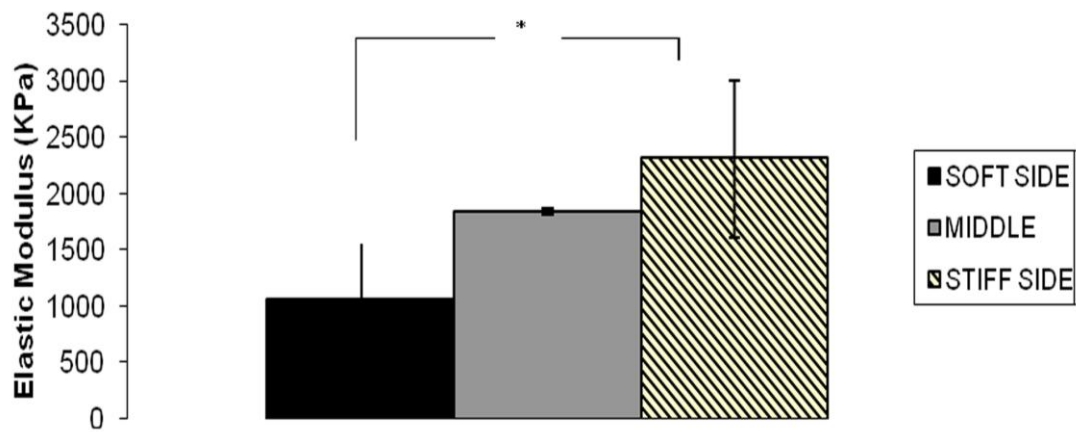


Fig. 1 Engineered stiffness gradient analysis. Young's moduli for the compliant (soft), middle and stiff regions of the construct, as measured by dynamic mechanical analysis. The >2 fold increase between the compliant and stiff ends was significant (* $p<0.05$).

Density gradient analysis

Uncompressed constructs were seeded with agarose marker beads in order to quantify the density gradient which generated this stiffness gradient. Seeding the constructs with marker beads also aimed to mimic the cellular density gradient that

would form if the constructs were cell-seeded. The use of agarose beads, instead of cells, eliminated any complications due to changes in cell morphology, cell movement during processing or cell-mediated collagen contraction. Mean agarose bead density along this gradient rose from 10 ± 1 to 71 ± 12 from the soft to stiff ends, respectively, and was 19 ± 5 in the middle (Fig 2a, b). This indicated successful engineering of a density gradient that partly corresponded to the stiffness gradient measured. The non-linear rise in bead density (contrast with linear increase in modulus) is likely to be a result of beads tending to settle under gravity and accumulate towards the thick lower end of the wedge during the short gelation period. A comparable non-linear shift would be expected for cell seeded gels, though its magnitude would probably be less and dependent on cell type and gelling conditions.

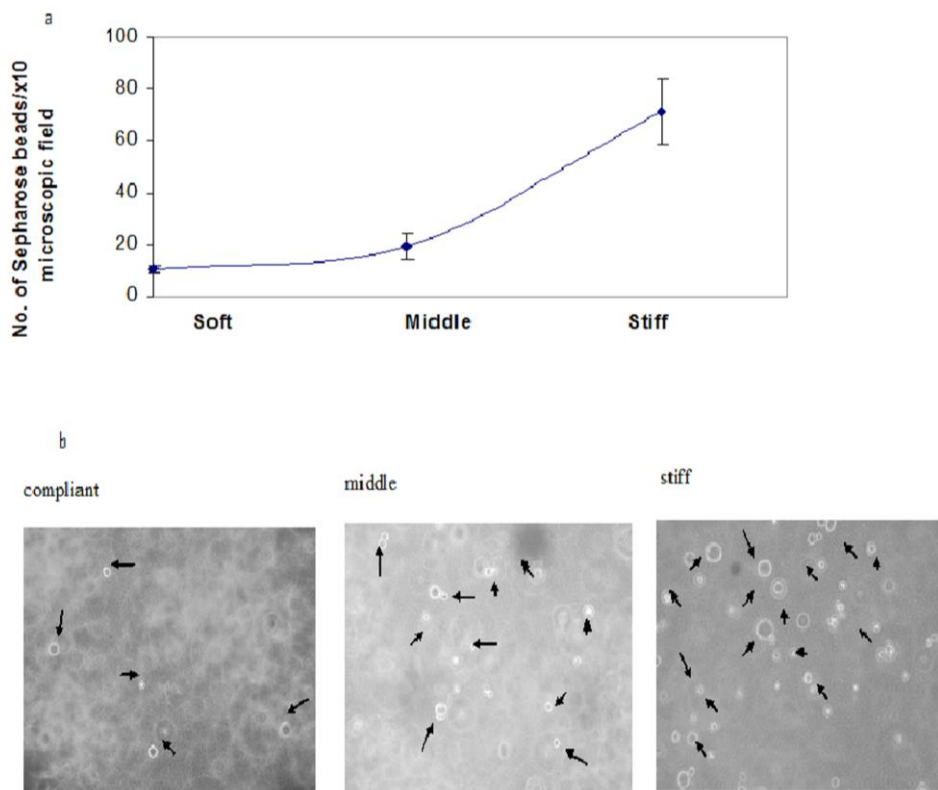


Fig. 2 Density gradient analysis. (a) Agarose marker beads in the soft, middle and stiff areas of the construct, as a measure of the density gradient. Readings are average

number of beads per x10 photographic field, 5 fields per area per construct, 3 constructs tested. (b) Phase contrast images (x10) of the soft, middle and stiff areas of the construct. Arrows show agarose beads.

Fibroblast guidance by durotaxis in 3D collagen matrices

To test the hypothesis that such 3D gradients could direct cell migration, cells were seeded in constructs with a stiffness gradient of 1057 ± 487 KPa to 2305 ± 693 KPa, from the soft to the stiff end respectively (over 40 mm length), and cultured over 3 and 6 days. Human dermal fibroblasts, treated with mitomycin C to block proliferation [265,266], were seeded at low density ($2\ 000$ cells/cm²) in wedge-shaped collagen constructs, using a 2 stage casting process (see methods), so that cell density was uniform along the gradient at the beginning of culture. Importantly, at this low seeding density, cell-cell contact was seen to be minimal. Average cell density was measured in the compliant, middle and stiff regions of the construct at 3 and 6 days of culture. Although there was a trend for preferential accumulation of cells towards the stiff region of the gradient at 3 days of culture, this only reached statistical significance after 6 days ($p < 0.05$) (Fig. 3a, b).

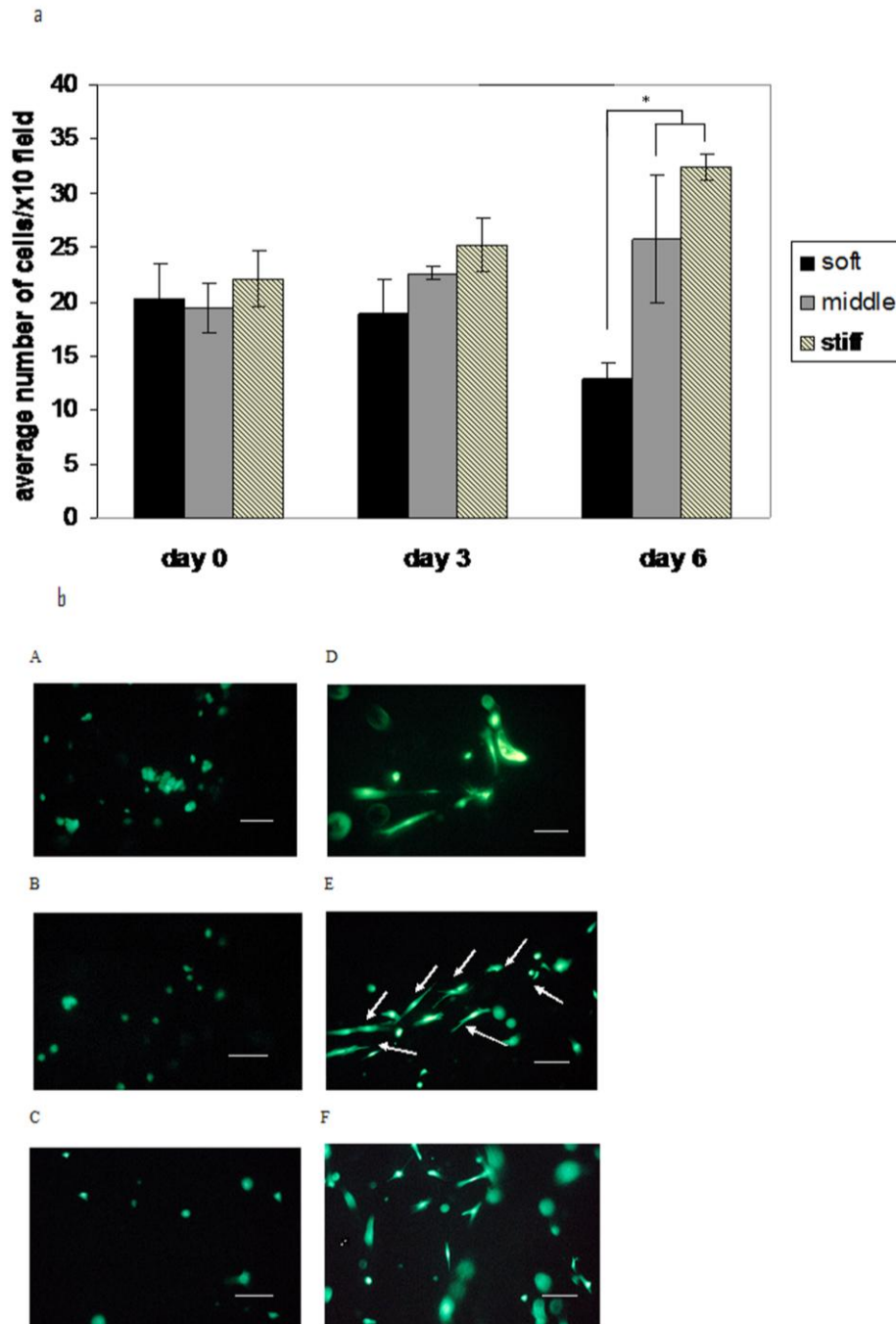


Fig. 3 Fibroblasts seeded in collagen matrices with a built-in stiffness gradient exhibit durotactic migration. (a) Measurements of the number of cells in the soft, middle and stiff regions of the construct at 0, 3 and 6 days of culture. Constructs were stained with calcein to visualise live cells. Readings are averages of 5 fields per region per construct with 3 constructs per time point ($*p < 0.05$). The average cell density within each construct did not significantly differ between day 0 and 3 or 6 days of culture ($p > 0.05$). (b) Fluorescence microscopy images (x10 field) at day 0 (A-C) and day 6 (D-F) of culture, at the soft (A, D), middle (B, E) and stiff regions of the construct (C, F).

Arrows in image E show bipolar, elongate fibroblasts migrating along the gradient axis, Bars=10 μ m.

This system produced a final difference in cell density along the gradient of 3 fold. This relatively slow rate of cell re-positioning is likely to be due to the high substrate density at the extreme which would retard cell locomotion. It is important to note that the increase in the average cell density in the stiff region was accompanied by a decrease in the compliant region, implying that cells migrated out of the soft and into the stiffer regions. Since the cells were growth-arrested, migration and not proliferation must have been responsible for this directional accumulation. Indeed, the average cell density within each construct did not significantly differ between day 0, 3 and 6 days of culture ($p>0.05$), confirming that the fall in cell density in the soft region was not a result of cell death.

6.2 DISCUSSION

***Original Hypothesis:** HDFs seeded within a 3D collagen matrix containing a stiffness gradient will preferentially migrate towards the stiff end of this gradient.*

In this study we successfully engineered a model of a continuous stiffness gradient within a three dimensional collagen scaffold. Previous studies of mechanotaxis have focused on culturing cells on two dimensional patterned substrates [68,125]. In addition to their obvious limitation as biomimetic models of cell function, the use of polyacrylamide as scaffold material is also poorly biomimetic. Here the choice of collagen, the most abundant protein component of the ECM, enabled the

development of a truly 3D, biomimetic environment in which the phenomenon of durotaxis could be tested.

In this model, casting preparation of the collagen gel scaffold is an one-step process, in contrast to that for synthetic polymer surfaces [68], with rapid fabrication of a density gradient. The density gradient nature of this model also has the advantage of exposing cells to a continuous stiffness gradient, in contrast to sharp boundaries of changing material stiffness as in previous studies [68]. This allows development of native-like durotactic gradients, which like chemical gradients, are characterised by long-range continuity[3].

It was possible to quantify this stiffness gradient by measuring the stiffness modulus in the compliant, middle and stiff regions of the construct. This gave a >2 fold increase in modulus for a 5 fold increase in collagen density. The range of matrix stiffness (1 to 2 MPa) tested here was in the native tissue range (e.g. skin, tendon). Varying the final construct thickness by adjusting the degree of compression can predictably change the magnitude of the collagen density gradient and thus the stiffness gradient. For example, matrix stiffness in the range of 20 to 50 KPa could be used to model granulation to scar tissue formation during wound healing [267]. In addition, the angle of inclination of the casting well will determine the rate of change of stiffness in the gradient. Indeed, the linearity or non-linearity of the gradient will be determined by the slope of the inclined surface of the gel (flat or curved). Furthermore, controlling the 3D spatial organisation of collagen sheets containing a stiffness gradient could provide a tool for engineering gradients with a specific spatial configuration within 3D scaffolds (e.g. longitudinal vs. radial gradients) (Fig.4). This could have important implications for precise guidance of cells within 3D tissue constructs. For example, constructs containing a longitudinal gradient

could be used to model axon guidance in a nerve conduit, while constructs containing radial gradients could be useful for modelling cell migration in vascular wall structures. In addition, bi-axial gradients could be applied to guide cells to a desired point within a 3D complex tissue. It is important to note that the high end of the stiffness range tested here was the same as that previously reported for plastically compressed cell-seeded collagen gels, with no significant cell damage [25]. Therefore, there is presently no reason to expect that cells in different parts of this gradient have been significantly (or differentially) affected by the initial compression. Indeed, previous studies have found preservation of cell viability even after double compression, which raises the matrix stiffness dramatically [268].

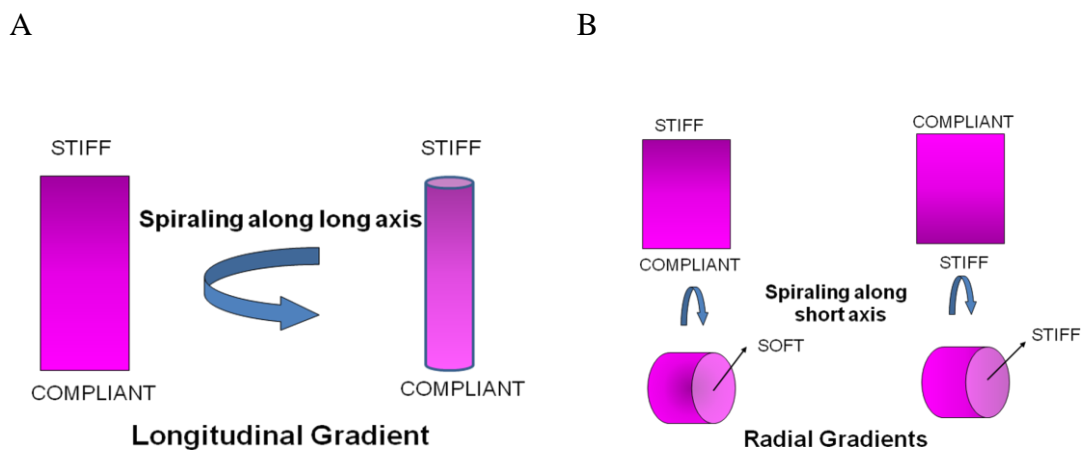
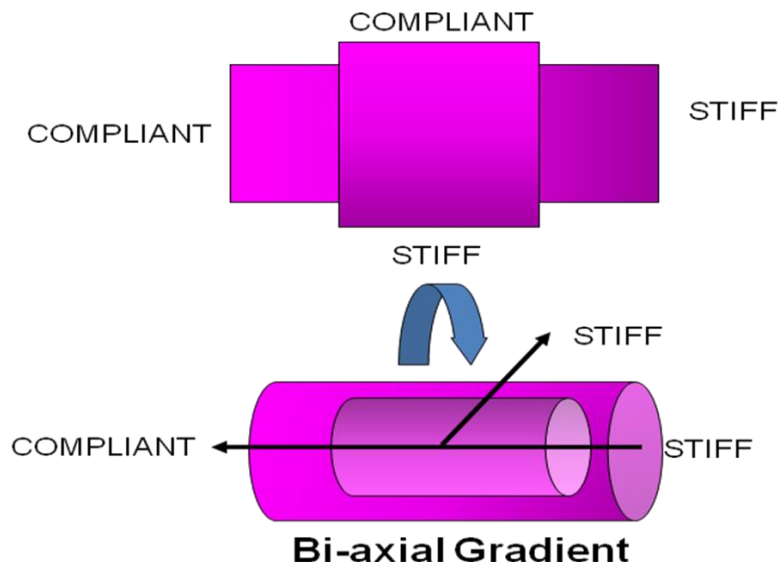


Fig.4 Schematic showing three possible 3D spatial arrangements of rectangular collagen sheets containing a stiffness gradient. A collagen sheet could be spiraled along its long axis (A) producing a longitudinal gradient or along its short axis (B) producing a radial gradient. In the latter, the direction of spiraling will determine the final direction of the gradient (i.e. stiff-to-compliant or compliant-to-stiff).

C



Layering two collagen sheets and spiraling along the longitudinal axis (C) would produce a construct with a bi-axial gradient. The order of layering and the direction of spiraling will determine the final direction of the bi-axial gradient.

We also demonstrated the preferential accumulation of cells towards the stiffer regions of the gradient. During cell seeding we employed a two step casting process, in order to produce a uniform cell density along the length of the construct. This allowed relative changes in cell density to be quantified. Had we seeded the whole wedge-shape construct with cells, a cell density gradient would have been formed from the start, as shown by the agarose bead experiment. The ability to observe mechanotaxis on a large population over a long period enables a statistical approach to studying the phenomenon in three dimensions and complements the cell by-cell, time-lapse observations that first reported durotaxis[145]. Early studies of durotaxis found that isolated cells were able to migrate only from compliant to stiff regions, but that cells with neighbours were able to migrate from stiff to compliant regions as

well[145]. This is not surprising as the measured migration is likely to be an average of movement events in all directions. The short time scale of these studies and the lack of population data did not enable the clarification of what the net effect would be on the whole population. Our findings are in agreement with that of a previous study that investigated the durotactic migration of larger cell populations in two dimensions [68], and show that over a sufficiently long time span, and averaged over many cells, a net migration into stiff regions occurs.

In this model the stiffness gradient corresponded to a collagen density gradient, from the compliant to the stiff end of the scaffold. This suggests that an integrin-binding ligand density gradient accompanied the formation of the rigidity gradient, leading to a concurrent gradient adhesiveness, which can also lead to a directed cell motility response (i.e., haptotaxis) [148,150]. This would imply that preferential accumulation of cells towards the stiff regions of the construct was not entirely caused by durotaxis. However, it has recently been suggested that, physiologically, matrix compliance and ligand density are not mutually exclusive, but highly coupled (orthogonal) variables that determine mean cell responses ranging from cell spreading to cell shape and molecular organization [269,270]. Sensing the stiffness of the substrate is associated with the binding of integrin receptors with ECM proteins that provide anchors to the cytoskeletal network via cytoplasmic scaffolding proteins [271]. Using the integrin-mediated mechanosensor, cells can probe the stiffness of the substrate to simply move or pull on their microenvironment. Indeed, it has been shown that smooth muscle cell spreading is driven by intracellular processes such as actin filament growth but modulated by external cues that include substrate stiffness as well as ligand density [272].

It has been shown that substrate stiffness can have profound effects on cell proliferation [125,154]. In Chapter 5 we showed that fibroblasts proliferated faster when seeded within stiffer 3D collagen gels [166]. In order to isolate the migratory response of cells, it was important to exclude these proliferative effects and this was done by treating cells with mitomycin C. Although trends were apparent at 3 days, accumulation of cells in stiff regions only became significant after 6 days of culture. This rate of migration seems to be comparable to the findings of a previous study where significant accumulation was observed after 5 days [68]. It is important, however, to note that in our model cells were seeded within a 3D matrix whereas in the previous study they were cultured on a 2D surface, and that matrix remodeling during cell locomotion in three dimensions has been shown to have a significant effect on the rate of migration [125]. In addition to matrix molecular composition and rigidity, the topography of a three-dimensional matrix affects the formation of cellular adhesions [269]. This is a key point, as physiologically, stromal cells must also migrate through the 3D ECM. Furthermore, the 3D matrix stiffness in this model was in the range of 1-2 MPa, compared to previously described 2D substrates, typically in the range of 1-40 KPa [68,125]. Increasing density/stiffness of the ECM (and with it durotactic migration) is accompanied, however, by greater 'matrix drag', as cells must penetrate more dense fibril networks with increasing overall cell adhesiveness and decreasing progression between fibrils. This dimension is key to physiological stromal cell migration as net progression is a balance of these two opposing factors, modified by the ability of the cell type in question to secrete matrix proteases, such as MMPs, and so degrade a pathway or modify a section of ECM. This is supported by the finding that a biphasic dependence of migration speed on ECM stiffness exists, with an optimal substrate stiffness capable of supporting

maximal migration[273]. As a result, the ability of cells to optimise migration rate, towards the ideal (durotaxis only) rate will depend on their ability to generate controlled, local proteolytic activity capable of reducing ‘matrix drag’ (Fig.5). Indeed, it has previously been shown that collagen matrix stiffness regulates MMP production by fibroblasts cultured within collagen constructs i.e. MMP secretion is mechanosensitive [165].

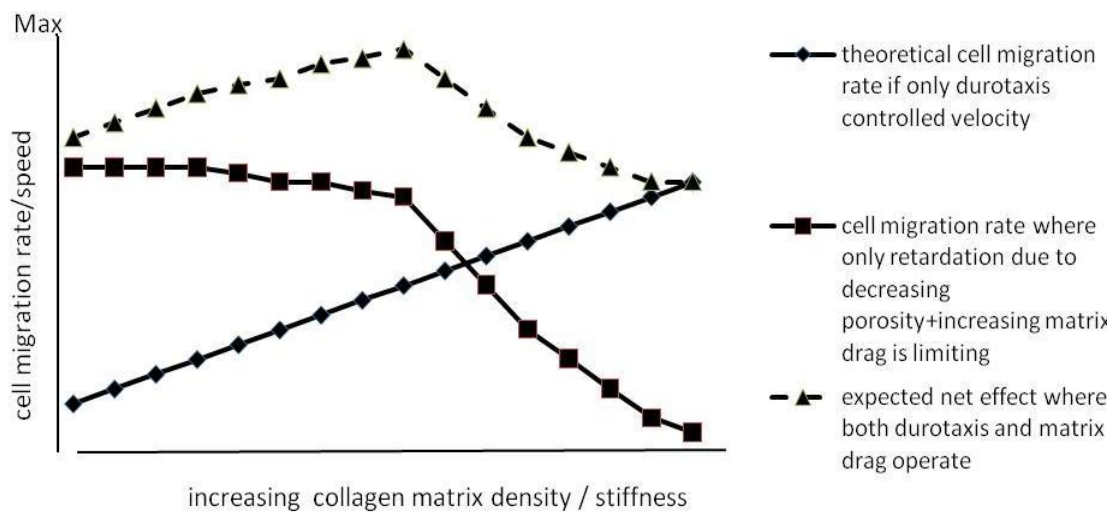


Fig. 5

Theoretical, predicted plot of the dual antagonistic effects of increasing matrix density on overall average cell speed. Increasing migration rate is predicted with increasing substrate stiffness (durotaxis) due to simple Newtonian mechanics and translation of cell force into motion. However in 3D, this must be balanced against the increase in ‘matrix drag’ as cells must penetrate more dense fibril networks with increasing overall cell adhesiveness and decreasing progression between fibrils. The net effect of these opposing factors (dashed line) is likely to give a maximal migration rate at an intermediate substrate density where ‘matrix drag’ is just becoming limiting. However , over longer periods (3-6 days) these cells would be expected to produce matrix degrading/modifying proteases, such as MMPs , capable of opening up pathways, so increasing cell motion above this relatively simple prediction.

The current model is based on progression through largely homogeneous, random (isotropic) collagen fibril meshes, as plastic compression of collagen hydrogels does not result in any significant fibril alignment [24]. However, these are almost never found in native ECMs, rather local or long-range fibre alignments produce matrix anisotropies[39]. The presence of fibril alignment on a directional stiffness/density gradient would be expected to generate the highest cell speeds (and so net migration velocities), parallel to fibril alignment or between fibril bundles where ‘matrix drag’ will be minimal and durotactic advantage maximal. Interestingly, this is consistent with common fibroblast behaviour to migrate between existing tissue planes. In this model it is possible that, after extended culture periods, such cell-mediated differential collagen matrix organization [25] could have a significant effect on the rate and direction of cell migration. Any such effect would be expected to gradually enhance the initial matrix gradient/anisotropy over extended periods (see Chapter 10).

Using this model, it will be possible to better understand factors governing the rate and direction of cell migration in tissues where spatio-temporal changes in ECM stiffness occur e.g. during embryonic development or wound healing and tissue repair[267]. The ability to guide cells in 3D using matrix stiffness gradients could also have important implications for engineering constructs with controlled tissue architecture and function. Matrix stiffness is indeed increasingly recognized as an important regulator of cell proliferation, adhesion and collagen deposition [125,166], cellular functions that are critical for biomimetic and functional tissue growth. As discussed above, the current model allows stiffness gradients of variable magnitude to be produced, matching the stiffness of the target tissue e.g. stiffer in bone tissue, elastic in cardiovascular or muscle tissue, and relatively softer in brain or skin tissue.

This model could thus be an important tool for designing and engineering tissue implants with a built-in ability to direct cell in growth, accumulation and transit.

6.3 CONCLUSIONS

We have developed a model of a 3D stiffness gradient within a collagen scaffold that will be valuable for investigation of cellular locomotion in 3D tissues where ECM stiffness is an important factor, such as embryogenesis, wound healing and tissue growth, remodeling or aging. Durotactic control of cell migration rate and direction may also be an important tool for engineering biomimetic structure and function into tissue implants or models for screening and research.

6.4 MATERIALS & METHODS

Fabrication of collagen constructs with graded stiffness

Collagen gels were prepared as previously described[25]. Collagen constructs with a gradient of biomaterial matrix stiffness were prepared by casting 7 ml of collagen solution in moulds (4x2.5x1.1cm), made from Derlin blocks (Intertech, UK), which were cast at an incline of 15° (Fig 6a). Collagen gels were incubated at 37°C in a 5% CO₂ humidified incubator for 20 min. After setting, the resulting wedge-shaped collagen constructs were compressed vertically by a horizontal/level plate, moved by a computer controlled motor (Dartec, UK) to produce sheets of 0.1mm uniform thickness (Fig 6b). This compressing stage used the same method as described for plastic compression fabrication of collagen-cell constructs [25]. It is important to

note that values of final collagen density were calculated based on the final construct thickness, in this case 100 μ m, as shown in Figure 7.

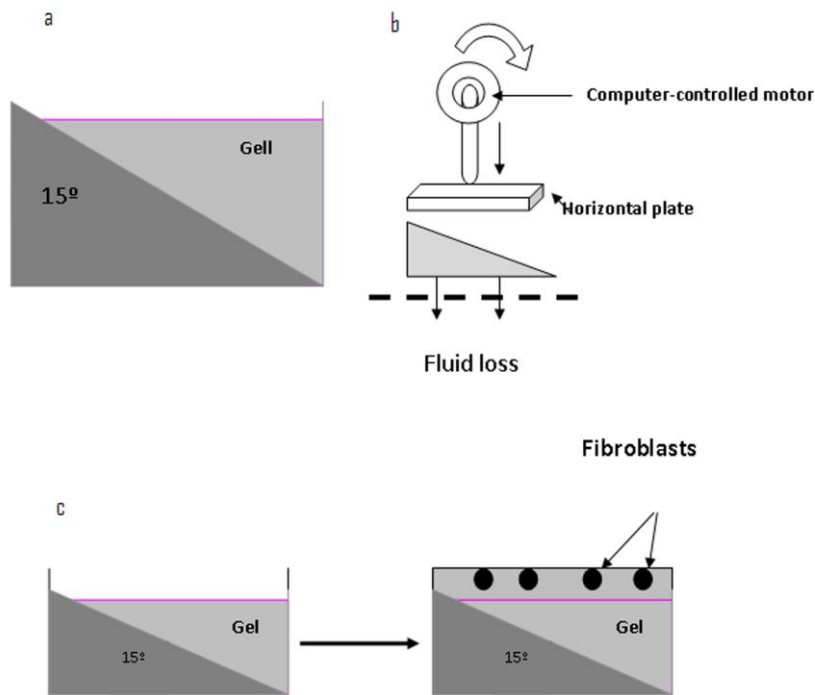
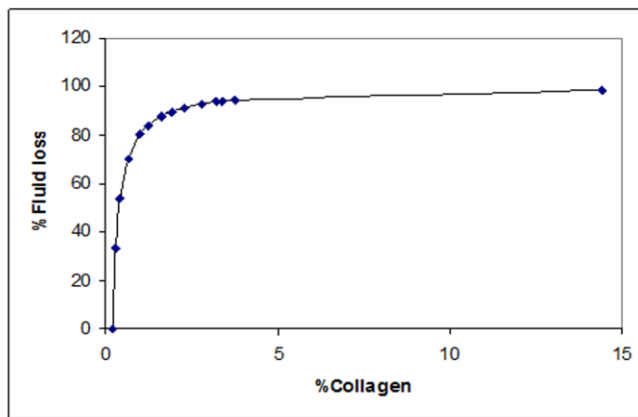
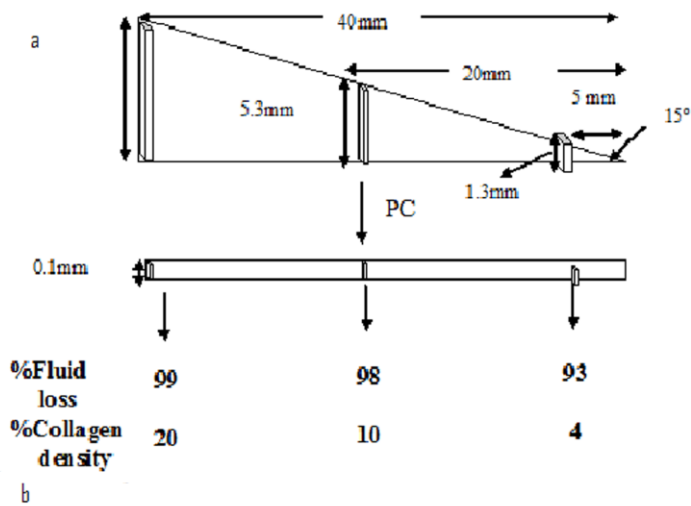


Fig. 6

Fabrication of collagen constructs with a gradient of biomaterial matrix stiffness. Collagen solution (light grey area) was cast in moulds (dark grey area) set at an incline of 15°, resulting in formation of wedge-shaped collagen constructs (a). After setting, the wedge-shaped collagen constructs were compressed vertically by a horizontal/level plate, moved by a computer-controlled motor, to produce sheets of 0.1mm uniform thickness (b). Cell-seeded constructs were fabricated by first pouring 5 ml of acellular collagen solution and after 1 min casting a second layer of cell-containing collagen solution (2ml). This ensured even distribution of cells, resulting in a uniform cell density along the construct after compression (c).



c

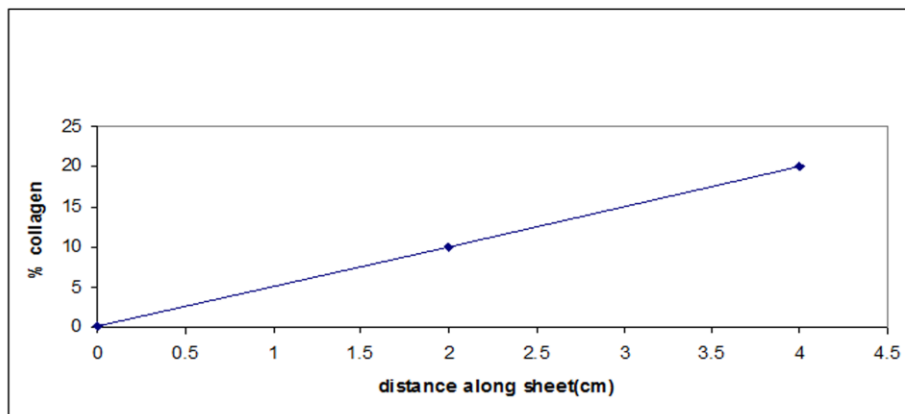


Fig. 7 (a) Schematic showing how the % fluid loss and % collagen density at the two ends and middle region of a construct can be calculated. Angle of inclination of the mould used to set the collagen gel was 15°. Compression was to a controlled final thickness of 0.1mm. **(b)** Plot of % fluid loss against % collagen density during compression of a collagen gel with initial collagen density of 2mg/ml (0.2%). Note that this is a mathematical calculation (i.e. collagen density is calculated based on wet gel

weight). (c) Plot showing how % collagen density varies with distance along a collagen sheet compressed to 0.1mm.

Measurement of collagen matrix Young's modulus

Compressed collagen constructs with a gradient of collagen density were divided equally into three regions, from less to more dense zones. Dynamic mechanical analysis (Perkin Elmer, UK) was carried out on 1 mm wide strips obtained from each region to measure the elastic modulus and thus the rigidity gradient that formed from the compliant to the stiff end of the construct [25]. Strips were uniaxially deformed along their longest axis with the amount of tension required to produce a 5–30% strain. Samples were perfused with PBS between measurements. The stress–strain relationships were linear for the tested samples. Young's modulus was calculated using the formula: $E = (F/A) \times (L/\Delta L)$, where A =unstressed cross sectional area, F =force, L = unstressed length, and ΔL =change in length. The values reported are the averages of at least three samples from each region.

Quantification of density gradient

As a measure of the density gradient resulting after compression, collagen gels were seeded with agarose marker beads (Sigma, UK) (0.15 ml of 0.2g/ml stock solution) before setting. After compression, each construct was divided in 3 equal areas, corresponding to the soft, middle and stiff parts of the gradient. The number of beads per x10 photographic field was manually counted in each of the three areas, using a phase contrast microscope. Averages based on five fields per area, per construct. Three constructs were analysed.

Cell-seeded constructs to test migration

HDF-seeded collagen constructs were prepared by first casting 5 ml of acellular collagen solution and after 1 min, before the collagen had fully set, casting a second layer of collagen solution (2ml) containing a total of 20, 000 fibroblasts (Fig 6c). The short duration between casting the first 5 ml and final cell-seeded 2ml of collagen solution ensured adequate integration across the interface of the two layers [274] so that after setting, a single collagen construct was obtained with no obvious line of separation. This method resulted in collagen constructs having a uniform fibroblast density (2000 cells/cm²) after compression. Seeding the whole collagen construct with cells was avoided, since this also generated a cell density gradient, due to accumulation of cells towards the thick end of the wedge. After casting, wedge-shaped cell-seeded constructs were compressed to produce sheets of (0.1mm) uniform thickness, as described above. Cells were growth arrested by 10 µg/mL of mitomycin C (Sigma, UK), which was left in the culture media for 2 h after cell seeding and removed by three washes of PBS. Collagen constructs were cultured at 37°C for up to 6 days, with replacement of culture media(5ml) every second day.

Quantification of cell accumulation

Collagen constructs were taken out of culture after 0, 3 and 6 days of culture and incubated for 1hr in phosphate-buffered saline (PBS) plus 5 µM calcein AM (Molecular Probes, Invitrogen) at 37°C. Samples were subsequently washed in PBS and viewed with a fluorescence microscope. Cells were counted manually. Each construct was divided into 3 equal regions (stiff, middle, soft) and cell density within each region was calculated as the average number of cells per x10 photographic field. Since cells had moved across a 3D space within the construct, the plane of

focus was manually set and kept constant during counting. Reported values are averages of 5 fields per region per construct with 3 constructs per time point.

CHAPTER 7

LAYERED COLLAGEN SCAFFOLDS WITH DEFINED MATRIX STIFFNESS: REGULATION OF CELL-MEDIATED INTERFACE INTEGRATION

In Chapter 3 we showed how Plastic Compression fabrication can be employed to rapidly engineer biomimetic collagen sheets with precise control of matrix collagen density and mesoscale structure. However, utilisation of compressed collagen sheets as bio-functional units (i.e. basic building blocks) for complex tissue reconstruction critically relies on the ability to assemble them in 3D (e.g. by layering). Indeed, optimal integration of construct components is a primary prerequisite for successful application of this and other types of sheet-based engineering (e.g. cell-sheet engineering[86]) in development of biomimetic (e.g. heterogeneous/complex) tissue constructs. As we have shown in the last two chapters, an important regulator of the cellular responses (migration, proliferation, collagen deposition) mediating interface integration is matrix stiffness. The aim of this study was to develop a sheet-based 3D model that would allow control of interface matrix stiffness, in order to investigate its effect on cell-mediated interface integration of sheet-based collagen constructs. A previous study by this group focused on engineering a collagen-based 3D interface model for assessing cell-dependent mechanical integration of tissue surfaces [158]. This construct, consisting of a fibroblast-seeded pre-contracted collagen gel embedded within a cell-free collagen hydrogel lattice, enabled solid interface formation *in vitro* with a well-defined geometry and the possibility of measuring mechanical linkage. In this study we have adapted this model by layering compliant collagen hydrogels, seeded with human dermal fibroblasts (HDFs), and then compressing them to obtain layered collagen sheets. We tested the hypothesis that

such bilayer-sheet scaffolds can undergo cell-mediated enhancement of interface integration. We also investigated the role of matrix stiffness in cell-mediated interface integration by measuring the interface adhesive strength of constructs compressed at the beginning (compressed culture; high stiffness) or the end (compliant-compressed culture; low stiffness) of the culture period. As a measurable outcome of cellular responses to varying matrix stiffness, interface integration was quantitatively correlated to cell migration across high and low stiffness interfaces.

7.1 RESULTS

The interface model used in this study, comprising two layered collagen hydrogels that were compressed to produce bilayer collagen-sheet scaffolds (see Methods), was effective in forming reliable and reproducible interfaces with known dimensions (bilayer construct thickness $\sim 200 \mu\text{m}$). Under these conditions, the pull-out force was proportional to the contact surface area, which was measurable (2cm^2) and reproducible between experiments. The interface adhesive strength was assessed by placing the bilayer construct on the t-CFM and pulling at a constant rate to give displacement and eventual fracture of the interface (see Methods).

Finite Element Analysis of interface stresses

In order to analyse the distribution of predicted stresses, acting on the interface during mechanical loading, we constructed an FE model of the interface system. The highest stresses were predicted in the xy plane perpendicular to the interface, parallel to the direction of loading (Fig.1a). Figure 1b shows that the predicted stress acting in the xy plane rises sharply at the interface, with higher stresses at the top part of the interface than in the middle, indicating that failure of the interface would start in this

region. A rise of normal stress at the interface was also observed in a collagen-based hydrogel interface construct, previously described by this group [158]. Debonding at any one point of the region of highest stress (top region) would lead to an increase in the stress throughout the remaining intact interface and rapid failure.

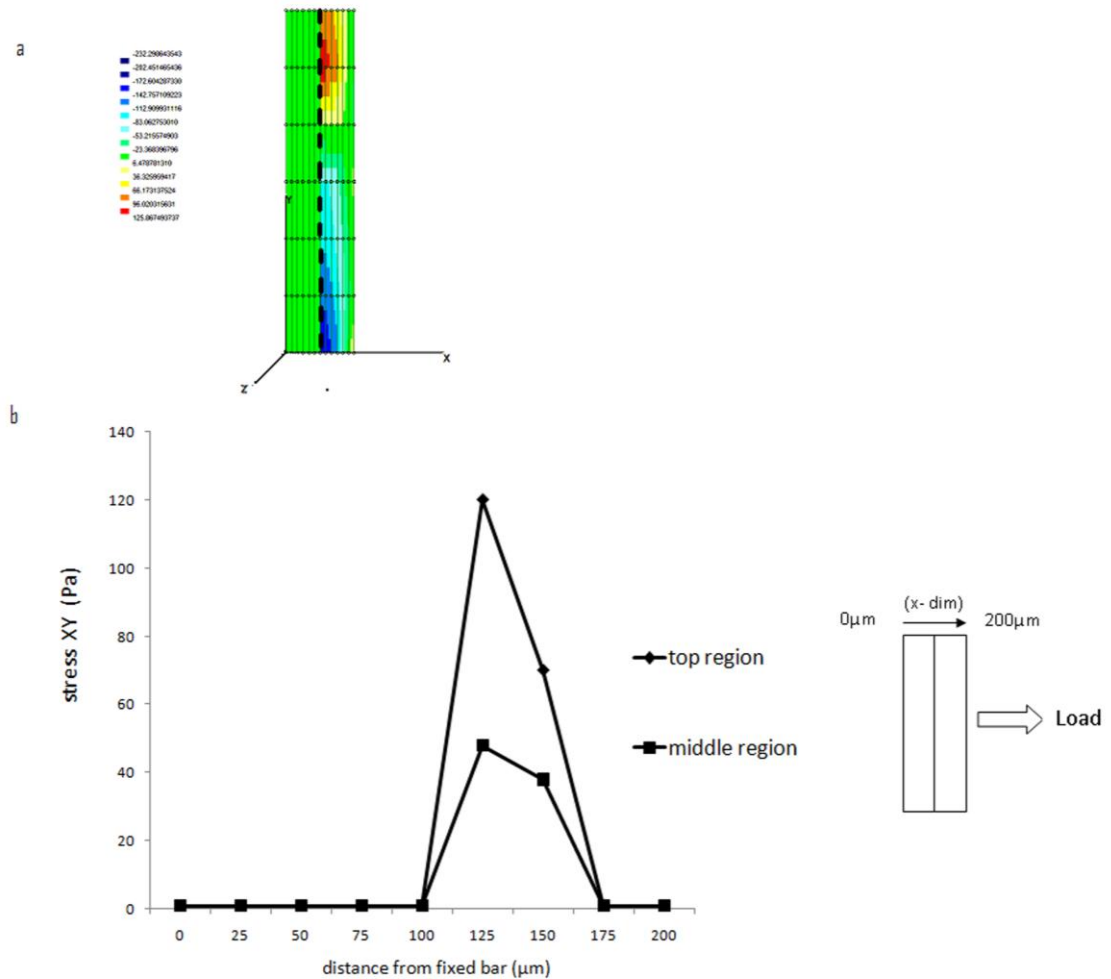


Fig. 1

Analysis of interface stresses by Finite Element Analysis. (a) Computer illustration of the finite element model of the interface construct (cross-sectional view) and the stress distribution predicted in the xy plane parallel to the direction of loading, as the interface was pulled apart. Dashed line represents the interface between the two layers. The scale of the coloured bar indicates the magnitude of the stresses (dark blue lowest, red highest). (b) Graph showing the predicted stress in the xy plane, in the top and middle regions of the construct, from the fixed bar to the distal end. The interface was at 100 μm distance (each layer was 100 μm thick). Insert schematic shows the cross-sectional view of the construct.

Interface integration of acellular vs. cellular matrices

In order to establish a baseline of interface adhesive strength, we characterized the integration of acellular bilayer constructs by varying the casting period (i.e. the time period the bottom gel was allowed to set before casting the top gel) from 5 to 2.5 min. Importantly, the bottom gel was observed to set (i.e. it was not in a liquid state) within the shortest (2.5 min) casting period tested. Upon mechanical testing, the interface was characterized by a clear maximum force required for fracture, followed by rapid failure (Fig.2a). This was in agreement with the FE model's prediction. The results showed that there was a more than 2 fold increase in peak force from 3.2 ± 1 to 8.6 ± 0.5 mN before interface fracture when the casting period was reduced from 5 to 2.5 min respectively ($p < 0.05$) (Fig.2a), indicating that a near inverse-linear relation exists between casting period and interface adhesive strength. The time required for interface fracture was also increased by more than 2 fold when the casting period was reduced to 2.5 min, implying that a greater number of bonds had formed between the two layers, in addition to individual bonds being stronger. These results indicate that the casting period, which determines the degree of gel stabilization during setting, is a critical factor controlling the integration of acellular collagen hydrogels.

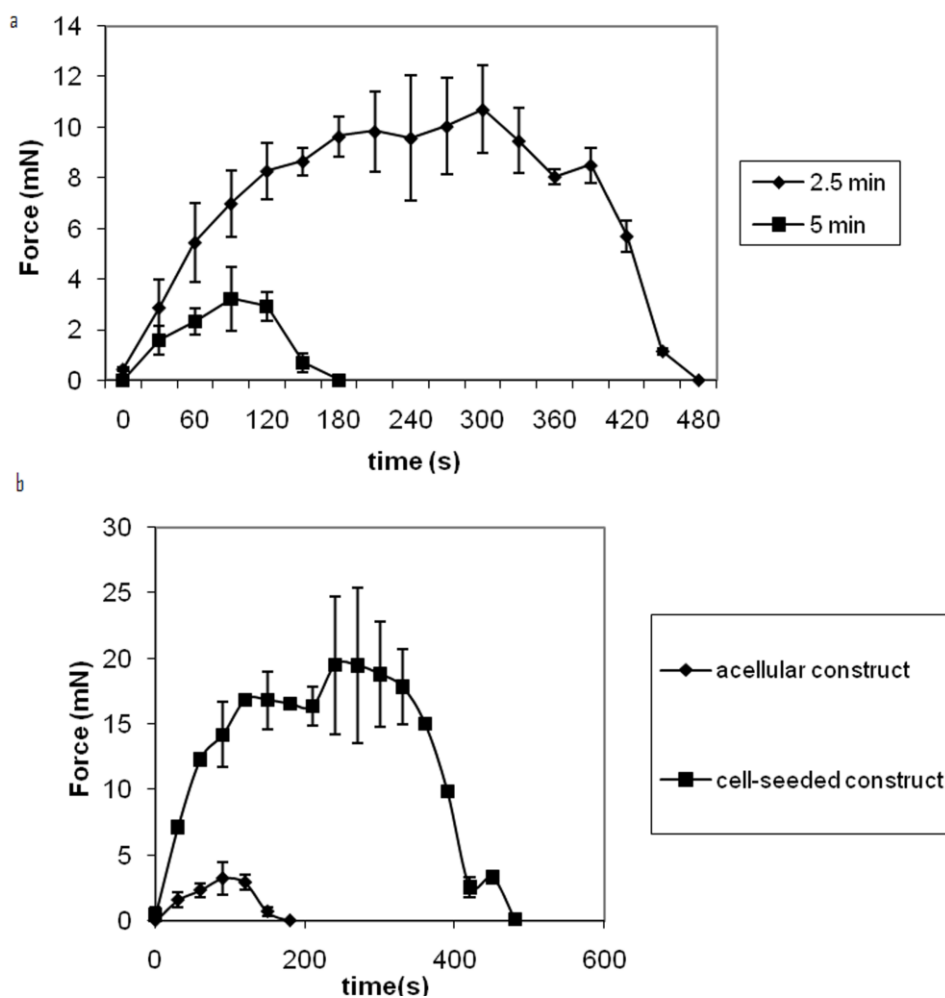


Fig. 2
Interface intergration of acellular and cell-seeded bi-layer collagen constructs. Plot of force developed during interface mechanical testing versus time, for (a) acellular constructs with a casting period of 2.5 or 5 min and (b) cell-seeded (compressed at day 0) versus acellular constructs with a casting period of 5 min after 1 week culture.

Cell-seeded constructs were cultured for 1 week, as our previously established model showed significant enhancement of interface integration after 1 week of culture [158]. Cell-seeded constructs with a 5 min casting period were used for assessing cell-mediated effects on interface integration, as these had the lowest baseline (without cells) adhesive strength (Fig. 2a). It is important to note that the baseline adhesive strength of acellular constructs was unaltered by prolonged culture (up to 7

days, data not shown), indicating that the collagen-collagen interaction alone did not play a significant role in any enhancement of interface integration with culture time. This was in agreement with data obtained from our previous model [158]. Figure 2b shows that cell-seeded constructs (compressed at day 0), cultured for 1 week, showed a more than six-fold increase in peak force before interface fracture (20 ± 5 mN) compared to acellular constructs (3 ± 1 mN). This was statistically significant ($p < 0.05$). The time required for interface fracture was also increased by 3 fold for cell-seeded constructs.

Effect of matrix stiffness on cell-mediated interface integration

Once it was established that this bilayer collagen model could undergo cell-mediated enhancement of interface integration, we investigated the effect of matrix stiffness on interface adhesive strength, by comparing the integration of constructs compressed at the beginning (compressed culture; stiff) or the end (compliant-compressed culture; compliant) of the 7 day culture period. As a means of controlling matrix stiffness, fluid was removed from constructs using plastic compression to increase collagen density and thus matrix stiffness (see Chapter 5). Compression typically resulted in an increase in collagen density from 0.2% (collagen hydrogels) to ~15% (collagen sheets), relating to ~99% fluid removal [25]. Matrix stiffness, previously quantified using dynamic mechanical analysis, was $42.2 \text{ kPa} \pm 22$ and $2240 \text{ kPa} \pm 846$ for compliant and stiff matrices, respectively [166]. We observed an increase in maximum interface adhesive strength from 16 ± 6 Pa for acellular constructs to 95 ± 26 Pa for stiff constructs (compressed cultures) and 129 ± 38 Pa for compliant constructs (compliant-compressed cultures) (Fig 3). While there was a trend for compliant matrices to show greater strengthening of the

interface compared to stiff matrices, this difference was not statistically significant ($p>0.05$). This suggests that within 1 week cells were capable of forming bonds of comparable strength between both stiff and compliant matrices.

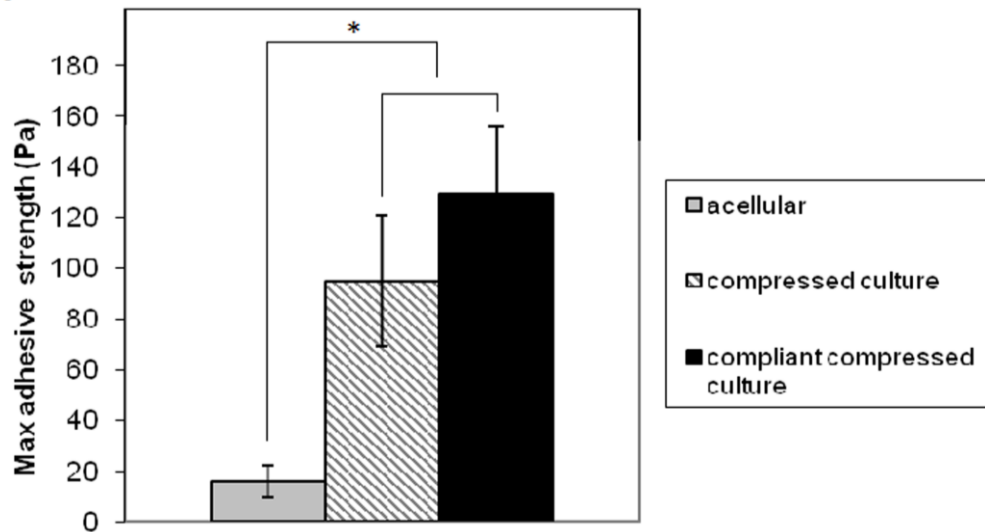


Fig.3 Comparison of cell-mediated interface integration of stiff vs. compliant bi-layer matrices. Histogram comparing the adhesive strength of acellular constructs with that of compressed (high stiffness) and compliant-compressed (low stiffness) 1 week cultures, $*p<0.05$. The peak force before failure was used to determine interface adhesive strength.

Dependence of cell-mediated interface integration on cell migration

Previous studies have showed that cell-mediated interface integration is dependent on cell migration across adjacent surfaces [158,160]. We thus quantified cell migration across the interface using a modification of the ‘nested collagen matrix’ model developed by Grinnell et al, where cells migrate out of a cell-seeded matrix into an acellular matrix [143] (see methods), and correlated this to interfacial matrix stiffness. Figure 4 shows that within 24hrs of culture, cells had migrated out of low stiffness (uncompressed) matrices, while minimal migration was observed out of stiff (compressed) matrices ($p<0.05$). In such stiff matrices cells were seen to align

along the boundary between inner and outer gel and maintain a longitudinal morphology (Fig 4b). However, after 7 days of culture there was no significant difference between the number of cells that had migrated out of stiff or compliant matrices (Fig.4a). Given that cell migration plays a critical role in the integration process, this finding seems to be supportive of our data showing that stiff (compressed) and compliant (compliant-compressed) cultures had similar interface adhesive strengths after 1 week.

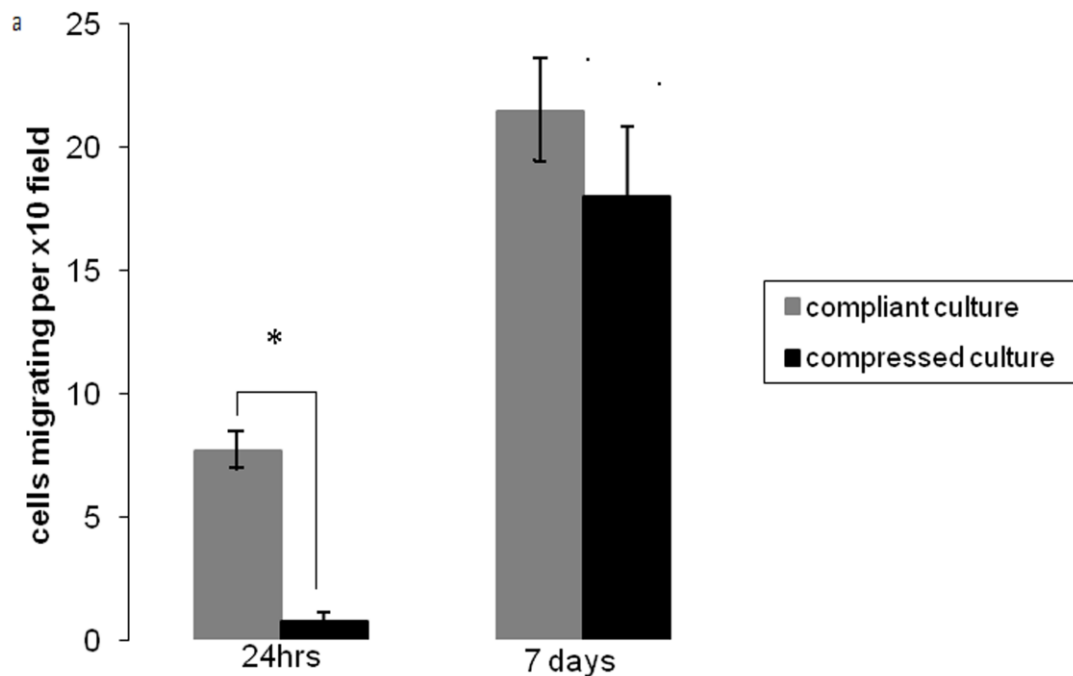
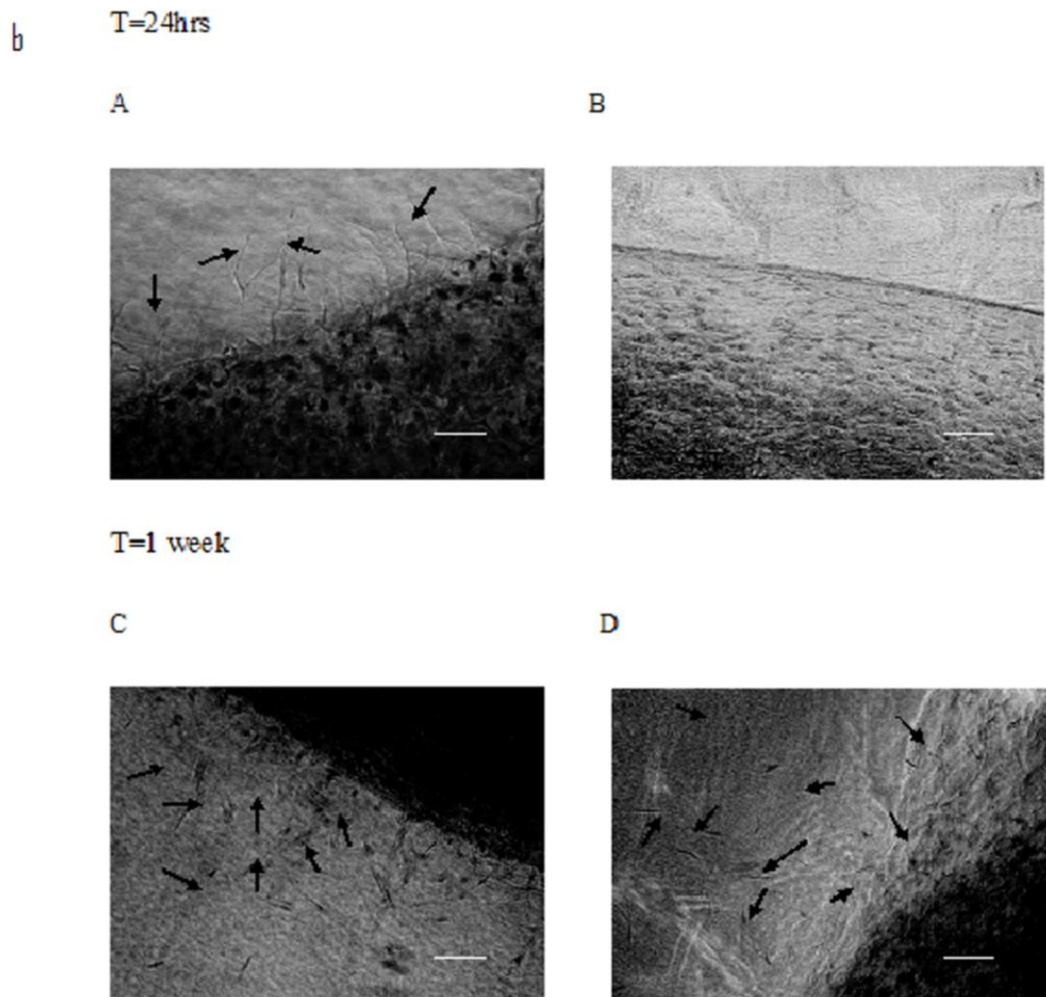


Fig.4
Comparison of cell migration across the interface in compliant and stiff collagen matrices. (a) Histogram showing the number of cells migrating out of cell-seeded matrices per x10 photographic field, for compliant (uncompressed) and compressed (high stiffness) cultures at 24hrs or 1 week, *p<0.05.



(b) Phase-contrast micrographs of the interface between cell-seeded and acellular matrix showing cells (arrowed) migrating across the interface in compliant (A, C) or compressed (B, D) cultures at 24hrs and 1 week. Bars=10 μ m.

Interface structural analysis

Visualization of the interface of acellular constructs, using SEM, showed that there was a well defined fusion line at the interface of the two collagen layers, after compression (fig 5). This was also observed in stiff (compressed culture) constructs cultured for 1 week, but was absent from 1 week compliant (compliant-compressed) constructs, indicating that fibroblasts cultured in compliant matrices had managed to

fuse the two collagen layers. Fusion of the two layers could imply a greater degree of interface integration in compliant constructs which, while not significant, could be measured after 1 week (Fig.3).

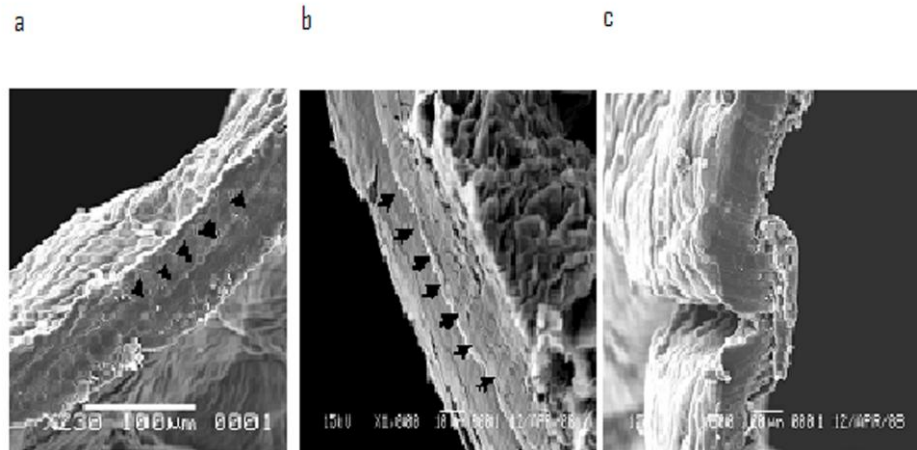


Fig.5

Interface structural analysis for acellular, stiff and compliant cell-seeded bi-layer constructs. SEM images of transverse cross sections of the interface for acellular bilayer constructs (a), compressed (high stiffness) 1 week cultures (b) and compliant-compressed (low stiffness) 1 week cultures (c). Arrows show fusion line at the interface.

7.2 DISCUSSION

Original Hypothesis: Layered collagen matrices can undergo cell-mediated integration, while interface adhesive strength will depend on matrix stiffness at the interface.

This study investigated the interface integration of layered collagen-sheet scaffolds. We previously showed that plastic compression of collagen hydrogels (~0.2% collagen w/w) produces dense (up to 15-20% collagen w/w), mechanically strong (stiffness modulus ~2240 KPa) collagen sheets (~100µm thick) that can support a

high cell viability [25]. Plastic compression of collagen constructs results in irreversible water loss from the matrix, however, as we discussed in Chapter 6 the fluid loss vs. collagen density curve is not linear. For example, while 50% fluid loss roughly doubles the collagen density, removing 99% of the gel's fluid results in a ~75 fold increase in collagen density. This enables rapid, as well as predictable, control of the gel (average) collagen density and matrix stiffness. Here we show that the interface between such layered collagen sheets with defined matrix stiffness can undergo cell-mediated integration.

The simple geometry of this model enabled the application of the FE method to predict and locate the maximal stresses along the interface during mechanical loading. The ability to precisely predict stress distribution within a heterogeneous construct, and thus the regions where failure of the interface is likely to occur, would be invaluable when engineering multilayer structures (e.g. blood vessels [95]) or where material properties vary from one layer to the next e.g. hybrid constructs of two biomaterials [275].

This model allowed reproducible quantification of the mechanical strength of the interface. The baseline adhesive strength could be modified by changing the total contact surface area (data not shown) and the casting period. We found that there was a near inverse-linear relation between interface integration strength and casting period, indicating that bond strength/number of bonds between two adjacent collagen gels is reduced with increasing gel stabilization during setting. However, increasing the casting period beyond 5 min did not significantly alter (reduce) adhesive strength (data not shown). This suggests that there is a threshold in the degree of stabilization

of the bottom gel, above which interface integration is not time dependent. An important feature that might relate to this threshold behaviour was the formation of a 'skin-like' layer on the surface of the bottom gel, within 5 min of setting [44], which coincided with the lowest level of adhesive strength. This 'skin-like' layer occurring at the gel-air casting interface represents a thin but ordered (packed fibrillar) structure at the gel's surface that is different from the homogeneous, random fibril centre of the gel [44].

Culturing cell-seeded bilayer constructs for 1 week resulted in increased interface integration compared to acellular constructs. Such cell-mediated enhancement of interface integration has been previously reported by this group, using a hydrogel-based interface construct [158]. Interestingly, we found no significant difference in interface adhesive strength between stiff (compressed) and compliant (compliant-compressed) constructs after 1 week. This suggests that cells are equally capable of forming functional bonds between stiff, as well as between compliant matrices. Indeed, compressed collagen scaffolds have been shown to undergo functional cellular remodelling (and change in material properties) *in vitro* [25], as previously reported for compliant collagen hydrogels [126]. This could have important implications for engineering heterogeneous constructs that require a greater initial matrix stiffness and mechanical strength [276]. On the other hand, this finding could perhaps explain why engineered tissues based on cell-sheets, that contain relatively little ECM, and are thus compliant, can rapidly integrate with host tissues [86]. However, the above findings do not exclude the possibility that matrix stiffness could be a critical determinant of the strength of mechanical linkages formed at an interface, over longer culture periods.

It has previously been shown that cell migration across an interface is partly responsible for cell-mediated integration of adjacent surfaces [158,160]. A possible mechanism by which single cells could build up collagen bridges while migrating could depend on their ability to drag and bend collagen fibres during locomotion within 3D collagen matrices [277]. We found that while a greater number of cells had migrated across the interface in compliant matrices compared to stiff matrices at 24hrs, no significant difference was observed after 1 week of culture. This lag phase exhibited by fibroblasts cultured within stiff matrices is likely to be due to lower initial migratory speeds, as cells migrated through a denser ECM. Previous studies have indeed shown that when fibroblasts were cultured on substrates of increasing stiffness, migration speed decreased noticeably with increasing substrate mechanics [125]. However, within a 3D ECM cells can optimise their migration rate, a process that depends on their ability to generate controlled, local proteolytic activity (e.g. MMPs) capable of reducing matrix resistance/drag. Indeed, increasing matrix stiffness has been shown to upregulate MMP expression by HDFs [140,165]. While cell migration speed within stiff matrices would be expected to increase with time, the opposite would occur for cells migrating through compliant matrices, as cell-mediated matrix contraction would gradually result in increased matrix density (and stiffness), thus slowing down cell locomotion. This would imply that at some point in time the two migration rates would become comparable. We did observe similar rates of cell migration between stiff and compliant matrices after 1 week. This could, at least partly, explain the lack of any significant difference in interface adhesive strength between stiff (compressed) and compliant (compliant-compressed) cultures. The above findings also suggest that regulation of matrix density/stiffness could

enable the formation of selectively permeable migration barriers to cells within interfaced (e.g. layered) 3D ECMs, to provide spatial cues that can influence cell behaviour [278].

Collagen deposition has also been implicated in the mechanical integration of tissue surfaces cultured in partial apposition [91]. In fact, it has been suggested that pre-existing collagen at an interface is responsible for the assembly of new collagen fibres at the boundary [279]. Importantly, collagen gene expression and collagen synthesis have been shown to depend on matrix stiffness [165], implying that the two culture conditions examined with this model (compressed versus compliant-compressed) could have differed with respect to the amount of collagen deposited at the interface. While such differences might be difficult to quantify in the short term, by assessing interface adhesive strength, they could potentially have a significant effect on the degree of interface integration over longer culture periods. The ability to quantitatively correlate matrix stiffness with the extent of interface integration could have important implications for modelling the behaviour of heterogeneous constructs cultured in loading bioreactors, where mechanical stimulation of cells to improve ECM (mainly collagen) synthesis is inevitably accompanied by an increase in matrix stiffness [280]. Indeed, a study by Hoerstrup et al showed that tubular copolymer constructs exposed to shear and cyclic distension achieved higher burst pressures after 4 weeks in culture and that increased integration of construct components was accompanied by a significant increase in collagen deposition [281]. Furthermore, the biodegradable behaviour of collagen scaffolds and their ability to undergo functional (and quantifiable) cellular remodelling makes the current model a useful tool for modelling host integration of tissue-engineered constructs *in vivo*. For

example, a previous study by this group showed that when plastic compressed cellular and acellular constructs were implanted *in vivo* in a lapine model, cell-seeded constructs underwent remodelling up to 5 weeks and had a higher matrix stiffness compared to acellular constructs, implying that cell seeding contributed to this process post-implantation[54].

Visualization of the interface showed that cells cultured within compliant matrices had managed to completely fuse the two collagen layers, while cells cultured within stiff matrices had failed to do so, after 1 week. While it has been shown that fibroblasts cultured within compliant collagen matrices contract and remodel the matrix within 24hrs [126], stiff matrices undergo a much lesser degree of remodelling. Indeed, increased matrix stiffness has previously been shown to reduce generation of quantifiable cellular force (by HDFs) over 24 hrs and delayed the onset of matrix contraction [165]. Cell-mediated matrix contraction in compliant matrices presumably played a role in increasing the displacement of fluid (water) from one collagen layer to the other. This movement, in turn, probably dragged collagen fibrils across the interface, resulting in fusion of the two layers [158]. Translation of such micro-structural differences between the interface of compliant and stiff matrices into measurable differences in adhesive strength may, however, require longer periods of culture. Nevertheless, the ability to control cellular force generation, by regulating matrix stiffness, could provide an additional tool for forming stable interfaces between hydrogel matrices, against cell contraction [282].

7.3 CONCLUSIONS

We have successfully engineered a sheet-based 3D model of interface integration based on layered, biomimetic collagen-sheet scaffolds and showed that such constructs are able to undergo cell-mediated enhancement of interface integration. The ability to regulate cellular behaviour (proliferation, migration and collagen deposition) at an interface, by controlling matrix stiffness, could provide an important tool for modelling the integration of sheet-based (cell-sheets, biomaterial sheets or hybrids) constructs *in vitro* or *in vivo*. This could have important implications for the design of sheet-based bioengineered tissues and their application to complex tissue reconstruction.

7.4. MATERIALS & METHODS

Bilayer collagen scaffold development

Cell-seeded collagen gels were prepared as previously described [210]. The collagen gel or collagen-cell suspension (containing 5×10^5 human dermal fibroblasts) was then poured into a rectangular mould (size: 4×3×1 cm) made from Derlin blocks (Intertech, UK) and incubated at 37°C in a 5% CO₂ humidified incubator for either 2.5 min (acellular gels) or 5 min (acellular and cell-seeded gels). At the end of the incubation period, the gel was removed from the incubator and two spacers (1×3cm) were placed on its top surface, at each end. A second acellular gel or collagen-cell suspension containing 5×10^5 fibroblasts, was then poured on top of the first gel (Fig. 6a). The bilayer collagen gel was incubated at 37°C in a 5% CO₂ humidified incubator for 30 min.

Interface models

Acellular bilayer collagen constructs

Following setting and incubation, bilayer collagen gels were compacted by plastic compression for 5 min (Fig. 6a), using a combination of compression and blotting, to remove ~99% of the fluid (water) [25]. This led to formation of a flat, dehydrated bilayer collagen sheet (200 μm thick) protected between two nylon meshes. Compressed matrices were peeled off the nylon meshes and underwent mechanical testing. Note that plastic compression typically results in an increase in collagen density from 0.2% (collagen hydrogels) to ~15% (collagen sheets) [25].

Compressed matrix culture (high stiffness)

Following setting and incubation, bilayer cell-seeded gels were compacted at day 0 by a combination of compression and blotting, as described above (plastic compression of cell-seeded collagen gels has previously been shown not to reduce cell viability [25]). Compressed matrices were peeled off the nylon meshes and placed in culture wells containing 5 ml complete culture medium and cultured for 7 days (Fig.6a). At the end of the culture period matrices underwent mechanical testing.

Compliant-compressed matrix culture (low stiffness)

Following setting and incubation, uncompressed bilayer cell-seeded gels were placed in culture wells containing 5 ml complete culture medium and cultured free-floating for 7 days. While the gels underwent some isometric (vertical) compaction (~30%, data not shown) over 1 week, the spacers placed between the two collagen layers prevented any significant cell-mediated contraction (data not shown). On day 7

matrices were taken out of culture and were compacted by a combination of compression and blotting as described above (Fig.6a). Compressed matrices were peeled off the nylon meshes and underwent mechanical testing.

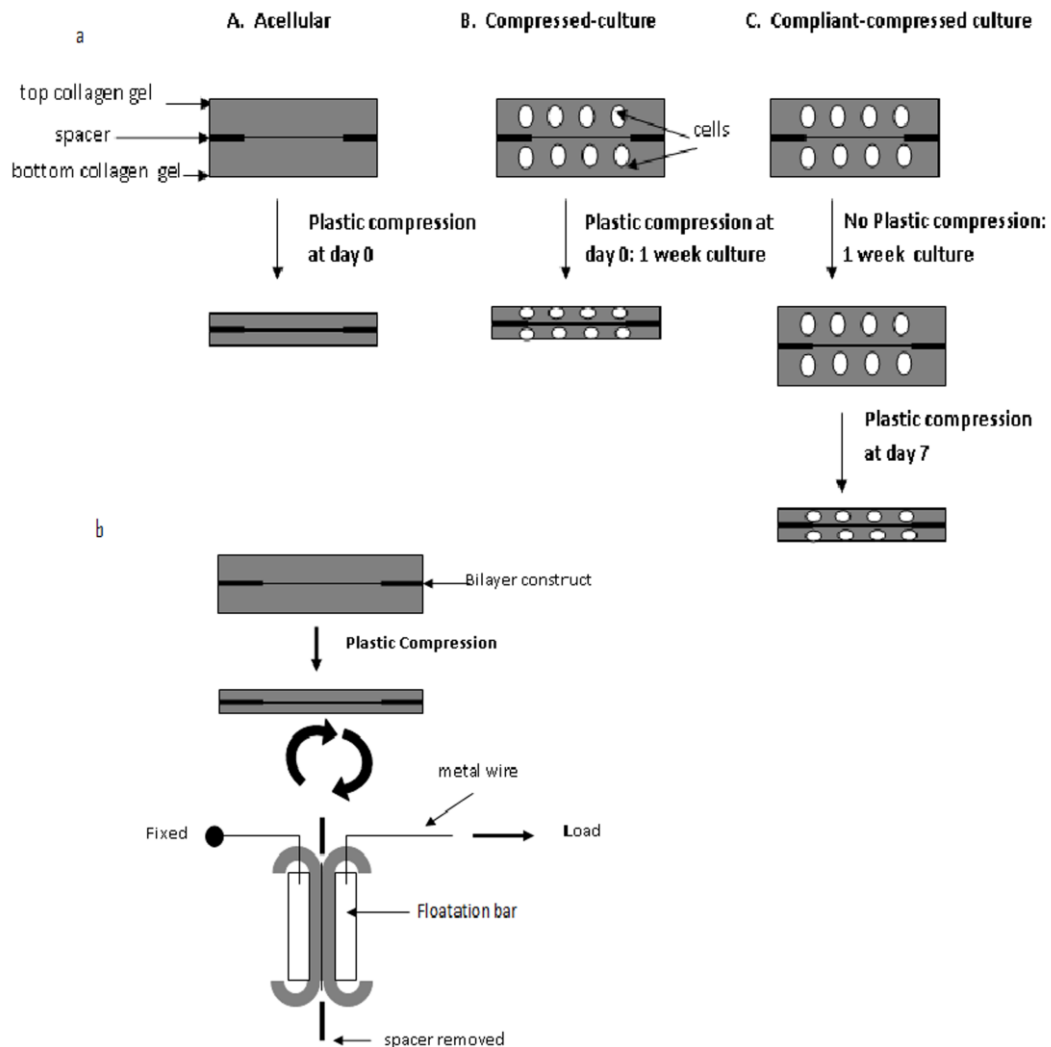
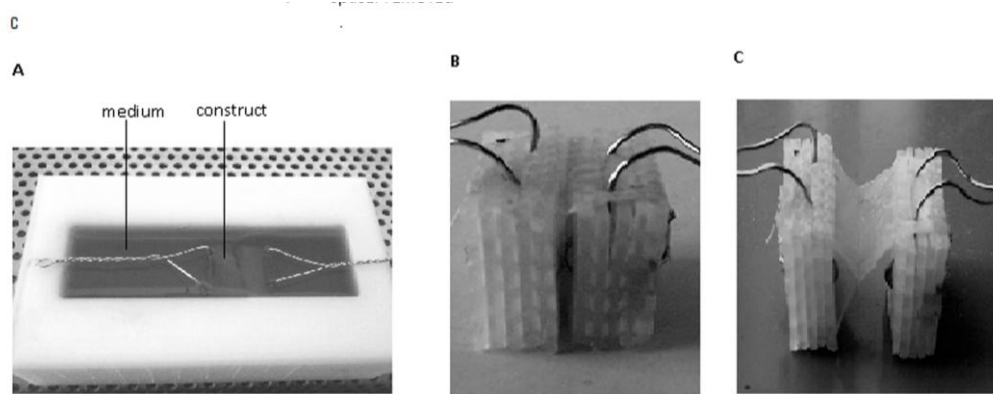


Fig.6

Experimental setup for measuring interface integration in bi-layer collagen constructs.

(a) Schematic of development of bilayer collagen constructs. Collagen gels were cast on top of each other with spacers placed at the two edges of the interface. Constructs underwent plastic compression for 5 min using a 120g load to obtain a 200µm thick bilayer sheet. The three models tested were acellular constructs (A), compressed cultures (high stiffness) (B) and compliant-compressed cultures (low stiffness) (C). (b)

Schematic showing the process for measuring interface adhesive strength. After compression, spacers were removed and the free ends of each sheet were attached to floatation bars, which were connected to the t-CFM through metal wire.



(c) Photograph of the full assembly placed in a culture well filled with culture medium (A). Desktop representation of bilayer construct before (B) and after (C) being subjected to mechanical loading, showing failure at the interface.

Finite Element Analysis

In order to analyse the distribution of predicted stresses acting throughout the bilayer construct during mechanical loading, a solid model of the interface construct was created in the FE package LISA (Finite element technologies, USA). The model consisted of two 8 node hexahedron elements joined at an interface. This model was then meshed by using 864 8-noded hexahedron 3D solid elements. Compressed collagen sheets were given a Young's Modulus of 2240 KPa, based on previous data [166]. Sheets were modelled as homogeneous isotropic linear elastic materials to keep calculations feasible [283]. This assumption was reasonable as long as the load rates were slow. The back end of the fixed collagen sheet was restrained in all directions with respect to the contact surface of the bar. The sheets were assumed to be completely and uniformly bonded at the interface. A load that was representative of the force magnitude applied by the t-CFM. was applied perpendicular to the face

of one collagen sheet to pull it off the fixed sheet. The distribution of stresses along the interface was then computed.

Assessment of mechanical integration of interfaces

The mechanical integration of bilayer collagen constructs was assessed by subjecting them to a single-lap test to failure by using the tensioning culture force monitor (t-CFM), a previously described computer driven tensional loading device [158]. After compression of bilayer collagen constructs (acellular and cell-seeded), the engineered interfaces were attached onto floatation bars through their free ends (after spacers were removed) and connected to the t-CFM by surgical metal wire (0.35 mm in diameter), as shown in figure 6b, c. The t-CFM consisted of a stress-strain measuring system composed of an x-y stage placed on a linear table moved by a stepper-motor (SY561T, Parker, Germany) attached to a microdrive (XL25i, Parker). The force sensor, composed of a copper beryllium beam (0.15 mm thick) coupled with a strain gauge (Measurement Group UK, UK), was mounted vertically onto a static reference point to the moving x-y. Shear stresses developing from the floatation bars were avoided by connecting and suspending the whole assembly in culture medium before applying strain. Unidirectional tensile loads were programmed into the computer-based software X150 (Parker Automation, City, USA) and applied to the interface. Signal from the force transducer was acquired by a data acquisition card (National Instruments, USA), displayed in real time and recorded by LabVIEW 6.0 software (National Instruments, USA). Data were recorded at a rate of 1 point/second. Each data point was the average of 1,000 points (acquisition rate: 1,000 points/s) giving a good signal to noise ratio. For each

measurement, the x-y stage was moved at a constant velocity of 4.8 mm/min until interface fracture was achieved, as indicated by a force drop after a steady rise to the peak adhesive strength. The movement of the stage was maintained until full separation was observed. The interface surface area (2 cm²) was used to normalize peak force values and to obtain adhesive strength values.

Assessment of cell migration

In order to quantify cell migration we used the ‘nested collagen matrix’ model, described by Grinnell et al [143]. The experimental setup is shown in figure 7. Nested collagen matrices were prepared by embedding cell-seeded collagen matrices (1ml) into cell-free matrices (5ml). For compressed cultures (high stiffness), the nested matrices were compressed at day 0, while for compliant cultures (low stiffness), nested matrices were left uncompressed and free-floating during the culture period. For both conditions, inner gel final cell density was 2x10⁶ cells/ml. Nested matrices were cultured for 1 or 7 days in 5ml complete medium and then removed from culture, fixed in 2.5% glutaraldehyde in 0.1M phosphate buffer, pH 7.5, at 4⁰C for 1 h, followed by washing in PBS. The gels were then stained with 1ml 1% toluidine blue. They were then destained through a series of 30 min washes in PBS. Migration across the interface was quantified with a phase-contrast microscope. Since cells had moved across a 3D space within the construct, the plane of focus was manually set and kept constant during counting. The number of cells migrating across the interface per x10 field was counted. Reported numbers are the average of 5 fields per sample, with 3 samples per condition.

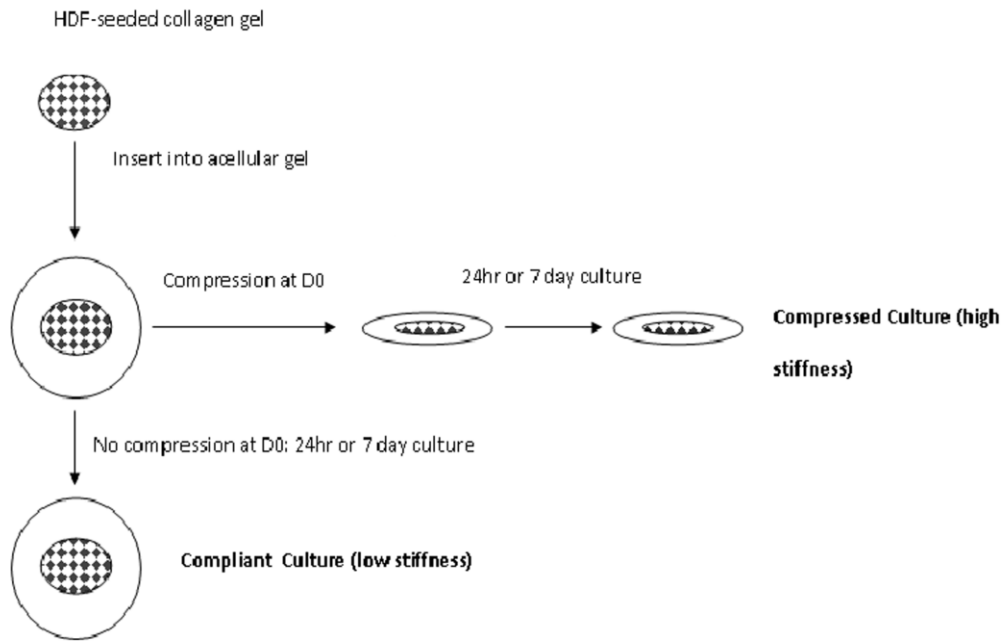


Fig. 7

Assessment of cell migration out of cell-seeded collagen matrices using the ‘nested collagen matrix’ model. Schematic showing model development. HDF-seeded collagen gels were placed into acellular gels and either compressed at day 0 and cultured for 24hrs or 1 week (compressed culture; high stiffness) or cultured uncompressed for 24hrs or 1 week (compliant culture; low stiffness). For both conditions, inner gel final cell density was 2×10^6 cells/ml.

SEM interface analysis

Conventional SEM (Philips CM12 electron microscope; Agar Scientific, UK) was used to study the morphology of collagen fibrils at the interface following compression. Acellular or cell-seeded bilayer constructs cultured for 7 days were routinely processed for SEM as described in Chapter 2. Air-dried constructs were sectioned transversely to expose the interface. They were mounted vertically onto stubs, sputter coated, and examined with SEM.

CHAPTER 8

IDENTIFICATION OF KEY FACTORS IN DEEP CELL O₂ PERFUSION

Cell behaviour is inherently linked to the prevailing O₂ micro-environment, as this critically directs the most basic cellular activities (i.e. metabolic and synthetic functions). Identification of the factors that determine deep cell O₂ perfusion is therefore a key pre-requisite to regulating cell behaviour in 3D engineered tissues. In this study we have quantified O₂ consumption by Pulmonary Artery Smooth Muscle Cells (PASMCs), seeded under a range of conditions in dense collagen 3D tubular constructs, to establish a working experimental model of the system. We hypothesize that O₂ consumption by resident cells, rather than matrix density/diffusion coefficient or diffusion path length, is the primary determinant of prevailing local O₂ tension in a 3D nanofibrillar collagen construct. In particular, we tested the hypothesis that cellular O₂ consumption will generate natural (i.e. biomimetic) radial O₂ gradients from the outer surface of the construct to the core (lumen), while such gradients will not form in acellular constructs. In this study we have dissociated the effects of matrix density/diffusion coefficient, diffusion path length and cellular O₂ consumption on deep O₂ perfusion, and have correlated O₂ consumption gradients with cell density to test if exposure of core cells to lower O₂ tension reduces cell survival (measured as cell viability along the radial consumption gradient), under both static and dynamic perfusion culture conditions. Furthermore, to show how different cell types behave in terms of O₂ consumption, we compared PASMC responses to those of human dermal fibroblasts (HDFs), cultured under identical conditions in the same 3D model [173] up to 6 days in culture.

8.1 RESULTS

Correlation of core O₂ tension with construct cell density

We first measured O₂ diffusion into the core of cell-free plastically compressed collagen tubular constructs (~1.5 mm radial wall thickness). Such validation and calibration studies without cells (Fig. 1a) provided a steady-state base level O₂ tension at the core and surface over 24 hrs (note that the fluctuations in core O₂ tension over 24hrs were not statistically significant, $p>0.05$). The core O₂ level was not significantly different from that on the surface (~148mmHg), indicating a 'zero' gradient with free radial O₂ diffusion through the nano-fibrillar collagen matrix of the wall. This concurs with our previous work showing a high O₂ diffusion coefficient through this dense collagen. In contrast, cellular constructs (~1.5 mm radial thickness) exhibited time-dependent O₂ depletion in their core over a period of 24 hrs (Fig. 1a). O₂ tension fell rapidly over 0-5 hrs depending on cell density and reaching 10 ± 6.2 mmHg for high cell density constructs (23.2×10^6 cells/ml) and 80 ± 11.7 mmHg at the low cell density (11.6×10^6 cells/ml). The 2 and 8 fold decrease in O₂ tension at low and high cell densities, respectively, was significant ($p<0.05$) indicating that cell O₂ consumption (i.e. the number of cells consuming O₂ along the diffusion path) was a central determinant of core O₂ tension in the system over 24hrs. Importantly, core O₂ tension was found to be inversely proportional to cell density. Figure 1b illustrates the relationship between cell density and O₂ consumption rate, with constructs seeded at twice the cell density having a 2 fold greater O₂ consumption rate over the 12 to 24hrs period of culture. The initial consumption rate (0-5hrs) was 3 fold higher at the high cell density, perhaps due to pre-adaptational differences in core cell metabolism at different O₂ tensions (going from culture hypoxia to tissue-like normoxia). Core O₂ tension was found to be

stable over extended periods, from 24-72hrs, at ~20mmHg (Fig.1c). This contrasts with the same system previously established using HDFs, which adapted over the 24-72 hr period to reduce O₂ consumption such that core O₂ tension rose to 65mmHg by 30hrs [173]. This 3-fold difference between the PASC and HDF O₂ level became statistically significant at 40 hrs (fig. 1c).

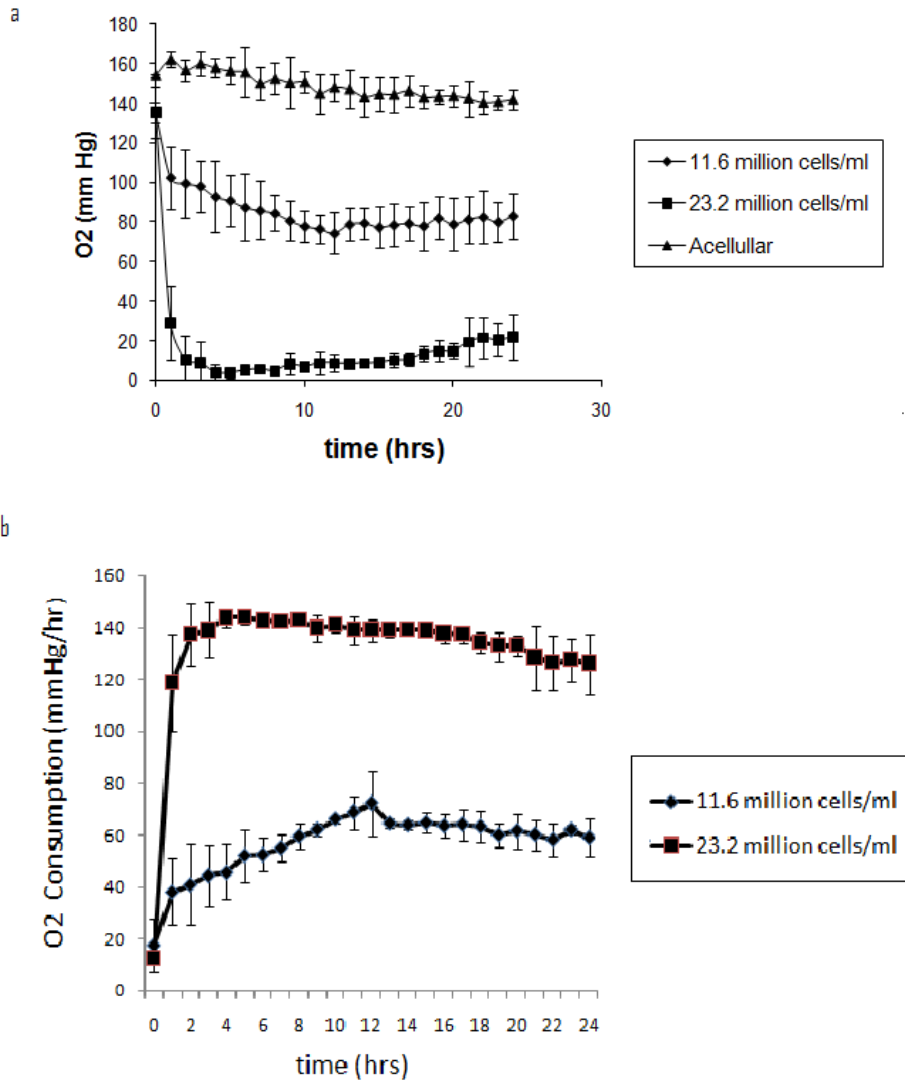
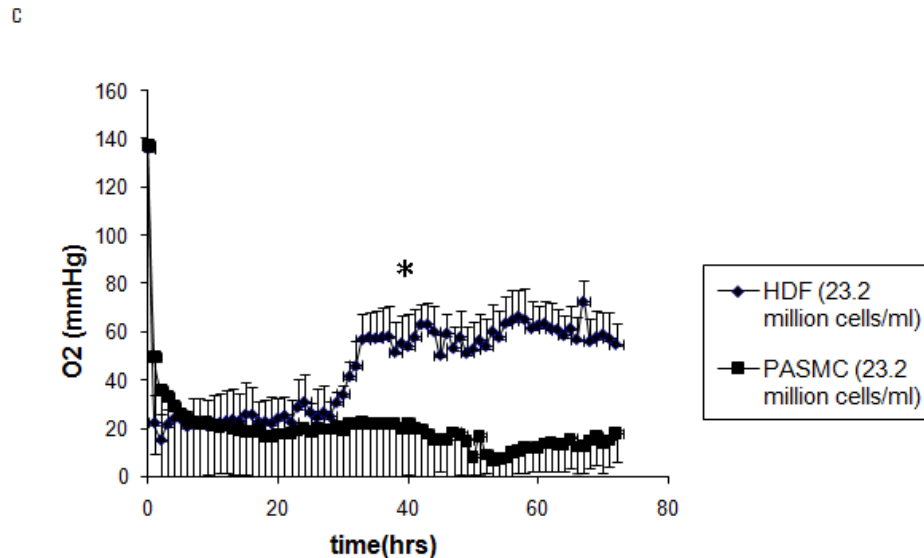


Fig.1 Correlation O₂ tension in the core of 3D collagen constructs with cell density and cell type. (a) O₂ tension in the centre of acellular and PASC-seeded spiral constructs cultured for 24hrs. Two different cell densities were measured, 11.6 million cells/ml and 23.2 million cells/ml (average of n = 5 for each data set is presented here). Time-zero is taken as the time point when the probe was positioned in the construct.(b) Rate

of O₂ consumption within constructs seeded with 11.6 million cells/ml and 23.2 million cells/ml and cultured for 24hrs.



(c) O₂ tension in the centre of spiral constructs seeded with 23.2 million cells/ml and cultured for 3days (n=3). Comparative HDF data has been derived from Cheema et al [173], *p<0.05.

Correlation of core O₂ tension with consumption path length

We also tested the effect of increasing diffusion distance on core O₂ tension within the lower cell density (11.6×10^6 cells/ml) constructs. This compared the effects of increasing the diffusion distance (i.e. construct wall radial thickness) from ~1.5 mm to ~2 mm. This not only resulted in increased wall thickness, but also increased the total number of cells along that diffusion path (i.e. consumption gradient increased with distance). To dissociate between the effects of cell O₂ consumption from that of diffusion path length, acellular constructs of each radial wall thickness were also compared. Figure 2 shows that for acellular constructs, increasing the diffusion distance had no significant effect on core O₂ tension. For cell-seeded constructs an

increase in diffusion and consumption path-length of 33% resulted in an increase in O_2 consumption and a ~30% reduction in core O_2 tension (marked here as significant after 12hrs, $p < 0.05$). Importantly, even though the increase in diffusion/consumption path-length generated a proportionately lower core O_2 tension this difference emerged as a new basal value of core O_2 tension post 12hrs, rather than an altered initial rate of consumption (0-10 hr slope).

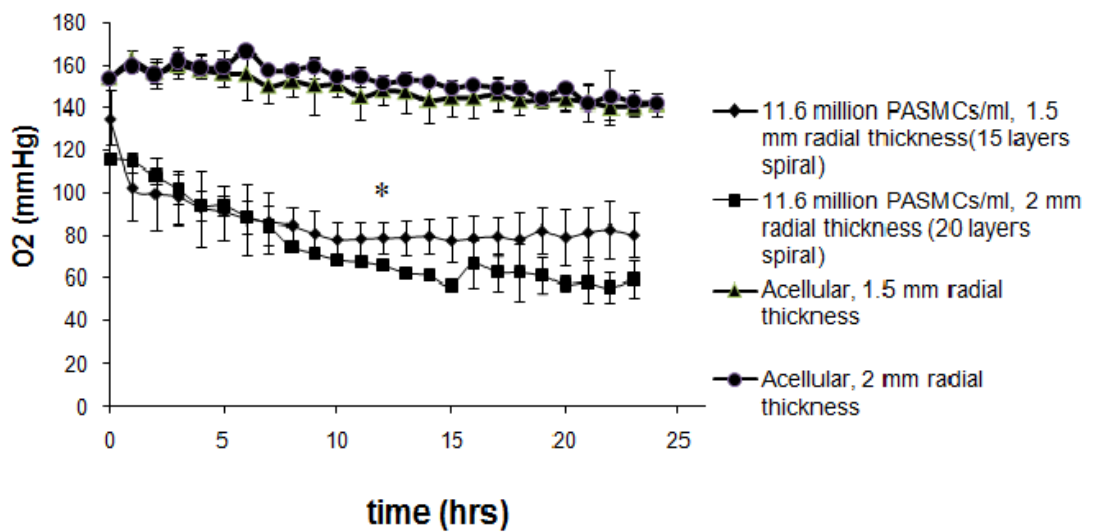


Fig. 2 Effect of increasing consumption path length on core O_2 tension. O_2 tension in the centre of acellular spiral constructs and constructs seeded with 11.6 million cells/ml and cultured for 24hrs. Constructs had a radial thickness of 1.5mm (15 layers spiral) or 2 mm (20 layers spiral), * $p < 0.05$.

Comparison of PASC vs HDF viability in static cultures

We have previously established that human dermal fibroblasts (HDFs) seeded at 23.2×10^6 cells/ml within 3D compressed collagen constructs retained high (80%) core cell viability for up to 5 days in culture [173]. To compare the effect of physiological (1-10% O_2 or 7.6-76 mmHg) hypoxia on HDF and PASC viability

we measured the difference in PASMC viability between core and surface cells (high cell density cultures) over 0-6 days. Exposure of PASMCs to the lowest levels of O₂ (~10 mmHg) in the core had no significant effect on 24 hr cell viability (Fig 3a, b), which was over 95% in both the core and surface regions of the construct, indicating that this cell type is not significantly susceptible to short term hypoxia. However, after 6 days of static culture, there was a significant reduction in cell viability both at the construct core (55%) and surface (75%) (p<0.05) (fig. 3a, b). This decrease in cell viability was accompanied by a gradual increase in core O₂ tension from 20 mmHg at 72hrs to 100 mmHg at day 6, as overall O₂ consumption was reduced apparently due to reduced cell number (fig. 3c). It is important to note, however, that this increase in core cell death, at low O₂ tension, was accompanied by a smaller but still significant level of cell death at the surface, where O₂ was not depleted.

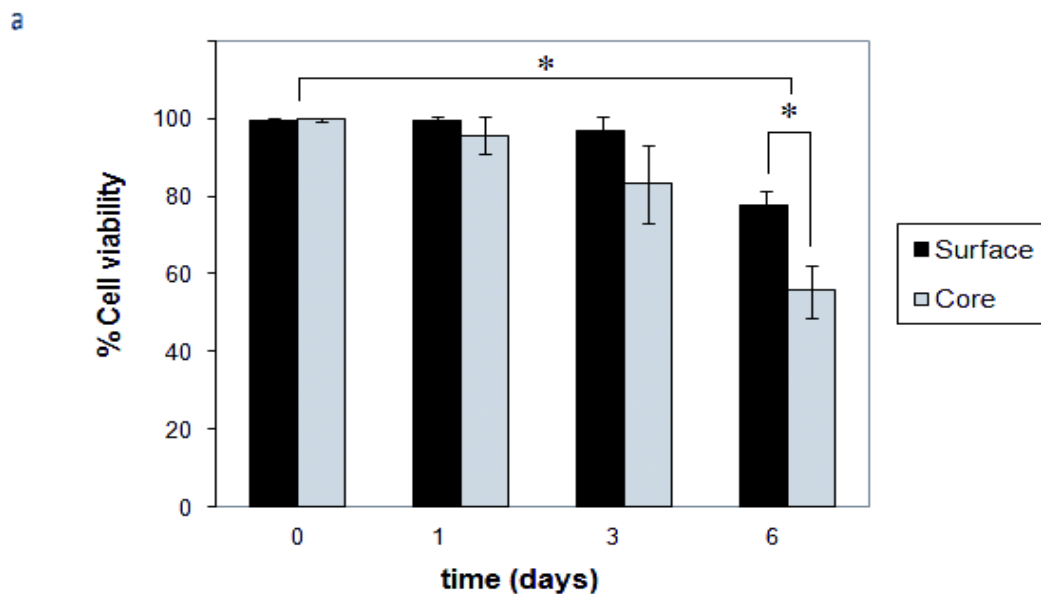
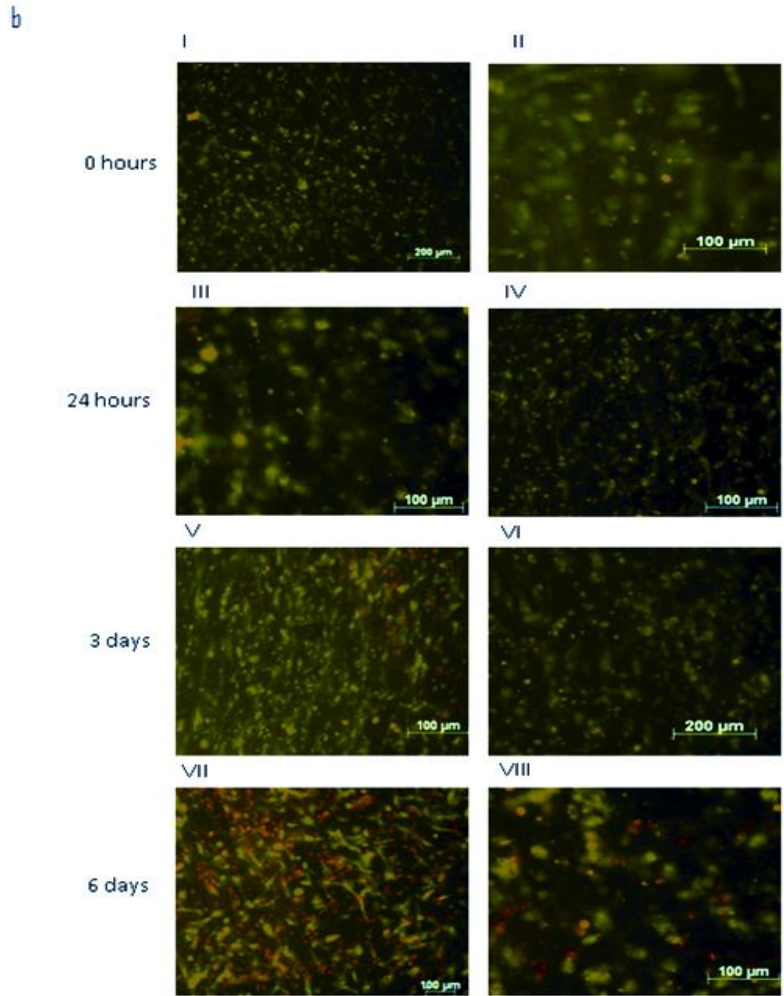


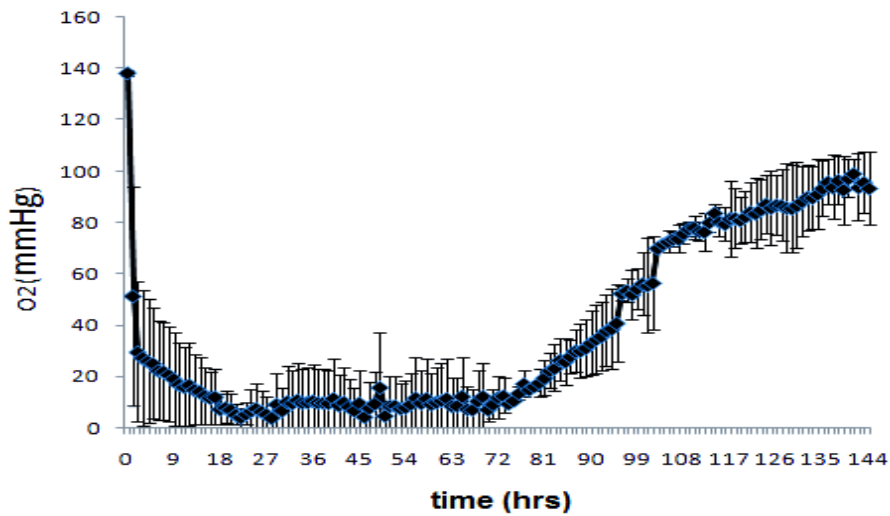
Fig. 3 Comparison of PASMC core and surface viability over a 6 day culture period.

(a) Cell viability measured at time zero and then at 1, 3 and 6 days in static cultures (23.2 million cells/ml), *p<0.05.



(b) Fluorescent images of the central (core; I, III, V, VII) and outer (surface; II, IV, VI, VIII) region of constructs seeded with 23.2 million cells/ml and cultured for up to 6 days under static conditions. Green (calcein) and red (ethidium homodimer) fluorescence indicate live and dead fibroblasts, respectively.

c



(c) O₂ tension in the centre of spiral constructs seeded with 23.2 million PASCs/ml and cultured for 6 days.

Effect of dynamic perfusion on PASC viability

We hypothesized that introduction of forced flow of medium to this static system would reduce O₂ gradient formation and improve cell viability. Constructs were thus cultured under dynamic perfusion. Dynamic perfusion culture of high cell density constructs for 6 days significantly improved core cell viability at day 6 (from 55% in static culture to 70% in dynamic perfusion culture, $p < 0.05$) (Fig. 4). 6 day surface cell viability (88%) was also increased relative to static conditions (75%) but this was not statistically significant, being effectively the same as short-term (day 1) with minimal cell death (Fig. 4). Dynamic perfusion culture, however, did not abolish the difference in cell viability between core and surface, observed with static culture, which remained statistically significant after 6 days ($p < 0.05$). The observed increase

in long term core cell viability under dynamic perfusion culture (which presumably increased O₂ perfusion to the construct core) was in agreement with our previous finding that cellular O₂ consumption imposed a limitation in core O₂ availability and compromised cell survival.

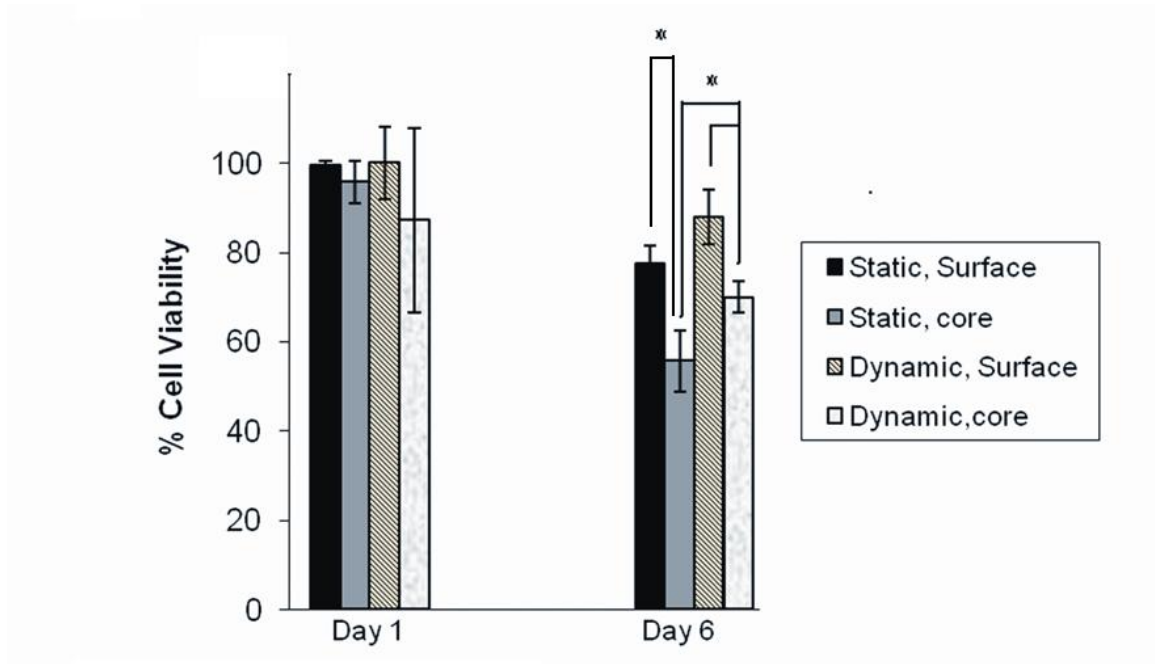


Fig.4 Dynamic perfusion increases PASMCM viability. Cell viability, as measured by live/dead assay for constructs seeded with 23.2 million PASMCM/ml and cultured for 1 and 6 days under static and dynamic perfusion culture conditions, * p<0.05.

8.2 DISCUSSION

Original Hypothesis: O_2 consumption by resident cells (pulmonary artery smooth muscle cells), rather than matrix density/diffusion coefficient or diffusion path length, is the predominant factor controlling O_2 tension in the core of 3D nano-fibrillar collagen scaffolds.

The findings of this study indicated that the major limiting factor resulting in O_2 depletion in the core of 3D nano-fibrillar collagen constructs was cell consumption of O_2 and not a limitation of O_2 diffusion caused by extended diffusion path-length through ECM (up to 1.5-2 mm, as tested in this model). Indeed, previous research carried out on thick fibrin matrices has indicated that gel thickness, in the order of centimetres, was not a limiting factor for O_2 diffusion[94]. Such components of native ECM (i.e. collagen, fibrin) have already been used in direct applications as biomimetic tissue engineering scaffolds[9]. Differentiating between diffusional and cell consumption limitations, in terms of nutrient supply to the scaffold core, is critical for the design of bioreactors (where constructs are cultured prior to implantation) that aim to improve deep cell perfusion until functional scaffold vascularisation is established. In effect, the extent of limitations in nutrient perfusion to the scaffold core will ultimately govern its maximum size/thickness, and therefore its utility as a tissue repair/regeneration tool.

It is important to note that while the current model's tubular geometry mimics '3D vascular tissue geometry', it effectively creates radial O_2 gradients (surface-to-core) which are reverse to the natural gradients (core-to-surface). The use of a tubular model in this case did not aim to reproduce the directional anisotropy of *in vivo* gradients, but made it feasible to engineer a 3D model tissue where cell density and

radial thickness could be easily and predictably controlled[25], in order to examine their effects on spatio-temporal changes in O₂ tension.

There was a direct linear relation between cell density and O₂ consumption by 24 hours, however the initial (0-5 hrs) rate of O₂ consumption was not directly proportional to cell density. In fact, for the higher cell density (double that of the lower cell density) initial O₂ consumption was 3 fold higher. This finding seems to be in agreement with the well established principle that rates of energy metabolism are dependent not only on a single substrate but on the entire nutrient–metabolite milieu . For instance, oxygen uptake is enhanced at low glucose concentrations (*the Crabtree effect*, [284]). Oxygen consumption rate also varies with oxygen concentration and pH [285]. The linear relationship which develops within 24 hours may represent an adaptive response by cells to the surrounding O₂ environment. There is likely to be an iterative feedback response with regards to O₂ consumed and O₂ available, which in turn will regulate the cellular metabolic response and other changes in gene expression, primarily extracellular matrix production and up-regulation of angiogenic signals (as discussed in Chapter 9) [286,287]. It is important to note that smooth muscle cell densities in the present study are comparable to those used in previous (vascular engineering) studies (40-100 x 10⁶ cells/ml)[288].

Cheema et al. have previously measured O₂ consumption by HDFs, cultured in the same 3D system. When HDFs were seeded at 23.2x10⁶ cells/ml O₂ tension was not significantly different compared to that observed with PSMCs, after 24hrs [173]. However, while core O₂ tension (~20mmHg) was found to be stable over extended periods, between 24-72hrs for PSMCs, this was not the case with HDF cultures where core O₂ tension rose back to 65mmHg by 30 hrs (Fig. 1c). As mentioned

above, this is likely to be due to differences in cell metabolism and O₂ utilization between the two cell types, with HDFs appearing to adapt to hypoxia by reducing their O₂ consumption (note that the higher O₂ tension in HDF cultures was not due to cell death, as core HDF viability was not significantly reduced for upto 5 days in this system). These findings suggest that PASMCs are high consumers of O₂ and that cell phenotype, as well as cell density, is an important determinant of O₂ consumption.

Constructs of varying radial wall thickness (15 vs. 20 layers, corresponding to ~1.5 vs. ~2 mm thickness), and thus of varying diffusion and consumption path length, exhibited different plateau values of O₂ tension. This response, however, was characterized by a 12 hr lag phase. Given the high diffusion coefficient of O₂ through acellular collagen (note: O₂ diffusion coefficient in compressed collagen is $4.5 \times 10^{-6} \text{ cm}^2/\text{s}^{-1}$, which is in the range of native intestinal submucosa[289]), the 33% increase in material thickness (i.e. diffusion path length) must have minimally limited O₂ diffusion, which was in agreement with experimental data (shown by the lack of significant difference in O₂ tension in the core of acellular constructs of 1.5 and 2 mm radial thickness). This indicates that the 12hr lag phase observed here was a function of the cell O₂ consumption gradient established in this system. Controlling construct thickness (i.e. the number of cell-seeded layers/consumption path length), as well as cell density (i.e. the number of cells per layer/unit area), could thus provide an additional means for controlling the rate of O₂ consumption through a construct (Fig.5). This ability to selectively and predictably ‘tune’ O₂ distribution and local tissue perfusion within a 3D construct could have important implications for the layer-by-layer assembly (e.g. cell-sheet and matrix-sheet engineering) approach which has been pursued by a number of groups due to its architectural relevance to native tissue (e.g. blood vessel) structure [86,290,291].

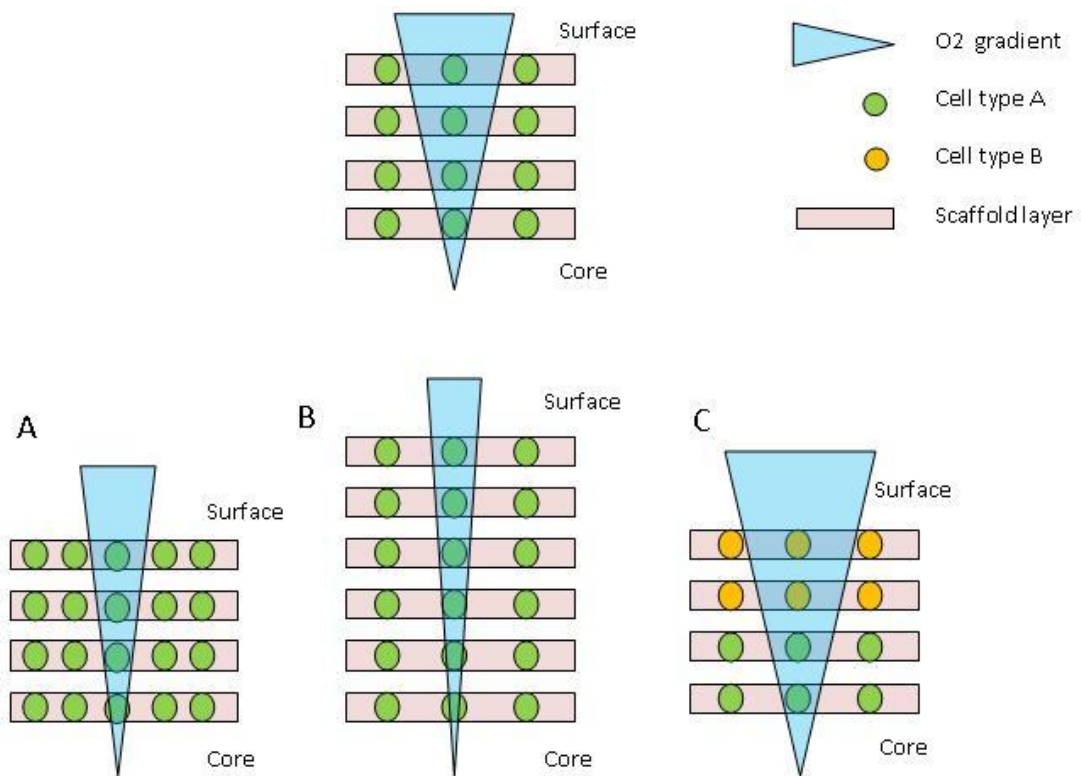


Fig.5 Schematic showing how O₂ tension could be ‘tuned’ within a 3D layer/sheet-based scaffold. Cell O₂ consumption generates an O₂ gradient from the surface to the core region of the scaffold. By controlling (A) the cell density (i.e. number of cells per layer/unit area), (B) the number of cell-seeded layers (i.e. consumption path length) and (C) the type of seeded cells (and their spatial position), it is theoretically possible to predictably define the local O₂ microenvironment at any chosen point in 3D. This is key for optimising deep cell O₂ perfusion and engineering correct, biomimetic O₂ gradients where they are functionally important.

While our data suggest that in cell-seeded collagen constructs the formation of O₂ gradients was the result of cell consumption, it is possible that changes in material properties through cell-mediated matrix remodelling could have also contributed at later stages to changes in O₂ diffusion[292]. Indeed, cell-seeded constructs cultured for 2 days had a 2.5 fold higher stiffness modulus compared to day 0 cell-seeded constructs (data not shown). Within such a short time period, however, and given the high initial stiffness (1.8 MPa [25]) of acellular compressed collagen matrix (~50

fold higher than the stiffness of uncompressed collagen hydrogels, 40 KPa [166], which undergo cellular remodelling within 24hrs), this increase in stiffness was likely contributed by cytoskeletal elements (cytoskeletal stiffness) which act additively to matrix stiffness [293]. Nonetheless, it is possible that over longer periods of culture, cell-mediated matrix remodelling (increase in density of collagen filaments or cross-linking between collagen fibrils i.e. change in the porosity of the material), could have a significant effect on O₂ diffusion[294].

Viability of PASMNC in the core of high cell density constructs exposed to levels <10mmHg of O₂, remained high (~80%) up to 3 days, however by day 6 this level decreased to 58%. We have established then that PASMNCs can survive physiological hypoxic conditions for at least 24hrs. While PASMNC exposure to hypoxia did not result in rapid cell death, continued exposure did kill cells, probably until the core O₂ rose again, sparing the remaining cells. It is important to note that while plastic compression has previously been shown not to significantly reduce cell viability [25], at such high seeding cell densities no cell proliferation occurred [166]. This implies that there was a net reduction in cell number within constructs at 6 days. Not surprisingly, this was accompanied by a gradual increase in core O₂ tension, in agreement with reduced overall O₂ consumption, representing a natural feedback mechanism, likely to mirror that found *in vivo*. A previous study has shown that the micro-environment within polymer scaffolds containing transplanted hepatocytes was hypoxic (pO₂ < 10 mmHg) after 5 days *in vivo*[295], indicating that the detrimental effect of hypoxia on long term cell survival is not limited to *in vitro* culture. However, this study highlights that the reported effect of hypoxia on cell viability has to be treated with caution, as different cell types show different consumption and sensitivity to reduced O₂ tension. As discussed above, HDFs can

adapt to hypoxia by reducing their O₂ consumption resulting in preservation of long term viability (Fig. 6). This has important implications for controlling deep cell O₂ perfusion in engineered complex/heterogeneous tissues where two or more cell types are present (such as blood vessels) (Fig.5).

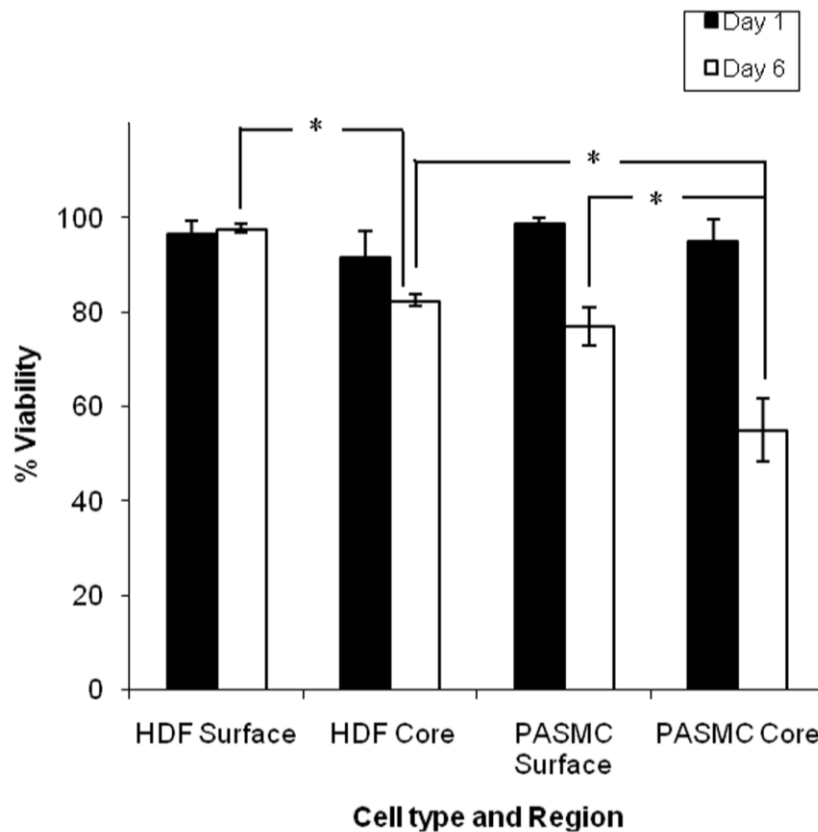


Fig.6 Comparison of core and surface cell viability for 3D collagen constructs seeded with HDFs or PASCs at high density over 6 days static culture. Cell viability, as measured by live/dead assay for constructs seeded with HDFs and PASCs at 23.2 million cells/ml and cultured for 1 and 6 days under static culture conditions, *p<0.05. Comparative HDF data has been derived from Cheema et al [296].

In our 3D model, in addition to O₂ availability, the diffusion of key higher molecular weight nutrients (e.g. glucose) could be a limiting factor for cell survival. Glucose diffusion coefficients have previously been established and this was not found to be limiting for cells in the same 3D model [297]. While glucose diffusion might not be a limiting factor, static culture of cells within this 3D model does produce a glucose consumption gradient from the construct surface to its core within 24hrs [297], implying that low core glucose levels could have contributed to decreased core cell viability. However, previous work has shown that fibroblasts exposed to hypoxia become tolerant to glucose starvation as they switch to amino acids as an energy source [298]. Whether PSMCs respond in a similar manner remains to be examined. It is also important to consider the possibility that cells cultured statically (without circulation of culture medium) were exposed to increased levels of toxic metabolic products (such as lactic acid, not measured here), diffusing away from the core cells. This could explain the observed reduction in surface cell viability (25% by day 6) which could not easily be explained by any limitations in O₂ or glucose availability. Indeed, a previous study has shown that effective pH buffering reduces cell death by attenuating the acidosis that accompanies anaerobic metabolism [299].

The above findings suggest that when engineering functional tissues, a trade-off needs to be established between the high cell density required and O₂ availability[300]. It has thus been suggested that in diffusion-limited (i.e. large) tissue constructs, a more sophisticated transport system must be employed [199,294,300]. Compared to static culture, dynamic perfusion culture has previously been shown to increase gas transport and maintain normoxic levels of O₂ tension within 3D constructs [301,302]. Here we showed that dynamic perfusion culture (over the outer construct surface) significantly improved core cell viability at day 6,

although this remained significantly lower than surface cell viability. These findings are in agreement with previous studies that showed that perfusion culture increases cell viability within a construct and improves the spatial uniformity of cell distribution [303-306]. Since we have shown that O₂ availability became limiting and impacted on core cell survival in static cultures, the improvement in core cell viability observed by medium perfusion was presumably due to an increase in O₂ transport. However, this does not preclude involvement of additional mechanisms such as prevention of nutrient depletion at the surface of the construct, as well as effective removal of harmful metabolic products released by core cells.

8.3 CONCLUSIONS

We have determined parameters for the successful culturing of PASMNC's within dense collagen tubular constructs resulting in prolonged cell survival. The current model establishes that O₂ perfusion is primarily dependent on cellular O₂ consumption, therefore being cell-phenotype and density specific. Our findings suggest that it could be possible to spatially organize cells within 3D constructs to control O₂ distribution throughout the construct, as well as to limit/control O₂ perfusion to certain well-defined construct areas. These controls could potentially act as effectors of metabolic or angiogenic cell signalling, as discussed in Chapter 9.

8.4. MATERIALS & METHODS

Preparation of 3D Plastic Compressed collagen gel constructs

Once detached, PSMCs were counted and embedded in 3D collagen type I gels (see Chapter 2). Collagen gels were set in a mould with dimensions 2.2 (width) x 3.3 (length) x 1 cm (height). Gels were then removed from the mold and routinely compacted by a combination of compression and blotting between layers of supporting nylon mesh and filter paper sheets [25] (see Chapter 2). Plastic compression produced flat collagen sheets ($96.4 \pm 8.7 \mu\text{m}$ thick [25]) protected between two nylon meshes. This did not significantly reduce cell viability [25]. These dense, dehydrated collagen sheets were then rolled around a 1mm external diameter hollow mandrel (0.8mm internal diameter) to produce tight spirally wound tubular constructs, ~4 mm in external diameter, 21 mm in length (Fig 7a). Use of a tubular construct model in this case enabled rapid and precise layering of collagen sheets which would be technically difficult with a planar model. Construct radial (wall) thickness was varied between ~1.5 mm and ~2 mm by controlling the starting sheet length of the collagen sheet, hence the number of spiral layers; PC collagen sheets of 3cm in length produced 15 layer spiral constructs, corresponding to $1.446 \pm 0.13\text{mm}$ radial wall thickness (each layer was $96.4 \pm 8.7 \mu\text{m}$ thick), while sheets of 4.5cm long produced 20 spiral layers and $1.93 \pm 0.17\text{mm}$ radial wall thickness. There was no significant change in radial wall thickness of cell-seeded constructs over a 3 day culture period (data not shown). Required cell densities were calculated in direct proportion to the initial cell seeding density and fluid loss during plastic compression. Final cell density was calculated as: initial cell density x fold volume change during PC. Hence for a typical initial gel volume of 5 ml, and collagen concentration of 0.2%, this increased to 11% following compression (measured by

dry/wet weight ratio), corresponding to a 58-fold increase. Since all seeded cells remain within the PC collagen gel, final cell density increased in proportion from 200,000 cells/ml (or 1 million cells/construct) to 11.6 million cells/ml, and from 400,000 cells/ml (or 2 million cells/construct) to 23.2 million cells/ml [173].

Oxygen monitoring

Fibre-optic O₂ probes (Oxford Optronix, Oxford, UK) were inserted into the lumen of acellular and cell-seeded 3D tubular constructs by first inserting the probe into the mandrel, positioning it halfway along the long axis of the construct and withdrawing the mandrel to leave the sensor probe (280 µm diameter) in the construct lumen (1mm diameter) (Fig. 7a). The constructs were then sealed at both ends using cyanoacrylate glue. In addition to preventing O₂ diffusing longitudinally into the construct from the two ends, sealing the ends also ensured that spiral constructs were kept from unwinding in culture and that the O₂ probe was secured in place to prevent its longitudinal and radial movement during the experiment. Hence, a diffusion length of >1 mm was dominant throughout the construct, radially across the tube wall from lumen to surface. The 3D monitoring set-up is shown schematically in figure 7b. 3D samples were cultured statically in standard 100ml universal tubes. Constructs attached to O₂ probes were bathed in 50 ml complete medium composed of F12 Ham's media supplemented with 10% (v/v) fetal calf serum (FCS, First Link,UK), 2 mmol/l glutamine (Gibco Life Technologies, UK), 1,000 U/ml penicillin and 100 mg/ml streptomycin (both from Gibco Life Technologies, UK). There was no change of medium during each experiment. The tip of the sensor probe incorporates an O₂-sensitive luminescent compound within an O₂-permeable matrix.

Quenching of the luminescence by molecular O₂ allows the luminescence emission lifetime to be used as a read-out of O₂ tension in immediate surroundings. The calibration of the optical O₂ probe is accurate to 0.7mmHg, with exceptional stability over 6 days at the slowest sampling rate [173]. Readings were taken continuously in real-time. O₂ tension in the construct core refers to measurements recorded within the construct lumen, while O₂ tension at the construct surface refers to O₂ tension recorded in the surrounding media. After each experiment, the probe reading was taken in the external medium to confirm minimal drift in response. Fibre-optic probes were used in conjunction with an OxyLab pO₂ETM system (Oxford Optronix Ltd, Didcot, UK) coupled to an A/D converter (12 bit) with data collection to Labview (National Instruments, Texas, USA). Results are presented as partial pressure values (i.e. pO₂) in mmHg (e.g., 7.6mmHg corresponds to 1% O₂). To calculate O₂ consumption rate (mmHg O₂/hr) in cell-seeded constructs, the hourly O₂ tension in cell-seeded constructs was subtracted from the 24hr average O₂ tension in acellular constructs.

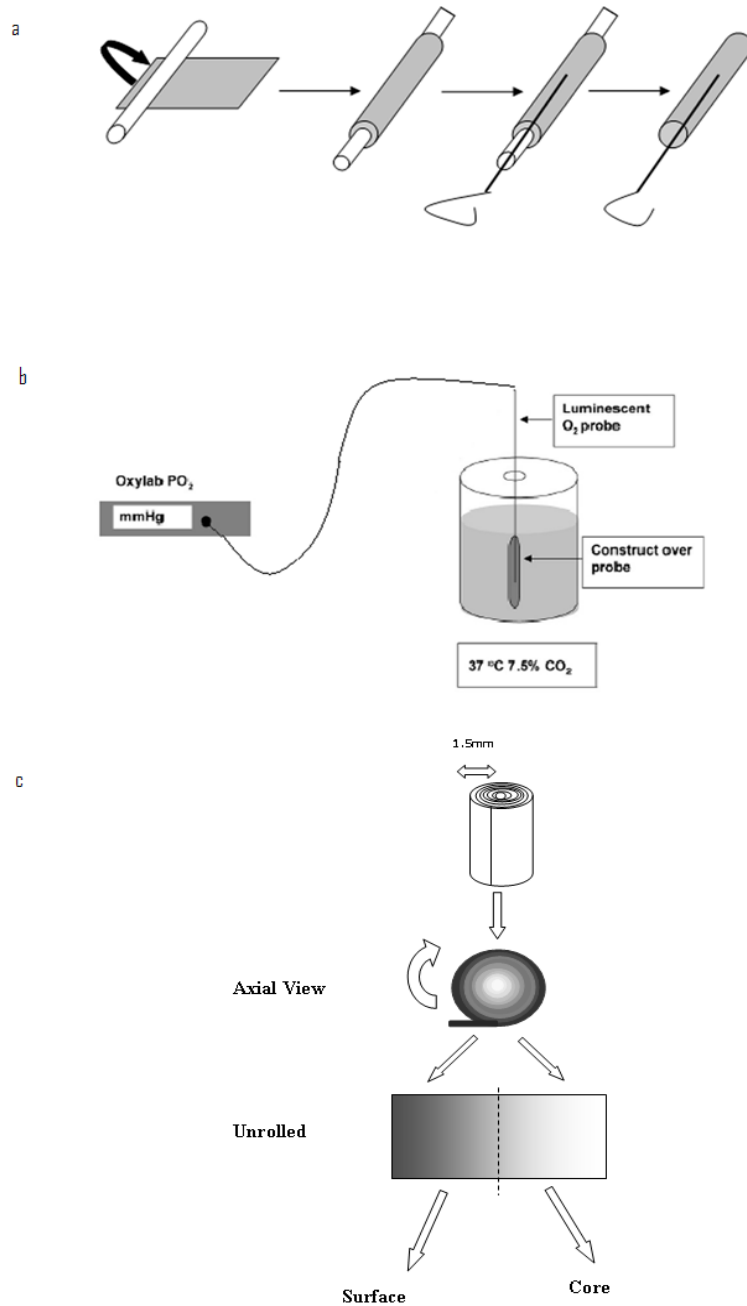


Fig.7 Experimental setup used for monitoring O₂ tension in the core of 3D collagen constructs. (a) Schematic of development of tubular spiral collagen constructs. Compressed collagen sheets were spiraled round a mandrel and an O₂ probe was inserted into the mandrel before the mandrel was withdrawn, leaving the probe in the centre of the construct. Constructs were then sealed at both ends using cyanoacrylate glue, which also ensured that spiral constructs were kept from unwinding in culture.

(b) Schematic of the experimental set up, with the O₂ probe in the centre of a spiraled plastic compression construct. Constructs were cultured in 50 ml media. (c) Assessment of cell viability involved unrolling 3D constructs and dissecting 2 regions corresponding to the core and surface of the spiral constructs.

Quantification of cell viability

Cell viability was qualitatively assessed using the Live/ Dead Viability/Cytotoxicity Kit (Molecular Probes, L-3224, Oregon, USA) based on the simultaneous staining of live and dead cells with calcein AM and ethidium homodimer (EthD-1), respectively. Quantitative analyses were carried out with Live/Dead Reduced Biohazard Viability/Cytotoxicity Kit (Molecular Probes, L-7013, Oregon, USA) according to the manufacturer's protocol. SYTO-10, a green fluorescent nucleic acid stain and Dead Red (ethidium homodimer-2) were used, and, after capturing images, live/dead nuclei were counted to give % cell viability. Spiral constructs were first unrolled and then cut into 2 sections, corresponding to core and surface regions and stained (fig.7c). Viability of cells in each construct was performed independently from the O₂ measurements. Representative areas were chosen in two regions (core and surface) of PC constructs and were visualized using confocal microscopy (Bio-Rad Radiance 2100, Carl Zeiss Ltd, Hertfordshire, UK). Five or more random fields were viewed per section with at least 3 samples for each experimental condition.

Dynamic perfusion cell culture

Collagen spiral constructs were produced by rolling PC cell-seeded collagen sheets round a solid mandrel (1mm diameter) and sealing the ends of each construct using cyanoacrylate glue. The mandrel supporting the constructs was then inserted into a silicone tube (8 mm internal diameter, 80cm length) connected at one end to a

peristaltic pump (Masterflex., Cole Parmer) and at the other end to a 500 ml media reservoir. The flow rate was adjusted so that the constructs were perfused with medium, round the outer construct surface (i.e. no medium flow through the lumen), at a constant rate of 1 ml/min throughout the culture periods of 24hrs or 6 days (Fig.8). 500 ml complete medium was re-circulated during the culture period.

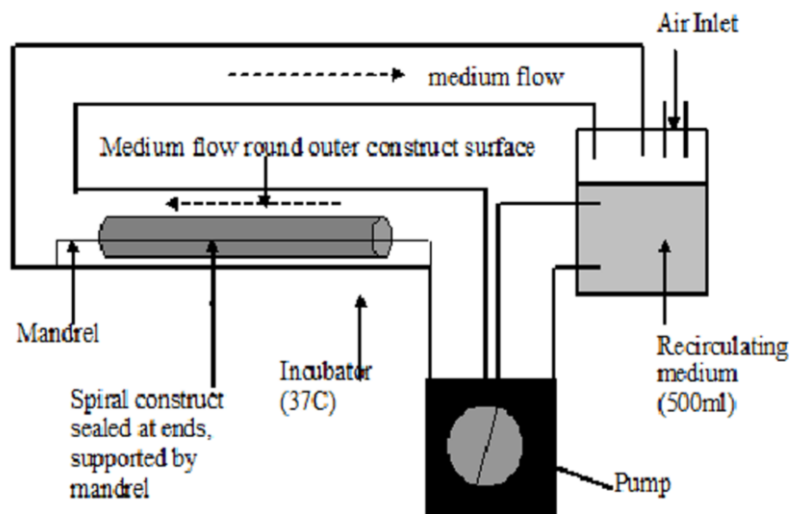


Fig.8 Schematic showing setup used for dynamic perfusion culture of constructs. Constructs were perfused with medium at a constant flow rate of 1ml/min in a recirculating bioreactor and were cultured for 1 or 6 days. Note that this model produced reverse flow, i.e. flow occurred round the outer construct surface and not through the construct lumen.

CHAPTER 9

CONTROLLING PHYSIOLOGICAL ANGIOGENESIS BY HYPOXIA-INDUCED SIGNALLING

The full sequence of signals leading to new blood vessel formation is a physiological response to tissue hypoxia, mediated by upregulation of a cascade of angiogenic factors. Controlled initiation of this mechanism for therapeutic/engineered angiogenesis must rely on precisely localised hypoxia. In Chapter 8 we showed that by controlling the seeding cell type, density and position, therefore cell-depot O_2 consumption, it is possible to define accurately where the hypoxia will develop within a 3D construct (i.e. core $O_2 < \text{surface } O_2$). In this study we have designed a 3D *in vitro* model able to test the effect and predictability of spatially positioned local hypoxic stimuli using defined cell depots in different locations within a 3D collagen matrix. Cell-mediated hypoxia was engineered using human dermal fibroblasts (HDFs), to generate a local population of Hypoxia-Induced Signaling (*HIS*) cells. We tested the hypothesis that 3D co-culture of a *HIS* cell population (HDFs) with endothelial cells (ECs), would rapidly induce a physiological angiogenic response. In this 3D *in vitro* model the directing *HIS* cells (hypoxic HDFs) and the responding ECs could be spatially positioned to prevent initial direct cell contact. HDFs were either exposed to normoxia (incubator levels) or localized physiological hypoxia to up-regulate critical angiogenic factors (HIF-1 α , VEGF). *In vitro* bioresponse was monitored in terms of EC migration and tube formation towards the angiogenic factor source (*HIS* cells). The practical effectiveness of spatially controlled hypoxia-induced signaling to promote and direct vascularisation *in vivo* was then tested by implanting collagen constructs, incorporating *HIS* cell

depots in their core, subcutaneously and intramuscularly in rabbits. The effect of pre-conditioning constructs prior to implantation, to optimize up-regulation of angiogenic signaling, was assessed using specific EC staining, while the functionality of newly formed vessels was assessed by extended real-time O₂ monitoring.

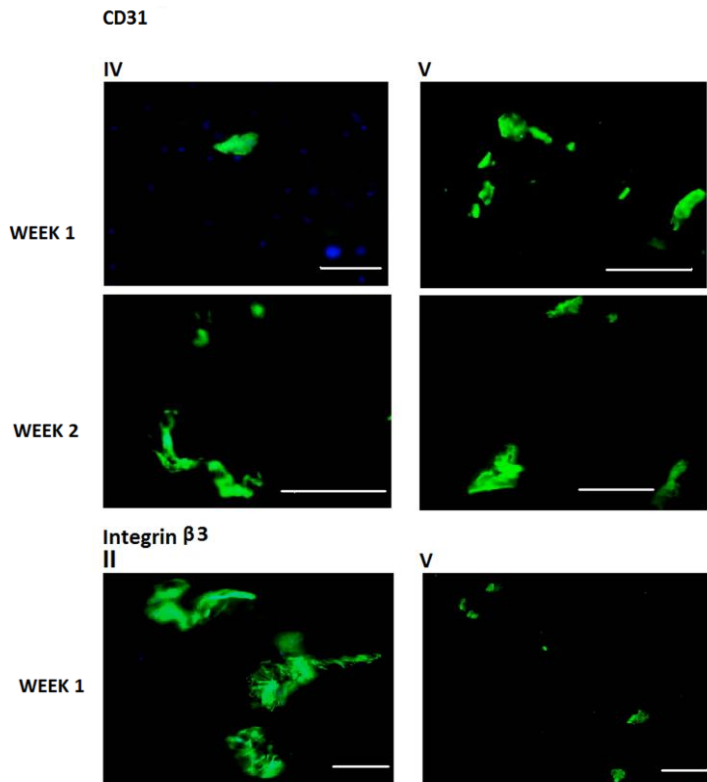
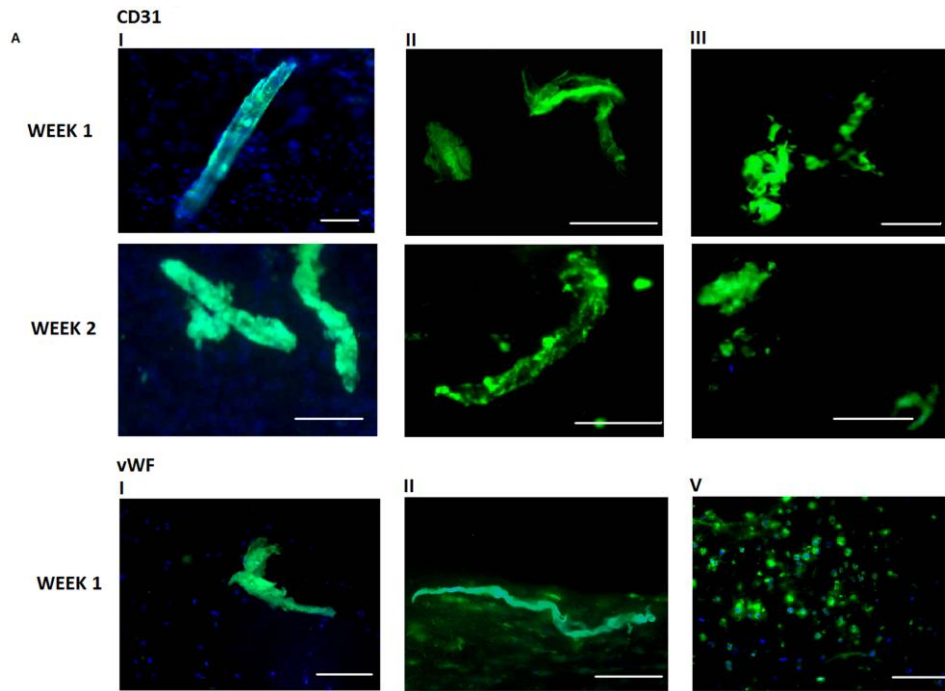
9.1 RESULTS

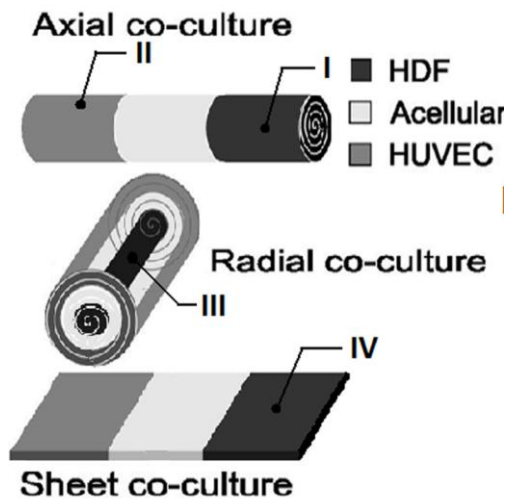
***In vitro* induction of angiogenesis by hypoxia-induced signaling**

HDFs and human umbilical vein endothelial cells (HUVECs) were spatially positioned within sheet or spiral collagen constructs such that the two cell populations were separated by an acellular region (Fig. 1A, also see methods). HDFs were seeded at high density (23.2×10^6 cells/ml) such that in the spiral constructs (axial and radial models) cell O₂ consumption rapidly (within 24h) generated physiological hypoxia (~25mmHg /3.2% O₂) in the HDF compartment's core [173]. In contrast, HDFs within sheet constructs (~200µm thick) were constantly exposed to near culture medium O₂ levels, i.e. non-hypoxia (140-160mmHg/ 18.4-21% O₂,) [173].

We tested the hypothesis that co-culturing hypoxia-induced signaling HDFs (*HIS*-HDFs) with ECs (HUVECs), within 3D spiral constructs, would result in a physiological angiogenic response. In such *HIS*-HDF/EC co-cultures ECs formed CD31 and vWF positive clusters and capillary-like structures (CLSs) with lumens after 1 week *in vitro* culture (Fig.1A). CLS formation in the *HIS*-HDF compartment indicated that ECs had migrated through the acellular region and invaded the *HIS*-HDF compartment by 1 week, suggesting that a functional angiogenic factor gradient was established from the *HIS*-HDFs towards the EC zone. In addition, CLSs in the

EC compartment stained positively for integrin $\alpha\beta3$ (Fig.1A), typical of migrating endothelial cells [307].





H&E

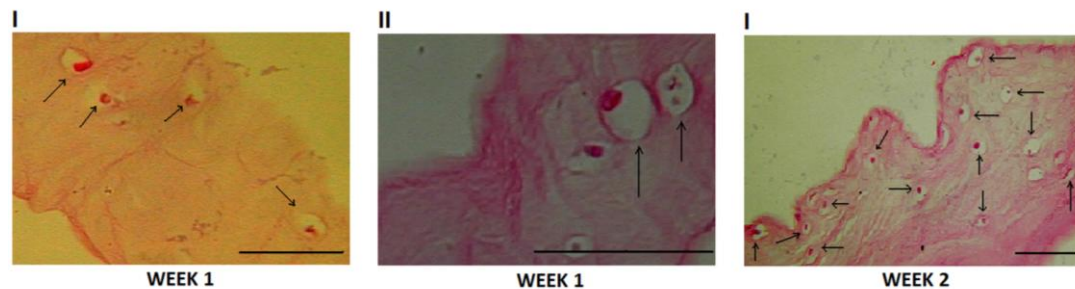
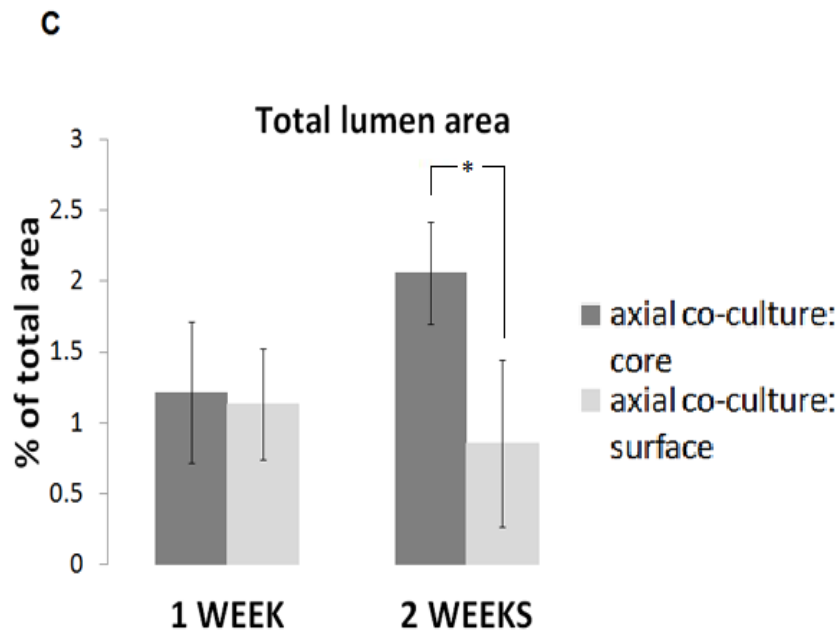
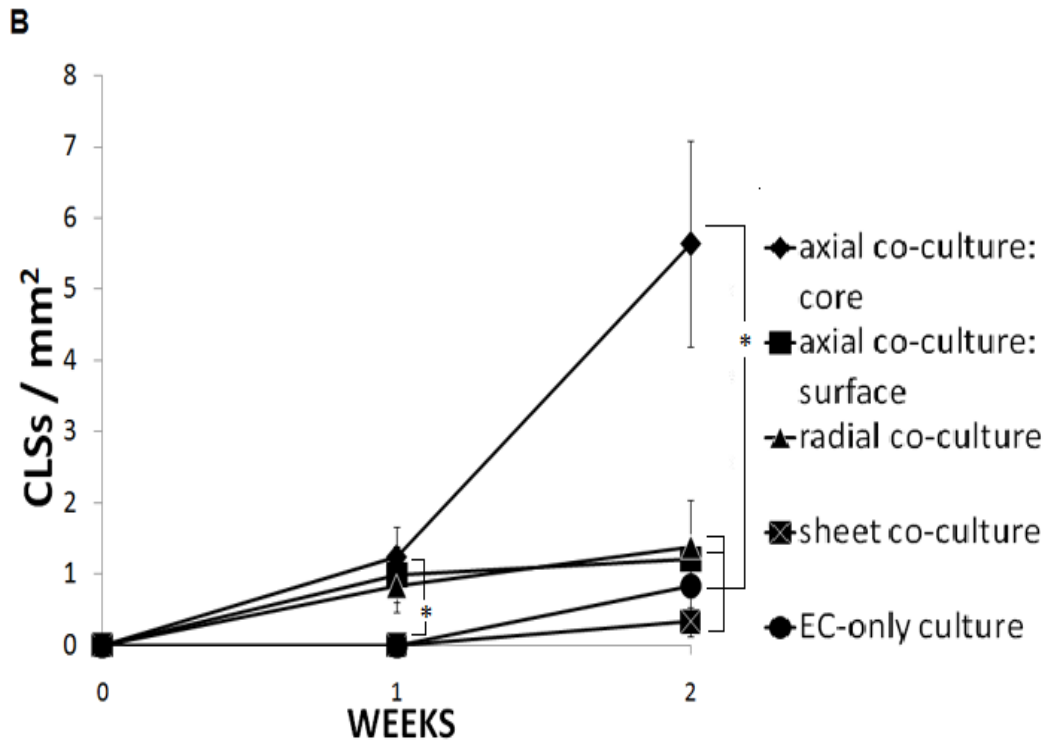
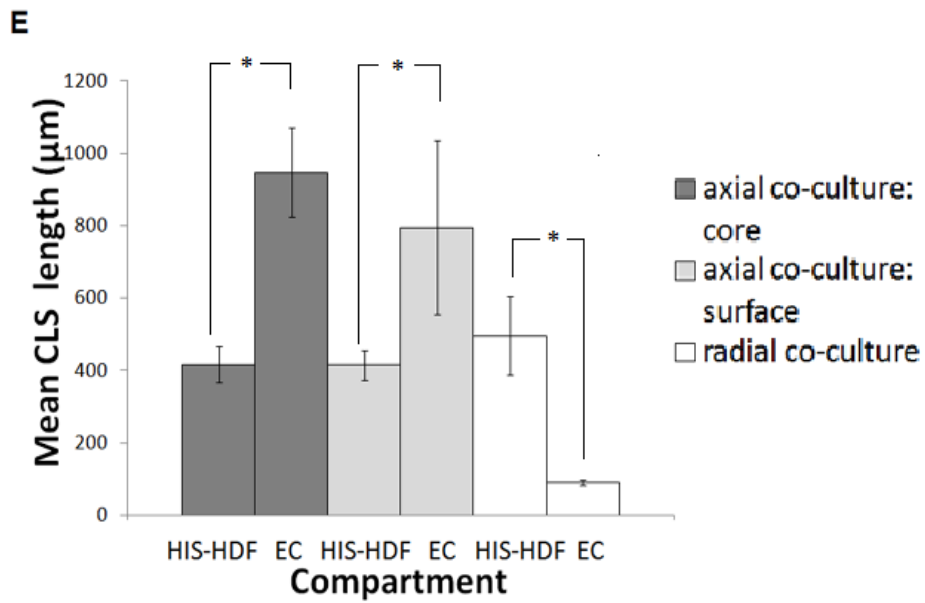
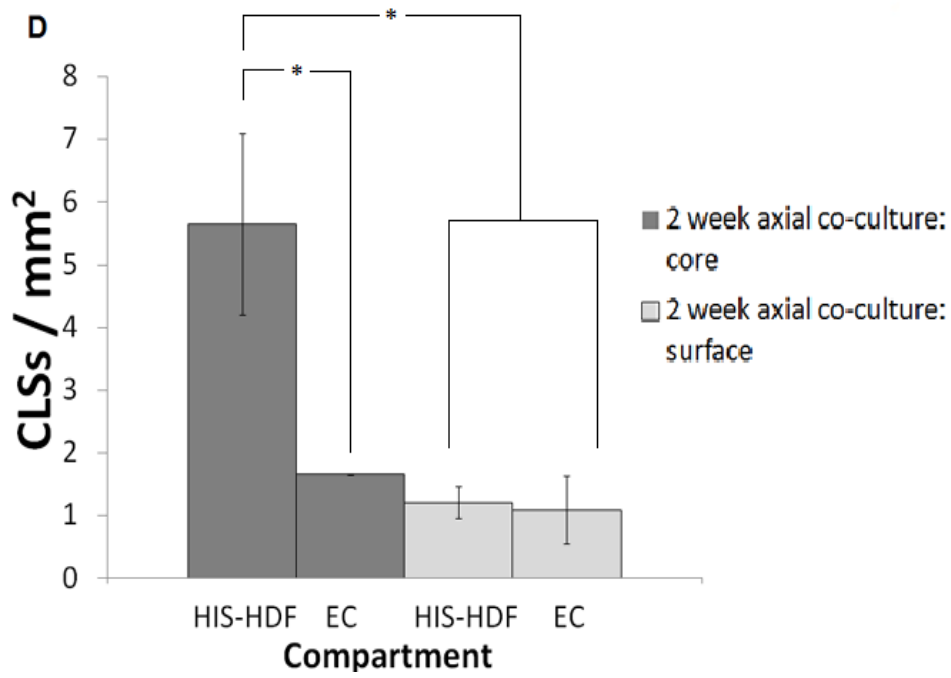


Fig.1

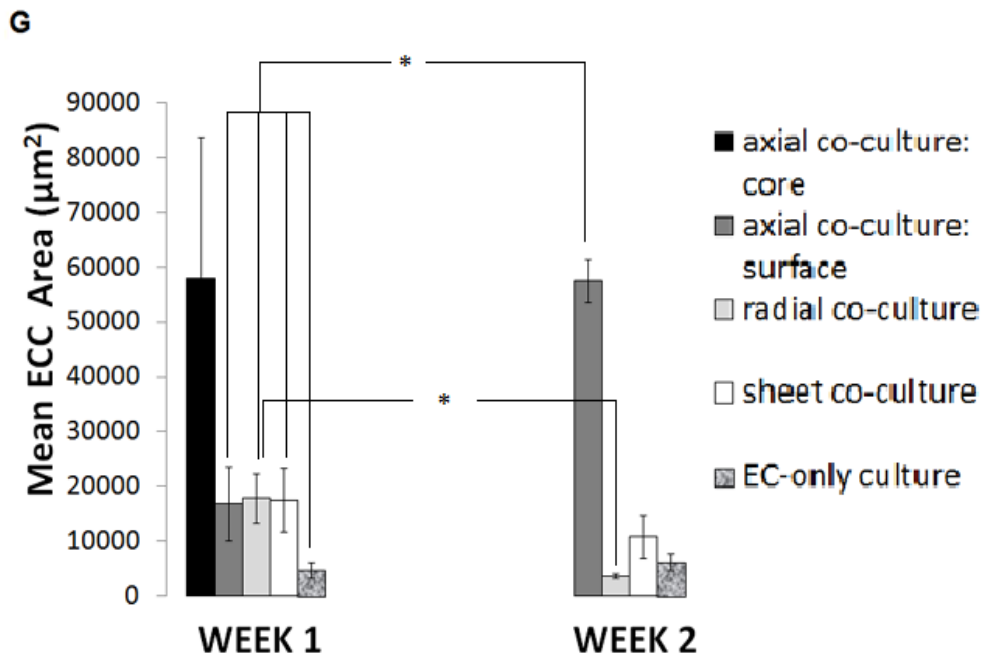
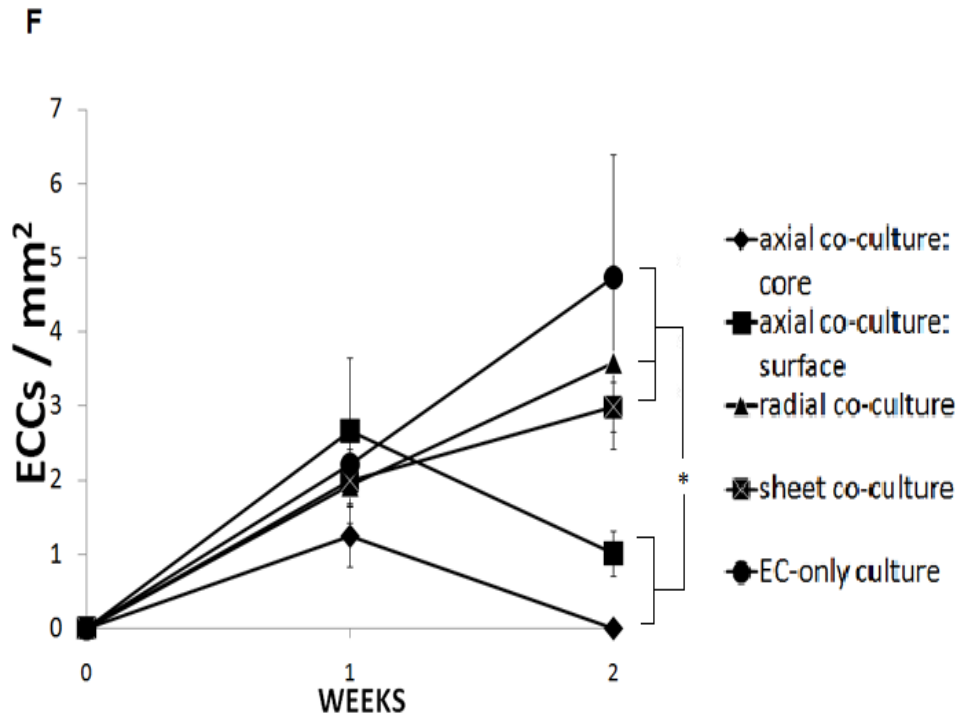
Induction of *in vitro* angiogenesis by hypoxia-induced signalling (*HIS*). (A) Capillary-like structures (CLSs) and endothelial cell clusters (ECCs) in (I) core of *HIS*-HDF/EC axial co-cultures, (II) surface of *HIS*-HDF/EC axial co-cultures, (III) *HIS*-HDF/EC radial co-cultures, (IV) HDF/EC sheet co-cultures and (V) EC only-cultures at 1 and 2 weeks; visualised with human anti-CD31, anti-vWF, anti-integrin $\alpha v \beta 3$ (green) and DAPI nuclear staining (blue) (bars=200 μ m). H&E staining of *HIS*-HDF/EC axial co-cultures (cross-sections) showed CLS lumens (arrowed, bars=100 μ m). Note the increase in the number of lumens in the core of axial co-cultures from 1 to 2 weeks. Schematic indicates the region in the construct where images were taken for the three different co-cultures.



(B) Quantification of CD31+ve CLSs (in HDF compartment) of *HIS*-HDF/EC axial co-cultures (core and surface analysed separately), *HIS*-HDF/EC radial co-cultures, HDF/EC sheet co-cultures and EC-only cultures (1 & 2 weeks). (C) Comparison of core and surface total lumen area (H&E stained sections as % total section area) for *HIS*-HDF/EC axial co-cultures (1 & 2 weeks).



(D) Comparison of CD31+ve CLSs in *HIS*-HDF and EC compartments of axial co-cultures (core & surface; 2 weeks). (E) Mean length of CD31+ve CLSs in *HIS*-HDF and EC compartments of axial co-cultures (core & surface) and radial co-cultures at 2 weeks.



(F) Mean CD31+ve endothelial cell clusters (ECCs) in the HDF compartment of *HIS*-HDF/EC axial and radial co-cultures, HDF/EC sheet co-cultures and EC-only cultures (1 & 2 weeks). (G) Mean ECC area for each condition (1 & 2 weeks). Note ECCs were absent in the core of axial co-cultures at 2 weeks. For plots B, D, E, F, G bars correspond +/-se of means, for plot C bars correspond +/-sd of means, *p<0.05. Four constructs were tested for each condition per time point.

At 1 week all 3D spiral co-cultures (axial and radial models) had significantly greater CLS scores than non-hypoxic sheet co-cultures or EC-only culture controls ($p < 0.05$) (Fig.1B). After 2 weeks only the core of axial co-cultures had significantly greater CLS density, though this was by a factor of 5 to 10 fold depending on which zones/models were compared. Specifically, CLS density was ~6 fold higher in the core of axial co-cultures compared to the surface ($p < 0.05$) (Fig.1B).

In *HIS*-HDF/EC co-cultures the spatial positioning of the two cell populations had a direct effect on the pattern of angiogenesis. In axial model co-cultures there was a significant increase in the number of CLSs, within the *HIS*-HDF compartment, in the core, but not on the surface, from 1 to 2 weeks (Fig.1B). A similar response was also seen for total lumen area, which increased from 1 to 2 weeks only in the core of axial co-cultures, in this case by ~2 fold (Fig.1C). The number of CLSs in the *HIS*-HDF and EC compartments of axial co-cultures was the same at the construct surface, but ~3 fold greater within the core *HIS*-HDF compartment than in the core EC compartment, at 2 weeks ($p < 0.05$) (Fig.1D). In contrast, radial model co-cultures produced a small CLS response at 1 week (same as axial model) but no increase in core CLS score was seen in the radial model from 1 to 2 weeks (Fig.1B), consistent with the idea that the 3D growth factor diffusion barrier is also important.

Mean CLS length within the *HIS*-HDF compartment (both axial and radial models) did not significantly change between weeks 1 and 2 (data not shown). However, the 3D positioning of the *HIS*-HDF and EC populations did significantly influence CLS length at 2 weeks. In axial model co-cultures, CLS length was over 2 fold greater in the EC compartment compared to the *HIS*-HDF compartment, both in the core and on the surface ($p < 0.05$) (Fig.1E). In complete contrast, CLS length in the radial co-culture model was 5 fold greater in the *HIS*-HDF compartment ($p < 0.05$).

Importantly, CLS elongation index (ratio of straight line separation of CLS ends / total CLS length) in the *HIS*-HDF and EC compartments was in the range of 0.8-1 for both culture models, indicating that longer CLSs were straight and directional, rather than tortuous (i.e. guided).

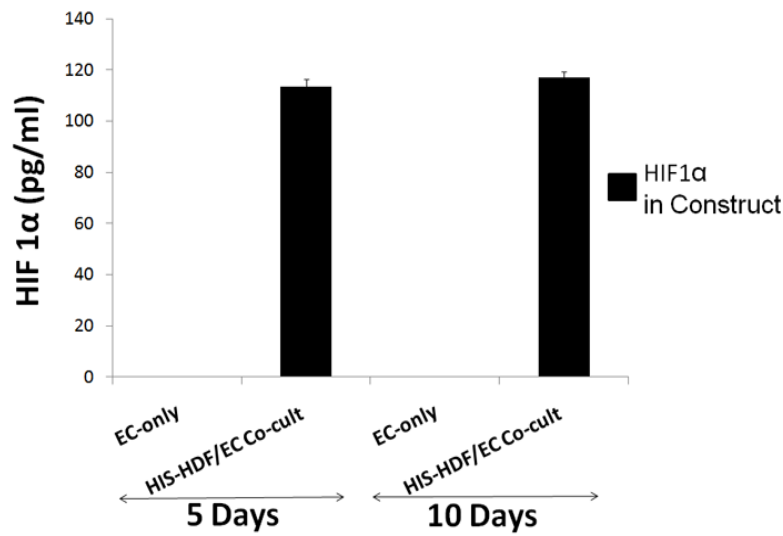
Endothelial cell clusters (ECCs) formed in all culture models by 1 week (Fig. 1F), but while ECC density showed a near-linear increase over 1 to 2 weeks in radial co-cultures, sheet co-cultures and EC-only cultures, it fell by at least a half in axial co-cultures, both in the core and surface regions (Fig.1F). Mean ECC area was inversely correlated to ECC number, showing an increase on the surface of axial co-cultures (no ECCs were detectable in the core of axial co-cultures at 2 weeks) and a reduction (or no significant change) in all other conditions tested, from 1 to 2 weeks (Fig.1G). In combination, these findings would suggest that in axial co-cultures ECCs progressively fused to form larger aggregates or CLSs (in the core), while in all other conditions tested endothelial cells continued to form clusters with no significant change in cluster size.

Hypoxia-induced generation of angiogenic factors

Previous work by this group has shown a dramatic upregulation of VEGF gene expression under physiological hypoxia in the core of 3D HDF-collagen constructs, over 8 days [173]. Figure 2 shows the expression of key angiogenic factors at the protein level over the 5-10 day period of culture. 3D constructs of EC-only cultures (1.16×10^6 HUVECS/ml) and *HIS*-HDF/EC axial co-cultures (23.2×10^6 HDFs/ml and 1.16×10^6 HUVECS/ml in the *HIS*-HDF and EC compartments, respectively) were compared. ELISA was used to quantify HIF1 α and VEGF₁₆₅ protein secreted in

the media or retained within the constructs. As expected no HIF1 α (a nuclear transcription factor) was detected in any of the media. HIF1 α was present within *HIS*-HDF/EC co-culture constructs, but there was no significant difference in HIF1 α levels between 5 and 10 days, indicating that HIF1 α expression had peaked early on during culture (Fig. 2A). This was in agreement with previous data that showed that HDFs were exposed to hypoxia within 24hrs in this system[173]. Importantly, HIF1 α was not detectable within EC-only culture constructs, indicating that ECs in co-cultures were not exposed to hypoxia (EC density was identical in EC-only cultures and co-cultures) (Fig.2A). VEGF₁₆₅ was found both in the media and within the constructs of *HIS*-HDF/EC co-cultures, at 5 and 10 days, indicating that VEGF was partially retained within these nano-porous collagen scaffolds (Fig.2B). VEGF retention: release ratio was approx. 3:1 (construct : medium) at 10 days. While VEGF protein levels showed an increase from 5 to 10 days culture, both in the media and within constructs, this increase was statistically significant only for constructs, with VEGF levels increasing by 7 fold ($p < 0.05$). This was consistent with increasing VEGF gene expression over 8 days [173]. No VEGF was detectable in either the media or within constructs of EC-only cultures, at both 5 and 10 days (Fig. 2B), which was in agreement with the absence of HIF1 α expression.

A



B

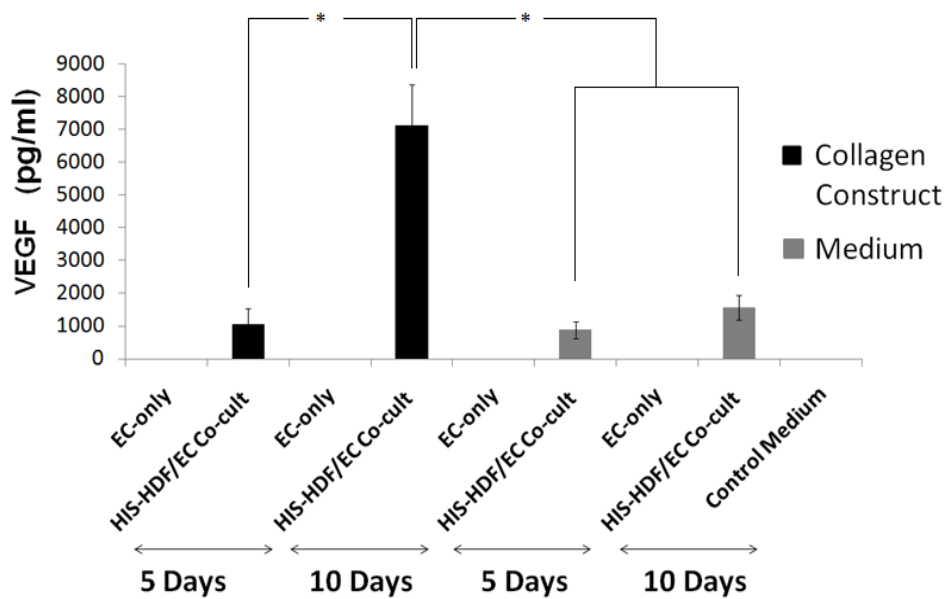


Fig.2

Localised exposure of HDFs to physiological hypoxia resulted in up-regulation of angiogenic factor protein expression *in vitro*. ELISA was used to analyse protein levels of HIF-1 α (A) and VEGF₁₆₅ (B) secreted in the media or retained within collagen constructs of either EC-only cultures (1.16×10^6 /ml) or *HIS*-HDF/EC axial co-cultures (23.2×10^6 HDFs/ml and 1.16×10^6 HUVECs/ml) at 5 and 10 days . Plot (A) shows HIF-1 α within collagen constructs only as no HIF-1 α could be detected in the media. VEGF

was produced into both collagen constructs and media, though not by ECs. Basal (zero) control medium was DMEM supplemented with 5% FCS. Bars correspond +/-sd of means, * $p < 0.05$. For each factor three samples were analysed per time point, per condition tested.

Reversal of angiogenic response to hypoxia-induced signaling

The basic hypothesis here suggests that blocking the function of one of the key angiogenic factors (e.g. VEGF) would reverse the cellular angiogenic response to hypoxia-induced signaling in this 3D system. Ability to block the *HIS* angiogenic response was tested in *HIS*-HDF/EC axial co-cultures pre-incubated with either non-specific IgG or anti-VEGF neutralizing IgG. Anti-VEGF blockade did not affect the previous response in terms of number of CLSs formed within the *HIS*-HDF compartment, either in the core or on the surface at 1 week (data not shown). However, figure 3 shows that anti-VEGF blockade did reduce the mean length of CLSs formed within the *HIS*-HDF compartment. While this inhibition of function was seen in both the core and surface zones compared to non-specific IgG controls, at 1 week, the difference was only significant on the surface ($p < 0.05$). This could be due to partial diffusion of antibody through the construct. Indeed, measurement of IgG permeability through compressed collagen membranes (by filtration test) showed that at least 7% of IgG was retained per collagen layer of the spiral (each spiral comprising 5 layers). The significant, but partial, abolition of function seen at the surface, where VEGF blockade was not limited (constructs incubated at saturating concentration of anti-VEGF IgG) indicated that anti-VEGF treatment was only partially effective in blocking the *HIS* mediated angiogenic response.

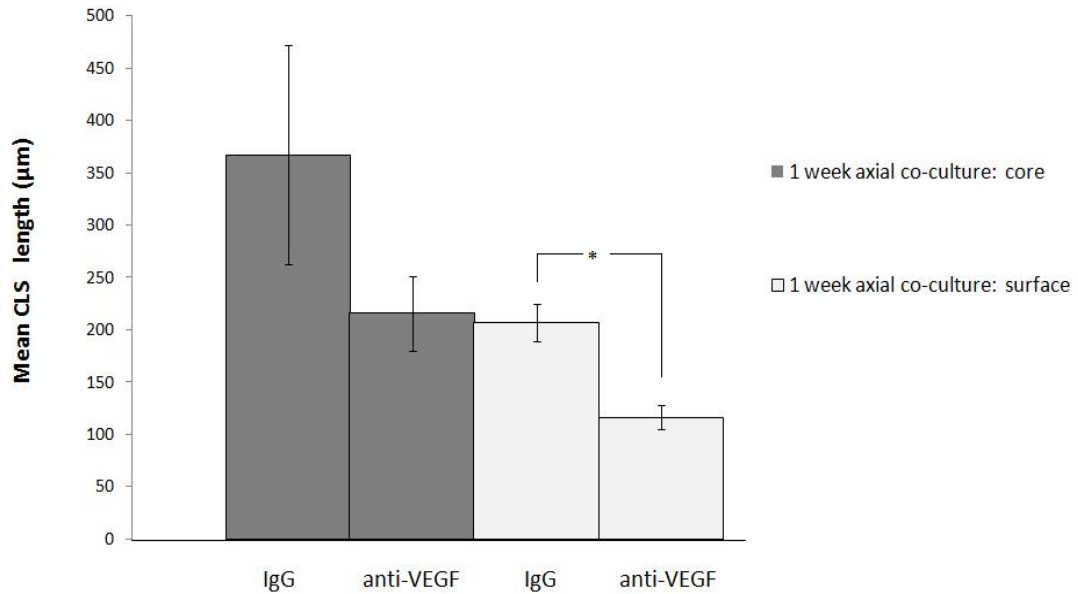


Fig.3

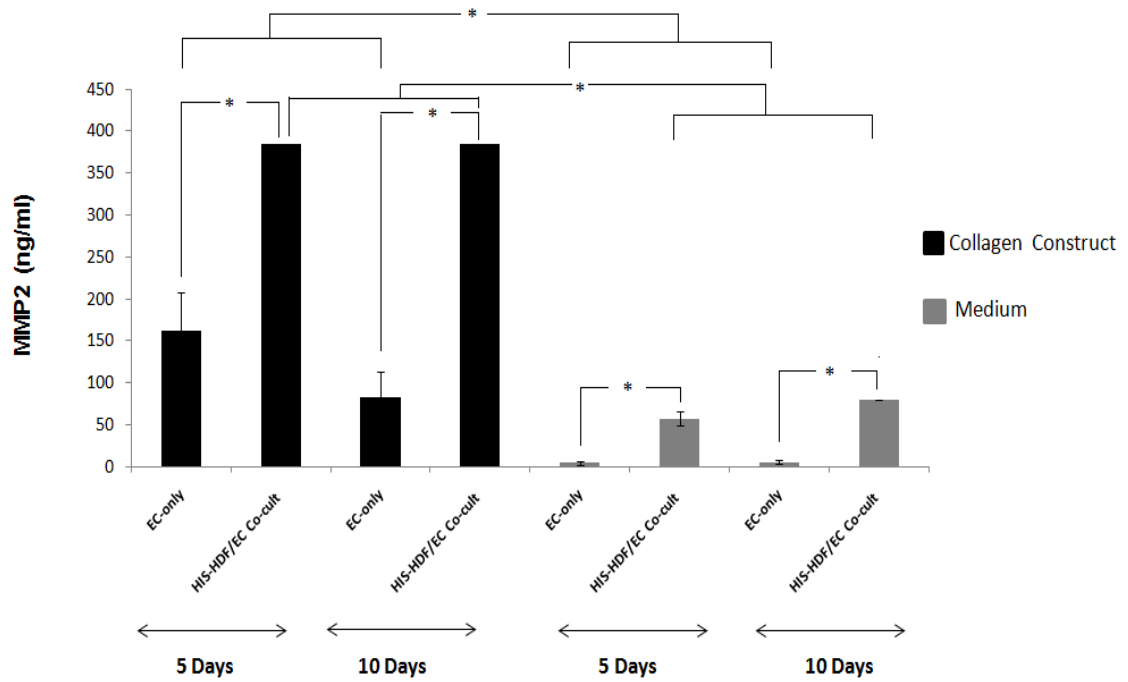
Blocking the function of VEGF only partially abolished the angiogenic response to hypoxia-induced signalling. *HIS*-HDF/EC axial co-cultures were incubated with either non-specific IgG or anti-VEGF IgG, at saturating concentration (10µg/ml), for 1 week and the length of CD31+ve CLSs within the HDF compartment was analysed for the core and surface zones separately. Bars correspond +/-se of means, *p<0.05. Four constructs were tested for each condition.

Matrix remodelling during angiogenic induction

It is well documented that during the early stages of vessel growth, controlled local dissolution of the ECM by proteolytic enzymes, including the matrix metalloproteinases (MMPs), is important not only for the coordinated movement of endothelial cells, but also for the release of sequestered angiogenic molecules [308]. We therefore investigated the expression of two angiogenic factor-regulated MMPs, MMP-2 and MMP-9[308], during angiogenic induction in this 3D system. ELISA was used to analyse protein levels of MMP-2 and MMP-9 secreted in the media or retained within collagen constructs of HUVEC only-cultures and *HIS*-HDF/EC axial

co-cultures over the 5-10 day period of culture. For both culture conditions MMP-2 was present in the media and within collagen constructs, at 5 and 10 days, indicating that MMP-2 was partially retained within collagen scaffolds (Fig.4A). No significant difference in MMP-2 levels was observed, either in the media or within collagen constructs, from 5 to 10 days culture for either culture condition (Fig.4A). However, *HIS*-HDF/HUVEC co-cultures produced significantly higher levels of MMP-2 than HUVEC only-cultures at both 5 and 10 days (~2 and 10 fold difference in media and collagen construct levels, respectively), suggesting additional production of MMP-2 by *HIS* fibroblasts and/or differences in the regulation of MMP-2 expression by hypoxia-induced angiogenic factors [308,309]. Compared to levels of MMP-2, the amount of MMP-9 protein secreted in media or retained within collagen constructs was significantly lower (Fig.4A, B). While MMP-9 was detected in the media and collagen constructs of *HIS*-HDF/HUVEC co-cultures, at 5 and 10 days, no significant amounts were detected in HUVEC only-cultures (Fig.4B). As with the expression of MMP-2, the length of the culture period did not have any significant effect on the levels of MMP-9 protein. The expression of MMP-2 and MMP-9 in this system confirms that the hypoxia-induced angiogenic response observed in *HIS*-HDF/HUVEC co-cultures was accompanied by active matrix remodelling.

A



B

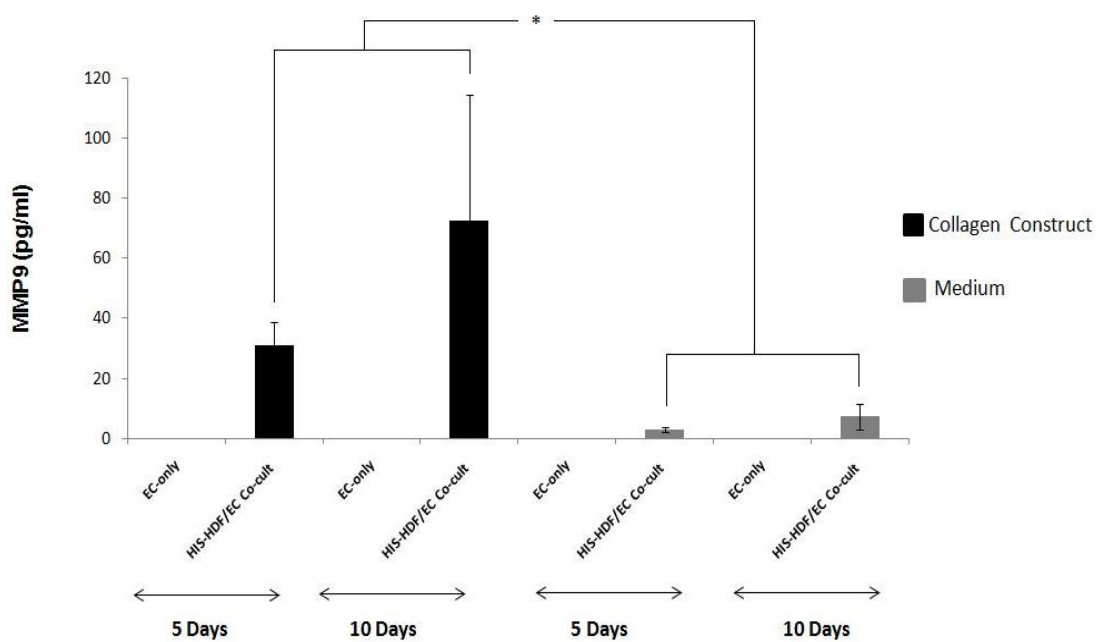


Fig.4 Localised exposure of HDFs to physiological hypoxia results in up-regulation of angiogenic factor-regulated MMPs *in vitro*. ELISA was used to analyse protein levels of MMP-2 (A) and MMP-9 (B) secreted in the media or retained within collagen constructs of HUVEC only-cultures and HIS-HDF/HUVEC co-cultures at 5 and 10

days *in vitro* culture. Bars correspond +/-sd of means, *p<0.05. Three samples per time point were analysed for each MMP, per condition tested.

***In vivo* vascularization of constructs by hypoxia-induced signaling**

We previously found that vascular in-growth into 3D spiral collagen constructs *in vivo*, without insertion of angiogenic signaling, was typically seen 3 weeks post-implantation [54]. We therefore tested if 3D constructs containing *HIS* fibroblasts would become vascularized earlier. The ability to further accelerate construct vascularisation by speeding up angiogenic factor expression through *in vitro* pre-conditioning was also tested. Acellular or rabbit dermal fibroblast (RDF)-seeded collagen constructs were implanted subcutaneously into the back of rabbits. All cell-seeded constructs comprised of a *HIS*-RDF core and an outer acellular wrap (Fig.5, also see methods). Cellular constructs were: (i) low density (5.8×10^6 RDFs/ml) pre-conditioned (LDPC), (ii) high density (23.2×10^6 RDFs/ml) pre-conditioned (HDPC) and (iii) high density (23.2×10^6 RDFs/ml) non-pre-conditioned (HD) constructs.

Total white blood cell count in rabbits implanted with cell-seeded constructs was 8.2, 15.5, 9.1, 5.5×10^9 cells/L on day 0, 1, 7 and 14 respectively, indicating that the inflammatory response had subsided by 7 days.

In contrast to acellular constructs, which showed no visible vascularisation at 1 week, LDPC, HDPC and HD constructs were all visibly vascularised by 1 week *in vivo* (Fig.5A). Importantly, host vessels that had invaded the engineered collagen constructs at 1 week contained intra-luminal red blood cells (RBCs), suggesting that these vessels were perfused by 1 week (Fig.5B). Furthermore, permeating host blood vessels stained positively with anti-CD31 (Fig.5B).

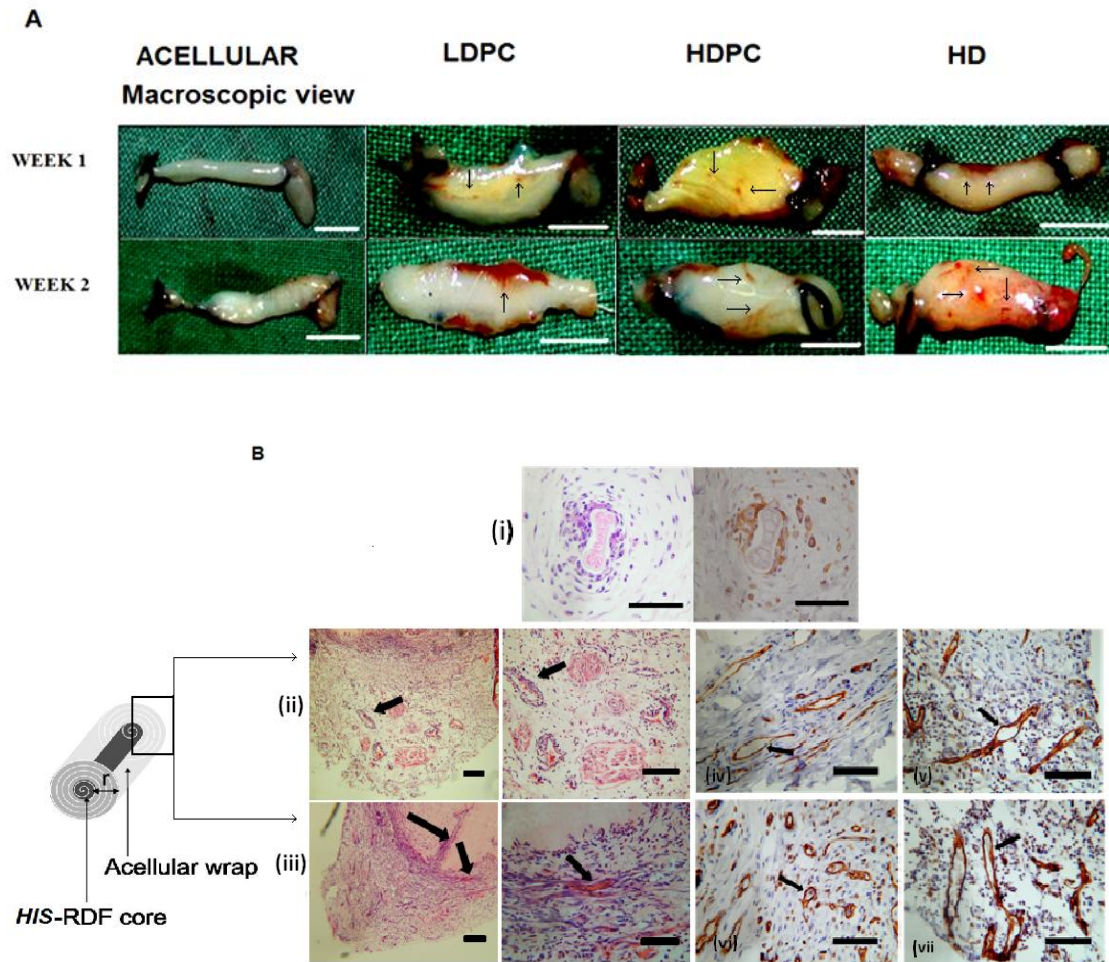
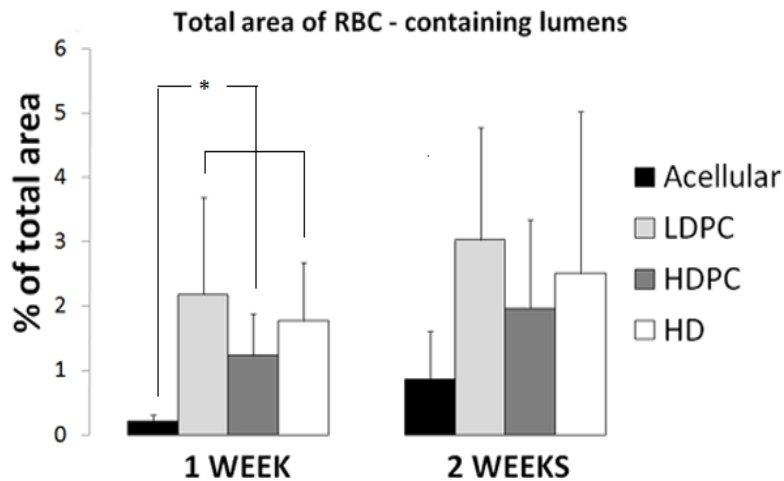
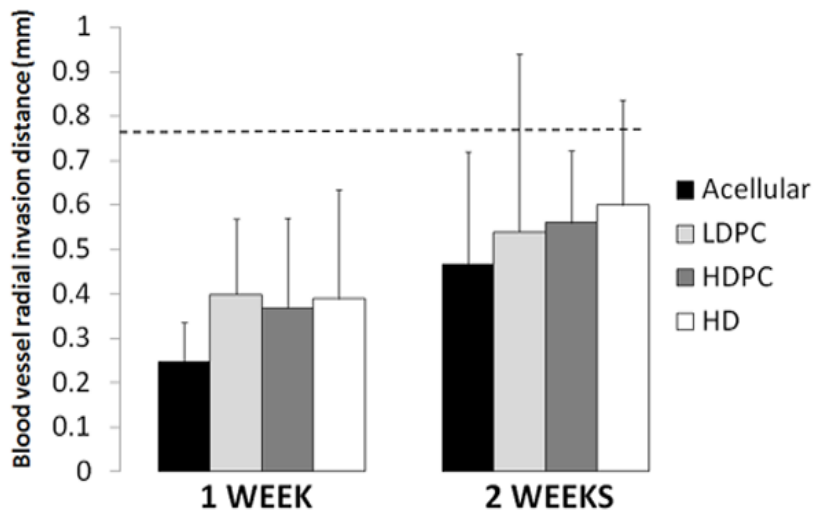


Fig.5

Hypoxia-induced signalling *in vivo* promoted rapid vascularization of cellular constructs. (A) Collagen constructs +/- RDF seeding were sutured subcutaneously into the back of rabbits for 1 or 2 weeks. Cell-seeded constructs were low density (5.8×10^6 RDFs/ml) pre-conditioned (LDPC), high density (23.2×10^6 RDFs/ml) pre-conditioned (HDPC) and high density (23.2×10^6 RDFs/ml) non-pre-conditioned (HD) constructs. Pre-conditioning involved 5 days static culture of constructs prior implantation. Macroscopic images were taken directly after suture removal and implant recovery. Arrows indicate host vessels that had infiltrated the implants (bars=0.5cm). (B) (i) Co-localisation of H&E staining (left panel, showing a red blood cell-filled vessel lumen) with CD31 (right panel, showing endothelial cells lining the lumen) in a 2 week HDPC construct. H&E staining, arrows indicate areas which have been magnified: (ii) Transverse section of 1 week HDPC construct with magnification image. Schematic indicates the corresponding plane within the construct. (iii) Transverse section of 2 week HDPC construct with magnification image. Long arrow indicates penetration of cells towards the construct core. CD31 staining counterstained with haematoxylin, arrows indicate CD31+ve endothelial cells lining vessel lumens: (iv) Positive control-muscle from rabbit. (v) 1 week LDPC construct. (vi) 1 week HDPC construct. (vii) 2 week LDPC construct. All magnification bars are 100 μ m.

C**D**

(C) Quantification of the total area of RBC-containing lumens (total area of all RBC-containing lumens in H&E stained sections as percentage of total section area) in subcutaneously implanted acellular, LDPC, HDPC and HD constructs, at 1 and 2 weeks implantation. (D) Quantification of host blood vessel radial invasion distance (average radial distance of RBC-containing lumens (H&E stained) from construct edge) for all conditions tested, at 1 and 2 weeks implantation. Dashed line indicates the distance (0.77mm) from the constructs' surface to the cellular core. Bars correspond to +/-sd of means, * $p < 0.05$. Six constructs were tested for each condition, for 1 and 2 weeks implantation.

LDPC constructs had the largest total area of invading RBC-containing host vessels, being 10 fold greater than acellular controls ($p < 0.05$), and HDPC constructs the least, after 1 week (Fig. 5C). Although differences between cellular constructs were not statistically significant ($p > 0.05$) due to high variance, the pattern was identical in 2 sets of constructs, harvested at 1 and 2 weeks, suggesting that these trends were real. There was an overall increase in the total area of RBC-containing host vessels in all implanted constructs, including acellular constructs, by 2 weeks post-implantation, consistent with the anti-CD31 staining (Fig. 5B). While all cellular constructs showed greater vascularisation than acellular constructs at 2 weeks, this difference was smaller than at 1 week and not statistically significant ($p > 0.05$) (Fig. 5C). Radial invasion distance of host blood vessels into the collagen spirals was approx. 2 fold higher for cellular constructs compared to acellular constructs at 1 week (Fig. 5D), though blood vessels had only penetrated into the acellular wrap (~0.77mm thickness) in cell-seeded constructs, without reaching the cellular core, at 1 week (Fig. 5D). Acellular construct vascularisation had caught up by 2 weeks, though by this stage some host blood vessels had penetrated into the core of LDPC and HD constructs (Fig. 5D).

In vivo vessel functionality was assessed by real-time monitoring of core O₂ levels in acellular or RDF-seeded spiral constructs, implanted intramuscularly in the back of rabbits, over 2 weeks (Fig. 6A). In this case, cellular constructs were seeded at low density (LD: 5.8×10^6 RDFs/ml) or high density (HD: 23.2×10^6 RDFs/ml) and implanted directly without any *in vitro* pre-conditioning. As before, by 2 weeks host vessels containing intra-luminal RBCs were present in acellular, LD and HD constructs, although both types of cellular constructs were more profoundly perfused than acellular constructs (Fig. 6B). Not surprisingly, initial (day 0, immediately post

surgery) core O₂ levels of LD and HD constructs were approx. 30% ($p>0.05$) and 90% ($p<0.001$) less compared to acellular constructs, respectively (Fig.6C). However, while core O₂ levels of acellular constructs continued to drop over the whole 2 weeks (due to inflammatory and connective tissue host cell infiltration [54]) core O₂ levels of LD constructs leveled off at a min (5-10 mmHg) by day 3. 2 week core O₂ levels in LD constructs were 4 fold higher than in acellular constructs. This correlated with a 2 fold greater area of RBC-containing vessels in LD constructs compared to acellular constructs (Fig. 6D). Core O₂ levels in HD constructs remained low in the first 5 days (due to their seeded cell O₂ consumption), but rose by 5 fold by 1 week. This high level of core O₂ (12-15 mmHg) was maintained over the second week, leaving the HD construct core O₂ 2 and 10 fold higher than LD and acellular constructs, respectively, at 2 weeks. The difference between total area of RBC-containing vessels in HD and acellular constructs was not significant (Fig.6D), despite the significant difference in core O₂ levels at 2 weeks ($p<0.05$) (Fig.6C).

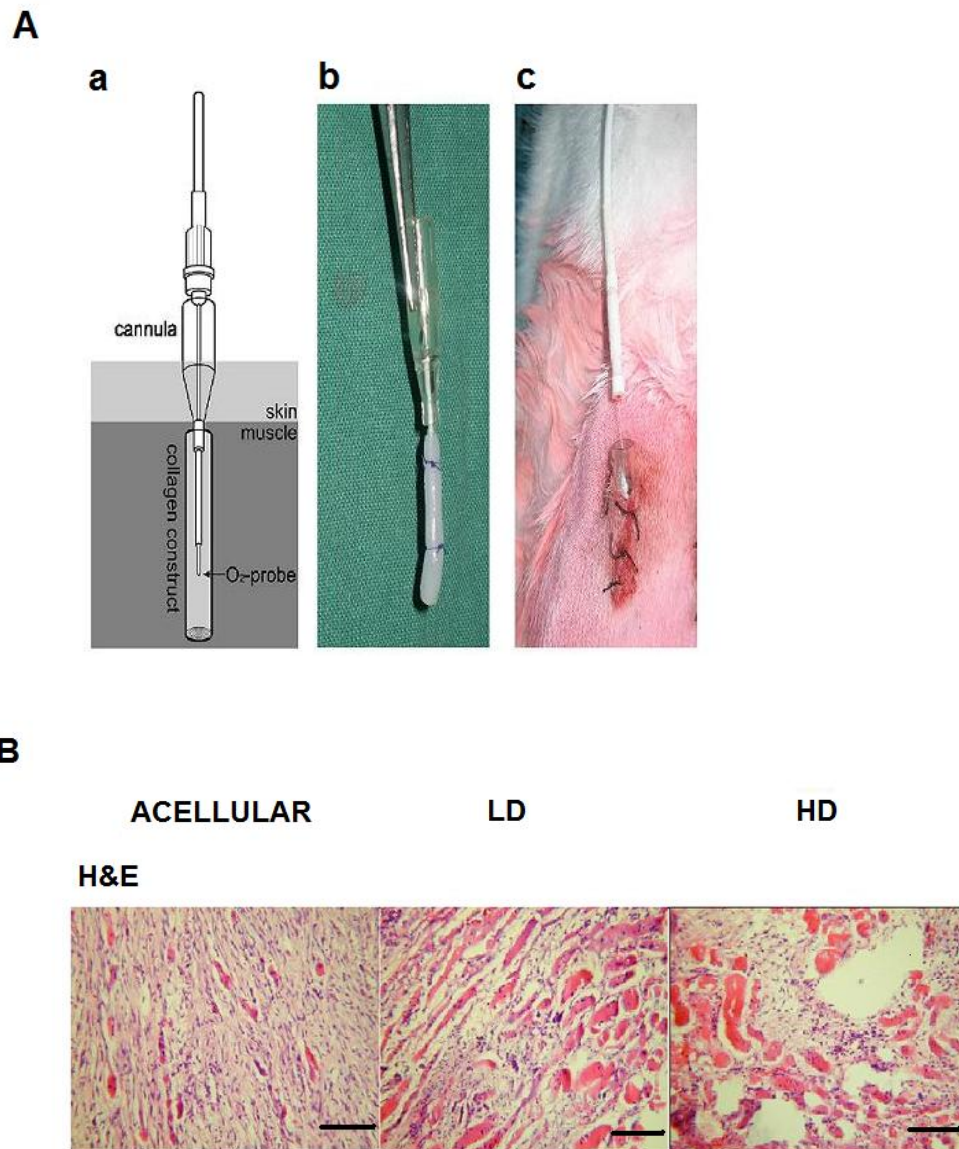
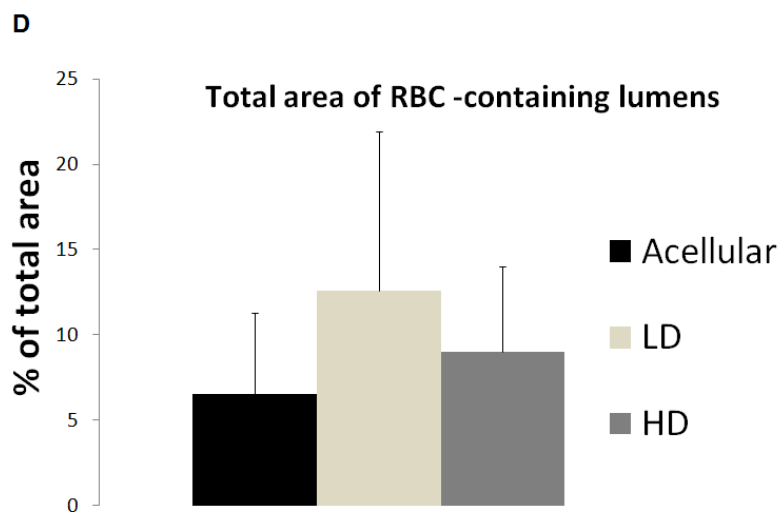
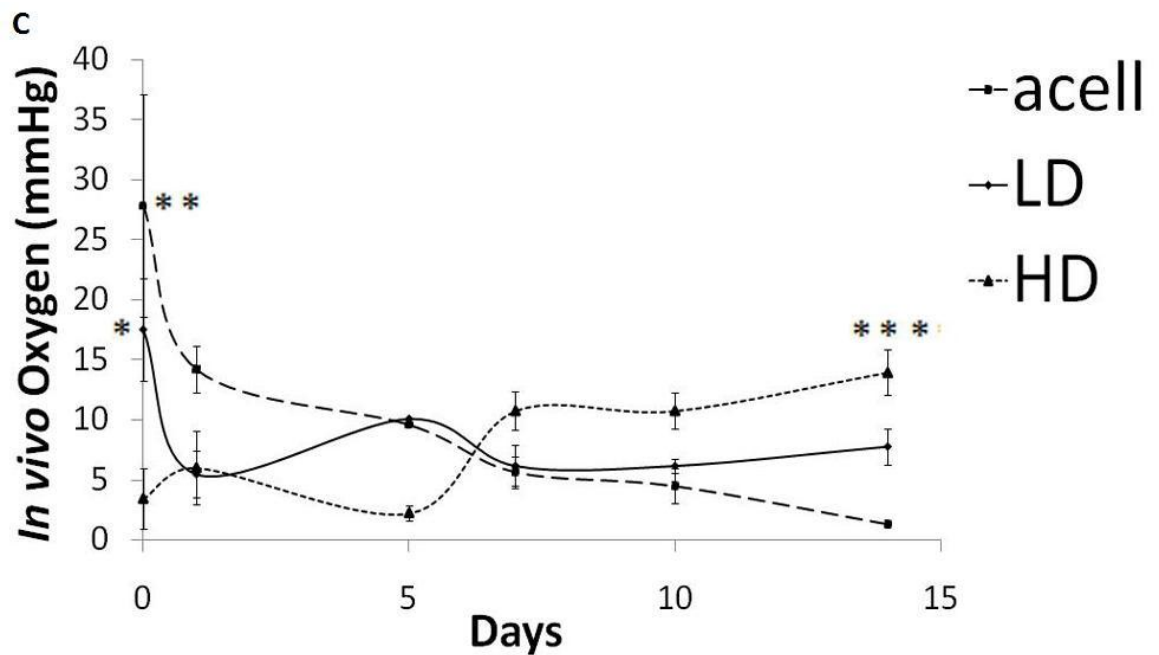


Fig.6

Assessment of the functionality of invading host blood vessels into implanted constructs by real-time monitoring of O_2 levels *in vivo*. (A) (a) Schematic of the setup used to monitor O_2 levels in the core of intramuscularly implanted acellular or cellular collagen constructs. (b) Collagen construct attached to a cannula ready to be implanted. (c) A fibre-optic O_2 probe being inserted into the cannula of a rabbit during real-time monitoring. (B) Vascularization of intramuscularly implanted constructs; acellular, low density (LD; 5.8×10^6 RDFs/ml), high density (HD; 23.2×10^6 RDFs/ml) after 2 weeks implantation. Construct tissue sections stained with H&E show clear increase in RBC-filled vessel lumens in both types of cellular constructs (bars=100 μ m).



(C) O_2 tension in the core of intramuscularly implanted acellular, LD and HD constructs over 2 weeks implantation. Results are presented as partial pressure values (pO_2) in mmHg (7.6mmHg corresponds to 1% O_2). Time zero values represent readings taken in constructs immediately after implantation. Bars correspond \pm se of means, * $p < 0.01$ (HD vs. LD at day 0), ** $p < 0.001$ (HD vs. acellular at day 0), *** $p < 0.05$ (HD vs. acellular at day 14). Three constructs were tested for each condition (one construct per rabbit). (D) Quantification of the total area of RBC-containing lumens (H&E stained cross sections, as percentage of total section area) in acellular, LD and HD constructs after 2 weeks implantation. Bars correspond to \pm sd of means). Three constructs ($n=3$) were tested for each condition.

9.2 DISCUSSION

Original Hypothesis: Spatially controlled hypoxia-induced angiogenic factor signalling by fibroblast populations, exposed to local cell-mediated hypoxia in 3D collagen matrices, will promote directed endothelial cell migration and tubule formation in vitro and in vivo.

The well recognized principle of complex spatio-temporal/chemical co-ordination in angiogenesis [196,310,311] was highlighted here in the finding that functional blocking of VEGF only partially abolished the *HIS* angiogenic response *in vitro*. This has important implications for engineering angiogenesis. Indeed, trying to mimic the necessary physiological complexity using bottom-up engineering of angiogenic cocktails appears to be near insurmountable at our current level of understanding [310,312,313]. A clear alternative is to engineer the onset of the process by producing local hypoxia (which is easier to control) in engineered cell populations to upregulate hypoxia-induced signaling (i.e. a physiological angiogenic cascade). The problem then shifts from trying to mimic a complex chemical language to engineering a predictable local cell-hypoxia.

Exposure of cells to physiological hypoxia has been shown to be effective in activating the production of cell-generated angiogenic factors [173,192,314]. In this study we have demonstrated that O₂ consumption by a high density depot of normal HDFs generated a self-sustaining *HIS* cell response leading to the production of a functional sequence of critical angiogenic factor proteins. While physiological regulation of the O₂ microenvironment in this system maintained a high cell viability (>80%) up to 5 days, some level of *HIS* cell damage or death is expected over longer culture periods[173]. It is important to note, however, that metabolic products

released from hypoxic tissues (e.g. lactate, pyruvate, adenosine, malate) have been reported to be intermediate effectors of angiogenesis[315], rather than inhibit the process. *In vitro* this resulted in EC migration and tubule formation towards the source of angiogenic factors (*HIS* cells) by 1 week. In contrast to other co-cultured (2D) models with mixed cell populations [207,316,317], this model enables the spatial segregation of distinct directing and responder cell populations to test the effect of contact-independent cell signalling i.e., endothelial cell migration/tubule formation along an angiogenic growth factor gradient (note: the stability of cell segregation in this model was achieved by the large separation distance (1.5cm) between the cell compartments and the retardation of fibroblast migration in compressed/dense collagen matrix (see Chapter 7). The ability to spatially position *HIS* cells within a 3D construct also means that exposure of endothelial cells to cell-generated hypoxia (and its negative impact on cell viability[318]) is avoided, which would not be possible with mixed co-culture. Importantly, this novel seeding technique lays the foundation for developing endothelial cell-free angiogenic implants (tested here *in vivo*), eliminating cell source limitations and ethical considerations. The absence of angiogenic responses in both EC-only cultures and sheet co-cultures (no hypoxia) demonstrates the need for hypoxia-induced signaling, rather than simple presence of HDFs. Although readily available HDFs were used for *HIS* generation, for simplicity, work from this group and others has shown that multiple cell types (e.g. bone marrow-derived stromal cells, vascular smooth muscle cells) respond to physiological hypoxia by upregulating angiogenic signaling [55,201,204,319,320], suggesting that different cell types could be used as the source of *HIS* cells, provided that cells are exposed to optimum (i.e. cell-type specific)

levels of physiological hypoxia [173,204]. It is likely then that this mechanism of engineered angiogenesis can be adapted to many tissues.

The target of this study was to test and evaluate the ability of *HIS* cells, controlled using a model engineered tissue, to induce effective vascularisation. Importantly, a collagen type I support material was used to ensure a biomimetic tissue microenvironment [25]. The predictive importance of the 3D collagen model for practical, precise operation of the engineered angiogenesis cannot be overemphasized. It is clearly possible to use the demonstration of hypoxia-induced angiogenesis by simply packing a large number of cells deep into any 3D construct. However, while this is eventually likely to generate some form of angiogenic growth factor cascade, it is actually of very limited practical significance without the precision and control. The key new element here is that it is possible in principle, not only to predict and tune when the angiogenic burst is released, but to what extent, how long for and most importantly, where from. The anisotropy of the 3D collagen model reflects the anisotropy found in almost all native tissues. There are two levels of important anisotropy. The first and least obvious, lies in the ability for small molecules (e.g. oxygen, glucose, lactate) to diffuse rapidly in most directions through the collagen nano-fibre mesh, even at high collagen densities [173,297]. Therefore, in spiral constructs O_2 tension is almost entirely determined by cell O_2 consumption (as discussed in Chapter 8) [55]. Importantly, work from this group previously showed that the generated O_2 consumption gradient (core $O_2 <$ surface O_2) correlates with greater VEGF gene expression in the core compared to the surface [173]. A functional output of this anisotropic effect was the stronger angiogenic response observed in the core vs. the surface of *HIS*-HDF/EC axial co-cultures at 2 weeks. The second level of anisotropy relates to the diffusion of macromolecules.

Since these have longer transit times through the nano-porous collagen mesh, the direction and magnitude of macromolecular (e.g. angiogenic factor protein) gradients will mainly be determined by the diffusive properties of the matrix [237]. In spiral collagen constructs macromolecule diffusion would predominantly occur along the path of least resistance i.e. primarily between collagen matrix layers, with slower diffusion through layers. In axial model co-cultures this would generate a strong axial angiogenic factor gradient from the *HIS*-HDFs to the ECs, while in radial model co-cultures the presence of this diffusion barrier would reduce the radial angiogenic factor gradient established between the two cell populations (Fig.7). This could explain why a greater CLS score was obtained in axial model co-cultures (core) than in radial model co-cultures at 2 weeks.

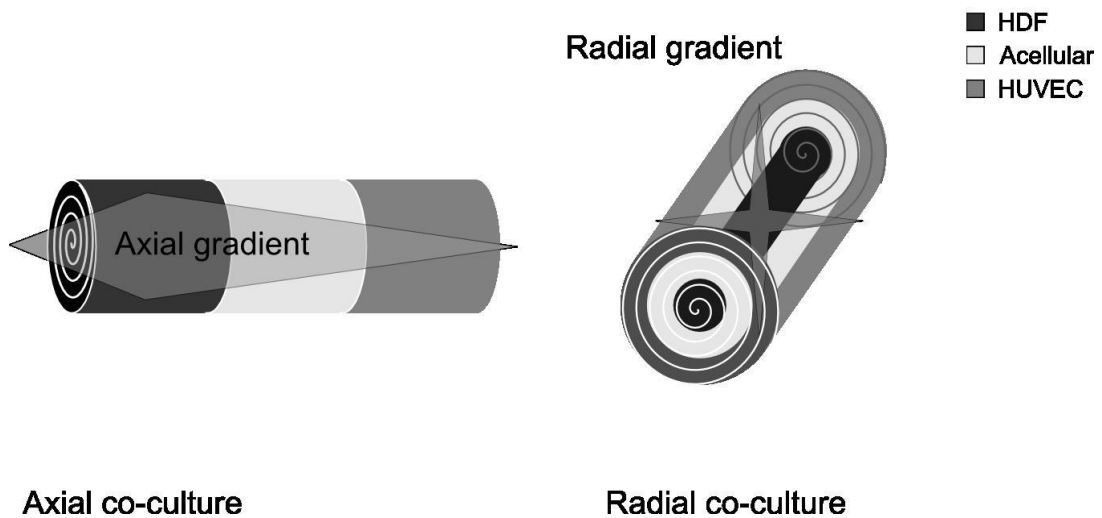


Fig.7 Schematic showing the proposed 3D spatial organisation of angiogenic factor gradients in the *in vitro* model used to investigate the induction of angiogenesis by hypoxia-induced signalling. In spiral collagen constructs, diffusion of macromolecules (i.e. angiogenic factor proteins), produced by *HIS* cells (HDFs), is predicted to follow predominantly the path of least resistance, primarily between collagen matrix layers. Diffusion will be far slower through the layers (i.e. across the thickness of the dense collagen layers). Based on this analysis, in *HIS*-HDF/EC axial co-cultures (left panel) a strong axial angiogenic factor gradient would be generated from the *HIS* cells at one end to the ECs at the other (i.e. between the spiral layers). However, in *HIS*-HDF/EC

radial co-cultures (right panel) a much smaller diffusion gradient would be expected to develop between the two cell populations, limited by the reduced protein diffusion rate through the dense collagen layers. This prediction, tested here, suggests that spatially-defined, biomimetic depot-release can be achieved, making it possible to direct the angiogenic gradient to a required 3D tissue position.

EC migration has previously been observed in response to gradients of VEGFA 165 [195]. In the present system far more HIF-1 α and VEGF was generated in the *HIS*-HDF compartment than the EC compartment, where growth factor proteins were undetectable (as demonstrated in the EC-only cultures). This expression correlated closely with the larger number of CLSs formed in the *HIS*-HDF compartment than in the EC compartment at 2 weeks (core of axial co-cultures). In contrast, CLS length was influenced primarily by the spatial position of ECs relative to *HIS* cells in the spiral. In axial model co-cultures, where ECs were aligned with the axial angiogenic factor gradient (Fig.7), longer CLSs formed in the EC compartment than in the *HIS*-HDF compartment, i.e. furthest away from the growth factor source, at 2 weeks. This is consistent with ECs forming tubular structures back along a gradient, towards its source. Importantly, in radial model co-cultures, where protein growth factors had to cross the low permeability collagen layers (i.e. a diffusion barrier) to reach the responder ECs, CLSs in the EC compartment were shorter. The proposed generation of angiogenic factor gradients in this system, then, seems to recapitulate the native tissue in that the effects of protein factors are superimposed (sometimes dominated) by the ECM 3D structure and its enabling or restricting effects on growth factor diffusion [321]. This was further highlighted by the finding that *HIS*-HDF/EC co-cultures produced higher levels of angiogenic-factor regulated MMPs (MMP-2 and -9) [308] than EC-only cultures, which supports the idea that the *HIS* angiogenic

response may also mediate ECM remodeling, a critical component of physiological angiogenesis[308].

In contrast to CLS formation ‘clustering’ appeared to be an intrinsic EC behavior rather than a response to hypoxia and angiogenic protein generation [316]. While there was minimal or no HIF-1 α and VEGF accumulation in EC-only cultures up to 10 days, this did not prevent EC clustering. However, CLS formation only occurred where a *HIS*-HDF population was present, suggesting that whilst there may be a cluster-to-CLS transition, it critically depends on the presence of angiogenic factors to progress all the way to CLS formation. Importantly, cluster formation did precede CLS formation, suggesting that it is a prerequisite step.

HIS cell-generated *in vivo* angiogenesis was achieved within 1 week compared to studies where scaffold vascularisation by exogenous delivery of growth factor cocktails takes a minimum of 2 weeks [310,312,313]. This time delay is critical for implanted tissues, inevitably governing their dimensions and success rate [94]. *HIS* cell-generated growth factor production, in the present study, successfully accelerated the formation of functional vessels *in vivo* by 1 week. The proposed mechanism is recapitulation of angiogenic sprouting from the host, as it is known that sprouts are formed from existing vasculature in response to gradients of angiogenic proteins from avascular (as in this model) or ischaemic tissue [202]. As discussed above, the *HIS* approach to engineered angiogenesis removes the need to seed constructs with endothelial cells [317], eliminating cell source limitations and ethical considerations. A previous study by this group showed that a minimum of 3 weeks is required for functional vascularisation of low cell density implants [54]. The present study showed that even these low cell density constructs have enhanced vascularisation (by 1 week) when pre-conditioned for 5 days *in vitro*, to optimally

up-regulate angiogenic signaling [173]. Other groups have reported that hypoxic pre-conditioning of implanted bone marrow cells increases their angiogenic potency through up-regulation of VEGF expression [319,322,323]. This might have important implications for use of hypoxic pre-conditioning as an additional strategy to vascularise *HIS* cell-seeded constructs post-implantation. In our model there was no histomorphometric improvement of angiogenesis *in vivo* using high cell density constructs, suggesting that an angiogenic factor cascade is generated at threshold O₂ levels or that *in vivo* there is a maximum speed of response, independent of growth factor levels. This has practical, bio-processing importance where cell availability is a limiting factor.

Real time measurement of changing *in vivo* local O₂ levels, deep inside the implant, is probably the most effective/relevant functional outcome of angiogenic engineering currently available. This provides direct readout of the integration and likely survival of constructs [324], making close analysis of the core O₂ data particularly important. While core O₂ tension was initially determined by resident (seeded) cell consumption, competition for O₂ (and likely other nutrients, not measured here) between implant and native tissue became increasingly dominated by surrounding/in-growing host cell consumption, as shown by the acellular construct baseline which dropped below that of cellular constructs by 5-7 days. Furthermore, since there was clear histological evidence of greater infiltration of RBC filled vessels in 14 day LD and HD constructs than in acellular constructs, it is probable that the 4 and 10 fold difference in core O₂ at day 14, respectively, was due to increased vascular perfusion. Histological analysis demonstrated that there was some level of cell death within LD and HD constructs, indicated by the presence of cell sparse areas (especially in the core, data not shown), by 2 weeks implantation.

However, since cell death is hypoxia-driven, it cannot have exceeded the acellular construct baseline, confirming the histological data which suggest that the higher 14 day O₂ levels measured within cell-seeded constructs were a result of increased vascularisation and not reduced cell O₂ consumption. These results further indicate that the *HIS* response was sustained long enough for effective angiogenic induction. While it is intended that rapid vascularization of native tissue surrounding the implant will also rescue the *HIS* cell depot, maintaining angiogenic signaling, further *in vivo* work is required to identify the precise effect of initial nutrient deprivation on *HIS* cell viability. Importantly, the O₂ level obtained in HD implants at 14 days (~15mmHg / 2%) was near the range reported for normal muscle (20-30mmHg / 2.6-3.9%) [325], indicating that the implants had at least partially integrated with the host tissue.

9.3 CONCLUSIONS

While it is widely accepted that long-term exposure of cells to hypoxia can be detrimental to cell viability, the results of this study demonstrate for the first time that spatially controlled, cell-mediated hypoxia can be employed as a stimulus to trigger the complete angiogenic factor cascade for induction of a rapid, physiological angiogenic response *in vitro* and *in vivo*. The control and predictability of this system means that this can genuinely claim to be engineered angiogenesis. Indeed, the system not only allows the timed switching ‘on’ of local angiogenesis, but also its spatial location and even direction. Our findings suggest that while it might not yet be possible to contain the extent of engineered ‘on-off’ angiogenesis *in vivo* (as assessed by histological appearance), this system can be used to successfully

engineer early functional vascular perfusion of implants, as seen by deep tissue oxygenation. The ability to spatially localize *HIS* cells within a 3D tissue construct provides a powerful tool for tissue modeling *in vitro* (e.g. tumour angiogenesis [326,327], drug testing [207]), as well as pre-vascularization or pre-conditioning of engineered constructs for improving perfusion post-implantation [294,328]. Furthermore, the system is sufficiently flexible and robust to form the platform for a range of practical angiogenic therapies. A key strength of this study is the correlation of engineered angiogenesis with *in vivo* O₂ monitoring. This is a powerful indicator of successful construct vascularization, survival and integration. Assessment of O₂ and nutrient delivery to any implanted tissue forms the ultimate test of the ability of an engineered vasculature to function effectively.

9.4 MATERIALS & METHODS

Scaffold fabrication and culture

HDF-, HUVEC- and RDF-seeded rat-tail type I collagen gels were prepared as previously described [25] (see Chapter 2). For preparing HDF/HUVEC co-seeded gels, separately pre-cast collagen gels (size:1.5(L) x 1.5(W) x 1(H) cm) containing 2×10^6 HDFs or 1×10^5 HUVECs were co-transferred into rectangular moulds (size: 4.5(L) x 1.5(W) x 1(H) cm), maintaining a 1.5cm separation distance between them and bathed in 2.25ml acellular collagen solution. The acellular collagen was allowed to set and integrate between the 2 other cellular gels in a 37°C, 5% CO₂ humidified incubator for 30min (Fig.8A) prior to plastic compression (see Chapter 2). For preparing RDF-seeded gels, collagen gels (size:1.5(L) x 1.5(W) x1(H) cm)

containing 5×10^5 or 2×10^6 RDFs were transferred into one end of rectangular moulds (size: 4.5(L) x 1.5(W) x 1(H) cm), 4.5ml acellular collagen solution was poured into the mould (to fill the other end) and allowed to set and integrate at 37°C for 30min (Fig.8B). Following 30 min setting gels were compacted by plastic compression, which did not significantly reduce cell viability [25]. Cell densities increased proportionally to the reduction in gel volume by fixed mass loading over a porous filter paper support [25]. Post-compression cell densities (calculated based on fluid loss) were 1.16×10^6 HUVECs/ml in HUVEC-seeded constructs; 23.2×10^6 HDFs/ml and 1.16×10^6 HUVECs/ml in the HDF and HUVEC compartments of HDF/HUVEC co-seeded constructs, respectively; 5.8×10^6 or 23.2×10^6 RDFs/ml in the RDF compartment of RDF-seeded constructs. Compressed collagen sheets were immediately rolled either along their long or short axis, to produce tightly wound spirals of 45mm length, 1mm diameter or 15mm length, 2.3mm diameter, respectively. HUVEC-only seeded and RDF-only seeded constructs were spiraled along their short axis. RDF-seeded spiral constructs comprised of a cellular core and an acellular wrap (Fig.8B). HDF/HUVEC co-seeded constructs were either not spiralled, i.e. cultured as flat sheets (sheet co-culture) or spiralled before culture. Spiralling along the long axis axially aligned the HDF and HUVEC compartments (axial co-culture), while spiralling along the short axis positioned the HDF compartment in the core and the HUVEC compartment on the surface (radial co-culture) (Fig.8A). HDFs and RDFs in spiral constructs were referred to as *HIS*-HDFs and *HIS*-RDFs, respectively, to indicate their function as hypoxia-induced signaling (*HIS*) cells.

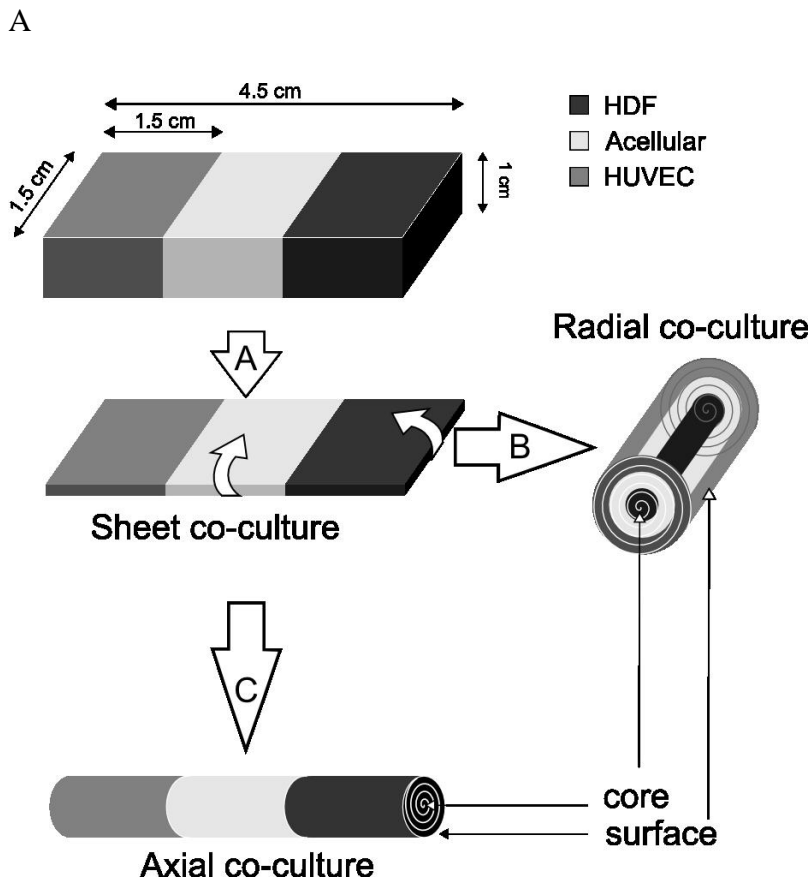
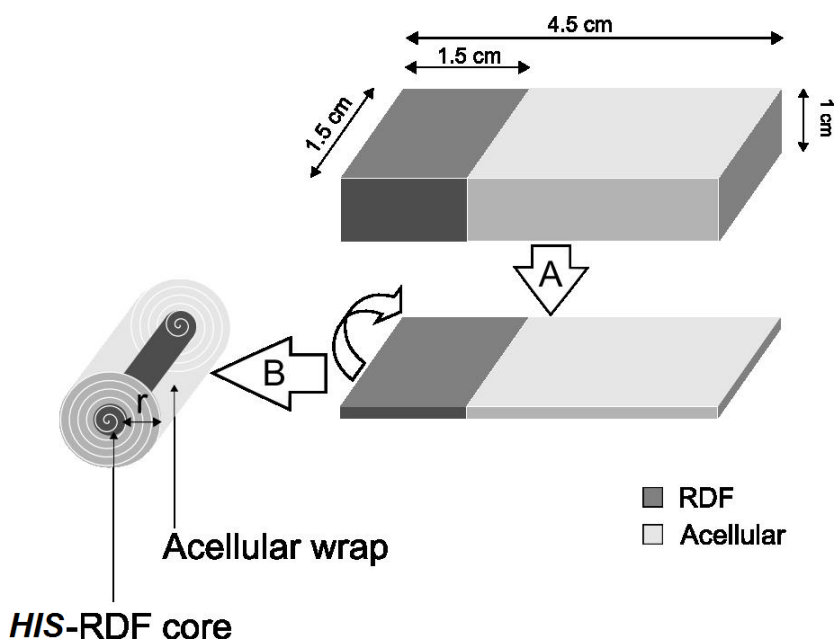


Fig.8 Experimental design for development of constructs used for *in vitro* and *in vivo* testing. (A) Schematic of the fabrication process for HDF/HUVEC co-seeded collagen constructs. Collagen hydrogels (size: 4.5x1.5x1cm) were cast to give three equal sized (1.5x1.5x1cm) compartments; (i) HDF compartment (2×10^6 HDFs), (ii) middle acellular compartment, (iii) HUVEC compartment (1×10^5 HUVECs). Once set, all were compacted together by plastic compression (A) to a $\sim 200\mu\text{m}$ thick sheet, without significant reduction in cell viability. Post-compression HDF and HUVEC cell densities were 23.2×10^6 and 1.16×10^6 cells/ml, respectively. Compressed constructs were cultured as flat sheets (sheet co-culture) or rolled along their short (B) or long (C) axis into tight wound spirals, 15mm x 2.3mm or 45mm x 1mm (length x diameter), respectively. The axial co-culture model (C) gave axial alignment of HDF and HUVEC compartments whilst the radial co-culture model (B) had an HDF compartment at the core and HUVECs on the surface. Cells in non-spiral, sheet co-cultures were always $\leq 100\mu\text{m}$ from medium O_2 levels, i.e. exposed to normoxia. In spiral constructs, core HDFs produced physiological hypoxia zones (measured[173]) and so were referred to as *HIS*-HDFs, reflecting their function as hypoxia-induced signalling (*HIS*) cells.

B



(B) Schematic showing fabrication of the implanted collagen constructs. Gels (size: 4.5x1.5x1cm) were cast as before but with a rabbit dermal fibroblast (RDF) compartment (size: 1.5x1.5x1cm) containing 5×10^5 or 2×10^6 RDFs next to an acellular compartment (size: 3x1.5x1cm). Following setting, plastic compression (A) gave a ~200 μ m thick sheet with post-compression RDF densities of 5.8×10^6 or 23.2×10^6 RDFs/ml. Compressed collagen sheets were rolled along their short axis (B) into spirals of 15mm length, 2.3mm diameter. Spiralling along the short axis positioned the RDF compartment in the spiral core, forming a hypoxia-induced signalling RDF (HIS-RDF) core, and the acellular compartment on the spiral surface (acellular wrap), radius (r) 0.77mm.

For *in vitro* experiments, constructs were cultured statically in 5ml medium (50% DMEM, 50% endothelial growth medium) in a 37°C, 5% CO₂ humidified incubator for the time indicated. Axial HDF/HUVEC co-cultures were also cultured in the presence of anti-VEGF neutralizing IgG (R&D, USA) at saturating concentration (10 μ g/ml) [208] or control goat IgG (10 μ g/ml) (Sigma, UK) for 1 week. For *in vivo* experiments, RDF-seeded constructs were either cultured *in vitro* in 5ml fully supplemented DMEM for 5 days prior to implantation (pre-conditioning) or

implanted immediately (no pre-conditioning). A minimum of three replicate constructs was used to test each condition.

Quantification of IgG permeability through compressed collagen

Since blockade of VEGF function was tested here by incubating spiral collagen constructs in the presence of anti-VEGF neutralizing IgG, it was important to assess the permeability of IgG through compressed collagen matrix. A stirred cell ultrafiltration unit was used (see Fig. 13, Chapter 3) to deliver an IgG-FITC containing PBS feed (IgG-FITC concentration= 50 μ g/ml) through collagen membranes by applying a transmembrane pressure of 9.8KPa. The collagen membrane to be tested was assembled in a 16.9 ml stirred cell, with a membrane area (A) of 5cm². To measure the portion of fluorescently-labeled antibody retained by the collagen membrane, the membrane was washed with 5ml PBS after testing and digested with 1 ml collagenase-PBS solution (1mg/ml). 100 μ l were sampled from the digested membrane solution and permeate and tested with a fluoremeter. A standard curve of known IgG-FITC concentrations vs. fluorescence was used to calculate the concentration of IgG-FITC in the digested collagen membrane solution and permeate.

ELISA

VEGF₁₆₅, MMP-2 and MMP-9 concentrations were measured using Quantikine ELISA kits, while total HIF-1 α concentrations were measured using Surveyor IC ELISA kit (all from R&D). Triplicates of each sample were analyzed using a MicroPlate reader (Biorad, UK). Readings were taken at 450nm with 570nm λ correction. Two culture conditions were tested for each marker protein; HUVEC-

only cultures and HDF/HUVEC axial co-cultures. Constructs were cultured for 5 or 10 days in 50% DMEM –50% endothelial growth medium. Media and collagen construct samples were analysed separately. Collagen constructs were removed from culture and snap frozen in liquid nitrogen for 5min. They were powderized with a Mikro-dismembrator (Sartorius, Germany) and dissolved in 1.2ml PBS. For each factor, triplicate samples were analysed per time point for each culture condition tested.

Implantation of collagen constructs

Subcutaneous implantations

An institutional review committee of Shanghai Second Medical University approved all animal study protocols. Twelve adult female New Zealand white rabbits weighing 2-2.5kg were used. Surgery was performed under general anaesthesia. A longitudinal skin incision was made on the rabbit's back and implants were sutured onto subcutaneous tissue. Three acellular constructs were sutured onto the left side and three cellular constructs (of the same series) on the right. Cell densities were either low (5.8×10^6 RDFs/ml) or high (23.2×10^6 RDFs/ml) with pre-conditioning and high (23.2×10^6 RDFs/ml) cell density with no pre-conditioning. Post-operative wounds were treated with topical benzylpenicillin-sodium antimicrobial powder. Rabbits were nursed until full recovery and returned to their single cage. Rabbits were sacrificed at 1 and 2 weeks. There were six rabbits in each of the 1-week and 2-week groups allowing testing of 6 constructs per condition for each implantation period.

Intramuscular implantations

Acellular and cell-seeded compressed collagen constructs were spiralled along their short axis round 0.9mm diameter intravenous cannulas (Becton Dickinson Medical Devices Ltd., China). The cannula was withdrawn to expose half of the construct's length (7.5mm) and the construct was sutured in place with a 5.0 surgical suture. A longitudinal skin incision was made on the rabbit's back and the muscle layer immediately underlying the skin was divided. The cannula with a spiralled construct was inserted into a pouch made within the back muscles. The muscle and skin layers were closed with interrupted 3.0 sutures, such that the cannula's opening protruded through the skin. The cannulas were sealed with cotton wool to prevent atmospheric exposure. One construct was implanted per rabbit with three rabbits used to test each condition; acellular, low (5.8×10^6 RDFs/ml) and high (23.2×10^6 RDFs/ml) cell density constructs (no pre-conditioning). The rabbits were sacrificed at 2 weeks.

In vivo Oxygen monitoring

O₂ levels in the core of acellular and RDF-seeded intramuscularly implanted constructs were monitored *in vivo* over 2 weeks. Rabbits were removed from their cages and manually restrained. A fibre-optic O₂ probe (Oxford Optronix Ltd, Oxford, UK) was inserted into the cannula of each rabbit. The insertion distance was measured for each construct prior implantation to ensure the probe was inserted into the cannula-free end of the construct's core (Fig.6A), providing real-time measurement of pO₂ (by luminescence quenching, see Chapter 8). Calibration of the optical O₂ probe was accurate to 0.7mmHg. Readings were taken in real-time every 30 seconds for 5min. Time zero values represent readings taken in constructs immediately after implantation. Fibre-optic probes were used in conjunction with an

OxyLab pO₂ETM system (Oxford Optronix Ltd, UK). Results are presented as partial pressure values (pO₂) in mmHg (7.6mmHg corresponds to 1% O₂).

Tissue processing and immunohistochemical staining

For immunofluorescent staining *in vitro* cultured spiral constructs were unrolled, washed in 5ml PBS and fixed in 100% ice-cold methanol for 1h. The primary antibodies used were mouse anti-human CD31 (Dako, USA); rabbit anti-human vWF (Sigma, UK); rabbit anti-human anti-phospho-Integrin β 3 (Sigma, UK). The secondary antibodies used were anti-mouse IgG-FITC (R&D, UK); anti-rabbit IgG-FITC (Sigma), followed by DAPI (Sigma, UK) nuclear staining. Unrolled specimens were fixed, routinely processed and embedded in paraffin, transversely sectioned (4 μ m) and H&E stained (see Chapter 2). Implanted spiral constructs were fixed (without unrolling), embedded and sectioned transversely and longitudinally (4 μ m). Immunohistochemical staining was carried out using Vectastain ABC-HRP kit (Vector Laboratories, USA) (see Chapter 2). Primary antibody used was mouse monoclonal anti-rabbit CD31 (Abcam, UK). Enzyme substrate used was DAB (brown) (Vector Laboratories, USA), with haematoxylin counterstaining.

Image analysis

Micrographs of immunofluorescent-stained specimens were captured with a fluorescent microscope (Olympus BX61) using a x10 objective, while H&E stained micrographs were captured with a light microscope (Olympus BH2) using x10 and x20 objectives. A minimum of 10 random fields were photographed per sample. An imaging software (Image J, NIH, USA) was used to determine the area of endothelial

cell clusters (aggregates of >2 endothelial cells with an elongation index (ratio of major/minor axis) of <2), the length of capillary-like structures (CLSs), the CLS elongation index (ratio of straight line separation of CLS ends / total CLS length), the total lumen area, the total area of red blood cell (RBC)-containing lumens, host blood vessel invasion distance (average radial distance from construct edge where RBC-containing lumens were present) and the total field area. Total number of CLSs and endothelial cell clusters was counted manually.

CHAPTER 10

10.1 GENERAL DISCUSSION

The aim of this work was to determine the effect and utility of physical cues as tools for controlling/regulating cell behaviour in biomimetic scaffolds. We have shown that Plastic Compression fabrication can be reliably employed to precisely and predictably control the material properties (e.g. matrix density, stiffness) and architecture (e.g. topography) of collagen hydrogel scaffolds. Processing can also generate structural anisotropy (e.g. collagen density gradients, zonal heterogeneity at the meso-scale) (Chapters 3, 4, 5, 6). Importantly, the process produces building-block type scaffolds (i.e. dense sheets) whose 3D spatial organisation can be easily controlled (e.g. through layering, spiralling etc) to form complex integral 3D tissue structures (Chapters 7, 8, 9).

The functionality of these biomimetic scaffolds as ‘bioresponse regulators’ was verified by testing a range of (semi) ‘closed’ cue -cell function coupling systems. These were; substrate surface/interface topography - cell alignment/stratification (Chapter 4), matrix stiffness - cell proliferation (Chapter 5), matrix stiffness gradient - cell migration (Chapter 6), matrix stiffness - cell-mediated interface integration (Chapter 7), scaffold 3D spatial organisation - cell O₂ consumption (Chapter 8) and hypoxia-induced signalling - cell migration/differentiation (Chapter 9). Of course, in reality no system can be completely closed, i.e. isolated from its surrounding environment. As in other physical systems the presence of cue cross-interactions and cell-cue feedback regulating mechanisms means that only varying degrees of closure are feasible. This principle was encountered at multiple points throughout this work,

in the form of interdependence between inevitably coupled cues e.g. matrix density and ligand density (Chapter 6) or superimposed cues e.g. growth factor gradients acting in the background of the dominating 3D matrix structure (Chapter 9). Clearly, then, monitored bioresponse must be the weighted average of multiple, concurrent (even co-operating) effects. Indeed, this realisation was evident in our finding that in every system tested there was concurrence of at least two of the four possible mechanisms of directed cell motility, i.e. durotaxis, haptotaxis, chemotaxis and topographic-based guidance (Chapters 6, 9). The key point, however, is that such engineered (defined) tissues suffer far less cross-talk (so allowing a clearer interpretation) than any other 3D system (*in vivo*, *ex vivo* etc).

Dynamic functions (e.g. cell motility, ECM remodeling) are essential to 3D cell systems as they not only *depend upon*, but are also used to *generate* biomimetic characteristics such as structural anisotropies, layers, zones, and fiber orientations [3,122]. The ability (and rate) of particular cell types to migrate through 3D scaffolds is a question of growing importance as we consider the relevance and operation of some of our 3D culture systems. For example, model tissues or systems may be designed to resemble metastatic cell invasion or wound cell recruitment in some instances. At the other extreme, they may need properties that prevent cells leaving or entering the scaffold material (e.g. secretory glands such as pancreas). Native protein materials will be degraded by migrating cells as long as the cell type can synthesize suitable levels of active enzyme (e.g., MMPs, plasmin, plasminogen activators, etc.) [3]. Understanding when and where resident cells will create, as opposed to use existing migration tracts in dense homogeneous materials hinges on the cell's ability to degrade such tracks versus the suitability of existing guidance

topography. Lysis of substrate material ahead of a migrating cell will depend on the composition of the substrate material and the rate at which extracellular proteases (chiefly MMPs) are secreted and activated. However, entry into these analyses already implies that the scaffold is being designed to *facilitate*, rather than to *regulate* cell migration (in any given plane). Rather, we have shown that the key to control cell migration, ECM remodeling, and ultimately tissue structure is to build strong directional cues into the scaffold structure (e.g. channels, lamellae, cleavage planes and/or density/stiffness gradients), irrespective of how fast resident cells can degrade or remodel the bulk matrix (Chapters 6, 9). The intended utility of a scaffold then shifts from a simple, inert cell carrier into a powerful tool that can be used to regulate cell function.

While it has generally been assumed that control of cell orientation/motility and ECM remodeling through topography will lead to control of 3D tissue structure, cell utilization of gaps between scaffold elements is only one extreme example of the principle that cells tend to follow the path of least resistance (e.g. a channel larger than 1 cell diameter provides zero resistance). It is now becoming clear that the detailed operation of such guidance is more complex than that implied by contact guidance. Rather, it is achieved by the physical interplay of at least four key factors: (1) ability of cells to generate tensional forces (cytoskeletal motor[4]), (2) ability to apply those forces to the solid support (by integrin-ligand linkage), (3) nature of the material properties of the supporting scaffold elements (surface chemistry, mechanical properties, anisotropy/orientation) [3]), and (4) ability of repetitive external force vectors to influence scaffold stiffness and anisotropy (e.g. connective tissues around joint articulations[3,329]. The fact that support elements of

biomimetic scaffolds are normally *deformable* in three dimensions (unlike a stiff 2D plastic surface) introduces a control element, which is both unfamiliar in conventional biology and yet simplifying. This is the parameter of *anisotropic material properties*, that effectively links mechanical, chemical and topographic cell control processes in 3D scaffolds [3,330] (Fig.1a).

A

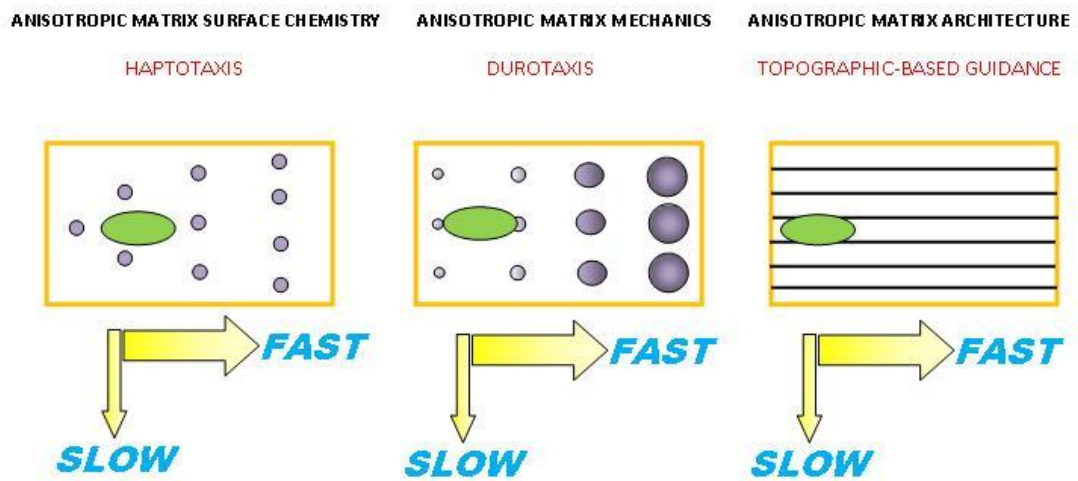
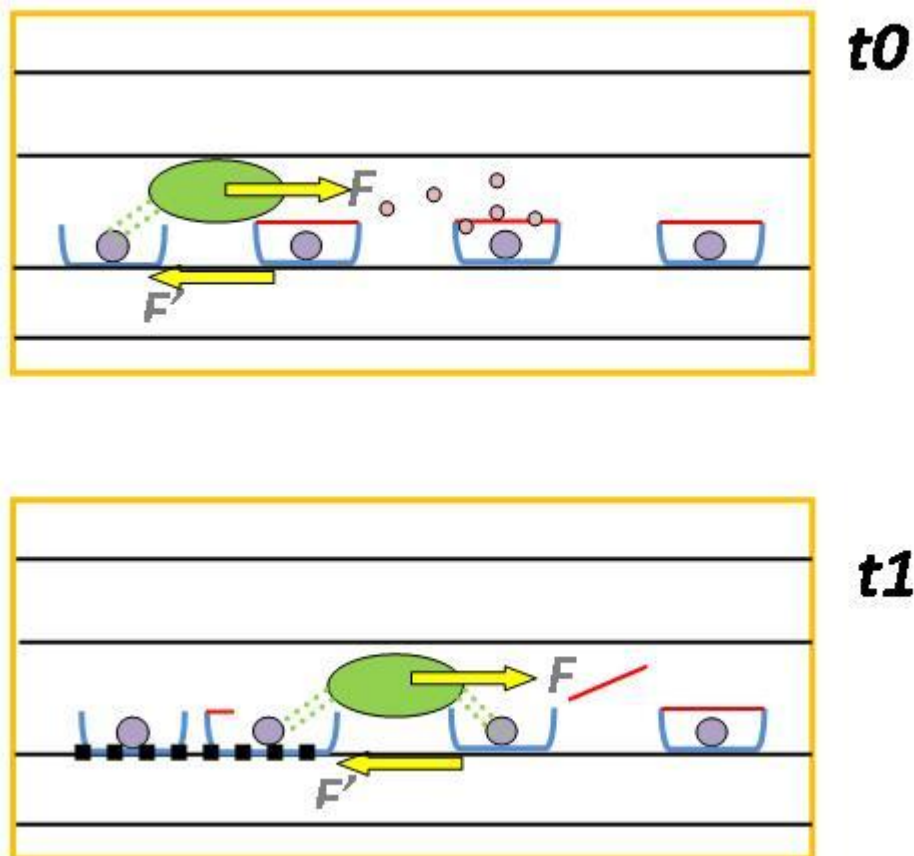
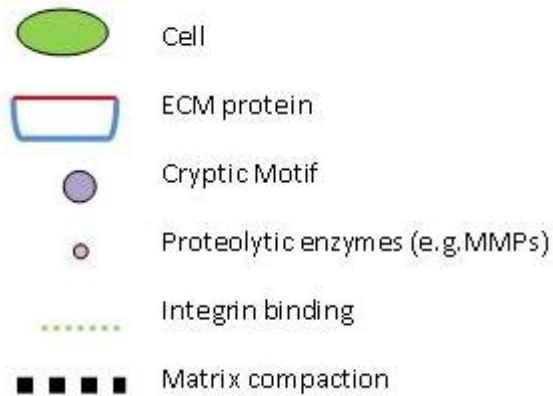


Fig.1 Anisotropic material properties form the link between mechanical, chemical and topographic cell control processes. (A) Schematic showing movement of cells over three different types of anisotropic substrates by haptotaxis (i.e. along a gradient of increasing ligand density), durotaxis (i.e. over a gradient of increasingly stiff ligands), and topographic-based guidance (i.e. within channels or between aligned fibres). Substrate anisotropy (in all three cases) guides cell direction by increasing cell velocity in one plane over another. Clearly, in native tissues combinations of such mechanisms operate together to control cell locomotion.

B



(B) Schematic showing how cell-force generation during cell traction and locomotion inevitably works within the matrix structure, accentuating the initial anisotropy. As a cell moves through a substrate comprising of anisotropic structures (e.g. channels, aligned fibres etc.) it generates force onto that substrate. Part of that force (F) will move the cell over the substrate, but an equal and opposite force (F') is applied to the

attachment points, resulting in local matrix compaction. This will inevitably result in changes in the number of integrin-ECM interactions per unit area, producing changes in local matrix stiffness. Matrix surface chemistry could be further modified by exposure of cryptic motifs within ECM proteins through mechanical distortion (e.g. stretching) or proteolytic cleavage by enzymes (e.g. MMPs) released by the cell as it moves. Through such mechanisms, dynamic cell functions (i.e. motility, ECM remodelling) play a key role in generating energetically favourable gradients (e.g. haptotactic and durotactic gradients) within native tissues.

In cell biology terms, perhaps the best initial illustration of this linkage can be found in the process of durotaxis. As discussed in Chapter 6, durotaxis describes the behavior in which cells apparently migrate from less stiff to more stiff substrate areas. The mechano-interpretation of durotaxis can be most clearly understood in the context of Newton's Third Law of Motion which states that action and reaction are equal and opposite. In cell terms, this means that contraction forces generated within the cell cytoskeleton are equally liable to move the cell and the immediate substrate to which it is attached. In other words, if a cell generates force onto a compliant substrate, part of that force will move the cell over the substrate, but an equal and opposite force (reaction) is applied to the attachment points, which may also move. Where the underlying substrate is stiff, it will move or deform very little, and most of the force will go to moving the cell. However, when the same cell force is applied to a more compliant substrate, the substrate material is deformed, absorbing a substantial proportion of the applied force, with a corresponding reduction in net cell motion. This almost inevitably leads to substrate deformation in the most compliant direction(s) and cell movement in the plane of greatest stiffness. In other words, cell

movement is greater on stiffer substrates (or stiffer planes of a given substrate), and so, statistically, cells move along stiffness gradients. Importantly, stiffness of the cell-ECM ligand interface will be proportional to the *number* of integrin-ECM interactions per unit area, as well as ligand elasticity[3]. Indeed, as we have previously discussed, durotaxis and haptotaxis (cell movement up a ligand density gradient) are highly coupled variables (Chapter 6). The dynamic mechanical consequence of cell force generation will be that the cell-substrate coupling proteins are most highly deformed when both the cell and bulk substrate material move little. Therefore, for stiff bulk materials less or more stiff ECM ligand elements such as fibronectin vs. type I collagen, respectively, will influence cell-matrix coupling. In contrast, more compliant bulk scaffold materials will be maximally deformed and will gradually come to dominate cell-substrate coupling.

The reciprocal nature of this mechano-interaction means that the motion of many cells through soft substrates causes compaction and physical remodeling; stiffer substrates are little affected. This is demonstrated most clearly by the fibroblast contraction of native collagen gels, which are highly compliant in the first instance. However, in contrast to the circular gel model that it is predominantly symmetrical and isotropic in nature, rectangular gels have been shown to contract anisotropically, as compaction propagates from the edges of the matrix into the bulk (i.e. gel contraction is a boundary effect) [331]. Similarly, shape asymmetry and anisotropic structures are normal in natural systems[3], and in these cases, cell-force generation during cell traction and locomotion inevitably works within the structures and frequently *preserves, or even accentuates, the starting structure* (Fig.1b). Indeed, forces exerted by cells embedded within a collagen gel irreversibly compact the

matrix and permanently render it anisotropic [331], i.e. cell contraction results in plastic deformation of the gel, similar to Plastic Compression. The dynamic interdependent nature of this relationship, then, means that cell contraction in soft substrates tends to produce low motility but leads to increased ECM compaction, even alignment, as the past strain history of the matrix is permanently stored in its microstructure [4,210,331]. Furthermore, it has been suggested that as a consequence of the convoluted nature of protein folding, cryptic binding sites hidden within the structure of ECM molecules may be exposed through mechanisms that proteolytically cleave or mechanically distort (e.g. stretching) the proteins of the ECM, as occurs during cell locomotion. In time, this mechano-modelling will feed back to increase cell motility and alignment, as the substrate's surface chemistry is modified and is made stiffer and/or anisotropic [331] (Fig.1b). In this way, apparently complex cell 'behaviors' will be driven by non-biological (physical) factors inherent in the matrix materials and the external loads they carry. These will include any fiber direction, points of tethering to adjacent structures (force vector generators) and interaction of external loading with the ECM material[122].

A major question relating to the development of biomimetic anisotropy is how do pre-aligned fibrils (e.g. collagen fibrils) in engineered tissue constructs cause cell-produced ECM fibrils to exhibit the same alignment. One possibility is through direct influence, by providing a physical template for assembly of the nascent ECM fibrils. Another possibility is by indirect influence via the cell alignment associated with the contact guidance response (i.e., new ECM fibrils grow in direct association with the cell surface). Since a cell is typically elongated and aligned with fibrils and moves bi-directionally with respect to them, new ECM fibrils become aligned with

pre-aligned fibrils. In this mechanism, cell alignment/migration would clearly play a key role in generating nano-/micro-scale structural anisotropy.

In the foregoing discussion cell motility has been used as a ‘bridge’ concept. It partly provides a starting point in understanding how mechanical forces act through the 3D cell substrate to influence behavior. However, it also illustrates the hidden level of dependence between the apparently distinct substrate controls considered so far. This makes cell motility a key linker between the familiar intracellular biological control cues (e.g., receptor-mediated second messenger systems) and the ability of the physical microenvironment to directly regulate cell behaviors. In effect, it may be possible to reverse the need to generate ever more complex theories of receptor-mediated signaling (and ‘cell decision’), such as in the ‘rigidity sensing’ mechanism proposed for cell durotaxis [332], where the unavoidable effects of substrate mechanics are considered. The intimate interdependence of surface chemistry, mesoscale topography, and mechanics in 3D substrates is only just becoming clear in cell biological systems as the importance of mechano-biological controls is understood. It is now clear that data management and interpretation by resident cells based largely, let alone simply, on receptor recognition and molecular signaling would be implausibly complex. For example, while vital genetic and biochemical signals drive developmental processes during embryogenesis, they are not sufficient alone to explain how 3D tissues are physically constructed so that they exhibit unique forms (e.g., glandular epithelium, branching vascular networks) and mechanical load-bearing functions (tension-generating muscle, compression-resistant bone) [333]. On the other hand, incorporation of current concepts of cytomechanics with the well-understood mechanical behavior of materials now makes it possible to

understand how a much more reasonable form of substrate/ECM control system might operate. Indeed, both epithelial and lung morphogenesis have been shown to be under micro-mechanical control[333]. Interestingly, this suggests that 3D spatial controls could operate through far simpler mechanisms, based on physical factors, producing *energetically favorable gradients* to drive cell responses. Not only are such energetic drivers more plausible models of cell control systems, but also they would be present and act on cells, even in the absence of complex molecular control systems. In such biosensing systems activation of cell receptors and second messenger systems are neither precluded nor necessary for cytomechanical control mechanisms, but they would operate against the background of these ‘Newtonian rules of engagement’.

Although it is clearly wrong to suggest that cytomechanical cues always dominate 3D cell systems, it is likely that they are hugely important in musculoskeletal connective tissues and culture models. Examples of these are the familiar tension-dominated mechanics of fibroblasts (tendon, skin, etc. [139,334]) and compression-dominated mechanics typical of chondrocytes and osteoblasts [335,336]. In contrast, it is interesting that receptor/second messenger signaling mechanisms of mechano-transduction (more correctly, mechano-sensing) are presently so ill-defined and apparently complex. Indeed, the molecular basis for most of these mechano-sensing effects is presently uncertain and ranges from stretch- and voltage- dependent ion-transport channels in the cell membrane (leading to strain-related disturbances in intracellular ion levels, normally Ca^{2+}) [336] to second messenger activation resulting from simple integrin occupancy [337] or deformation of the integrin-cytoskeletal system [338]. It has been suggested that

similar signal transduction pathways may play a role in the mechanism by which cells respond to substrate topography. These include integrin-mediated signaling cascades such as extracellular signal–regulated protein kinase, focal adhesion kinase, and protein kinase A[339]. Nanoscale surface features may also affect the adsorption and conformation of integrin binding proteins, changing the availability of binding sites and modifying integrin signalling. However, an important aspect applicable to cell behavior on patterned surfaces is the *bidirectional* nature of cell signalling[123]. It has been shown, for example, that micro-patterning and anisotropic topography induce dramatic changes in cell shape (and cell shape-dependent modulation of cytoskeletal tension and nucleus shape), i.e. outside-in signalling, which alters cytoskeletal tension, that then feeds back to induce local changes in focal adhesion assembly, i.e. inside-out signalling. This provides further evidence to the significant role that physical cues might play in controlling such processes. Importantly, the minimum effective dimension of grooved features has now fallen to as low as 11 nm [72], emphasizing the likely importance of cell-matrix attachment. Interestingly, this size scale falls within the scale of collagen fibrils, which makes up the majority of ECM in native tissues. It seems very possible, then, that cellular mechano-sensing systems are far simpler than commonly imagined but appear to be complex because they operate *in conjunction* with cytomolecular controls built into the ECM and cell cytoskeleton.

This interplay makes it easier to understand intricate cell behaviors (e.g. developmental processes) without the need to postulate implausibly complex biological controls with neocognitive sensory-motor feedbacks. For example, it has been shown that tissue shape crucially influences the development of tension by

contractile cells and modulates cell behaviour, giving rise to spatial patterns of cell and matrix organization (i.e. irreversible changes in matrix microstructure) [331]. Such a purely mechanical *structure-follows-shape* principle may be crucial for explaining complex cell behaviours as found in embryogenesis, where large deformations are involved and mechanical tension is known to be essential. Furthermore, it carries important implications for regulating cell behaviour in engineered tissues through fabrication of scaffold structural controllers. A promising example, illustrated by this work, is the ability to control physiological angiogenesis by Hypoxia-Induced Signaling (Chapter 9). Here, we have shown that despite our current inability to reproduce the complex chemical language of a complete angiogenic factor cascade, it is possible to control the end bioresponse (i.e. endothelial cell differentiation, migration and tubule formation) by engineering the onset of the process, i.e. local cell-mediated hypoxia, through control of physical parameters such as cell density and spatial positioning, diffusion/consumption path length and anisotropy. Clearly, this does not replace the importance of biomolecular mechanisms (signaling, attachment, protease control, etc.), which constantly operate in the background of such drivers. Rather, it provides an inevitable context in the form of a rapidly acting, simplifying framework of physical rules into which simple cell systems must integrate.

It is now becoming evident that the many different types of information encoded into the extracellular environment combine to form a ‘multidimensional map’[5]. Cells use this map to guide their activities and maintain their differentiation within tissues. Dynamic changes in physicochemical cue gradients across the map provide directionally encoded signals, while each cell type fabricates (through synthesis and

degradation) its own network of precisely encoded ECM proteins to enable an exact tailoring of the structural properties and information content of each ECM environment throughout the body [5]. Indeed, in a fascinating and well-accepted, yet poorly understood feedback process, cell phenotype, which dictates the nature of a cell's *future* ECM remodeling ability (through migration/differential traction generation, proliferation, ECM degradation/synthesis, and gene expression) is determined by the nature of its *past* ECM remodeling as this determines the current local ECM composition and mechanics [13]. This framework then provides a starting point for understanding how *multiple behaviour maps* form the basis of tissue-specific function and cell-matrix adaptation to external events (e.g. tissue damage or deformation). Importantly, this work illustrates that engineering these dynamic ECM mechanisms into the *initial* structure of 3D scaffolds could provide a tool for controlling/regulating *future* cell behaviour in a manner that closely recapitulates native tissue operation. It could indeed be envisaged that scaffolds could be 'programmed' into bio-functional devices through a simple physical cue-based language that contains all the required information (in the form of a multidimensional map) for control/regulation of cell (and engineered tissue) function (Fig 2).

SCAFFOLD STRUCTURE



ECM Chemistry

-anisotropy (direction)



ECM Mechanical properties

(e.g. stiffness)

-anisotropy (direction)



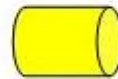
ECM Architecture

-pseudo-3D / true 3D

-topography (e.g. fiber alignment)

-density/porosity

-anisotropy (e.g. zonal heterogeneity)



Scaffold 3D Spatial Organisation


-thickness/size

-homo-/heterogeneity

-layering/interface topography

CELL RESPONSES

COLLECTIVE FUNCTIONS

Differentiation 

Viability/Proliferation 


DYNAMIC FUNCTIONS 


Morphology/Orientation/Adhesion

Migration

Contractile Force generation

METABOLIC FUNCTIONS

Synthetic Activity (e.g. ECM, GFs, MMPs) 

Consumption (O₂, nutrients) 

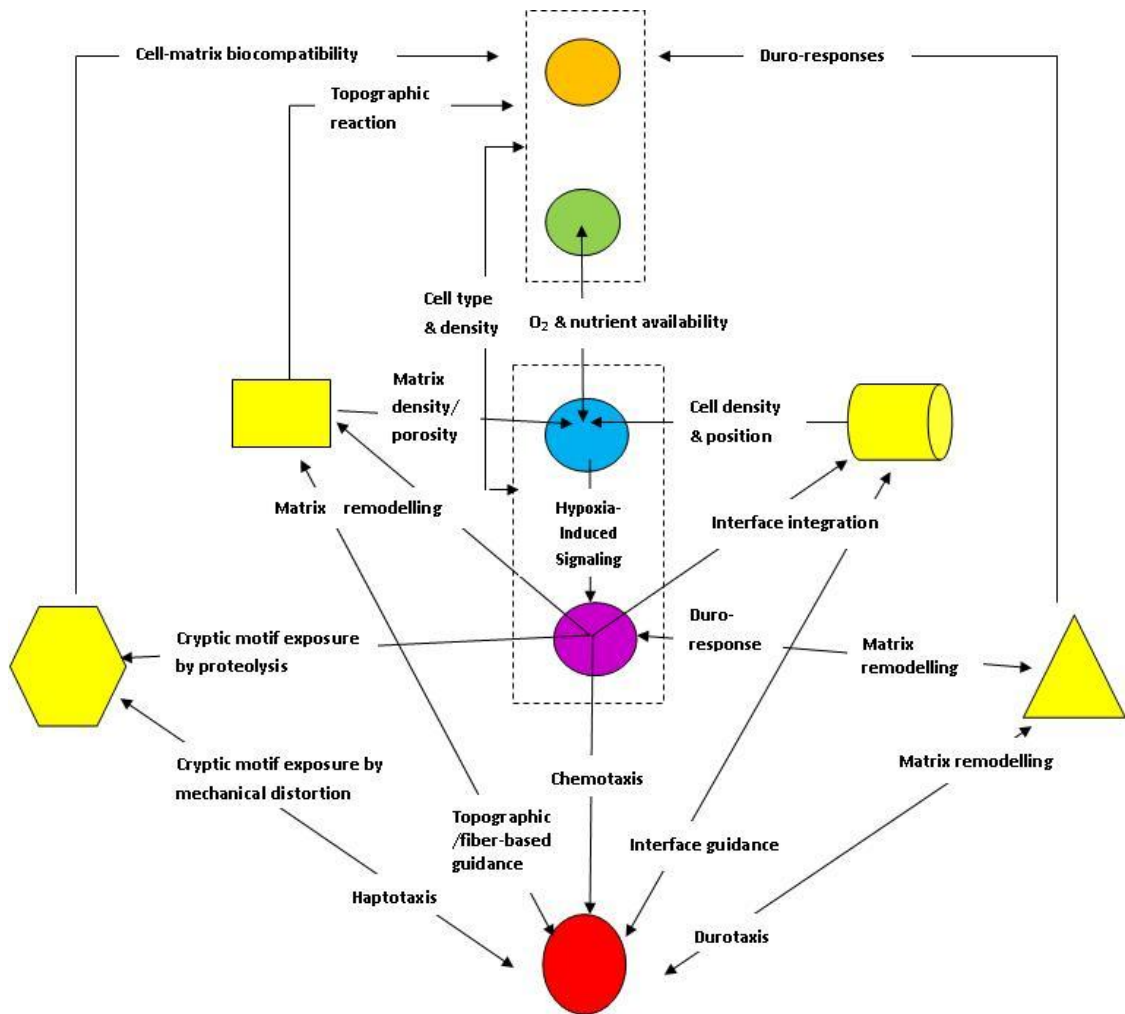


Fig 2. Schematic illustration of how a tissue-like multidimensional map could be ‘encoded’ into the structure of a 3D biomimetic scaffold for driving/regulating cell function. The map represents a network linking the nano/micro-scale elements of scaffold structure (i.e. matrix architecture, surface chemistry and mechanical properties) and macro-scale structure (i.e. 3D spatial organisation) with various cell functions. These can be categorised into collective, dynamic and metabolic functions. The map highlights the interdependence of the four elements of scaffold structure and how each element can be used to control multiple cell functions, directly or indirectly. It also demonstrates the key role of dynamic functions (e.g. cell motility, matrix remodelling) as these not only depend upon, but are also used to generate biomimetic characteristics such as structural anisotropies, layers, zones, and fiber orientations through feedback regulation of all elements of scaffold structure.

It is sometimes possible in refined models of 3D cell spatial control to postulate that we can provide clear, unambiguous cues to cells via their substrates. However, as we have previously discussed, the impression that we can deliver a single scaffold cue (or multiple cues, one-at-a-time) is, in most instances, an illusion or an impractical experimental system. Like most forms of communication and information collection/propagation, it is neither possible nor even desirable to base strategies on single cue systems because cells react to complex, *language-like*, dynamic signals from their environment. This realization can be best understood through the example of mesenchymal cells and their continuous monitoring of local substrate stiffness and anisotropic mechanical properties through small contractile forces and the resulting matrix deformation. This is directly analogous to how we measure material properties at the human scale [44,330]. It is almost inevitable that substitution of scaffold surfaces with large biomimetic attachment molecules will increase/decrease the substrate mechanics, as perceived by the cell (depending on the stiffness of the added ligand). On the other hand, controlling substrate mechanics (e.g. stiffness) by varying matrix density will inevitably be accompanied by changes in ligand density. Consequently, the effects of a mechanical gradient (i.e., durotaxis) would be influenced by the effects of a co-existing ligand gradient (i.e., haptotaxis), and vice versa (as discussed in Chapter 6). Similarly, practical biomimetic topographic cues (e.g. fibers and flexible channels) are most likely to be incorporated into relatively compliant scaffolds. By definition, structures such as these will deform the matrix, introducing accompanying predictable gradients in mechanical properties of the cell substrate.

Evidently, then, the driving capacity of such biomimetic scaffolds must inevitably rely on *all* three elements of physical scaffold structure, i.e. matrix mechanics, architecture, and surface chemistry. The proposition here is that the statistically dominant cue(s) at any one stage would dynamically move from one factor to another, depending on the cell system and the target mimetic feature (Fig.3). A further layer of complexity, in terms of a temporal ‘4th dimension’ could be introduced in any given system, such that the interplay of the three structural elements is regulated in a time-dependent manner. This dynamic, temporal control could, for example, be achieved by incorporating into the scaffold vehicles with controlled release kinetics for delivering proteolytic enzymes that alter the matrix chemistry and/or architecture.

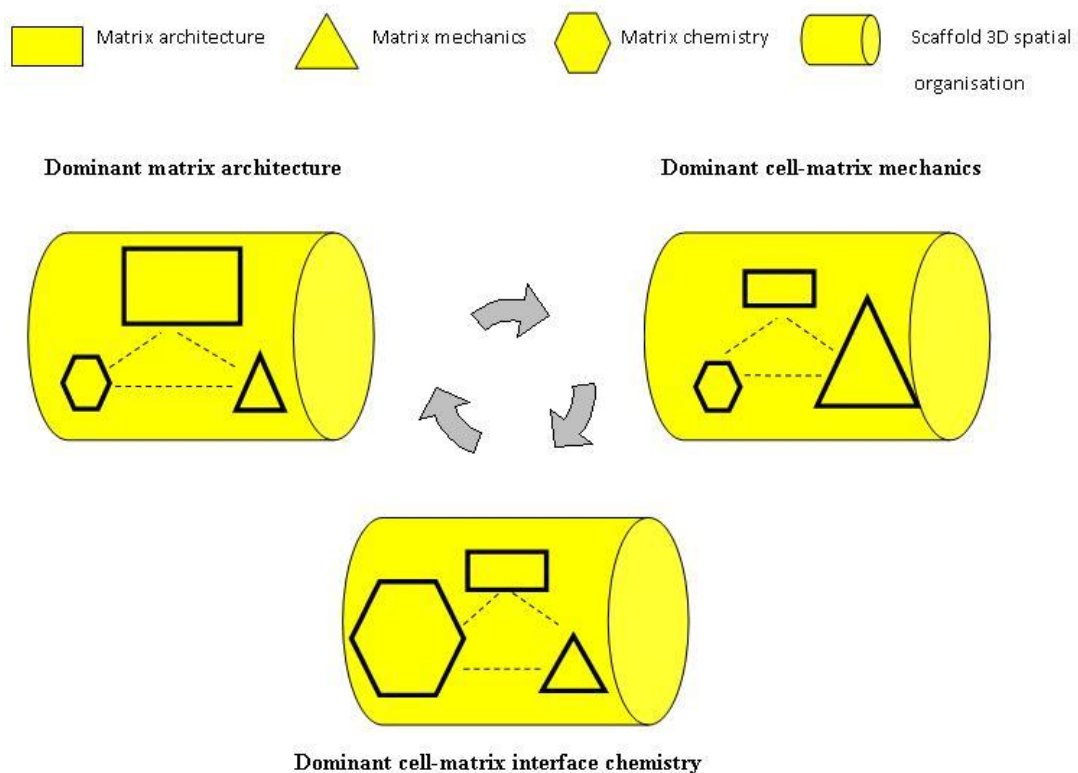


Fig.3 Schematic showing the proposed model of dynamic interplay of scaffold structural elements for regulation of cell function. The obligatory interdependence (dashed lines) of matrix architecture (e.g.substrate topography), cell-matrix interface chemistry, and cell-matrix mechanics means that in practical terms all three factors

inevitably contribute to the overall cell response seen in any given substrate. However, it is likely that the diversity of responses seen in 3D scaffolds is a consequence of shifting importance between the three control elements for any given system, similar to multiple behavioral maps seen in natural tissues, where their context is dependent on tissue type and/or external events (e.g. tissue damage or deformation). Modified from Brown and Phillips, 2007 [3].

Fabrication of biofunctional scaffolds could inspire new strategies for tissue repair and regeneration. It has been suggested, for example, that in the future it may be possible to regenerate injured tissues (e.g. infarcted myocardium) by using self-assembling nanoscale biomaterials with unique physicochemical properties that mimic natural ECMs, while simultaneously harnessing the inherent regenerative potential of host stem cells[333]. It is envisaged that cues built-in within scaffolds could stimulate proliferation and differentiation of recruited stem cells and endothelial progenitor cells to form vascular networks, while stimulating development of functional tissue structures (e.g., muscle bundles, nerves, connective tissue), thus mimicking normal embryological development. In this manner, ‘fractal-like’ tissue structures could be formed that contain key 3D anisotropic nano-/microscale patterns, mimicking those observed during normal development. This type of ‘*in situ*’, and by extrapolation ‘*in vivo* tissue engineering’ approach may potentially lead to development of simpler, and hence more cost-effective, therapeutics for tissue and organ regeneration.

10.2 CONCLUSIONS

In this study, the use of a *cell independent* method (Plastic Compression fabrication) for engineering the physical micro-environment removed the need to rely on cellular activity from the initial scaffold fabrication stage, therefore allowing us to position desired cues (matrix mesoscale anisotropy, surface/interface topography, density/stiffness gradients, and 3D spatial organisation) into the scaffold structure, to test their propagating effect on cell function. Inevitably, as resident cells modify these structures through ECM synthesis and remodelling, dynamic cue-cell function systems are established based on continuous feedback regulation. The ability to deliberately introduce such cues into the *initial* scaffold structure, through cell-independent fabrication, means that bioresponse monitoring can be carried out at the very beginning of a physiological feedback cycle. This has important implications for achieving effective temporal control over a range (or combination) of cues that could be potentially presented to cells within 3D biomimetic scaffolds, both for *in vitro* tissue modelling and repair/regeneration applications.

The findings of this work not only suggest that we may indeed be closer to understanding spatiotemporal control (e.g. how to control the onset/direction of engineered angiogenesis) in 3D cell culture systems than we think, but it also indicates that the key to its control is early imposition of mesoscale, biomimetic scaffold structure and mechanics, as cell responses seem to preserve and enhance such early cues. This study demonstrates the utility of cell-independent fabrication as a tool for transforming the function of scaffolds from that of inert cell carriers to dynamic cell drivers.

10.3 SUMMARY

The main experimental findings of this study were:

1. Fluid expulsion during plastic compression of collagen hydrogel scaffolds produces anisotropic structuring (i.e. a collagen density gradient) along the compression axis and can be modelled as an ultrafiltration process with cake formation at the fluid leaving surface.
2. Pattern template embossing can be used to engineer topography in plastically compressed 3D collagen hydrogel scaffolds for surface, as well as interface regulation of epithelial cell function (e.g. alignment, attachment, differentiation).
3. The hydration level of a collagen hydrogel, which determines matrix collagen density, is directly related to matrix stiffness.
4. Collagen matrix stiffness directly influences fibroblast proliferation such that matrices of increasing stiffness support greater cell growth, while fibroblast quiescence in compliant matrices is reversible by increasing matrix stiffness *in situ*.
5. Collagen matrix stiffness/density gradients can be used to guide fibroblast migration in 3D collagen scaffolds through durotaxis/haptotaxis.
6. Interface matrix stiffness influences the cell-mediated integration of adjacent (e.g. layered) collagen matrices by, in part at least, regulating cell migration across the interface.
7. Cell O₂ consumption is the major factor determining O₂ tension in a (plastically compressed) nano-fibrillar collagen matrix.
8. Fibroblasts exposed to spatially-controlled, cell-mediated hypoxia within a 3D collagen matrix upregulate production of angiogenic factor protein cascades which can induce a directed, functional angiogenic response *in vitro* and *in vivo*.

10.4 FUTURE WORK

The findings of this study lay down the foundation for understanding how directing physical cues could be built into the structure of 3D biomimetic scaffolds for control and regulation of cell function. As we have shown, a key feature of plastically compressed collagen scaffolds is their tunable structural characteristics (e.g. collagen density) which directly determine their mechanical properties (e.g. stiffness modulus), and can be precisely controlled by varying the matrix hydration level. Importantly, collagen density can be increased to levels approaching those of native tissue (i.e. 20-30% w/w). Since most tissue engineering applications are likely to require cell seeding of scaffolds, it is important to be able to precisely control fluid expulsion from cellular, as well as acellular, collagen hydrogels. In the present model the effect of cell seeding (and downstream effects of cell-mediated matrix remodelling) on fluid loss kinetics during compression was not tested. Extension of the model's predictive capacity to cellular gels would improve its applicability to engineering biomimetic constructs for *in vitro* tissue modelling and repair/regeneration purposes.

Plastic compressed collagen sheets provide an example of engineered bio-functional units (i.e. basic building blocks) that can be assembled into complex (e.g. heterogeneous) 3D tissue structures. This strongly contrasts with the 'farming' approach where tissues are gradually grown through cell-dependent cultivation (e.g. in a bioreactor). As we have shown, the advantage of relying on tissue engineering (as opposed to tissue farming) is that it creates the opportunity to embed cell guiding mechanisms into the initial scaffold structure (e.g. mechanical and topographic cues) that facilitate optimal tissue function and development. However, reconstruction of complex 3D tissue structure from such simple units critically relies on the ability to

organise and integrate them successfully, without compromising their functionality. For example, engineering large tissue constructs of clinically relevant dimensions (e.g. thickness in the cm range) is limited by inadequate deep cell O₂ and nutrient perfusion that inevitably leads to reduction in core cell viability. This problem could be further aggravated by the high collagen density of each sheet/layer which, while not significantly restricting O₂ diffusion, could limit macromolecular (e.g. growth factor) transport and removal of harmful metabolic products. Engineering the angiogenic component of integration is therefore an important prerequisite for any attempt to build large/complex 3D tissues. One of the early processes mediating physiological angiogenesis is directed endothelial cell migration. In this study we used hypoxia-induced angiogenic factor gradients to drive endothelial cell migration to specific locations within 3D matrices. However, while it was hypothesised that gradients developed in this system, this was not directly tested. To optimise the induced angiogenic response (i.e. its extent, timing and direction) it is important to establish quantitative correlations between hypoxia trigger levels, angiogenic factor protein levels, and the magnitude/range of operating angiogenic factor gradients. Future studies could also investigate the effect of modifying key cell-scaffold controllers (e.g. consumption path length, matrix density/diffusion coefficient, matrix anisotropy, cell type and density) for optimizing the angiogenic effectiveness of implantable *HIS* cell depots.

In addition, the ability to regulate endothelial cell migration through a combination of *HIS* cell guidance (i.e. chemotaxis) and other guiding cues (e.g. durotaxis/haptotaxis, topographic guidance) could be tested. As we have discussed, presenting cells with more than one cue at a time faithfully complies with

physiological rules of tissue function regulation, and would thus be expected to produce improved bioresponses.

Reference List

1. R.Langer, J.P.Vacanti . Tissue engineering. *Science* **260**, 920-926,1993.
2. D.F.Williams . To engineer is to create: the link between engineering and regeneration. *Trends Biotechnol.* **24**, 4-8,2006.
3. R.A.Brown, J.B.Phillips . Cell responses to biomimetic protein scaffolds used in tissue repair and engineering. *Int.Rev Cytol.* **262**, 75-150,2007.
4. J.J.Tomasek, G.Gabbiani, B.Hinz, C.Chaponnier, R.A.Brown . Myofibroblasts and mechano-regulation of connective tissue remodelling. *Nat.Rev Mol.Cell Biol.* **3**, 349-363,2002.
5. M.M.Stevens, J.H.George . Exploring and engineering the cell surface interface. *Science* **310**, 1135-1138,2005.
6. D.J.Mooney, C.L.Mazzoni, C.Breuer, K.McNamara, D.Hern, J.P.Vacanti, R.Langer . Stabilized polyglycolic acid fibre-based tubes for tissue engineering. *Biomaterials* **17**, 115-124,1996.
7. I.V.Yannas, J.F.Burke . Design of an artificial skin. I. Basic design principles. *J Biomed Mater.Res.* **14**, 65-81,1980.
8. E.Bell, B.Ivarsson, C.Merrill . Production of a tissue-like structure by contraction of collagen lattices by human fibroblasts of different proliferative potential in vitro. *Proc.Natl.Acad.Sci.U.S A* **76**, 1274-1278,1979.
9. B.C.Isenberg, C.Williams, R.T.Tranquillo . Small-diameter artificial arteries engineered in vitro. *Circulation Research* **98**, 25-35,2006.
10. M.E.Fini, M.T.Girard, M.Matsubara . Collagenolytic/gelatinolytic enzymes in corneal wound healing. *Acta Ophthalmol.Suppl* 26-33,1992.
11. M.A.Moses, M.Marikovsky, J.W.Harper, P.Vogt, E.Eriksson, M.Klagsbrun, R.Langer . Temporal study of the activity of matrix metalloproteinases and their endogenous inhibitors during wound healing. *J Cell Biochem.* **60**, 379-386,1996.
12. A.Page-McCaw, A.J.Ewald, Z.Werb . Matrix metalloproteinases and the regulation of tissue remodelling. *Nat.Rev Mol.Cell Biol.* **8**, 221-233,2007.
13. L.E.Freed, F.Guilak, X.E.Guo, M.L.Gray, R.Tranquillo, J.W.Holmes, M.Radisic, M.V.Sefton, D.Kaplan, G.Vunjak-Novakovic . Advanced tools for tissue engineering: Scaffolds, bioreactors, and signaling. *Tissue Engineering* **12**, 3285-3305,2006.
14. I.Elloumi-Hannachi, M.Yamato, T.Okano . Cell sheet engineering: a unique nanotechnology for scaffold-free tissue reconstruction with clinical applications in regenerative medicine. *J Intern.Med.* **267**, 54-70,2010.

15. A.Kushida, M.Yamato, C.Konno, A.Kikuchi, Y.Sakurai, T.Okano . Temperature-responsive culture dishes allow nonenzymatic harvest of differentiated Madin-Darby canine kidney (MDCK) cell sheets. *J Biomed Mater.Res.* **51**, 216-223,2000.
16. L.Cen, W.Liu, L.Cui, W.Zhang, Y.Cao . Collagen tissue engineering: development of novel biomaterials and applications. *Pediatr.Res.* **63**, 492-496,2008.
17. K.Gelse, E.Poschl, T.Aigner . Collagens--structure, function, and biosynthesis. *Adv.Drug Deliv.Rev* **55**, 1531-1546,2003.
18. R.S.Narins, P.H.Bowman . Injectable skin fillers. *Clin.Plast.Surg.* **32**, 151-162,2005.
19. D.M.Supp, S.T.Boyce . Engineered skin substitutes: practices and potentials. *Clin.Dermatol.* **23**, 403-412,2005.
20. A.K.Lynn, I.V.Yannas, W.Bonfield . Antigenicity and immunogenicity of collagen. *J Biomed Mater.Res.B Appl.Biomater.* **71**, 343-354,2004.
21. S.F.Badylak, D.O.Freytes, T.W.Gilbert . Extracellular matrix as a biological scaffold material: Structure and function. *Acta Biomater.* **5**, 1-13,2009.
22. N.Dubey, P.C.Letourneau, R.T.Tranquillo . Guided neurite elongation and schwann cell invasion into magnetically aligned collagen in simulated peripheral nerve regeneration. *Exp.Neurol.* **158**, 338-350,1999.
23. J.W.Freeman, F.H.Silver . The effects of prestrain and collagen fibril alignment on in vitro mineralization of self-assembled collagen fibers. *Connect.Tissue Res.* **46**, 107-115,2005.
24. Cheema U, Chuo CB, Sarathchandra P, Nazhat SN, Brown RA. Engineering functional collagen scaffolds: cyclical loading increases material strength and fibril aggregation. *Advanced Functional Materials* 17, 2426-2431. 2007.
Ref Type: Journal (Full)
25. R.A.Brown, M.Wiseman, C.B.Chuo, U.Cheema, S.N.Nazhat . Ultrarapid engineering of biomimetic materials and tissues: Fabrication of nano- and microstructures by plastic compression. *Advanced Functional Materials* **15**, 1762-1770,2005.
26. P.G.Buxton, M.Bitars, K.Gellynck, M.Parkar, R.A.Brown, A.M.Young, J.C.Knowles, S.N.Nazhat . Dense collagen matrix accelerates osteogenic differentiation and rescues the apoptotic response to MMP inhibition. *Bone* **43**, 377-385,2008.
27. E.M.Engelhardt, E.Stegberg, R.A.Brown, J.A.Hubbell, F.M.Wurm, M.Adam, P.Frey . Compressed collagen gel: a novel scaffold for human bladder cells. *J Tissue Eng Regen.Med.*,2009.
28. E.Campitiello, C.A.Della, A.Fattopace, D.D'Acunzi, S.Canonico . The use of artificial dermis in the treatment of chronic and acute wounds: regeneration of dermis and wound healing. *Acta Biomed* **76 Suppl 1**, 69-71,2005.
29. Y.Hori, T.Nakamura, K.Matsumoto, Y.Kurokawa, S.Satomi, Y.Shimizu . Tissue engineering of the small intestine by acellular collagen sponge scaffold grafting. *Int.J Artif.Organs* **24**, 50-54,2001.

30. C.S.Kim, J.I.Kim, J.Kim, S.H.Choi, J.K.Chai, C.K.Kim, K.S.Cho . Ectopic bone formation associated with recombinant human bone morphogenetic proteins-2 using absorbable collagen sponge and beta tricalcium phosphate as carriers. *Biomaterials* **26**, 2501-2507,2005.
31. J.B.Zwischenberger, R.L.Brunston, Jr., J.R.Swann, V.R.Conti . Comparison of two topical collagen-based hemostatic sponges during cardiothoracic procedures. *J Invest Surg.* **12**, 101-106,1999.
32. K.W.Ng, H.L.Khor, D.W.Hutmacher . In vitro characterization of natural and synthetic dermal matrices cultured with human dermal fibroblasts. *Biomaterials* **25**, 2807-2818,2004.
33. G.Chan, D.J.Mooney . New materials for tissue engineering: towards greater control over the biological response. *Trends Biotechnol.* **26**, 382-392,2008.
34. L.A.Smith, X.Liu, P.X.Ma . Tissue Engineering with Nano-Fibrous Scaffolds. *Soft Matter* **4**, 2144-2149,2008.
35. S.Kinoshita, N.Koizumi, T.Nakamura . Transplantable cultivated mucosal epithelial sheet for ocular surface reconstruction. *Exp.Eye Res.* **78**, 483-491,2004.
36. S.C.Yiu, P.B.Thomas, P.Nguyen . Ocular surface reconstruction: recent advances and future outlook. *Curr.Opin.Ophthalmol.* **18**, 509-514,2007.
37. R.Murugan, S.Ramakrishna . Design strategies of tissue engineering scaffolds with controlled fiber orientation. *Tissue Eng* **13**, 1845-1866,2007.
38. S.A.Sell, M.J.McClure, K.Garg, P.S.Wolfe, G.L.Bowlin . Electrospinning of collagen/biopolymers for regenerative medicine and cardiovascular tissue engineering. *Adv.Drug Deliv.Rev* **61**, 1007-1019,2009.
39. D.R.Nisbet, J.S.Forsythe, W.Shen, D.I.Finkelstein, M.K.Horne . Review paper: a review of the cellular response on electrospun nanofibers for tissue engineering. *J Biomater.Appl.* **24**, 7-29,2009.
40. J.Venugopal, S.Low, A.T.Choon, S.Ramakrishna . Interaction of cells and nanofiber scaffolds in tissue engineering. *J Biomed Mater.Res.B Appl.Biomater.* **84**, 34-48,2008.
41. S.F.Badylak . Regenerative medicine and developmental biology: the role of the extracellular matrix. *Anat.Rec.B New Anat.* **287**, 36-41,2005.
42. M.Radisic, M.Euloth, L.Yang, R.Langer, L.E.Freed, G.Vunjak-Novakovic . High-density seeding of myocyte cells for cardiac tissue engineering. *Biotechnol.Bioeng.* **82**, 403-414,2003.
43. V.Kroehne, I.Heschel, F.Schugner, D.Lasrich, J.W.Bartsch, H.Jockusch . Use of a novel collagen matrix with oriented pore structure for muscle cell differentiation in cell culture and in grafts. *J Cell Mol.Med.* **12**, 1640-1648,2008.

44. D.Karamichos, R.A.Brown, V.Mudera . Complex dependence of substrate stiffness and serum concentration on cell-force generation. *Journal of Biomedical Materials Research Part A* **78A**, 407-415,2006.
45. D.G.Wallace, J.Rosenblatt . Collagen gel systems for sustained delivery and tissue engineering. *Adv.Drug Deliv.Rev* **55**, 1631-1649,2003.
46. R.C.Dutta, A.K.Dutta . Cell-interactive 3D-scaffold; advances and applications. *Biotechnol.Adv.* **27**, 334-339,2009.
47. J.GROSS, D.KIRK . The heat precipitation of collagen from neutral salt solutions: some rate-regulating factors. *J Biol.Chem.* **233**, 355-360,1958.
48. L.Yuan, A.Veis . The self-assembly of collagen molecules. *Biopolymers* **12**, 1437-1444,1973.
49. G.C.WOOD, M.K.KEECH . The formation of fibrils from collagen solutions. 1. The effect of experimental conditions: kinetic and electron-microscope studies. *Biochem.J* **75**, 588-598,1960.
50. U.Cheema, S.Nazhat, B.a.Alp, F.Foroughi, N.Anandagoda, V.Mudera, R.Brown . Fabricating tissues: Analysis of farming versus engineering strategies. *Biotechnology and Bioprocess Engineering* **12**, 9-14,2007.
51. R.T.Tranquillo, M.A.Durrani, A.G.Moon . Tissue engineering science: consequences of cell traction force. *Cytotechnology* **10**, 225-250,1992.
52. E.A.Abou Neel, U.Cheema, J.C.Knowles, R.A.Brown, S.N.Nazhat . Use of multiple unconfined compression for control of collagen gel scaffold density and mechanical properties. *Soft Matter* **2**, 986-992,2006.
53. M.Ananta, C.E.Aulin, J.Hilborn, D.Aibibu, S.Houis, R.A.Brown, V.Mudera . A poly(lactic acid-co-caprolactone)-collagen hybrid for tissue engineering applications. *Tissue Eng Part A* **15**, 1667-1675,2009.
54. V.Mudera, M.Morgan, U.Cheema, S.Nazhat, R.Brown . Ultra-rapid engineered collagen constructs tested in an in vivo nursery site. *J.Tissue Eng Regen.Med.* **1**, 192-198,2007.
55. U.Cheema, E.Hadjipanayi, N.Tammi, B.Alp, V.Mudera, R.A.Brown . Identification of key factors in deep O2 cell perfusion for vascular tissue engineering. *Int.J Artif.Organs* **32**, 318-328,2009.
56. S.Mi, B.Chen, R.A.Brown, B.Wright, A.Kureshi, C.J.Connon . Ex vivo construction of an artificial ocular surface by combination of corneal limbal epithelial cells and a compressed collagen scaffold containing keratocytes. *Tissue Eng Part A*,2010.
57. K.F.Leong, C.M.Cheah, C.K.Chua . Solid freeform fabrication of three-dimensional scaffolds for engineering replacement tissues and organs. *Biomaterials* **24**, 2363-2378,2003.
58. M.Aumailley, B.Gayraud . Structure and biological activity of the extracellular matrix. *J Mol.Med.* **76**, 253-265,1998.

59. N.Zagris . Extracellular matrix in development of the early embryo. *Micron*. **32**, 427-438,2001.
60. D.Gullberg, P.Ekblom . Extracellular matrix and its receptors during development. *Int.J Dev.Biol.* **39**, 845-854,1995.
61. D.J.Behonick, Z.Werb . A bit of give and take: the relationship between the extracellular matrix and the developing chondrocyte. *Mech.Dev.* **120**, 1327-1336,2003.
62. J.Taipale, J.Keski-Oja . Growth factors in the extracellular matrix. *FASEB J* **11**, 51-59,1997.
63. C.Bokel, N.H.Brown . Integrins in development: moving on, responding to, and sticking to the extracellular matrix. *Dev.Cell* **3**, 311-321,2002.
64. F.G.Giancotti, E.Ruoslahti . Integrin signaling. *Science* **285**, 1028-1032,1999.
65. G.Rossetti, M.Collinge, J.R.Bender, R.Molteni, R.Pardi . Integrin-dependent regulation of gene expression in leukocytes. *Immunol.Rev* **186**, 189-207,2002.
66. F.M.Watt . Role of integrins in regulating epidermal adhesion, growth and differentiation. *EMBO J* **21**, 3919-3926,2002.
67. E.R.P.D.R.S.a.K.M.Y.Cukierman. Taking cell-matrix adhesions to the third dimension. *Science* 294, 1708. 2001.
Ref Type: Journal (Full)
68. D.S.Gray, J.Tien, C.S.Chen . Repositioning of cells by mechanotaxis on surfaces with micropatterned Young's modulus. *Journal of Biomedical Materials Research Part A* **66A**, 605-614,2003.
69. G.D.Pins, M.Toner, J.R.Morgan . Microfabrication of an analog of the basal lamina: biocompatible membranes with complex topographies. *FASEB J* **14**, 593-602,2000.
70. Y.C.Lin, F.J.Tan, K.G.Marra, S.S.Jan, D.C.Liu . Synthesis and characterization of collagen/hyaluronan/chitosan composite sponges for potential biomedical applications. *Acta Biomater.* **5**, 2591-2600,2009.
71. C.D.Chin, K.Khanna, S.K.Sia . A microfabricated porous collagen-based scaffold as prototype for skin substitutes. *Biomed Microdevices* **10**, 459-467,2008.
72. A.Curtis, C.Wilkinson . New depths in cell behaviour: reactions of cells to nanotopography. *Biochem.Soc.Symp.* **65**, 15-26,1999.
73. J.Y.Lim, H.J.Donahue . Cell sensing and response to micro- and nanostructured surfaces produced by chemical and topographic patterning. *Tissue Eng* **13**, 1879-1891,2007.
74. D.M.Brunette, B.Chehroudi . The effects of the surface topography of micromachined titanium substrata on cell behavior in vitro and in vivo. *J Biomech.Eng* **121**, 49-57,1999.

75. J.Meyle, H.Wolburg, A.F.von Recum . Surface micromorphology and cellular interactions. *J Biomater.Appl.* **7**, 362-374,1993.
76. M.J.Biggs, R.G.Richards, N.Gadegaard, R.J.McMurray, S.Affrossman, C.D.Wilkinson, R.O.Oreffo, M.J.Dalby . Interactions with nanoscale topography: adhesion quantification and signal transduction in cells of osteogenic and multipotent lineage. *J Biomed Mater.Res.A* **91**, 195-208,2009.
77. J.Y.Lim, A.D.Dreiss, Z.Zhou, J.C.Hansen, C.A.Siedlecki, R.W.Hengstebeck, J.Cheng, N.Winograd, H.J.Donahue . The regulation of integrin-mediated osteoblast focal adhesion and focal adhesion kinase expression by nanoscale topography. *Biomaterials* **28**, 1787-1797,2007.
78. E.K.Yim, R.M.Reano, S.W.Pang, A.F.Yee, C.S.Chen, K.W.Leong . Nanopattern-induced changes in morphology and motility of smooth muscle cells. *Biomaterials* **26**, 5405-5413,2005.
79. B.M.Baker, R.L.Mauck . The effect of nanofiber alignment on the maturation of engineered meniscus constructs. *Biomaterials* **28**, 1967-1977,2007.
80. Z.Ahmed, R.A.Brown . Adhesion, alignment, and migration of cultured Schwann cells on ultrathin fibronectin fibres. *Cell Motil.Cytoskeleton* **42**, 331-343,1999.
81. B.Wojciak-Stothard, M.Denyer, M.Mishra, R.A.Brown . Adhesion, orientation, and movement of cells cultured on ultrathin fibronectin fibers. *In Vitro Cell Dev.Biol.Anim* **33**, 110-117,1997.
82. A.S.Curtis . Small is beautiful but smaller is the aim: review of a life of research. *Eur.Cell Mater.* **8**, 27-36,2004.
83. T.Yasui, Y.Tohno, T.Araki . Determination of collagen fiber orientation in human tissue by use of polarization measurement of molecular second-harmonic-generation light. *Appl.Opt.* **43**, 2861-2867,2004.
84. Y.Takano, C.H.Turner, I.Owan, R.B.Martin, S.T.Lau, M.R.Forwood, D.B.Burr . Elastic anisotropy and collagen orientation of osteonal bone are dependent on the mechanical strain distribution. *J Orthop.Res.* **17**, 59-66,1999.
85. L.E.Freed, F.Guilak, X.E.Guo, M.L.Gray, R.Tranquillo, J.W.Holmes, M.Radisic, M.V.Sefton, D.Kaplan, G.Vunjak-Novakovic . Advanced tools for tissue engineering: Scaffolds, bioreactors, and signaling. *Tissue Engineering* **12**, 3285-3305,2006.
86. J.Yang, M.Yamato, T.Shimizu, H.Sekine, K.Ohashi, M.Kanzaki, T.Ohki, K.Nishida, T.Okano . Reconstruction of functional tissues with cell sheet engineering. *Biomaterials* **28**, 5033-5043,2007.
87. B.Hendrickx, K.Verdonck, B.S.Van den, S.Dickens, E.Eriksson, J.J.Vranckx, A.Luttun . Integration of Blood Outgrowth Endothelial Cells in Dermal Fibroblast Sheets Promotes Full Thickness Wound Healing. *Stem Cells*,2010.
88. I.Elloumi-Hannachi, M.Yamato, T.Okano . Cell sheet engineering: a unique nanotechnology for scaffold-free tissue reconstruction with clinical applications in regenerative medicine. *J Intern.Med.* **267**, 54-70,2010.

89. M.D.Resch, U.Schlotzer-Schrehardt, C.Hofmann-Rummelt, R.Sauer, C.Cursiefen, F.E.Kruse, M.W.Beckmann, B.Seitz . Adhesion structures of amniotic membranes integrated into human corneas. *Investigative Ophthalmology & Visual Science* **47**, 1853-1861,2006.
90. A.M.Chou, V.Sae-Lim, D.W.Hutmacher, T.M.Lim . Tissue engineering of a periodontal ligament-alveolar bone graft construct. *International Journal of Oral & Maxillofacial Implants* **21**, 526-534,2006.
91. M.A.DiMicco, R.L.Sah . Integrative cartilage repair: adhesive strength is correlated with collagen deposition. *Journal of Orthopaedic Research* **19**, 1105-1112,2001.
92. M.Moretti, D.Wendt, D.Schaefer, M.Jakob, E.B.Hunziker, M.Heberer, I.Martin . Structural characterization and reliable biomechanical assessment of integrative cartilage repair. *Journal of Biomechanics* **38**, 1846-1854,2005.
93. J.E.Phillips, K.L.Burns, J.M.Le Doux, R.E.Guldberg, A.J.Garcia . Engineering graded tissue interfaces. *Proc.Natl.Acad.Sci.U.S A* **105**, 12170-12175,2008.
94. C.K.Griffith, C.Miller, R.C.A.Sainson, J.W.Calvert, N.L.Jeon, C.C.W.Hughes, S.C.George . Diffusion limits of an in vitro thick prevascularized tissue. *Tissue Engineering* **11**, 257-266,2005.
95. N.L'Heureux, S.Paquet, R.Labbe, L.Germain, F.A.Auger . A completely biological tissue-engineered human blood vessel. *Faseb Journal* **12**, 47-56,1998.
96. T.Shimizu, H.Sekine, J.Yang, Y.Isoi, M.Yamato, A.Kikuchi, E.Kobayashi, T.Okano . Polysurgery of cell sheet grafts overcomes diffusion limits to produce thick, vascularized myocardial tissues. *Faseb Journal* **20**, 708+,2006.
97. G.A.Georgeu, E.T.Walbeehm, R.Tillett, A.Afoke, R.A.Brown, J.B.Phillips . Investigating the mechanical shear-plane between core and sheath elements of peripheral nerves. *Cell Tissue Res.* **320**, 229-234,2005.
98. J.B.Phillips, X.Smit, Z.N.De, A.Afoke, R.A.Brown . Peripheral nerves in the rat exhibit localized heterogeneity of tensile properties during limb movement. *J Physiol* **557**, 879-887,2004.
99. E.T.Walbeehm, A.Afoke, W.T.de, F.Holman, S.E.Hovius, R.A.Brown . Mechanical functioning of peripheral nerves: linkage with the "mushrooming" effect. *Cell Tissue Res.* **316**, 115-121,2004.
100. T.Shimizu, H.Sekine, J.Yang, Y.Isoi, M.Yamato, A.Kikuchi, E.Kobayashi, T.Okano . Polysurgery of cell sheet grafts overcomes diffusion limits to produce thick, vascularized myocardial tissues. *Faseb Journal* **20**, 708+,2006.
101. R.G.Flemming, C.J.Murphy, G.A.Abrams, S.L.Goodman, P.F.Nealey . Effects of synthetic micro- and nano-structured surfaces on cell behavior. *Biomaterials* **20**, 573-588,1999.
102. C.Oakley, D.M.Brunette . The sequence of alignment of microtubules, focal contacts and actin filaments in fibroblasts spreading on smooth and grooved titanium substrata. *J Cell Sci.* **106 (Pt 1)**, 343-354,1993.

103. B.Wojciak-Stothard, A.S.Curtis, W.Monaghan, M.McGrath, I.Sommer, C.D.Wilkinson . Role of the cytoskeleton in the reaction of fibroblasts to multiple grooved substrata. *Cell Motil.Cytoskeleton* **31**, 147-158,1995.
104. X.F.Walboomers, L.A.Ginsel, J.A.Jansen . Early spreading events of fibroblasts on microgrooved substrates. *J Biomed Mater.Res.* **51**, 529-534,2000.
105. E.T.den Braber, J.E.de Ruijter, L.A.Ginsel, A.F.von Recum, J.A.Jansen . Orientation of ECM protein deposition, fibroblast cytoskeleton, and attachment complex components on silicone microgrooved surfaces. *J Biomed Mater.Res.* **40**, 291-300,1998.
106. A.I.Teixeira, G.A.Abrams, P.J.Bertics, C.J.Murphy, P.F.Nealey . Epithelial contact guidance on well-defined micro- and nanostructured substrates. *J Cell Sci.* **116**, 1881-1892,2003.
107. F.Johansson, P.Carlberg, N.Danielsen, L.Montelius, M.Kanje . Axonal outgrowth on nano-imprinted patterns. *Biomaterials* **27**, 1251-1258,2006.
108. B.Zhu, Q.Lu, J.Yin, J.Hu, Z.Wang . Alignment of osteoblast-like cells and cell-produced collagen matrix induced by nanogrooves. *Tissue Eng* **11**, 825-834,2005.
109. B.Wojciak-Stothard, A.Curtis, W.Monaghan, K.MacDonald, C.Wilkinson . Guidance and activation of murine macrophages by nanometric scale topography. *Exp.Cell Res.* **223**, 426-435,1996.
110. L.Chou, J.D.Firth, V.J.Uitto, D.M.Brunette . Substratum surface topography alters cell shape and regulates fibronectin mRNA level, mRNA stability, secretion and assembly in human fibroblasts. *J Cell Sci.* **108 (Pt 4)**, 1563-1573,1995.
111. M.J.Dalby, M.O.Riehle, S.J.Yarwood, C.D.Wilkinson, A.S.Curtis . Nucleus alignment and cell signaling in fibroblasts: response to a micro-grooved topography. *Exp.Cell Res.* **284**, 274-282,2003.
112. A.M.Green, J.A.Jansen, J.P.van der Waerden, A.F.von Recum . Fibroblast response to microtextured silicone surfaces: texture orientation into or out of the surface. *J Biomed Mater.Res.* **28**, 647-653,1994.
113. M.J.Dalby, S.J.Yarwood, M.O.Riehle, H.J.Johnstone, S.Affrossman, A.S.Curtis . Increasing fibroblast response to materials using nanotopography: morphological and genetic measurements of cell response to 13-nm-high polymer demixed islands. *Exp.Cell Res.* **276**, 1-9,2002.
114. A.S.Andersson, F.Backhed, E.A.von, A.Richter-Dahlfors, D.Sutherland, B.Kasemo . Nanoscale features influence epithelial cell morphology and cytokine production. *Biomaterials* **24**, 3427-3436,2003.
115. E.Martinez, E.Engel, J.A.Planell, J.Samitier . Effects of artificial micro- and nano-structured surfaces on cell behaviour. *Ann.Anat.* **191**, 126-135,2009.
116. Z.Ahmed, S.Underwood, R.A.Brown . Low concentrations of fibrinogen increase cell migration speed on fibronectin/fibrinogen composite cables. *Cell Motil.Cytoskeleton* **46**, 6-16,2000.

117. S.N.Nazhat, E.A.bou Neel, A.Kidane, I.Ahmed, C.Hope, M.Kershaw, P.D.Lee, E.Stride, N.Saffari, J.C.Knowles, R.A.Brown . Controlled microchannelling in dense collagen scaffolds by soluble phosphate glass fibers. *Biomacromolecules* **8**, 543-551,2007.
118. R.L.Price, K.Ellison, K.M.Haberstroh, T.J.Webster . Nanometer surface roughness increases select osteoblast adhesion on carbon nanofiber compacts. *J Biomed Mater.Res.A* **70**, 129-138,2004.
119. C.M.Lo, H.B.Wang, M.Dembo, Y.L.Wang . Cell movement is guided by the rigidity of the substrate. *Biophysical Journal* **79**, 144-152,2000.
120. T.Yeung, P.C.Georges, L.A.Flanagan, B.Marg, M.Ortiz, M.Funaki, N.Zahir, W.Y.Ming, V.Weaver, P.A.Janmey . Effects of substrate stiffness on cell morphology, cytoskeletal structure, and adhesion. *Cell Motility and the Cytoskeleton* **60**, 24-34,2005.
121. F.H.Silver, L.M.Siperko, G.P.Seehra . Mechanobiology of force transduction in dermal tissue. *Skin Research and Technology* **9**, 3-23,2003.
122. D.Dado, S.Levenberg . Cell-scaffold mechanical interplay within engineered tissue. *Semin.Cell Dev.Biol.* **20**, 656-664,2009.
123. D.E.Discher, P.Janmey, Y.L.Wang . Tissue cells feel and respond to the stiffness of their substrate. *Science* **310**, 1139-1143,2005.
124. Y.L.Wang, R.J.Pelham . Preparation of a flexible, porous polyacrylamide substrate for mechanical studies of cultured cells. *Molecular Motors and the Cytoskeleton, Pt B* **298**, 489-496,1998.
125. K.Ghosh, Z.Pan, E.Guan, S.R.Ge, Y.J.Liu, T.Nakamura, X.D.Ren, M.Rafailovich, R.A.F.Clark . Cell adaptation to a physiologically relevant ECM mimic with different viscoelastic properties. *Biomaterials* **28**, 671-679,2007.
126. E.Bell, B.Ivarsson, C.Merrill . Production of A Tissue-Like Structure by Contraction of Collagen Lattices by Human-Fibroblasts of Different Proliferative Potential In vitro. *Proceedings of the National Academy of Sciences of the United States of America* **76**, 1274-1278,1979.
127. J.Fringer, F.Grinnell . Fibroblast quiescence in floating or released collagen matrices. *Journal of Biological Chemistry* **276**, 31047-31052,2001.
128. F.Grinnell, M.F.Zhu, M.A.Carlson, J.M.Abrams . Release of mechanical tension triggers apoptosis of human fibroblasts in a model of regressing granulation tissue. *Experimental Cell Research* **248**, 608-619,1999.
129. J.J.Tomasek, G.Gabbiani, B.Hinz, C.Chaponnier, R.A.Brown . Myofibroblasts and mechano-regulation of connective tissue remodelling. *Nat.Rev.Mol.Cell Biol.* **3**, 349-363,2002.
130. F.Grinnell . Fibroblasts, Myofibroblasts, and Wound Contraction. *Journal of Cell Biology* **124**, 401-404,1994.

131. F.Grinnell, C.H.Ho, E.Tamariz, D.J.Lee, G.Skuta . Dendritic fibroblasts in three-dimensional collagen matrices. *Molecular Biology of the Cell* **14**, 384-395,2003.
132. R.A.Clark . Biology of dermal wound repair. *Dermatol.Clin.* **11**, 647-666,1993.
133. A.Desmouliere, M.Redard, I.Darby, G.Gabbiani . The Decrease in Cellularity During Scar Establishment Is Mediated Through Apoptosis. *Faseb Journal* **8**, A903,1994.
134. A.Desmouliere, M.Redard, I.Darby, G.Gabbiani . Apoptosis Mediates the Decrease in Cellularity During the Transition Between Granulation-Tissue and Scar. *American Journal of Pathology* **146**, 56-66,1995.
135. J.Fluck, C.Querfeld, T.Krieg, S.Sollberg . Seeding normal fibroblasts in 3-dimensional collagen matrices induces apoptosis. *Journal of Investigative Dermatology* **107**, 284,1996.
136. J.Fluck, C.Querfeld, A.Cremer, S.Niland, T.Krieg, S.Sollberg . Normal human primary fibroblasts undergo apoptosis in three-dimensional contractile collagen gels. *Journal of Investigative Dermatology* **110**, 153-157,1998.
137. J.M.Fringer, F.Grinnell . Mechanical unloading of fibroblasts changes the localization of signaling molecules. *Molecular Biology of the Cell* **11**, 395A,2000.
138. Y.C.Lin, C.H.Ho, F.Grinnell . Decreased PDGF receptor kinase activity in fibroblasts contracting stressed collagen matrices. *Experimental Cell Research* **240**, 377-387,1998.
139. R.A.Brown, R.Prajapati, D.A.McGrouther, I.V.Yannas, M.Eastwood . Tensional homeostasis in dermal fibroblasts: Mechanical responses to mechanical loading in three-dimensional substrates. *Journal of Cellular Physiology* **175**, 323-332,1998.
140. C.C.Berry, J.C.Shelton, D.L.Bader, D.A.Lee . Influence of external uniaxial cyclic strain on oriented fibroblast-seeded collagen gels. *Tissue Engineering* **9**, 613-624,2003.
141. P.Friedl, K.S.Zanker, E.B.Brocker . Cell migration strategies in 3-D extracellular matrix: Differences in morphology, cell matrix interactions, and integrin function. *Microscopy Research and Technique* **43**, 369-378,1998.
142. L.R.Bernstein, L.A.Liotta . Molecular mediators of interactions with extracellular matrix components in metastasis and angiogenesis. *Curr.Opin.Oncol.* **6**, 106-113,1994.
143. F.Grinnell, L.B.Rocha, C.Iucu, S.Rhee, H.M.Jiang . Nested collagen matrices: A new model to study migration of human fibroblast populations in three dimensions. *Experimental Cell Research* **312**, 86-94,2006.
144. S.L.Schor, I.R.Ellis, K.Harada, K.Motegi, A.R.A.Anderson, M.A.J.Chaplain, R.P.Keatch, A.M.Schor . A novel 'sandwich' assay for quantifying chemo-regulated cell migration within 3-dimensional matrices: Wound healing cytokines exhibit distinct motogenic activities compared to the transmembrane assay. *Cell Motility and the Cytoskeleton* **63**, 287-300,2006.

145. C.M.Lo, Y.L.Wang . Guidance of cell movement by substrate rigidity. *Molecular Biology of the Cell* **10**, 259A,1999.
146. J.T.H.Mandeville, M.A.Lawson, F.R.Maxfield . Dynamic imaging of neutrophil migration in three dimensions: Mechanical interactions between cells and matrix. *Journal of Leukocyte Biology* **61**, 188-200,1997.
147. A.Huttenlocher, R.R.Sandborg, A.F.Horwitz . Adhesion in Cell-Migration. *Current Opinion in Cell Biology* **7**, 697-706,1995.
148. S.R.Brandley BK. Tumor-Cell Haptotaxis on Covalently Immobilized Linear and Exponential Gradients of A Cell-Adhesion Peptide. *Developmental Biology* **135**, 74-86. 1989.
Ref Type: Journal (Full)
149. C.S.Chen, M.Mrksich, S.Huang, G.M.Whitesides, D.E.Ingber . Micropatterned surfaces for control of cell shape, position, and function. *Biotechnology Progress* **14**, 356-363,1998.
150. SB Carter. Haptotaxis and Mechanism of Cell Motility. *Nature* **213**, 256-270. 1967.
Ref Type: Journal (Full)
151. A.M.Rajnicek, S.Britland, C.D.Mccaig . Contact guidance of CNS neurites on grooved quartz: influence of groove dimensions, neuronal age and cell type. *Journal of Cell Science* **110**, 2905-2913,1997.
152. M.J.Loftis, D.Sexton, W.Carver . Effects of collagen density on cardiac fibroblast behavior and gene expression. *Journal of Cellular Physiology* **196**, 504-511,2003.
153. C.Gaudet, W.A.Marganski, S.Kim, C.T.Brown, V.Gunderia, M.Dembo, J.Y.Wong . Influence of type I collagen surface density on fibroblast spreading, motility, and contractility. *Biophysical Journal* **85**, 3329-3335,2003.
154. T.Yeung, P.C.Georges, L.A.Flanagan, B.Marg, M.Ortiz, M.Funaki, N.Zahir, W.Y.Ming, V.Weaver, P.A.Janmey . Effects of substrate stiffness on cell morphology, cytoskeletal structure, and adhesion. *Cell Motility and the Cytoskeleton* **60**, 24-34,2005.
155. R.J.Pelham, Y.L.Wang . Cell locomotion and focal adhesions are regulated by the mechanical properties of the substrate. *Biological Bulletin* **194**, 348-349,1998.
156. A.Saez, M.Ghibaudo, A.Buguin, P.Silberzan, B.Ladoux . Rigidity-driven growth and migration of epithelial cells on microstructured anisotropic substrates. *Proceedings of the National Academy of Sciences of the United States of America* **104**, 8281-8286,2007.
157. J.P.Spalazzi, S.B.Doty, K.L.Moffat, W.N.Levine, H.H.Lu . Development of controlled matrix heterogeneity on a triphasic scaffold for orthopedic interface tissue engineering. *Tissue Eng* **12**, 3497-3508,2006.
158. M.Marenzana, D.J.Kelly, P.J.Prendergast, R.A.Brown . A collagen-based interface construct for the assessment of cell-dependent mechanical integration of tissue surfaces. *Cell and Tissue Research* **327**, 293-300,2007.

159. C.S.D.Lee, J.P.Gleghorn, N.W.Choi, M.Cabodi, A.D.Stroock, L.J.Bonassar . Integration of layered chondrocyte-seeded alginate hydrogel scaffolds. *Biomaterials* **28**, 2987-2993,2007.
160. A.S.Gobin, C.E.Butler, A.B.Mathur . Repair and regeneration of the abdominal wall musculofascial defect using silk fibroin-chitosan blend. *Tissue Engineering* **12**, 3383-3394,2006.
161. C.Scotti, M.S.Buragas, L.Mangiavini, C.Sosio, A.Di Giancamillo, C.Domeneghini, G.Fraschini, G.M.Peretti . A tissue engineered osteochondral plug: an in vitro morphological evaluation. *Knee Surgery Sports Traumatology Arthroscopy* **15**, 1363-1369,2007.
162. B.Obradovic, I.Martin, R.F.Padera, S.Treppo, L.E.Freed, G.Vunjak-Novakovic . Integration of engineered cartilage. *J Orthop.Res.* **19**, 1089-1097,2001.
163. Z.J.Zhang, J.M.McCaffery, R.G.S.Spencer, C.A.Francomano . Growth and integration of neocartilage with native cartilage in vitro. *Journal of Orthopaedic Research* **23**, 433-439,2005.
164. J.V.Bravenboer, C.D.I.der Maur, P.K.Bos, L.Feenstra, J.A.N.Verhaar, H.Weinans, G.J.V.M.van Osch . Improved cartilage integration and interfacial strength after enzymatic treatment in a cartilage transplantation model. *Arthritis Research & Therapy* **6**, R469-R476,2004.
165. Karamichos D, Brown R.A, Muder V. Collagen stiffness regulates cellular contraction and matrix remodelling gene expression. *Journal of Biomedical Materials Research Part A* **83A**, 887-894. 2007.
Ref Type: Journal (Full)
166. E.Hadjipanayi, V.Mudera, R.A.Brown . Close dependence of fibroblast proliferation on collagen scaffold matrix stiffness. *J.Tissue Eng Regen.Med.* **3**, 77-84,2009.
167. E.Hadjipanayi, V.Mudera, R.A.Brown . Guiding cell migration in 3D: a collagen matrix with graded directional stiffness. *Cell Motil.Cytoskeleton* **66**, 121-128,2009.
168. W.C.Bae, A.W.Law, D.Amiel, R.L.Sah . Sensitivity of indentation testing to step-off edges and interface integrity in cartilage repair. *Ann.Biomed Eng* **32**, 360-369,2004.
169. J.P.Petersen, P.Ueblacker, C.Goepfert, P.Adamietz, K.Baumbach, A.Stork, J.M.Rueger, R.Poertner, M.Amling, N.M.Meenen . Long term results after implantation of tissue engineered cartilage for the treatment of osteochondral lesions in a minipig model. *J Mater.Sci.Mater.Med.* **19**, 2029-2038,2008.
170. H.M.Jiang, F.Grinnell . Cell-matrix entanglement and mechanical anchorage of fibroblasts in three-dimensional collagen matrices. *Molecular Biology of the Cell* **16**, 5070-5076,2005.
171. F.Grinnell . Fibroblast biology in three-dimensional collagen matrices. *Trends Cell Biol.* **13**, 264-269,2003.

172. J.Lee, M.J.Cuddihy, N.A.Kotov . Three-dimensional cell culture matrices: state of the art. *Tissue Eng Part B Rev* **14**, 61-86,2008.
173. U.Cheema, R.A.Brown, B.Alp, A.J.MacRobert . Spatially defined oxygen gradients and vascular endothelial growth factor expression in an engineered 3D cell model. *Cellular and Molecular Life Sciences* **65**, 177-186,2008.
174. B.M.Gillette, J.A.Jensen, B.Tang, G.J.Yang, A.Bazargan-Lari, M.Zhong, S.K.Sia . In situ collagen assembly for integrating microfabricated three-dimensional cell-seeded matrices. *Nat.Mater.* **7**, 636-640,2008.
175. K.Jakab, A.Neagu, V.Mironov, R.R.Markwald, G.Forgacs . Engineering biological structures of prescribed shape using self-assembling multicellular systems. *Proc.Natl.Acad.Sci.U.S A* **101**, 2864-2869,2004.
176. U.Cheema, S.Y.Yang, V.Mudera, G.G.Goldspink, R.A.Brown . 3-D in vitro model of early skeletal muscle development. *Cell Motil.Cytoskeleton* **54**, 226-236,2003.
177. E.Volkmer, I.Drosse, S.Otto, A.Stangelmayer, M.Stengele, B.C.Kallukalam, W.Mutschler, M.Schieker . Hypoxia in static and dynamic 3D culture systems for tissue engineering of bone. *Tissue Eng Part A* **14**, 1331-1340,2008.
178. M.Radisic, J.Malda, E.Epping, W.Geng, R.Langer, G.Vunjak-Novakovic . Oxygen gradients correlate with cell density and cell viability in engineered cardiac tissue. *Biotechnol.Bioeng.* **93**, 332-343,2006.
179. S.Zhou, Z.Cui, J.P.Urban . Nutrient gradients in engineered cartilage: metabolic kinetics measurement and mass transfer modeling. *Biotechnol.Bioeng.* **101**, 408-421,2008.
180. G.Mehta, K.Mehta, D.Sud, J.W.Song, T.Bersano-Begey, N.Futai, Y.S.Heo, M.A.Mycek, J.J.Linderman, S.Takayama . Quantitative measurement and control of oxygen levels in microfluidic poly(dimethylsiloxane) bioreactors during cell culture. *Biomed Microdevices* **9**, 123-134,2007.
181. K.Kellner, G.Liebsch, I.Klimant, O.S.Wolfbeis, T.Blunk, M.B.Schulz, A.Gopferich . Determination of oxygen gradients in engineered tissue using a fluorescent sensor. *Biotechnol.Bioeng.* **80**, 73-83,2002.
182. A.G.Tsai, P.C.Johnson, M.Intaglietta . Oxygen gradients in the microcirculation. *Physiological Reviews* **83**, 933-963,2003.
183. K.M.Okazaki, E.Maltepe . Oxygen, epigenetics and stem cell fate. *Regenerative Medicine* **1**, 71-83,2006.
184. S.M.Hall, A.Soueid, T.Smith, R.A.Brown, S.G.Haworth, V.Mudera . Spatial differences of cellular origins and in vivo hypoxia modify contractile properties of pulmonary artery smooth muscle cells: lessons for arterial tissue engineering. *J Tissue Eng Regen.Med.* **1**, 287-295,2007.
185. S.Li, Y.S.Fan, L.H.Chow, D.C.Van Den, D.van, V, S.M.Sims, J.G.Pickering . Innate diversity of adult human arterial smooth muscle cells: cloning of distinct subtypes from the internal thoracic artery. *Circ.Res.* **89**, 517-525,2001.

186. S.Sartore, R.Franch, M.Roelofs, A.Chiavegato . Molecular and cellular phenotypes and their regulation in smooth muscle. *Rev Physiol Biochem.Pharmacol.* **134**, 235-320,1999.
187. V.Falanga, R.S.Kirsner . Low Oxygen Stimulates Proliferation of Fibroblasts Seeded As Single Cells. *Journal of Cellular Physiology* **154**, 506-510,1993.
188. B.Annabi, Y.T.Lee, S.Turcotte, E.Naud, R.R.Desrosiers, M.Champagne, N.Eliopoulos, J.Galipeau, R.Beliveau . Hypoxia promotes murine bone-marrow-derived stromal cell migration and tube formation. *Stem Cells* **21**, 337-347,2003.
189. T.Ma, S.T.Yang, D.A.Kniss . Oxygen tension influences proliferation and differentiation in a tissue-engineered model of placental trophoblast-like cells. *Tissue Engineering* **7**, 495-506,2001.
190. C.H.Coyle, N.J.Izzo, C.R.Chu . Sustained hypoxia enhances chondrocyte matrix synthesis. *J Orthop.Res.* **27**, 793-799,2009.
191. K.M.Okazaki, E.Maltepe . Oxygen, epigenetics and stem cell fate. *Regenerative Medicine* **1**, 71-83,2006.
192. A.Namiki, E.Brogi, M.Kearney, E.A.Kim, T.G.Wu, T.Couffinhal, L.Varticovski, J.M.Isner . Hypoxia induces vascular endothelial growth factor in cultured human endothelial cells. *Journal of Biological Chemistry* **270**, 31189-31195,1995.
193. G.L.Semenza . HIF-1 and mechanisms of hypoxia sensing. *Current Opinion in Cell Biology* **13**, 167-171,2001.
194. G.L.Semenza . Hypoxia-inducible factor 1: master regulator of O-2 homeostasis. *Current Opinion in Genetics & Development* **8**, 588-594,1998.
195. I.Barkefors, S.Le Jan, L.Jakobsson, E.Hejll, G.Carlson, H.Johansson, J.Jarvius, J.W.Park, N.L.Jeon, J.Kreuger . Endothelial cell migration in stable gradients of vascular endothelial growth factor a and fibroblast growth factor 2 - Effects on chemotaxis and chemokinesis. *Journal of Biological Chemistry* **283**, 13905-13912,2008.
196. P.Carmeliet . Mechanisms of angiogenesis and arteriogenesis. *Nat.Med.* **6**, 389-395,2000.
197. P.Fraisl, M.Mazzone, T.Schmidt, P.Carmeliet . Regulation of Angiogenesis by Oxygen and Metabolism. *Developmental Cell* **16**, 167-179,2009.
198. G.L.Semenza . Regulation of tissue perfusion in mammals by hypoxia-inducible factor 1. *Exp.Physiol* **92**, 988-991,2007.
199. Y.Martin, P.Vermette . Bioreactors for tissue mass culture: design, characterization, and recent advances. *Biomaterials* **26**, 7481-7503,2005.
200. I.Papandreou, A.Powell, A.L.Lim, N.Denko . Cellular reaction to hypoxia: sensing and responding to an adverse environment. *Mutat.Res.* **569**, 87-100,2005.

201. J.Rouwkema, N.C.Rivron, C.A.van Blitterswijk . Vascularization in tissue engineering. *Trends Biotechnol.* **26**, 434-441,2008.
202. G.D.Yancopoulos, S.Davis, N.W.Gale, J.S.Rudge, S.J.Wiegand, J.Holash . Vascular-specific growth factors and blood vessel formation. *Nature* **407**, 242-248,2000.
203. L.Coultas, K.Chawengsaksophak, J.Rossant . Endothelial cells and VEGF in vascular development. *Nature* **438**, 937-945,2005.
204. H.Sakuda, Y.Nakashima, S.Kuriyama, K.Sueishi . Media conditioned by smooth muscle cells cultured in a variety of hypoxic environments stimulates in vitro angiogenesis. A relationship to transforming growth factor-beta 1. *Am.J.Pathol.* **141**, 1507-1516,1992.
205. J.Ke, Y.Liu, X.Long, J.Li, W.Fang, Q.Meng, Y.Zhang . Up-regulation of vascular endothelial growth factor in synovial fibroblasts from human temporomandibular joint by hypoxia. *J.Oral Pathol.Med.* **36**, 290-296,2007.
206. C.K.Griffith, S.C.George . The Effect of Hypoxia on In Vitro Prevascularization of a Thick Soft Tissue. *Tissue Eng Part A*,2009.
207. P.L.Tremblay, F.Berthod, L.Germain, F.A.Auger . In vitro evaluation of the angiostatic potential of drugs using an endothelialized tissue-engineered connective tissue. *J.Pharmacol.Exp.Ther.* **315**, 510-516,2005.
208. Z.Chen, A.Htay, S.W.Dos, G.T.Gillies, H.L.Fillmore, M.M.Sholley, W.C.Broadus . In vitro angiogenesis by human umbilical vein endothelial cells (HUVEC) induced by three-dimensional co-culture with glioblastoma cells. *J.Neurooncol.* **92**, 121-128,2009.
209. K.Bailly, A.J.Ridley, S.M.Hall, S.G.Haworth . RhoA activation by hypoxia in pulmonary arterial smooth muscle cells is age and site specific. *Circ.Res.* **94**, 1383-1391,2004.
210. M.Eastwood, V.C.Mudera, D.A.McGrouther, R.A.Brown . Effect of precise mechanical loading on fibroblast populated collagen lattices: Morphological changes. *Cell Motility and the Cytoskeleton* **40**, 13-21,1998.
211. Ronald F.Probstein, *Ultrafiltration. Physicochemical Hydrodynamics: an introduction*, John Wiley and Sons, 1994, pp. 154-158.
212. R.F.Boyd, A.L.Zydney . Analysis of protein fouling during ultrafiltration using a two-layer membrane model. *Biotechnol.Bioeng.* **59**, 451-460,1998.
213. A.L.Zydney, C.C.Ho . Effect of membrane morphology on system capacity during normal flow microfiltration. *Biotechnol.Bioeng.* **83**, 537-543,2003.
214. C.C.Ho, A.L.Zydney . A Combined Pore Blockage and Cake Filtration Model for Protein Fouling during Microfiltration. *J Colloid Interface Sci.* **232**, 389-399,2000.
215. T.S.Girton, V.H.Barocas, R.T.Tranquillo . Confined compression of a tissue-equivalent: Collagen fibril and cell alignment in response to anisotropic strain.

Journal of Biomechanical Engineering-Transactions of the Asme **124**, 568-575,2002.

216. K.B.Kosto, W.M.Deen . Hindered convection of macromolecules in hydrogels. *Biophys J* **88**, 277-286,2005.
217. W.Y.Gu, H.Yao, C.Y.Huang, H.S.Cheung . New insight into deformation-dependent hydraulic permeability of gels and cartilage, and dynamic behavior of agarose gels in confined compression. *J.Biomech.* **36**, 593-598,2003.
218. W.J.McCarty, M.Johnson . The hydraulic conductivity of Matrigel (TM). *Biorheology* **44**, 303-317,2007.
219. K.Klaentschi, J.A.Brown, P.G.Niblett, A.C.Shore, J.E.Tooke . Pressure-permeability relationships in basement membrane: effects of static and dynamic pressures. *Am.J.Physiol* **274**, H1327-H1334,1998.
220. B.Reynaud, T.M.Quinn . Anisotropic hydraulic permeability in compressed articular cartilage. *J.Biomech.* **39**, 131-137,2006.
221. J.L.Bert, R.K.Reed . Flow conductivity of rat dermis is determined by hydration. *Biorheology* **32**, 17-27,1995.
222. Y.Huang, D.Rumschitzki, S.Chien, S.Weinbaum . A fiber matrix model for the filtration through fenestral pores in a compressible arterial intima. *Am.J.Physiol* **272**, H2023-H2039,1997.
223. R.F.Fisher . The deformation matrix theory of basement membrane: a study of water flow through elastic and rigid filaments in the rat. *J.Physiol* **406**, 1-14,1988.
224. G.B.Robinson, H.A.Walton . Glomerular basement membrane as a compressible ultrafilter. *Microvasc.Res.* **38**, 36-48,1989.
225. P.D.Weinberg, S.L.Carney, C.P.Winlove, K.H.Parker . The contributions of glycosaminoglycans, collagen and other interstitial components to the hydraulic resistivity of porcine aortic wall. *Connect.Tissue Res.* **36**, 297-308,1997.
226. F.M.Price, R.M.Mason, J.R.Levick . Radial organization of interstitial exchange pathway and influence of collagen in synovium. *Biophys.J.* **69**, 1429-1439,1995.
227. J.R.Levick . Flow through interstitium and other fibrous matrices. *Q.J.Exp.Physiol* **72**, 409-437,1987.
228. N.Mao, S.J.Russell. Directional permeability in homogeneous nonwoven structures part I: The relationship between directional permeability and fibre orientation. *Journal of the Textile Institute* , 235. 2000.
Ref Type: Journal (Full)
229. F.Wang, V.V.Tarabara . Pore blocking mechanisms during early stages of membrane fouling by colloids. *J.Colloid Interface Sci.* **328**, 464-469,2008.

230. M.Bitar, V.Salih, R.A.Brown, S.N.Nazhat . Effect of multiple unconfined compression on cellular dense collagen scaffolds for bone tissue engineering. *J.Mater.Sci.Mater.Med.* **18**, 237-244,2007.
231. J.Hua, L.E.Erickson, T.Y.Yiin, L.A.Glasgow . A review of the effects of shear and interfacial phenomena on cell viability. *Crit Rev.Biotechnol.* **13**, 305-328,1993.
232. V.Morel, T.M.Quinn . Cartilage injury by ramp compression near the gel diffusion rate. *J.Orthop.Res.* **22**, 145-151,2004.
233. J.A.Pedersen, F.Boschetti, M.A.Swartz . Effects of extracellular fiber architecture on cell membrane shear stress in a 3D fibrous matrix. *J.Biomech.* **40**, 1484-1492,2007.
234. S.H.De Paoli Lacerda, B.Ingber, N.Rosenzweig . Structure-release rate correlation in collagen gels containing fluorescent drug analog. *Biomaterials* **26**, 7164-7172,2005.
235. F.J.O'Brien, B.A.Harley, M.A.Waller, I.V.Yannas, L.J.Gibson, P.J.Prendergast . The effect of pore size on permeability and cell attachment in collagen scaffolds for tissue engineering. *Technol.Health Care* **15**, 3-17,2007.
236. Z.M.Rong, U.Cheema, P.Vadgama . Needle enzyme electrode based glucose diffusive transport measurement in a collagen gel and validation of a simulation model. *Analyst* **131**, 816-821,2006.
237. E.M.Johnson, D.A.Berk, R.K.Jain, W.M.Deen . Hindered diffusion in agarose gels: test of effective medium model. *Biophys J* **70**, 1017-1023,1996.
238. J.V.Trapp, S.A.Back, M.Lepage, G.Michael, C.Baldock . An experimental study of the dose response of polymer gel dosimeters imaged with x-ray computed tomography. *Phys.Med.Biol.* **46**, 2939-2951,2001.
239. B.R.Downing, K.Cornwell, M.Toner, G.D.Pins . The influence of microtextured basal lamina analog topography on keratinocyte function and epidermal organization. *J Biomed Mater.Res.A* **72**, 47-56,2005.
240. P.Uttayarat, G.K.Toworfe, F.Dietrich, P.I.Lelkes, R.J.Composto . Topographic guidance of endothelial cells on silicone surfaces with micro- to nanogrooves: orientation of actin filaments and focal adhesions. *J Biomed Mater.Res.A* **75**, 668-680,2005.
241. P.Zorlutuna, Z.Rong, P.Vadgama, V.Hasirci . Influence of nanopatterns on endothelial cell adhesion: Enhanced cell retention under shear stress. *Acta Biomater.* **5**, 2451-2459,2009.
242. R.M.Lavker, T.T.Sun . Heterogeneity in epidermal basal keratinocytes: morphological and functional correlations. *Science* **215**, 1239-1241,1982.
243. W.G.Carter, Symington B.E., Kaur P. Cell adhesion and the basement membrane in early epidermal morphogenesis. *Epithelial Organization and Development* , 299-327. 1992.
- Ref Type: Journal (Full)

244. A.el-Ghalbzouri, S.Gibbs, E.Lamme, C.A.van Blitterswijk, M.Ponec . Effect of fibroblasts on epidermal regeneration. *Br.J Dermatol.* **147**, 230-243,2002.
245. Matoltsy G.A., Odland G.F. Investigation of the structure of the cornified epithelium of the human skin. *J.Biophysic.and Biochem.Cytol.* **1**, 191. 1955.
Ref Type: Journal (Full)
246. Binnig G, Quate C.F. Atomic Force Microscope. *Phys.Rev.Lett.* **56**, 930-933. 1986.
Ref Type: Journal (Full)
247. S.L.Schor . Cell-Proliferation and Migration on Collagen Substrata Invitro. *Journal of Cell Science* **41**, 159-175,1980.
248. G.Boyer, H.Zahouani, B.A.Le, L.Laqueize . In vivo characterization of viscoelastic properties of human skin using dynamic micro-indentation. *Conf.Proc.IEEE Eng Med.Biol.Soc.* **2007**, 4584-4587,2007.
249. T.Nishiyama, I.Horii, Y.Nakayama, T.Ozawa, T.Hayashi . A Distinct Characteristic of the Quiescent State of Human Dermal Fibroblasts in Contracted Collagen Gel As Revealed by No Response to Epidermal Growth-Factor Alone, But A Positive Growth-Response to A Combination of the Growth-Factor and Saikosaponin-B1. *Matrix* **10**, 412-419,1990.
250. K.Ghosh, E.Guan, X.Ren, S.Ge, Y.Liu, T.Nakamura, M.Rafailovich, R.A.Clark . Cell adaptation to substrate mechanics: implications for tissue engineering design of wound healing products. *Journal of Investigative Dermatology* **126**, 34,2006.
251. J.Folkman, A.Moscona . Role of Cell-Shape in Growth-Control. *Nature* **273**, 345-349,1978.
252. S.Niland, A.Cremer, J.Fluck, J.A.Eble, T.Krieg, S.Sollberg . Contraction-dependent apoptosis of normal dermal fibroblasts. *Journal of Investigative Dermatology* **116**, 686-692,2001.
253. R.L.Juliano, S.Haskill . Signal Transduction from the Extracellular-Matrix. *Journal of Cell Biology* **120**, 577-585,1993.
254. T.Kono, T.Tanii, M.Furukawa, N.Mizuno, J.Kitajima, M.Ishii, T.Hamada, K.Yoshizato . Cell-Cycle Analysis of Human Dermal Fibroblasts Cultured on Or in Hydrated Type-I Collagen Lattices. *Archives of Dermatological Research* **282**, 258-262,1990.
255. J.Fringer, F.Grinnell . Fibroblast quiescence in floating collagen matrices - Decrease in serum activation of MEK and RAF but not Ras. *Journal of Biological Chemistry* **278**, 20612-20617,2003.
256. T.Nishiyama, M.Tsunenaga, Y.Nakayama, E.Adachi, T.Hayashi . Growth-Rate of Human-Fibroblasts Is Repressed by the Culture Within Reconstituted Collagen Matrix But Not by the Culture on the Matrix. *Matrix* **9**, 193-199,1989.
257. T.Nishiyama, N.Akutsu, I.Horii, Y.Nakayama, T.Ozawa, T.Hayashi . Response to Growth-Factors of Human Dermal Fibroblasts in A Quiescent State Owing to Cell-Matrix Contact Inhibition. *Matrix* **11**, 71-75,1991.

258. R.A.F.Clark . Biology of Dermal Wound Repair. *Dermatologic Clinics* **11**, 647-666,1993.
259. W.B.Rockwell, I.K.Cohen, H.P.Ehrlich . Keloids and Hypertrophic Scars - A Comprehensive Review. *Plastic and Reconstructive Surgery* **84**, 827-837,1989.
260. A.R.Harrop, A.Ghahary, P.G.Scott, N.Forsyth, A.Ujifriedland, E.E.Tredget . Regulation of Collagen-Synthesis and Messenger-Rna Expression in Normal and Hypertrophic Scar Fibroblasts In-Vitro by Interferon-Gamma. *Journal of Surgical Research* **58**, 471-477,1995.
261. A.Desmouliere, C.Badid, M.L.BochatonPiallat, G.Gabbiani . Apoptosis during wound healing, fibrocontractive diseases and vascular wall injury. *International Journal of Biochemistry & Cell Biology* **29**, 19-30,1997.
262. H.Nakaoka, S.Miyauchi, Y.Miki . Proliferating Activity of Dermal Fibroblasts in Keloids and Hypertrophic Scars. *Acta Dermato-Venereologica* **75**, 102-104,1995.
263. L.Y.Matsuoka, J.Uitto, J.Wortsman, R.P.Abergel, J.Dietrich . Ultrastructural Characteristics of Keloid Fibroblasts. *American Journal of Dermatopathology* **10**, 505-508,1988.
264. S.Al-Nasiry, N.Geusens, M.Hanssens, C.Luyten, R.Pijnenborg . The use of Alamar Blue assay for quantitative analysis of viability, migration and invasion of choriocarcinoma cells. *Human Reproduction* **22**, 1304-1309,2007.
265. J.T.Daniels, N.L.Occleston, J.G.Crowston, P.T.Khaw . Effects of antimetabolite induced cellular growth arrest on fibroblast-fibroblast interactions. *Experimental Eye Research* **69**, 117-127,1999.
266. A.Nieto, C.M.Cabrera, P.Catalina, F.Cobo, A.Barnie, J.L.Cortes, A.B.del Jesus, R.Montes, A.Concha . Effect of mitomycin-C on human foreskin fibroblasts used as feeders in human embryonic stem cells: Immunocytochemistry MIB1 score and DNA ploidy and apoptosis evaluated by flow cytometry. *Cell Biology International* **31**, 269-278,2007.
267. B Hinz. Formation and function of the myofibroblast during tissue repair. *Journal of Investigative Dermatology* **127**, 526-537. 2007.
Ref Type: Journal (Full)
268. M.Bitar, V.Salih, R.A.Brown, S.N.Nazhat . Effect of multiple unconfined compression on cellular dense collagen scaffolds for bone tissue engineering. *J.Mater.Sci.Mater.Med.* **18**, 237-244,2007.
269. E.Cukierman, R.Pankov, .R.Stevens, K.M.Yamada. Taking cell-matrix adhesions to the third dimension. *Science* **294**, 1708-1712. 2001.
Ref Type: Journal (Full)
270. B Geiger. Encounters in space. *Science* **294**, 1661-1663. 2001.
Ref Type: Journal (Full)

271. Chen CS, Tan J, Tien J. Mechanotransduction at cell–matrix and cell–cell contacts. *Annu Rev Biomed Eng* 6, 275-302. 2004.
Ref Type: Journal (Full)
272. Engler A, Bacakova L, Newman C, Hategan A, Griffin M, Discher D. Substrate compliance versus ligand density in cell on gel responses. *Biophys J* 86 (Part1), 617-628. 2004.
Ref Type: Journal (Full)
273. S.R.Peyton, A.J.Putnam . Extracellular matrix rigidity governs smooth muscle cell motility in a biphasic fashion. *J Cell Physiol* **204**, 198-209,2005.
274. E Hadjipanayi, V Mudera, R.A Brown. Interface integration of rapidly engineered multi-layer collagen scaffolds. *Tissue Engineering* 14, 748. 2008.
Ref Type: Journal (Full)
275. M.Watanabe, T.Shin'oka, S.Tohyama, N.Hibino, T.Konuma, G.Matsumura, Y.Kosaka, T.Ishida, Y.Imai, M.Yamakawa, Y.Ikada, S.Morita . Tissue-engineered vascular autograft: inferior vena cava replacement in a dog model. *Tissue Eng* **7**, 429-439,2001.
276. B.C.Isenberg, C.Williams, R.T.Tranquillo . Small-diameter artificial arteries engineered in vitro. *Circulation Research* **98**, 25-35,2006.
277. A.S.Meshel, Q.Wei, R.S.Adelstein, M.P.Sheetz . Basic mechanism of three-dimensional collagen fibre transport by fibroblasts. *Nat.Cell Biol.* **7**, 157-164,2005.
278. B.M.Gillette, J.A.Jensen, B.Tang, G.J.Yang, A.Bazargan-Lari, M.Zhong, S.K.Sia . In situ collagen assembly for integrating microfabricated three-dimensional cell-seeded matrices. *Nat.Mater.* **7**, 636-640,2008.
279. B.M.Gillette, J.A.Jensen, B.Tang, G.J.Yang, A.Bazargan-Lari, M.Zhong, S.K.Sia . In situ collagen assembly for integrating microfabricated three-dimensional cell-seeded matrices. *Nat.Mater.* **7**, 636-640,2008.
280. J.H.Wang, B.P.Thampatty, J.S.Lin, H.J.Im . Mechanoregulation of gene expression in fibroblasts. *Gene* **391**, 1-15,2007.
281. S.P.Hoerstrup, G.Zund, R.Sodian, A.M.Schnell, J.Grunenfelder, M.I.Turina . Tissue engineering of small caliber vascular grafts. *Eur.J.Cardiothorac.Surg.* **20**, 164-169,2001.
282. B.M.Gillette, J.A.Jensen, B.Tang, G.J.Yang, A.Bazargan-Lari, M.Zhong, S.K.Sia . In situ collagen assembly for integrating microfabricated three-dimensional cell-seeded matrices. *Nat.Mater.* **7**, 636-640,2008.
283. I.B.Bischofs, U.S.Schwarz . Cell organization in soft media due to active mechanosensing. *Proc.Natl.Acad.Sci.U.S.A* **100**, 9274-9279,2003.
284. Bywaters EGL. The metabolism of joint tissues. *J Path Bact* 44(1), 247-268. 1937.
Ref Type: Journal (Full)

285. S.R.Bibby, D.A.Jones, R.M.Ripley, J.P.Urban . Metabolism of the intervertebral disc: effects of low levels of oxygen, glucose, and pH on rates of energy metabolism of bovine nucleus pulposus cells. *Spine (Phila Pa 1976.)* **30**, 487-496,2005.
286. V.B.Kumar, R.I.Viji, M.S.Kiran, P.R.Sudhakaran . Endothelial cell response to lactate: implication of PAR modification of VEGF. *J Cell Physiol* **211**, 477-485,2007.
287. G.F.Mac, J.W.Ji, A.S.Popel . VEGF gradients, receptor activation, and sprout guidance in resting and exercising skeletal muscle. *J Appl.Physiol* **102**, 722-734,2007.
288. L.E.Niklason, J.Gao, W.M.Abbott, K.K.Hirschi, S.Houser, R.Marini, R.Langer . Functional arteries grown in vitro. *Science* **284**, 489-493,1999.
289. C.Androjna, J.E.Gatica, J.M.Belovich, K.A.Derwin . Oxygen diffusion through natural extracellular matrices: Implications for estimating "Critical thickness" values in tendon tissue engineering. *Tissue Engineering Part A* **14**, 559-569,2008.
290. K.Hobo, T.Shimizu, H.Sekine, T.Shin'oka, T.Okano, H.Kurosawa . Therapeutic angiogenesis using tissue engineered human smooth muscle cell sheets. *Arterioscler.Thromb.Vasc.Biol.* **28**, 637-643,2008.
291. N.L'Heureux, N.Dusserre, G.Konig, B.Victor, P.Keire, T.N.Wight, N.A.Chronos, A.E.Kyles, C.R.Gregory, G.Hoyt, R.C.Robbins, T.N.McAllister . Human tissue-engineered blood vessels for adult arterial revascularization. *Nat.Med.* **12**, 361-365,2006.
292. J.Yang, M.Yamato, T.Shimizu, H.Sekine, K.Ohashi, M.Kanzaki, T.Ohki, K.Nishida, T.Okano . Reconstruction of functional tissues with cell sheet engineering. *Biomaterials* **28**, 5033-5043,2007.
293. T.Wakatsuki, M.S.Kolodney, G.I.Zahalak, E.L.Elson . Cell mechanics studied by a reconstituted model tissue. *Biophys J* **79**, 2353-2368,2000.
294. J.Malda, T.J.Klein, Z.Upton . The roles of hypoxia in the in vitro engineering of tissues. *Tissue Eng* **13**, 2153-2162,2007.
295. M.K.Smith, D.J.Mooney . Hypoxia leads to necrotic hepatocyte death. *J Biomed Mater.Res.A* **80**, 520-529,2007.
296. M.K.Smith, D.J.Mooney . Hypoxia leads to necrotic hepatocyte death. *J Biomed Mater.Res.A* **80**, 520-529,2007.
297. Z.M.Rong, U.Cheema, P.Vadgama . Needle enzyme electrode based glucose diffusive transport measurement in a collagen gel and validation of a simulation model. *Analyst* **131**, 816-821,2006.
298. H.Esumi, K.Izuishi, K.Kato, K.Hashimoto, Y.Kurashima, A.Kishimoto, T.Ogura, T.Ozawa . Hypoxia and nitric oxide treatment confer tolerance to glucose starvation in a 5'-AMP-activated protein kinase-dependent manner. *J Biol.Chem.* **277**, 32791-32798,2002.

299. D.A.Brown, W.R.MacLellan, J.C.Dunn, B.M.Wu, R.E.Beygui . Hypoxic cell death is reduced by pH buffering in a model of engineered heart tissue. *Artif.Cells Blood Substit.Immobil.Biotechnol.* **36**, 94-113,2008.
300. D.A.Brown, W.R.MacLellan, H.Laks, J.C.Dunn, B.M.Wu, R.E.Beygui . Analysis of oxygen transport in a diffusion-limited model of engineered heart tissue. *Biotechnol.Bioeng.* **97**, 962-975,2007.
301. K.Y.Chan, H.Fujioka, R.B.Hirshl, R.H.Bartlett, J.B.Grotberg . Pulsatile blood flow and gas exchange across a cylindrical fiber array. *J Biomech.Eng* **129**, 676-687,2007.
302. D.Wendt, S.Stroebel, M.Jakob, G.T.John, I.Martin . Uniform tissues engineered by seeding and culturing cells in 3D scaffolds under perfusion at defined oxygen tensions. *Biorheology* **43**, 481-488,2006.
303. R.L.Carrier, M.Rupnick, R.Langer, F.J.Schoen, L.E.Freed, G.Vunjak-Novakovic . Perfusion improves tissue architecture of engineered cardiac muscle. *Tissue Eng* **8**, 175-188,2002.
304. T.Dvir, N.Benishti, M.Shachar, S.Cohen . A novel perfusion bioreactor providing a homogenous milieu for tissue regeneration. *Tissue Eng* **12**, 2843-2852,2006.
305. M.T.Raimondi, F.Boschetti, L.Falcone, F.Migliavacca, A.Remuzzi, G.Dubini . The effect of media perfusion on three-dimensional cultures of human chondrocytes: integration of experimental and computational approaches. *Biorheology* **41**, 401-410,2004.
306. Y.Xie, P.Hardouin, Z.Zhu, T.Tang, K.Dai, J.Lu . Three-dimensional flow perfusion culture system for stem cell proliferation inside the critical-size beta-tricalcium phosphate scaffold. *Tissue Eng* **12**, 3535-3543,2006.
307. F.W.Luscinskas, J.Lawler . Integrins As Dynamic Regulators of Vascular Function. *Faseb Journal* **8**, 929-938,1994.
308. T.L.Haas, J.A.Madri . Extracellular matrix-driven matrix metalloproteinase production in endothelial cells: Implications for angiogenesis. *Trends in Cardiovascular Medicine* **9**, 70-77,1999.
309. J.E.Rundhaug . Matrix metalloproteinases and angiogenesis. *J.Cell Mol.Med.* **9**, 267-285,2005.
310. N.C.Rivron, J.J.Liu, J.Rouwkema, B.J.de, C.A.van Blitterswijk . Engineering vascularised tissues in vitro. *Eur.Cell Mater.* **15**, 27-40,2008.
311. L.Cao, D.J.Mooney . Spatiotemporal control over growth factor signaling for therapeutic neovascularization. *Adv.Drug Deliv.Rev* **59**, 1340-1350,2007.
312. S.T.Nillesen, P.J.Geutjes, R.Wismans, J.Schalkwijk, W.F.Daamen, T.H.van Kuppevelt . Increased angiogenesis and blood vessel maturation in acellular collagen-heparin scaffolds containing both FGF2 and VEGF. *Biomaterials* **28**, 1123-1131,2007.
313. T.P.Richardson, M.C.Peters, A.B.Ennett, D.J.Mooney . Polymeric system for dual growth factor delivery. *Nat.Biotechnol.* **19**, 1029-1034,2001.

314. M.W.Laschke, Y.Harder, M.Amon, I.Martin, J.Farhadi, A.Ring, N.Torio-Padron, R.Schramm, M.Rucker, D.Junker, J.M.Haufel, C.Carvalho, M.Heberer, G.Germann, B.Vollmar, M.D.Menger . Angiogenesis in tissue engineering: Breathing life into constructed tissue substitutes. *Tissue Engineering* **12**, 2093-2104,2006.
315. B.Murray, D.J.Wilson . A study of metabolites as intermediate effectors in angiogenesis. *Angiogenesis*. **4**, 71-77,2001.
316. M.Raghunath, Y.S.Wong, M.Farooq, R.Ge . Pharmacologically induced angiogenesis in transgenic zebrafish. *Biochemical and Biophysical Research Communications* **378**, 766-771,2009.
317. S.Levenberg, J.Rouwkema, M.Macdonald, E.S.Garfein, D.S.Kohane, D.C.Darland, R.Marini, C.A.van Blitterswijk, R.C.Mulligan, P.A.D'Amore, R.Langer . Engineering vascularized skeletal muscle tissue. *Nat.Biotechnol.* **23**, 879-884,2005.
318. A.Stempien-Otero, A.Karsan, C.J.Cornejo, H.Xiang, T.Eunson, R.S.Morrison, M.Kay, R.Winn, J.Harlan . Mechanisms of hypoxia-induced endothelial cell death. Role of p53 in apoptosis. *J Biol.Chem.* **274**, 8039-8045,1999.
319. T.S.Li, K.Hamano, K.Suzuki, H.Ito, N.Zempo, M.Matsuzaki . Improved angiogenic potency by implantation of ex vivo hypoxia prestimulated bone marrow cells in rats. *Am.J.Physiol Heart Circ.Physiol* **283**, H468-H473,2002.
320. S.C.Hung, R.R.Pochampally, S.C.Chen, S.C.Hsu, D.J.Prockop . Angiogenic effects of human multipotent stromal cell conditioned medium activate the PI3K-Akt pathway in hypoxic endothelial cells to inhibit apoptosis, increase survival, and stimulate angiogenesis. *Stem Cells* **25**, 2363-2370,2007.
321. L.Lamalice, F.Le Boeuf, J.Huot . Endothelial cell migration during angiogenesis. *Circulation Research* **100**, 782-794,2007.
322. X.Y.Hu, S.P.Yu, J.L.Fraser, Z.Y.Lu, M.E.Ogle, J.A.Wang, L.Wei . Transplantation of hypoxia-preconditioned mesenchymal stem cells improves infarcted heart function via enhanced survival of implanted cells and angiogenesis. *Journal of Thoracic and Cardiovascular Surgery* **135**, 799-808,2008.
323. M.Kubo, T.S.Li, T.Kamota, M.Ohshima, S.L.Qin, K.Hamano . Increased expression of CXCR4 and integrin alphaM in hypoxia-preconditioned cells contributes to improved cell retention and angiogenic potency. *J Cell Physiol* **220**, 508-514,2009.
324. W.Wang, P.Vadgama . O₂ microsensors for minimally invasive tissue monitoring. *J.R.Soc.Interface* **1**, 109-117,2004.
325. C.Baudelet, B.Gallez . Effect of anesthesia on the signal intensity in tumors using BOLD-MRI: Comparison with flow measurements by laser Doppler flowmetry and oxygen measurements by luminescence-based probes. *Magnetic Resonance Imaging* **22**, 905-912,2004.
326. D.Liao, R.S.Johnson . Hypoxia: A key regulator of angiogenesis in cancer. *Cancer and Metastasis Reviews* **26**, 281-290,2007.

327. D.Shweiki, M.Neeman, A.Itin, E.Keshet . Induction of vascular endothelial growth factor expression by hypoxia and by glucose deficiency in multicell spheroids: implications for tumor angiogenesis. *Proc.Natl.Acad.Sci.U.S A* **92**, 768-772,1995.
328. E.A.Phelps, A.J.Garcia . Update on therapeutic vascularization strategies. *Regen.Med.* **4**, 65-80,2009.
329. T.C.Wright, E.Green, J.B.Phillips, O.Kostyuk, R.A.Brown . Characterization of a "blanch-blush" mechano-response in palmar skin. *J Invest Dermatol.* **126**, 220-226,2006.
330. I.B.Bischofs, U.S.Schwarz . Cell organization in soft media due to active mechanosensing. *Proc.Natl.Acad.Sci.U.S A* **100**, 9274-9279,2003.
331. P.Fernandez, A.R.Bausch . The compaction of gels by cells: a case of collective mechanical activity. *Integr.Biol.(Camb.)* **1**, 252-259,2009.
332. G.Jiang, A.H.Huang, Y.Cai, M.Tanase, M.P.Sheetz . Rigidity sensing at the leading edge through alphavbeta3 integrins and RPTPalpha. *Biophys J* **90**, 1804-1809,2006.
333. K.Ghosh, D.E.Ingber . Micromechanical control of cell and tissue development: implications for tissue engineering. *Adv.Drug Deliv.Rev* **59**, 1306-1318,2007.
334. R.T.Prajapati, M.Eastwood, R.A.Brown . Duration and orientation of mechanical loads determine fibroblast cyto-mechanical activation: monitored by protease release. *Wound Repair Regen.* **8**, 238-246,2000.
335. J.H.Lee, J.Kisiday, A.J.Grodzinsky . Tissue-engineered versus native cartilage: linkage between cellular mechano-transduction and biomechanical properties. *Novartis.Found.Symp.* **249**, 52-64,2003.
336. A.J.El Haj, M.A.Wood, P.Thomas, Y.Yang . Controlling cell biomechanics in orthopaedic tissue engineering and repair. *Pathol.Biol.(Paris)* **53**, 581-589,2005.
337. R.S.Carvalho, J.L.Schaffer, L.C.Gerstenfeld . Osteoblasts induce osteopontin expression in response to attachment on fibronectin: demonstration of a common role for integrin receptors in the signal transduction processes of cell attachment and mechanical stimulation. *J Cell Biochem.* **70**, 376-390,1998.
338. P.S.Khalsa, W.Ge, M.Z.Uddin, M.Hadjigaryrou . Integrin alpha2beta1 affects mechano-transduction in slowly and rapidly adapting cutaneous mechanoreceptors in rat hairy skin. *Neuroscience* **129**, 447-459,2004.
339. M.A.Wozniak, K.Modzelewska, L.Kwong, P.J.Keely . Focal adhesion regulation of cell behavior. *Biochim.Biophys Acta* **1692**, 103-119,2004.

APPENDIX

TABLE OF ABBREVIATIONS

2D: 2-Dimensional

3D: 3-Dimensional

CLS: Capillary-like structure

DMEM: Dulbecco's Modification of Eagle's Medium

ECC: Endothelial Cell Cluster

ECM: Extracellular Matrix

FCS: Fetal Calf Serum

FEA: Finite Element Analysis

FLS: Fluid Leaving Surface

HDF: Human Dermal Fibroblast

HIF: Hypoxia-Inducible Factor

HIS: Hypoxia-Induced Signaling

HUVEC: Human Umbilical Vein Endothelial Cell

MEM: Minimum Essential Medium

MMP-2: Matrix Metalloproteinase - 2

MMP-9: Matrix Metalloproteinase - 9

PASMC: Pulmonary Artery Smooth Muscle Cell

PBS: Phosphate buffered saline

PC: Plastic Compression

t-CFM: Tensioning-Culture Force Monitor

VEGF: Vascular Endothelial Growth Factor

LIST OF SYMBOLS

A = Area (m^2)

E = Elastic (Young's) Modulus (Pa)

g = Standard gravity (m/s^2)

J = Volumetric flux ($\text{m}^3 \cdot \text{s}^{-1} \cdot \text{m}^{-2}$)

k = Permeability (m^2)

L = Length (m)

M = Mass (Kg)

μ = Dynamic Viscosity (Pa.s)

P = Pressure (Pa)

Q = Volumetric flow rate ($\text{m}^3 \cdot \text{s}^{-1}$)

R² = Coefficient of determination

PUBLICATIONS

E.Hadjipanayi, M.Ananta, M. Binkowski, I. Streeter, Z.Lu, Z.F.Cui, R.A Brown and V.Mudera Mechanisms of Structure Generation during Plastic Compression on Collagen Hydrogel Scaffolds: Towards Engineering of Collagen. *J Tissue Eng Regen Med*, 2010

E.Hadjipanayi, R.A.Brown, V.Mudera, D.Deng, W.Liu, U.Cheema. Controlling Physiological Angiogenesis by Hypoxia-Induced Signaling.

J Control Release. 2010, 15;146 (3):309-17

Hadjipanayi E., Mudera V., Brown R.A.

Modeling fluid kinetics during plastic compression of collagen Scaffolds. *Regen. Med.* (2007) 2(5)

U.Cheema, E. Hadjipanayi, N.Tamimi, B.Alp, V.Mudera, R.A Brown. Identification of Key Factors in Deep O₂ Cell Perfusion for Vascular Tissue-Engineering.

Int..J.Artif.Organs.,2009, 32 (6):318-28.

Hadjipanayi E., Mudera V., Brown R.A. Interface Integration of Layered Collagen Scaffolds: Implications for Sheet-based Tissue Engineering.

J Tissue Eng Regen Med 2009;3:230-241

Hadjipanayi E., Mudera V., Brown R.A. Guiding Cell Migration in 3D by Durotaxis: A Collagen Matrix with Graded Directional Stiffness.

Cell Motility and the Cytoskeleton. 2009; 66:121-128.

Hadjipanayi E., Mudera V., Brown R.A. Close Dependence of Fibroblast Proliferation on Collagen Scaffold Matrix Stiffness.

J Tissue Eng Regen Med 2009; 3:77-84.

Hadjipanayi E., Fredricsson C., Mudera V., Brown R.A. Rapid Engineering of a Biomimetic Skin Substitute

Tissue Engineering Volume: 14 Issue: 5

